The University Of Sheffield.

Cold Sintering of Oxide Ceramics

Daniel Joseph Button

A thesis submitted in partial fulfilment of the requirements for the degree of Doctor of Philosophy

The University of Sheffield
Faculty of Science and Engineering
Department of Materials Science and Engineering

February 2022

“With magic, you can turn a frog into a prince. With science, you can turn a frog into a Ph.D. and you still have the frog you started with.”

— Terry Pratchett, The Science of Discworld

Acknowledgements

I would like to thank my supervisors Prof. Ian M Reaney and Prof. Derek. C. Sinclair for the help and support provided throughout this project. I would also like to thank my industrial supervisors Dr Hong Ren and Johnathan Booth for support and analysis they provided across the project.

I would like to express gratitude to Johnson Matthey for sponsoring this project, and I hope the work in this thesis proves useful.

Thank you to all of the research staff in the university that have provided training and support, allowing me to complete my project. Particular thanks to our fantastic senior engineering technician Kerry McLaughlin for all of the support, and keeping the lab running through these unprecedented times.

To all of my office and lab colleagues, thank you for the help and great memories in and out of the lab, and particular thanks to Dr Jessica Andrews for all of the cold sintering help through the project, Dr Edoardo Mantheakis for helping me with all the tape-casting work, and James Watt for without whom, Impedance Spectroscopy would still remain a mystery to me.

To my all of my friends, especially: Dave, Jacki, Sean, Vicki, and Efford, whose laughter and support have kept me sane through this PhD. Thank you to Claire and Sarah for always helping calm my anxiety when I'd had a bad day. Thank you to my family who have believed in me and helped set me on this path 12 years ago. Finally, to my wonderful partner Rachel, whose laughter, love, support, and silliness these past 4 years I couldn't have been without.

Declaration

I, the author, confirm that the Thesis is my own work. I am aware of the University's Guidance on the Use of Unfair Means (www.sheffield.ac.uk/ssid/unfair-means). This work has not been previously been presented for an award at this, or any other, university.

Abstract

The Cold Sintering Process (CSP) is a recently developed ultra-low temperature (<300^{o}C) hydrothermal sintering technique. The process involves the pressing of a powder at moderate temperatures and pressures with a small amount of transient solvent to achieve densification. It has the potential to revolutionise ceramic processing by significantly lowering energy requirements, allowing for co-sintering of previously incompatible materials due to the low sintering temperature. However, many questions relating to its mechanisms, and problems with processing remain to be solved before commercial scale up can be achieved. Two materials, zinc oxide (ZnO) and the alumina precursor, boehmite (AlO(OH)), were cold sintered in this work.

3 aspects of the cold sintering of ZnO were investigated to determine if, and understand how, ZnO transparent conducting oxides could be produced:

- The effect of starting powder size on cold sintering was examined. A 90-250nm coarse powder, and 40-80nm nano-powder were used. Both powders densified with the coarse powder results agreeing closely with published literature. Nano-powder was more difficult to densify, showing greater sensitivity to change in sintering pressure and temperature, with uncontrolled grain growth and broad grain size distribution at 300^{o}C. Preliminary impedance data revealed a OH defect core-shell structure.
- The effects of the introduction of 2% Ga doping into ZnO was studied. Ga additions significantly restricted densification, with notable grain growth not occurring until 300^{o}C. It is also likely that Ga contributed to the broad grain size distribution. The cold sintering of $Ga_{0.2}Zn_{0.98}O$ however, showed a lower volume fraction of unwanted Zinc Gallate ($ZnGa_2O_4$) spinel compared to conventionally sintered material.
- Proof-of-concept of a tape cast transparent thick-layer nano-ZnO directly cold sintered onto Kapton® was demonstrated with up to 4-layer stacked examples produced. Grain size decreased with increasing number of layers, with adhesion requiring optimisation.

The cold sintering of Boehmite focused on improving the properties of γ-alumina for catalyst applications, and lowering the sintering temperature of α-alumina.

- Cold sintering of boehmite produced translucent samples which proved to be fragile. The addition of PVA binder resulted in a mechanically stable sample, with translucency decreasing with increase in binder concentration.
- Heat treated, cold sintered boehmite transformed to γ-alumina. This method of producing γ-alumina resulted in a significant improvement in mechanical stability over conventional materials with preliminary tests showing a ~12-40x increase in compression strength and ~1.7-2.5x increase in Young's modulus.
- α-alumina produced from cold sintered boehmite showed >90% relative density at 1400°C, compared to 50-59% for conventional at the same temperature. However, CSP samples heat treated at 1400°C require optimising after showing significant cracking due to shrinkage. Crushing strength of CSP samples heat treated at 1200°C were ~2.5-8.7x higher than that of conventional at 1400°C.

Overall, the results presented in the thesis demonstrate the commercial potential of cold sintering in addition to contributing to understanding of the process.

Contents

Table of Figures

Table of Tables

Chapter 1 – Introduction

1.1 The Need for Low Temperature Sintering Techniques

1.1.1 The Need for Low Temperature Sintering

Successful densification of powdered material via sintering conventionally requires sintering temperatures at 50-75% of the material's melting temperature to achieve high relative density. Due to the high melting temperature of many materials this often leads to processing temperatures of >1000^{o}C [1]. Such high processing temperatures lead to high energy requirements and severely limit the co-sintering compatibility of many materials. It is estimated that sintering accounts for ~30% of total energy costs in the ceramic industry [2].

1.1.2 Low Temperature Sintering Techniques

Traditional methods of lowering sintering temperature include Liquid Phase Sintering (LPS), but this typically only reaches temperatures as low as ~900^{o}C, and leaves a residual secondary phase that impacts final properties [3]. Newer sintering techniques such as Spark Plasma Sintering (SPS) and Field Assisted Sintering Technology (FAST) rely on application of an electric field to produce joule heating and can achieve densification temperatures as low as 700^{o}C [4]–[6]. 'Flash' sintering has allowed for significantly lower sintering temperatures in limited cases [7], but on average requires temperatures significantly above the melting point of polymers, even if it is for short periods [8], [9].

More recently however, the focus has shifted towards hydrothermal sintering methods [10], and in particular Cold Sintering [11]–[13], a new ultra-low temperature technique that can achieve near-theoretical densities on a large range of oxide materials at <300^{o}C; a temperature range compatible with polymers. Figure 1.1 illustrates the maximum co-sintering temperatures of a number of materials, compared against several common sintering techniques.

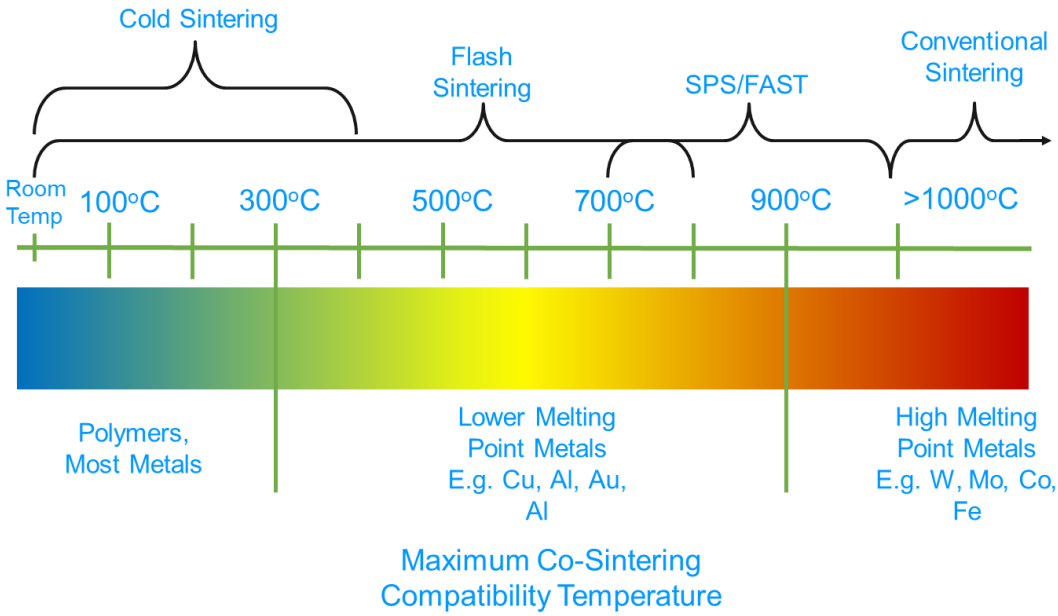

Figure 1.1: Diagram comparing the maximum co-sintering temperatures of a number of materials against the typical operating temperatures of a number of sintering techniques.

1.2 The Cold Sintering Process (CSP)

In cold sintering, the powder phase is combined with a small amount of 'transient solvent' in which it is at least slightly soluble. When placed under pressure, a significantly lower sintering temperatures (usually <300°C) can be achieved.

The mechanisms of cold sintering remain under debate but are more complex than first thought. Early works discussed a dissolution-rearrangement mechanism similar to Liquid Phase Sintering (LPS) [11]. However, newer works have disputed this, and have put forward a defect-assisted plastic deformation as the primary mechanism [14], [15]. Early cold sintered studies focused on hygroscopic materials (e.g Li_2MoO_4 [11]) which showed densification could be achieved with water as the solvent phase. Later work revealed that non-hygroscopic materials such as ZnO require more complex solvents such as acetic acid or zinc acetate solution [16]–[20].

Although the ability to densify at lower temperatures with previously incompatible materials [11], [18], [21]–[23] is attractive for commercial applications, significantly more work must be done to understand the mechanisms, and how to optimise processing conditions.

1.3 This Project

1.3.1 Overview

The aim of this project was to investigate several avenues of cold sintering that may lead to commercial applications based on questions raised in 2.14. The first of these focused on ZnO for transparent conducting oxide (TCO) applications; the second on improving current γ-alumina products and lowering the sintering temperature of α-alumina.

1.3.2 Cold Sintering of ZnO for Transparent Conducting Oxides (TCO)

TCOs are high conductivity transparent materials critical in the manufacture of a broad number of products from LCD touchscreens to photo-voltaic cells [24]. Ga doped ZnO is touted as a possible replacement for the widely used Indium-Tin Oxide (ITO) [25]–[27], a material with environmental, cost, and toxicity problems [28]–[30]. 3 different studies were conducted on ZnO to help improve understanding of CSP and to determine if ZnO-based TCOs may be feasible by this approach:

- ZnO nano-(40-90nm) and coarse-(90-250nm) powders were cold sintered at a range of temperatures (125-300^{o}C) and pressures (190-375MPa).
- 2% Ga-doped nano-powder (25-40nm) was cold sintered to investigate the effects of doping on densification, as doping is a critical component in achieving high conductivities required for TCO applications.
- A proof-of-concept method of directly cold sintering transparent ZnO (~20-30μm) onto Kapton polymer sheets was demonstrated.

1.3.3 Improving Alumina Manufacture via Cold Sintering of Boehmite

In this study, boehmite, an important precursor, was cold sintered and used to fabricate γ and α alumina pellets:

- Development of a process to cold sinter mechanically stable boehmite pellets through the addition of 5wt% PVA binder to help prevent cracking.
- Conventional γ-alumina from boehmite produces catalyst supports of poor structural integrity, as the polymorph stability window (500-800^{o}C) is well below that required for densification. Cold sintered boehmite pellets were then used to fabricate γ-alumina pellets to investigate the influence of the densification and mechanical properties.

- Full densification of α-alumina from boehmite often requires temperatures of >1600^{o}C [31], [32]. α-alumina was produced from cold sintered boehmite precursor with the intention of creating to near fully densified samples at ≤1400^{o}C.

Although significantly more research is required, the work in this thesis helps contribute to the understanding of cold sintering and demonstrates some possible commercial applications for the process.

Chapter 2 – Literature Review

2.1 What is a Ceramic?

Ceramics are defined as non-metallic and inorganic materials and are most commonly found as oxides, e.g. barium titanate ($BaTiO_3$) and alumina (Al_2O_3). However, nitrides, e.g. silicon nitride Si_3N_4, carbides such as silicon carbide (SiC), borides (TiB_2) and fluorides (lithium fluoride, LiF), are also all classed as ceramics [1].

Ceramics are ionic and/or covalently bonded structures which are crystalline. Commonly, but not exclusively, they have intrinsic properties such that they are hard, brittle, and possess a high melting point. However, ceramics are also optimised for their electrical, optical, and magnetic properties through dopant strategies which permit an enormous range of applications across many industries [1].

2.2 History of Ceramics

Ceramics have been utilised as both an engineering and artistic material throughout human history with some of the earliest known examples dating back to 24,000BC. In 1924 at Dolní Věstonice, in the now Czech Republic, more than 10,000 examples of hand-modelled, fired ceramic pieces were found along with accompanying kilns. Materials analysis performed on these ceramics have shown that they were SiO_2-Al_2O_3 earthenware densified through impurity driven liquid phase sintering. These are currently the earliest examples of late stone-age ceramics in a culture where to that point, there had been no evidence of the development of pottery [33].

The earliest example of utilitarian ceramics were uncovered at the Xianrendong Cave in Jiangxi Province, dating back to ~18,000BC which questioned he idea that late stone age 'hunter-gatherer' cultures did not utilise ceramic pottery and cookware [34].

However, the development of "advanced" ceramics has only occurred within the past 100 years, due to our increased understanding of materials science and solid-state chemistry. Advanced ceramics have found an enormous number of applications and can be split into at least two classes: functional and structural ceramics. Functional ceramics include those which have electrical, magnetic, electronic, or optical applications, whereas structural are more suited to mechanical and high temperature applications [1]. There is also reasonable rationale

for a third classification, thermal ceramics, exploited for their thermal insulation. In modern society ceramic materials have found an enormous number of applications across industries such as construction, machine tool design [1], electronics [35], and biomedicine [36]. A brief discussion of the applications of ceramics is given in the following section.

2.3 Applications of Ceramics

2.3.1 Structural Ceramics

Ceramic materials such as cubic boron nitride (CBN) and alumina (Al_2O_3) are important in machine tools due to their hardness and abrasiveness. Despite their success in machine tools, there is still a significant push to increase tool life and improve cutting properties. Therefore, ceramics are often toughened/improved through the inclusion of particulates, fibres and whiskers, and by the application of coatings [1], [37], [38], [39].

Bearings for partial hip replacement (hemiarthroplasty) and total hip replacement (Total hip hemiarthroplasty, THP) have been a core mechanical application for ceramics for many decades. When a hip is totally replaced it is made up of 2 separate components, a femoral stem with a ball head attached into the centre of the femur and an acetabular cup which is placed into pelvis where the hip ball would normally sit. A partial hip replacement does not have an acetabular cup fitted [40]. A diagram and x-ray of a typical total hip replacement is shown in Figure 2.1.

The first ceramic to be used as the coating of the cup face and femur ball head was alumina, producing an alumina-alumina contact, chosen due to its high wear resistance in contrast with polymers. High occurrences of fracture in alumina heads led to the introduction of yttria-stabilised zirconia (YSZ), but it too was eventually replaced by alumina-zirconia composites in clinical applications due to problems of hydrothermal attack [41][36].

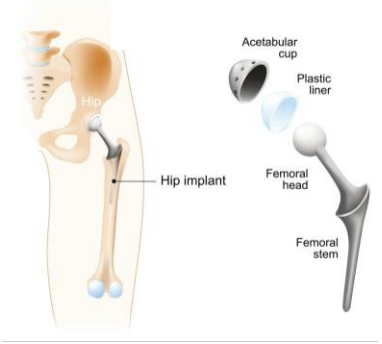

Figure 2.1: a) a diagram showing the construction of a typical total hip replacement and its position in the body [42].

2.3.2 Thermal Applications

Alumina is widely used in thermal applications due to its good heat and corrosion resistance, low reactivity, and low cost. Ceramics have consequently, the primary material for crucibles and kiln furniture for centuries. It is also widely used in thermal insulation bricks for industrial applications. The thermal properties of Al_2O_3 can be improved by fabricating highly porous materials through the addition of a pore forming agents (PFAs) such as polystyrene foam particles, and organic PFAs, such as starch and sawdust [43], [44], [45]. These agents are mixed with the alumina and burnt out at 300-600^{o}C during the sintering process leaving a porous structure. Final pore size is determined by the filler material, with rice starch found to produce 6µm pores and poppy seeds very large 1mm pores [45]. The addition of PFAs routinely leads to porosity of 60-70% with *state-of-the-art* >94% via foam gelation methods [43].

Ceramic materials also have important applications as Thermal Barrier Coatings (TBC). Gas turbines used for aircraft engines and power generation are under increasing demand to run at higher energy conversion efficiencies, and thus require ever increasing operating temperatures. Single crystal nickel based superalloys were therefore employed to reduce creep by elimination of grain boundaries with yttria stabilised zirconia (YSZ) TBCs applied to further reduce creep, thereby mitigating thermal fatigue [46]. A MCrAlY bond coat is applied between the blade and TBC to prevent surface oxidation, protect against thermal expansion differences, and improve adhesion. YSZ is then applied either through Electron Beam Assisted Vapour Deposition (EB-PVD) or Air Plasma Spraying (APS) [47].

2.3.3 Electrical Applications

Ceramics are critical to electrical applications due to their unique crystal structures. Many have insulating or semi-conducting properties or the ability to be electrically polarised (spontaneously and/or under external field). Taking advantage of these properties has formed the basis of many components and devices in modern electronics, facilitating the development of smartphones, TVs, computers, and pressure sensors [48].

Ceramics which exhibit spontaneous polarisation (polar or ferroelectric materials), allow the production of oscillators and filters, as well as components for blocking, coupling, and de-coupling of circuits. Ferroelectric $BaTiO_3$, for example, is used in the fabrication of multilayer ceramic capacitor [49], [48], [50] with ~3 trillion parts produced each year.

Pressure sensors and actuators take advantage of the piezoelectric properties of some ceramic materials, where the introduction of mechanical pressure produces an electrical response and vice versa. These applications require the use of materials that have non-centrosymmetric crystal structures. This allows an electric dipole to exist in which the centre of positive is non-coincident with that of the negative charge, with pressure adjusting the distance between the dipoles, thereby generating charge. Conversely, applying a voltage increases the distance between the dipoles and creates displacement [51].

The most commonly used piezoelectric is lead-zirconium titanate (PZT). PZT is a solid solution of ferroelectric $PbTiO_3$ and anti-ferroelectric $PbZrO_3$, which when combined in different ratios produces a variety of responses [52]. In recent years, there has been a push to produce lead-free alternatives due to the toxicity of lead oxide which, during the calcination and sintering steps, tends to volatilise. Alternatives such as barium zirconate titanate-barium calcium titanate (BZT-BCT) have shown recent promise for RT sensor/actuator applications, but no single satisfactory alternative to PZT has been developed thus far [51]–[54].

2.4 Electrical Conductivity of Ceramics

Electrical conduction through a material is caused by the transfer of charge (current) by a potential difference between two points (voltage). The ability for this charge to be transferred is governed by the density of available charge carriers. Electronic charge carriers are either electrons (e^-) or electron holes (h^+).

Materials are generally divided into conductors, semi-conductors, and insulators. Most ceramic materials fall under the insulator or semi-conductor definition, with the latter property advantageous for modern electronic devices.

2.4.1 Background Theory of Charge Transport

Classical theories of conduction describe an imaginary metal solid containing a sea of free electrons that in the absence of an applied field move via Brownian motion. From this, an initial relationship can be formed describing the proportionality under a DC field between the voltage (V) in volts, current (I) in amps, and resistance (R) in ohms, leading to Ohm's Law:

$$V = IR \qquad (2.1)$$

where the resistance is given by multiplying the resistivity (ρ) in Ohms by the length of the volume (L) being measured over its cross-sectional area (A) giving:

$$R = \frac{\rho L}{A} \tag{2.2}$$

By combining these 2 relationships and accounting for the application of an applied uniform electric field (E), an important relationship can be formed as V = EL. Therefore:

$$I = \frac{V}{R} = (\frac{EA}{\rho})A^{-1} = \frac{EA}{\rho} \tag{2.3}$$

Using these equations and taking into account of the charge carrier density (n_e), the magnitude of charge of an electron (e), and the drift velocity of electrons (v_d), a further relationship can be produced:

$$I = n_e e A v_d \quad \& \quad \rho = \frac{E}{n_e e v_d} \tag{2.4}$$

By considering the mean free path for electrons (l_t) with the average time between collisions (τ) and the equation for current density, a relationship between conductivity (σ), charge carrier density, and their mobility in a particular medium may be established:

$$\sigma = \frac{n_e e^2 \tau}{m_e^*} \tag{2.5}$$

where m_e^*, is the effective mass of electrons. Equation 2.5 is important in characterising the charge transport of conducting materials [55]. Most commonly, equation 2.5 is simplified and separated into its most recognisable form:

$$\sigma = \mu n_e e, \quad where\ \mu = \quad \frac{e\tau}{m_e^*} \tag{2.6}$$

A more in-depth proof and discussion of this is beyond the scope of these works. However a more in depth proof can be found in reference [55].

2.4.2 Mechanisms of Conduction

Mechanisms of conduction are generally described with either band theory and or through a hopping conduction mechanism. Band theory involves separating the electron energy levels closest to the fermi level into a valence band (VB) (electrons localised to the atomic outer shell) and conduction band (CB) (an electron free to conduct). Transference from the former to the latter represents the promotion of a valence electron to a conducting electron.

In conductors, the valence and conduction bands overlap with no gap, as the structure is considered as a sea of charge carriers with no electron localised to a single atom. However, for ionic and covalent bonded materials the VB and CB are separated by a zone containing forbidden energy states referred to as a 'band gap', since electrons are more strongly bonded and regarded as localised to their particular atoms/ions. For conduction to occur electrons must become de-localised from their atom and promoted to the conduction-band. This requires a certain amount of energy (known as the Fermi energy) and varies by material. For semiconductors the band gap typically tends to range from 0.5-3eV and for insulators >3eV.

In band theory, a Fermi level refers to the highest energy level occupied by an electron in the chosen material at 0K. At a given temperature, the fermi level is referred to as an imaginary energy state at which it has 50% chance of being occupied and is critical in determining electrical properties. To calculate the probability of an energy state being occupied at a given temperature the Fermi-Dirac distribution equation can be used:

$$f(E) = \frac{1}{e^{(E-E_f)/kT} + 1} \qquad (2.7)$$

Where $f(E)$ is the probability of occupation, T is absolute temperature, k is Boltzmann's constant, E_f is the Fermi energy, and E is the chosen energy for which the probability is to be found. From this equation, materials with a small band gap have enough thermodynamic energy for some electrons to be consistently promoted to the conduction band.

Electrons that originate from the valence band are defined as contributing to the intrinsic conduction. However, band gaps may be engineered via the addition of acceptor or donor dopant materials which produce a p-type or n-type response, respectively.

In semiconductors such as Si, acceptor dopants act as electron acceptors and make the dominant charge carrier of h^+, lowering the fermi level closer to the valance band and leads to what is known as a p-type material. Donors on the other hand perform the reverse, donating electrons to make them the dominant charge carrier, raising the fermi level to be closer to the conduction band and producing an n-type material. The situation however, is very different in oxides where impurities such as oxygen vacancies (V_O) and ionic compensation play a role in how dopants effect conductivity and are incorporated in the lattice [56].

2.5 Zinc Oxide

Zinc oxide (ZnO) is a commonly used II-VI, near-UV wide band gap (3.37eV) semi-conductor with a large excitation binding energy of 60meV. It has a broad range of applications from the primary pigment in 'zinc white' paint to electronic components such as a varistors [57].

2.5.1 Crystal Structures

ZnO can be found as one of 3 different polymorphs:

i) Hexagonal Wurtzite

The most common crystal structure found in zinc oxide is the hexagonal wurtzite with *P6₃mc* symmetry, which forms under ambient temperature and pressure and has a theoretical density of 5.605gcm^{-3}. The lattice structure is made up of Zn^{2+} ions surrounded by a tetrahedra of O^{2-} ions to form a polar hexagonal structure, Figure 2.2. This stable polarisation is present in the c-axis across the Zn (0001) and O $(000\bar{1})$ faces and is responsible for many of its physical and chemical properties. There is however, no polarisation in the *a*, *b* - plane [58], [59].

The bonding between the Zn and O in hexagonal form falls in-between ionic and covalent bonding, due to sp^3 hybridisation [59], [60], [61].

P6₃mc symmetry defines Wurtzite ZnO as non-centrosymmetric and thus piezoelectric. Wurtzite ZnO has one of largest piezoelectric coefficients for tetrahedrally coordinated oxides [62], [63], [64].

ii) Zinc Blende

If the angle of adjacent tetrahedral units in the Wurtzite structure is increased by 60°, the zinc blende structure is formed. This simple rearrangement of ions leads to a structure with lower ionicity than wurtzite giving it a firmly covalent structure and a higher crystallographic symmetry. This has resulted in significant interest in zinc blende ZnO in semiconductor device applications, due its lower carrier scattering and higher dopant efficiencies [62]. (Figure 2.3a)

The main issue with zinc blende ZnO is the metastable nature of the phase. Currently the only known way to stabilise this structure is epitaxial growth on a cubic substrate such as ZnS or GaAs/ZnS through molecular-beam epitaxy [58], thermal oxidation, or sol-gel deposition [62].

iii) Cubic Rock Salt

If wurtzite ZnO is placed under high pressures of ~9-13GPa, a metastable cubic rock salt structure is formed without the formation of any intermediates [58], [65]. A phenomenon enhanced by the inclusion of dopants such as Mg, Mn, and Co [66], [67]. Koster et al. [65] performed ab-initio density functional theory (DFT) modelling of $Mg_xZn_{1-x}O$ systems as a function of x. The rock salt phase became energetically favoured when $x > 0.67$ but it was noted that more theoretical studies and physical experimentation is required to fully understand this process. (Figure 2.3b)

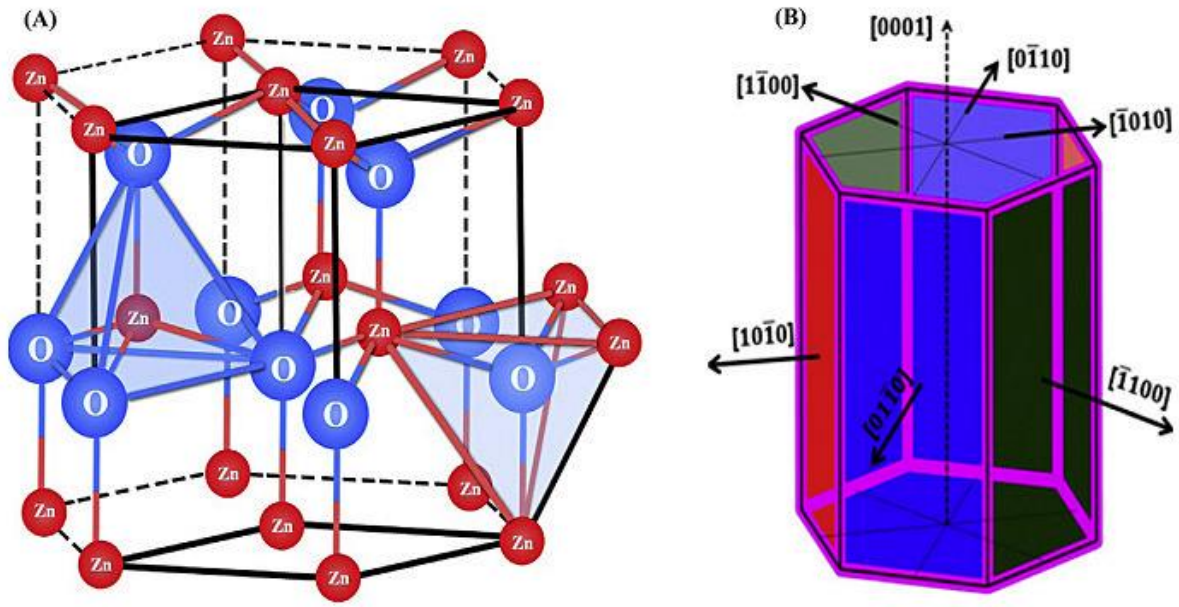

Figure 2.2: Diagram depicting the zinc hexagonal Wurtzite crystal structure. a) Depiction of the positions of Zn and O in the structure. b) Depiction of the primary crystal directions within the structure [68].

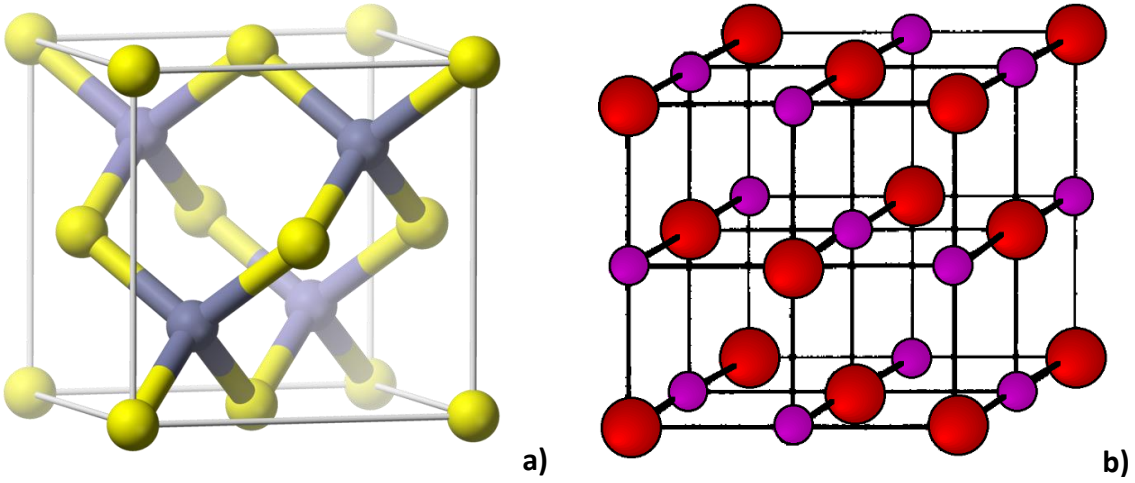

Figure 2.3: a) Depiction of the Zinc Blende ZnO structure. Where yellow atoms represent positions of O atoms and purple depicts Zn atom positions [69]. *b) Depiction of the cubic Rock Salt ZnO structure* [70].

2.5.2 Defect Chemistry of ZnO

Defect chemistry is important to understand within materials due to its impact on a wide range of material properties. The defect chemistry of ZnO is still not fully understood. Most debate revolves around the type of dominant charge carrier, the ease of Zn and O defect formation, and how these contribute to the electrical properties of ZnO and its intrinsic *n*-type behaviour.

Creation of a defect requires a formation energy (E^f) to be attained. This can be used to calculate the concentration of the different types of point defects within a solid (c) by utilising a form of the Boltzmann equation [71]:

$$c = N_{sites} \exp\left(-\frac{E^f}{k_B T}\right) \qquad (2.8)$$

where T is absolute temperature and k_B is Boltzmann's constant. N_{sites} is the concentration of sites per unit volume within a crystal where defects can occur [71]. As in equation 2.8, as E^f increases, the concentration of defects decreases. A high E^f leads to a lower likelihood of a defect to occur because of a high equilibrium defect concentration. E^f is not a constant

value and is determined by the growth and annealing conditions of the material. If the vacancy has a charge, it will be further affected by the position of the Fermi level (E_f) [72].

ZnO has native interstitial, vacancy, and Zn antisite (O_{zn}) defects. O_{zn} antisite defects are not found natively due to their high formation energy, but have been proposed as possible in nonequilibrium conditions, such as during irradiation or ion implantation. Modelling has shown however, that O_{zn} formation is unstable and they spontaneously relax to an off-site configuration [72].

The calculation of E^f for defects in ZnO has been performed by a number of methods. One of the most basic methods is to use a rearrangement of the Boltzmann equation [42] for Zn vacancies. However, this does not take interaction between defects into account and is only valid for the dilute concentrations of defects. It is nevertheless computationally efficient [73]. Another approach has been taken by Jug and Tikhomirov [74] who made use of binding energies to estimate E^f. These authors used the difference in the binding energies of similar crystal systems, but with a single oxygen atom removed. They also made the assumption that all defects were neutral which is not true for a real system. Van de Walle and colleagues [41], [44], [45] took a fuller approach, enhancing their method of calculation over several years. By taking chemical potential, the effects of the Fermi energy, and later, the valance band maximum as the basis for E^f, they produced a more flexible and realistic picture of formation energies within a ZnO crystal. However, this method is the most computationally expensive of the three discussed. This method may be used to calculate O vacancy formation energy via: [72], [75], [76]

$$E^f\left(V_O^q\right) = E_{tot}\left(V_O^q\right) - E_{tot}(ZnO) + \mu_O + q\left(E_f + E_{VBM}\right) \qquad (2.9)$$

where $E_{tot}\left(V_O^q\right)$ is the total energy of the supercell containing the O vacancy at a charge stage of q, $E_{tot}(ZnO)$ is the total energy of a perfect ZnO crystal of the same supercell, μ_O is the O chemical potential, and E_{VBM} is the energy of the valence band maximum.

The Kröger Vink defect notation displayed in Table 2.1 gives all the possible point defect types in ZnO [72]. The prevalence of each type of the native defects are dependent on the processing conditions and its stability.

Table 2.1: Table of the various possible defect types in pure ZnO [72]

Defect	Type	Vacancy Charge	Kröger Vink Notation
Zn	Interstitial	+2 / +1 / 0	$Zn_i^{\bullet\bullet}$ / $Zn_i^{\bullet}$ / Zn_i^{x}
Zn	Antisite	+4 / +3 / +2 / +1 / 0	$Zn_o^{\bullet\bullet\bullet\bullet}$ / $Zn_o^{\bullet\bullet\bullet}$ / $Zn_o^{\bullet\bullet}$ / $Zn_o^{\bullet}$ / Zn_o^{x}
Zn	Vacancy	0 / -1 / -2	V^{x}_{Zn} / V'_{Zn} / V''_{Zn}
O	Interstitial (Oct)	0 / -1 / -2	O_i^{x} / O_i' / O_i''
O	Interstitial (Split)	+2 / +1 / 0	$O_i^{\bullet\bullet}$ / $O_i^{\bullet}$ / O_i^{x}
O	Antisite	0 / -1 / -2	O_{zn}^{x} / O_{zn}' / O_{zn}''
O	Vacancy	+2 / +1 / 0	$V^{\bullet\bullet}_O$ / $V^{\bullet}_O$ / V_O^{x}

The prevalence of any given defect has been found to be strongly affected by the pO_2/pZn ratio. Oxygen vacancies have shown to form in their highest abundance in low pO_2, which is in agreement with a Brouwer diagram of the system (Figure 2.4) [77]. However, Zn interstitials have also been argued to dominate V_o in a low pO_2 atmosphere due to the low pO_2, making the Zn concentration more prominent. In high pZn vapour rich environments, Zn interstitials become prominent. Conversely, in a low pZn at >500^{o}C, Zn readily evaporates producing Zn vacancies. One of the major issues with gathering accurate measurement of individual Zn and O defect concentrations is that both donate two electrons on formation, making them hard to separate from each other [78][76].

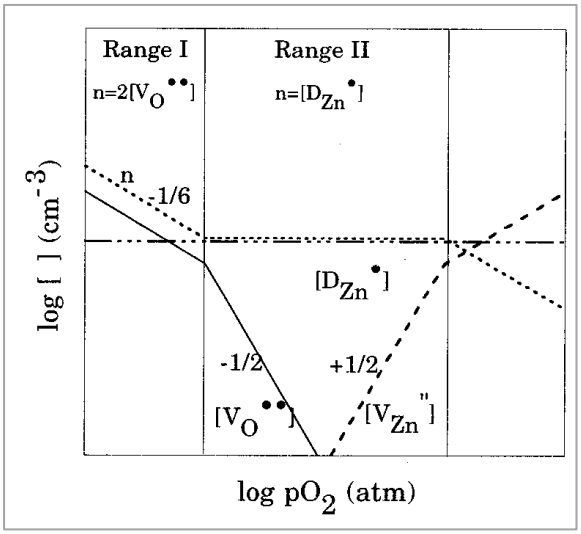

Figure 2.4: Brouwer diagram showing the effect of increased oxygen partial pressure, with intrinsic O defect concentration decreasing with increasing pO_2 concentration [77].

2.5.3 Defects and Semiconducting Properties of ZnO

Defects play a core role in the properties of semiconducting materials. However, the conduction mechanisms for ZnO are still the subject of much discussion due to the unique manner in which ZnO is an intrinsic n-type semiconductor [71].

2.5.3.1 n-type ZnO

Undoped ZnO has been postulated to exhibit an electron carrier dominant (*n*-type) response often attributed to native defects within the material. However, this native response has been the matter of significant debate for a number of years, with doubt being cast over the ability of these natural defects to act as donors [75].

Originally V_o and Zn interstitials were accredited as the reason for n-type conductivity [79], [80]. However, work has shown that V_o are unable to do this due to acting as deep donors [81][82]. While interstitial Zn is a shallow donor, and in high concentrations in a Zn rich environment, it is considered an unlikely source of the natural *n*-type conductivity, due to its high formation energy, low diffusion barrier, and low concentration [72], [74], [82].

Currently, it is thought that unintentional impurities are the source of n-type conductivity, but there is still debate as to which are the primary cause of *n*-type response. Impurities such as fluorine, hydrogen, and group III elements such as Al, Ga, B, and In have all been suggested. A brief overview of the role of impurities in semiconductor behaviour is given below: [41],[42]

i) *Hydrogen*

In many cases H can be an amphoteric dopant, either donating or accepting electrons depending on the local environment. In ZnO however, it has been observed exclusively as a donor dopant found in interstitial sites as H^+, creating a strong O-H bond with the O sub-lattice or, in some cases, substituting oxygen entirely. This is because H^+ has a low E^f and is stable, compared to H^- and H^0 which both have a high E^f and are unstable in ZnO [82][83]. The concept of hydrogen being present has come from the ease of its incorporation due to its small size, high diffusion rate and the number of ZnO manufacturing methods likely to expose the material to H impurities. Some concerns remain for H being the primary cause of stable n-type conductivity, as interstitial H has high mobility and can easily diffuse out of the material, especially at raised temperature. Thus, it is argued that H impurities do not sufficiently explain the stable electrical response at high temperatures in ZnO [75], [84], [85].

ii) *Fluorine*

In low pO_2 processing conditions, F will readily substitute for O (F_o) and, in high concentrations, will form interstitials (F_i). Florine doped ZnO has been reported to produce carrier concentrations of up to $5x10^{20}$ via chemical vapor deposition [86] and is thus thought to act as a shallow donor. However, F^+ causes a large crystal relaxation with neighbouring Zn ions, a behaviour often attributed to deep donor states [75]. However, more recent work by Liu et al. [87] argued that F cannot act as a shallow donor as first principles analysis shows F_o and F_i display deep donor and acceptor behaviour, respectively, and thus are unable contribute to carrier density. They instead suggested that F ions form a passivation layer at the grain boundaries, leading to the previously reported increase in carrier density and mobility, as well as contributing to the reduction of V_O.

iii) Group III Ions

The group III elements, Al and Ga are two of the most common substitutions to produce an *n*-type response in ZnO, but In has also been explored. Nonetheless, they all provide a large increase in donor carrier concentration. Research continues into Al and Ga doped ZnO, with the primary intention for its use as a replacement for indium

tin oxide (ITO) as a transparent conducting oxide [44], [45]. While these elements are likely to be present as impurities in some cases, contributing to the conduction, it does not explain the semi-conductive response from nominally undoped ZnO [89].

2.5.3.2 p-type ZnO

A *p*-type response occurs in a material in which holes are the dominant charge carrier. However, the difficulty of making a stable *p*-type ZnO continues to be one of the major barriers to ZnO entering many functional device applications due to the natural compensation effect produced by native defects within the material. When *p*-type dopants are added, counteracting defects form preventing the desired effect, known as ionic compensation. Current consensus suggests that additions of Group I and V elements, or ion implantation with transition metal elements such as Cu, Mn, or Co, can induce *p*-type behaviour. However, an easily reproducible device using these suggested methods is yet to be demonstrated [40][41].

2.6 Transparent Conducting Oxides

Transparent conducting oxides (TCOs) show high conductivity and transparency, with this unique combination of properties finding an enormous number of electronic applications such as in LCDs touchscreens, photo-voltaic cells, light-emitting diodes, and semiconductor lasers [24]. These materials are usually comprised of wide-band gap (>3eV) binary or ternary metal oxides. They show resistivities as low as 10^{-4}Ωcm, and an extinction coefficient (k) < 10^{-4}, where k defines how strongly a material absorbs a particular wavelength (λ) of light. However, it is also common in literature to state transparency instead of k [24].

To produce the highest conductivities and transparencies, TCOs are often heavily doped and/or contain large numbers of O vacancies. Practically all commercial TCO materials are *n*-type, including ZnO, indium tin oxide (ITO), and antimony or fluorine doped SnO_3. Out of these, ITO is by far the most commonly used due to its high conductivity and transparency [55], [91], [92].

In more recent years there has been a push to develop stable p-type TCO materials suitable for commercial use. NiO and $CuCrO_2$ are reported to have a *p*-type response, however no commercially viable device has been demonstrated to date [24]. Significant improvements in $CuCrO_2$ were shown with additions of Mg and N by Ahmadi et al. [93] who found a

conductivity of 278 S/cm^{-1}, 25% above the previous record with a transmittance of 69%. However, these still fall below commercial values available in *n*-type devices and further work is required.

2.6.1 Balancing Conduction and Transparency

The transparent nature of TCO materials originates from their wide band gap since wavelengths wider than a material's band-gap are absorbed and do not optically transmit. However, there are other factors that affect the transparency of films such as defect chemistry, crystal structure, thickness, uniformity, and surface roughness. All of these can be controlled by processing [55].

As dopant levels increase, so does carrier concentration, which increases absorption at the UV edge and decreases absorption at the IR edge. Conduction and transparency are also closely interlinked by film thickness, since an increase in film thickness leads to higher conductivity but lower transparency. This leads to compromises to produce a TCO with the best combination of properties [24].

The performance of a TCO is commonly given by the ratio of conductivity to optical absorption, or a relationship between the sheet resistance (R_s) (the resistance of a thin-film uniform in thickness) and the sum of the transmittance (T) and reflectance (R) of the material $(T + R)$. This association is shown in equation 2.10 and is dependent on wavelength: [55]

$$\frac{\sigma}{\alpha} = 1[R_s \ln (T + R)]^{-1} \qquad (2.10)$$

where α is the absorption coefficient given by:

$$\alpha = 4\pi k/\lambda \qquad (2.11)$$

Where k is the extinction coefficient and λ is wavelength.

2.6.2 Manufacturing of TCOs

Since the performance of TCOs are determined by the quality of the film, manufacturing methods that allow the best control of dimensions and a minimal number of defects are required. To achieve this high quality and low thickness, various deposition techniques are employed. However, more often techniques which produce the best films come at higher cost with cheaper techniques producing a lower quality film.

One of the most popular techniques for TCO film manufacture is magnetron sputtering. Magnetron sputtering is a physical vapour deposition method that encompasses radio frequency (rf) sputtering, dc sputtering, and reactive sputtering [55], [94]. The technique has proved popular due to its cost effectiveness and ability to produce thin films over a large area at good quality. However, the technique has the disadvantages of a low deposition rate and variations in plasma consistency, leading to film inhomogeneity, though the latter has found to be improved with a combination of rf/dc sputtering. Other techniques for film fabrication include pulsed laser deposition (PLD), chemical vapour deposition, solution deposition and spray pyrolysis [55], [95], [96].

2.6.3 Indium Tin Oxide (ITO)

Indium tin oxide is a wide band-gap (3.5-4.3eV), high conductivity, and high transparency TCO. This is achieved by doping In_2O_3 with so much tin it pushes the Fermi level into the conduction band and is thus termed a degenerative *n*-type material [95]. ITO's popularity arises from it having among the best electrical properties of currently available TCOs. However, both indium and ITO are toxic and environmentally detrimental, which has led to chronic health problems for workers handling the material during production [28], [29] and problems with disposal due to ITO leaching into the environment [30]. Materials sourcing has also proved to be an issue, with indium only being available in large quantities from a few countries. As of 2013, China was estimated to have a 59% mining production and hold 70% of the world's reserves [97].

2.6.4 Al/Ga Doped ZnO

Aluminium and/or gallium doped ZnO is one of the most promising replacements for ITO due it being non-toxic, cheap to produce, and easy to source; all while achieving high conductivity and transparency. Ga and Al donor ions substitute Zn^{2+} ions in the lattice leading to *n*-type extrinsic carriers, thereby raising the fermi level [98].

There have been a number of studies on Al and Ga doped ZnO (A/GZO) but Ga provides the best results to date, due to a much higher doping efficiency. Al ions, as well as substituting for Zn, have often been found to sit at interstitial sites where they are unable to act as donors [94]. Ga does not suffer from this problem but is significantly more expensive than Al [26], [27].

Investigations have also looked at the effect of co-doping to produce AGZO. Lui et al. [58] sintered AGZO, finding that additions of Ga increased density and improved conductivity with respect to AZO, however the material was still unable to reach the desired 10^{-4} Ωcm resistivity [25].

2.7 Alumina

2.7.1 Background

Alumina (Al_2O_3) is a widely used ceramic due to its good thermal, mechanical, and chemical durability. However, its manufacture is energy intensive, requiring sintering temperatures of 1400-1700^{o}C. Previous attempts to lower the sintering temperature have made use of better powder processing or the addition of defect or liquid phase forming additives. However, high densities are difficult at <1000^{o}C [99], [100].

2.7.2 Crystal Structure

Alumina's primary stable polymorph is α-alumina, however, there are many meta-stable polymorphs in either FCC or HCP arrangement of oxygen anions. Formation of these polymorphs is dependent on processing temperature and pre-cursor material. HCP forms of alumina phases include trigonal (α), orthorhombic (κ), and hexagonal (χ) forms, whereas FCC based phases are found in cubic (γ & η), mono-clinic (θ, θ′, θ′′, λ), and tetragonal or orthorhombic (δ for both) forms. Figure 2.5 gives a breakdown of these different forms with their relation to temperature and precursor material [101].

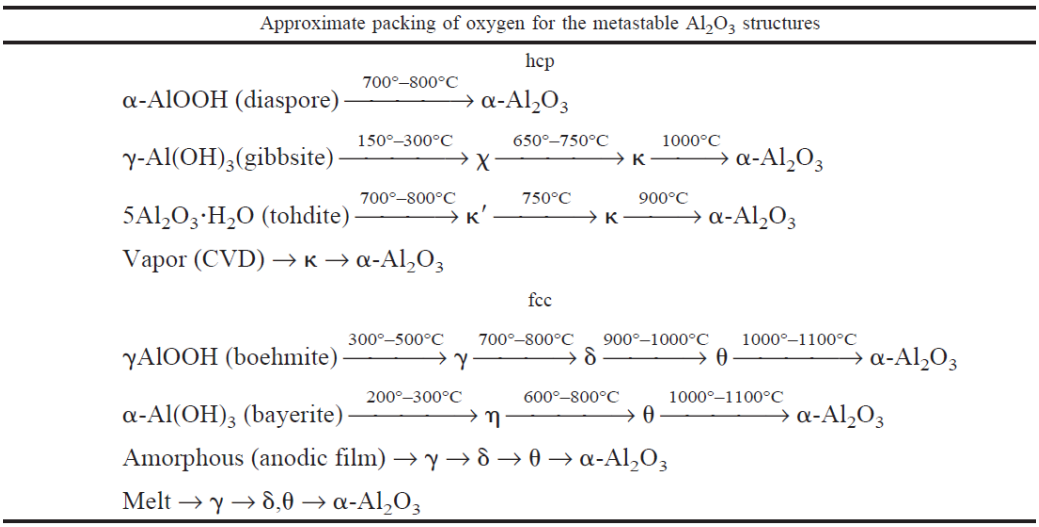

Figure 2.5: Depiction of the most common processing routes for the various precursor formations of Al_2O_3, showing the series of meta-stable and final alpha-Al_2O_3 phase transformations produced with temperature [101].

2.7.2.1 HCP Oxygen-Packing Polymorph

i) Trigonal (α)

α-Al_2O_3 has trigonal symmetry with a 10-ions per unit cell and is generally described using a rhombohedral Bravais lattice with an *R-3c* space group. The oxygen sublattice is HCP with 2/3 of the interstitial sites filled with an ordered array of Al cations. The trigonal symmetry along the $[10\bar{1}0]$ and $[\bar{1}010]$ directions means that translations have non-equivalence for the cation layer, which affects basal slip and twinning [101].

ii) Orthorhombic (κ)

κ-Alumina is a meta-stable polymorph that has been known for a significant period of time. However, the details of its unit cell parameters and space group were only determined within the last 30 years. Orthorhombic in structure, it contains a close packed oxygen stacking sequence of ABAC giving rise to $Pna2_1$ space group symmetry. Al cations sit in octahedral and tetrahedral sites at a 3:1 ratio. The crystal structure has two-layers stacked along the c-axis with the first layer containing edge-sharing AlO_6 octahedra in single chains, connected via single chains of corner-sharing AlO_4 tetrahedra. This is followed by the second layer which is made up of double chains of edge-sharing AlO_6 octahedra parallel to the a-axis, with networks of unoccupied octahedra in-between [102].

iii) Hexagonal (χ)

χ-Al_2O_3 is obtained by the dehydration of gibbsite and has several suggested unit cells. Stumpth et al. [103] and Ervin [104] both studied χ-Al_2O_3 and concluded it was a non-spinel type pseudocubic structure. However, Brindley [105] discussed χ-Al_2O_3 as having a hexagonal structure, questioning whether earlier works were mistaken, suggesting errors were possibly caused by improperly transformed Al_2O_3 in γ form.

A review by Levin and Brandon [101] reported the hexagonal structure was composed of layers with disorder in the c-direction, with oxygen anions arranged in the same structure as the gibbsite precursor, but with the aluminium cations sitting on octahedral interstitial sites of the oxygen sublattice. However, the authors cautioned that it is still difficult to ascertain which of the discussed structures is correct as current data is still subject to interpretation.

2.7.2.2 FCC oxygen-packing Polymorphs

*i) Cubic Spinel (*γ & η)

The cubic spinel polymorph is found in the γ and η forms of alumina and is described as having a "defect-spinel structure" with $Fd\bar{3}m$ space group symmetry. Oxygen anions have an ABCABC sublattice packing sequence, whereas Al cations have two possible alternating layers. Al cations can either sit only in octahedral sites, or in a mixed layer structure sitting in both octahedral and tetrahedral sites [101].

γ-Al_2O_3 is thought to have a random distribution of 8/3 aluminium vacancies across tetrahedral sites, deviating slightly from the perfect spinel [101]. The oxygen sublattice of γ-Al_2O_3 has been found to be more ordered than η-alumina, but on average has a more deformed c:a ratio of between 0.983-0.987, compared to 0.985-0.993 [106].

*ii) Monoclinic (*θ, θ′, θ″, *λ)*

The monoclinic structure is held by a large number of the metastable polymorphs. It is also one of the simplest and most well understood. It is known to have an equal distribution of Al cations across the octahedral and tetrahedral sites. θ and θ' have a *C2/m* space group symmetry, θ'' *A12/n1*, and *λ* $P2_1/c$. All of these monoclinic phases are thought to transform from γ-Al_2O_3 via cation reordering on the interstitial sites of the oxygen sublattice [101].

iii) Orthorhombic (δ)

δ-Al_2O_3 has proved to be a complex structure to decode, with much previous debate on its final structure. General agreement suggests it is formed from a spinel superlattice structure with ordered cation vacancies containing 160 ions per cell. However, further debate has surrounded its symmetry, being either tetragonal or orthorhombic. Original evidence argued that different precursors produced different structures, with δ-Al_2O_3 either tetragonal or orthorhombic when produced via melt quenching or thermal oxidation, respectively [101]. However, more recent investigations have shown that orthorhombic is the only crystal structure. Kovarik et al. [107] used atomic level high-angle annular dark field (HAADF) imaging and observed that δ-Al_2O_3 may be separated into δ_1-Al_2O_3 and δ_2-Al_2O_3. This complex pair of structures consisted of intergrowth arrangements that lacked long-range periodicity and would often superimpose upon one-another in different directions. The unit cell of δ_1-Al_2O_3 has a column-like alternating sequence of left- and right-hand Z-like patterns along the [010] direction. However, the left and right patterns are not mirror images of each other as might be expected, being offset along the [100] by 1/2α. In δ_2-Al_2O_3, the unit cell only contains one pattern in either the left or right-handed direction, with these patterns stacked directly on top of each other, leading to the periodicity of δ_2-Al_2O_3 being half that of δ_1-Al_2O_3. The complex interlinking of these two structures has led to it being described as a combined structure, denoted as $\delta_{1,2}$-Al_2O_3, which when observed represents a network of oppositely distorted parallelograms. Diagrams and HAADF images by Kovarik et al depicting this structure are shown in Figure 2.6.

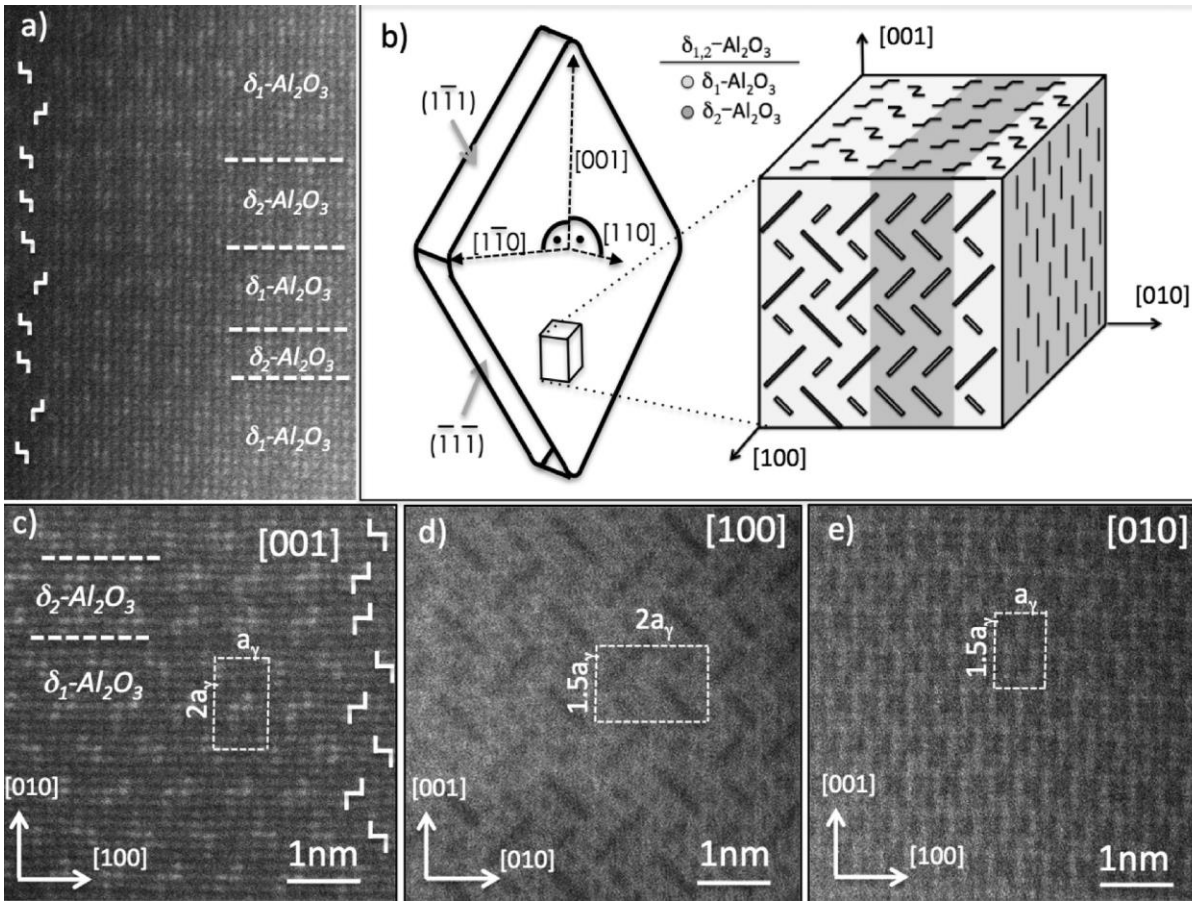

Figure 2.6: a) HAADF image in the [001] orientation showing the intergrowth of δ_1-Al_2O_3 & δ_2-Al_2O_3. b) Diagrams depicting the morphology and relationship of the observed δ_1-Al_2O_3 & δ_2-Al_2O_3 within the larger Al_2O_3 crystal. c-e) High detail atomic images of the δ_1-Al_2O_3 & δ_2-Al_2O_3 structures along the [001], [100], and [010] axes respectively [107].

2.7.3 Mineral Sources of Alumina

Most alumina comes from 3 primary mineral sources, boehmite, gibbsite, and diaspore, which are all produced via the Bayer process. In this process, bauxite is caustically digested in NaOH at 150-200°C and then filtered, before the desired minerals are acquired at the precipitation and calcining stages. Other precursor forms are possible including tohdite and bayerite however these are out of scope for this work [108], [109].

2.7.3.1 Boehmite (γ-AlO(OH))

Boehmite (or aluminium oxyhydroxide) is a widely used precursor material with special interest due to its ability to transform into γ-alumina for catalytic applications. Other possible uses include replacing Gibbsite as the primary source of Smelter Grade Alumina (SGA), due to it theoretically being less energy intensive. However, research is ongoing to develop a method of precipitating boehmite effectively during the Bayer process [110], [111].

The crystal structure of boehmite is a tetragonally distorted defect spinel arrangement with a CCP anion lattice structure in which the hydroxyl groups on the surfaces of each layer join to other hydroxyl groups in a zigzag arrangement of hydrogen bonds parallel to the α-axis [112].

Dehydration of boehmite takes place between 400-600^{o}C, dependent on its crystallinity and previous thermal history, transforming into γ-alumina [112]. The mechanism of dehydration is complex and still under investigation. However, it is currently thought that it is a chemically controlled topotactic process with elements of diffusion, which increases as the process progresses. Dehydration involves the removal of physiosorbed and then chemisorbed water from the system followed by the transfer of protons to adjacent hydroxyl groups between layers. This leads to a structural collapse which involves the migration of Al ions from the octahedral to tetrahedral sites, producing the spinel structure found in γ-alumina and the formation of a micro-pore system orientated parallel to the [001] direction inside a γ-Al_2O_3 skeleton [110], [112]–[114]. The specifics of this mechanism have been under debate over many years. In the 1970s, Wilson [115] argued that the system is incredibly similar to other dehydration mechanisms, such as in lepidocrocite. They proposed that Al migrated due to chains of octahedral Al becoming too close. However, computer simulations and further experimentation have shown that structural collapse does indeed take place. Wilson's mechanism also fails to take into account structural relaxation. It was also shown by Miller that the process is endothermic with Al migration being the rate-limiting step in the process [110], [112].

Post dehydration, further temperature increases can lead to the formation of several other polymorphs, with 700-800^{o}C producing δ-alumina, 900-1000^{o}C θ-alumina, and finally stable α-alumina at >1000^{o}C [101].

2.7.3.2 Gibbsite ($Al(OH)_3$)

Gibbsite is another of the primary components that make up bauxite. It has a sheet structure made up of double layers of OH^- ions, with two thirds of the octahedral sites occupied by Al ions. These platelets most commonly show monoclinic symmetry but triclinic can occur. Hydrogen bonding between OH^- groups between each double layer is also present [116]. Gibbsite has only 2 metastable polymorphs on heating: χ-alumina at 150-300^{o}C and κ-alumina at 650-750 ^{o}C, before transforming to α-alumina at >1000^{o}C [101].

2.7.3.3 Diaspore (α-AlO(OH))

Diaspore is an aluminium oxide hydroxide, the third major component of bauxite with an orthorhombic crystal structure. Al resides in octahedra within an HCP array of O atoms, where the octahedra share four edges. This forms a one-dimensional infinite aggregate parallel to the c-axis, with each anion being shared by three octahedra [117], [118]. Diaspore, unlike many other alumina precursor materials, shows no known pseudostable polymorphs and will directly transform into α-alumina at 700-800^{o}C [101]. One of the major applications of Diaspore is in the jewellery industry, as gem-quality materials is found in locations like Ilbir Dağ in south-west Turkey [119].

2.7.4 Defect Chemistry of Alumina

The defect chemistry of alumina is thought to be fairly well understood and has been the subject of interest for many decades, especially α-alumina. For stable undoped α-alumina, defects are most commonly found as Frenkel or Schottky pairs. However, all intrinsic defects have large formation energies, with even the lower formation energy types like Schottky defects requiring 4eV. This leads to a low equilibrium concentration at several ppm or fewer [120], [121].

2.7.5 Electrical Properties of Alumina

The electrical response of alumina varies significantly dependent on temperature, pO_2 concentration, and crystal structure. Under normal conditions at room temperature, it is a large band gap insulator. However, as the temperature increases, ionic transitions to mixed, then to electron/hole dominated conduction. Reported temperatures of some of these changes in conduction mechanism vary widely, and are heavily influenced by pO_2, crystal structure and the concentration of impurities. However, transfer to electrical conduction is reported at ~>1600^{o}C [122], [123].

Variation in pO_2 at high temperatures affects electron and hole concentration with *p*- and *n*-type dominant at high and low pO_2, respectively. This was originally attributed to Al^{3+} ion vacancies and interstitial conduction, as O vacancy conduction was deemed improbable due to a high activation energy [122], [123]. However, Harrop and Creamer [124] argued that variation in the valence of Fe impurities could be responsible, with pO_2 affecting the concentration of any given state and creating a source of electrons/holes. However, more

recent investigations by Will et al. [125] found conductivity slopes in their single crystal alumina samples indicating intrinsic semiconduction.

Much work has shown that single crystal alumina has a much higher conductivity than polycrystalline, as well as transitioning between conductive states at slightly lower temperatures. This is thought to be due to the absence of grain boundaries in single crystals. Impurities and pO_2 also show less of an effect on conductivity in single crystals compared to polycrystalline materials [122], [75], [76].

2.7.6 Mechanical Properties of Alumina

Like many ceramics, Al_2O_3 has low elasticity and toughness but high strength and hardness. This generally leads to a material with good wear resistance, depending on sintering conditions, porosity, grain size, and purity [126]. Hardy & Green [100] studied the mechanical properties of partially sintered alumina since maintaining a high porosity has important implications for industrial applications, such as in catalysts. A sintering temperature high enough to encourage necking is critical to produce significant density increase (<1100^{o}C) and leads to improved mechanical properties and density while maintaining the required porosity.

While alumina shows good general mechanical properties, flexural strength has always been low. Teng et al. [127] showed this could be improved by reducing the grain size and introducing Al_2O_3 and SiC nano-particles. The additions also led to the transition of the fracture mode from intergranular to transgranular, due to reinforcement of the grain boundary. Grain size reduction was also found to improve mechanical properties, a conclusion further supported by O et al. [128].

2.7.7 Chemical Properties of Alumina

Alumina is widely utilised for its chemical properties across its stable and metastable forms due to its high corrosion resistance and chemical stability, allowing it to be utilised effectively as a corrosion resistant coating [129] and catalyst support [130]. However, the quality of the alumina has a significant impact on its efficacy. Alumina often contains impurities and is also sintered at lower temperatures with the use of sintering aids such as Kaolin. With these impurities present, alumina tends to show excellent acidic resistance but incredibly poor strong alkaline resistance, showing significant corrosion after a reasonably short period, partly enabled by the formation of silicon glassy spheres which weaken the structure [131].

However, work by Qin et al. showed that if catalyst supports were manufactured using ultra-high purity (99.99%) alumina from boehmite [132], the corrosion resistance was excellent in both strong acid and strong alkali [133].

The most common forms of alumina for catalyst supports are of γ or η, which have applications in the automotive and petrochemical industries. The optimised response for γ- or η-alumina arise from the acidic character of their surfaces [134], [135] allowing for solid-acid catalysis of a number of species such as in methanol dehydration. Methanol is adsorbed onto the alumina surface, forming methoxy and hydroxyl groups, which are then independently converted into dimethyl ether and water [136].

2.8 Sintering

2.8.1 Process of Sintering

The process of sintering involves the diffusion and mass transport of particles to remove pores from a material and increase bulk-density. This is traditionally performed at ~$0.8T_m$ (in ^oC) however, there are a number of other techniques that will be discussed that allow for much lower densification temperatures [137], [138].

2.8.1.1 Stages of Sintering

It is generally agreed that there are 3 main stages of sintering:

i) *Initial Stage*

In this stage, rapid formation of necks occurs between particles in contact with each other. Only a small amount of densification takes place but the contact area between particles increases by 20%, with this stage ending when the particle neck radius is 0.4-0.5 of the total particle radii. This stage also takes into account micro-necking that occurs when particles initially come into contact which is sometimes argued as stage 0 [1].

ii) Intermediate Stage

This stage is where the majority of the material densification takes place to ~0.9 theoretical. The pores reach an equilibrium shape and the microstructure is made up of a near-continuous network of pore channels. These pore channels shrink and grain-growth occurs eventually leading to 'pinching off', leaving them isolated.

iii) *Final Stage*

In the final stage of sintering, pores become pinched off at the corners of grains and many continue to shrink until total elimination. However, it is common for some pores to trap gasses making their removal more difficult. As this stage, the pore volume fraction approaches zero in an asymptotic manner.

2.8.2 Driving Forces of Sintering

The core driving force behind the sintering process is the lowering of free energy within the system. A majority of the free energy is often described as being associated with the free-surface energy within the system, also called a solid-vapour interface. It is the replacement of the solid-vapour interface with a solid-solid interface that leads to lowering of free energy. This change in free energy can be described thermodynamically as:

$$\delta G_{system} = \delta \int \gamma_{SV} dA_{SV} + \delta \int \gamma_{SS} dA_{SS} \qquad (2.12)$$

where δG_{system} denotes the change in total energy of the system. γ_{SV} and γ_{SS} are the energies per unit area of the solid-vapour interface and solid-solid interfaces respectively, and A_{SV} and A_{SS} denote the surface area of the solid-vapour and solid-solid interfaces respectively [137].

For sintering to occur according to equation 2.12, δG_{system} will always be negative as it indicates there is a driving force. The first term will always be negative due to the reduction of the solid-vapour interface. The second term however can either be positive or negative depending on the speed of grain growth. If no grain-growth is taking place it will always be positive [137], [1].

There are different ways in which microstructural development can take place during sintering. The primary mode is densification, where the γ_{SV} is larger than γ_{SS} leading to the transport of atoms to the pore faces and an increase in A_{SS}. In contrast, there are competing non-densifying mechanisms: i) coarsening, which is the process whereby diffusion and transport leads to a reduction in pore surface-area; ii) lowering A_{SV} in which the total pore

volume does not change and iii) lowering of the free energy due to chemical reactions, which tend to have a much higher driving force than densifying mechanisms. These reactions are often unwanted and can cause problems in some sintering processes [137], [1].

2.8.3 Sintering Mechanisms in Conventional Techniques

Diffusion within a solid material involves the movement of defects which must meet specific activation energies to overcome adjacent atomic resistances. The diffusion coefficient of a thermally activated process is defined by the equation:

$$D = D_0 \exp\left(\frac{-Q}{RT}\right) \qquad (2.13)$$

where D_0 and Q are system dependent constants and Q defines the activation energy in joules.

The mechanism of diffusion is dependent on several factors, but is generally broken down into lattice, surface, and grain boundary diffusion [1].

Lattice diffusion occurs through the bulk material and is subject to a number of different mechanisms. Most commonly this involves diffusion through vacancies and interstitials in the bulk material. However, when these mechanisms become less favourable, interstitial diffusion takes place. This is where atomic/ionic exchange occurs between two neighbours that are not constrained to be of the same type.

Surface and grain boundary diffusion takes place within a few nm (~0.3-0.5nm) of either the surface of the particles or grain surfaces. Both are highly defective in nature, have fewer ionic neighbours, resulting in an activation energy is lower than the bulk. The relation between activation energies of each diffusion type is:

$$Q_l > Q_{gb} > Q_s \qquad (2.14)$$

where Q is activation energy, and the subscripts $l, gb, \& S$ represent lattice, grain boundary, and bulk solid states respectively [1].

2.8.3.1 Solid State Sintering (SSS):

SSS requires the highest temperatures by a significant margin of all densification processes as the only driving force is thermal activation of the core material. However, there are a number of different diffusion mechanisms that take place during SSS, dependent on whether the material is crystalline or amorphous.

2.8.3.1.1 Crystalline Densification

Densification may be split into 6 primary mechanisms which may be further divided into densifying and non-densifying (coarsening) [1], [39], [40], [137]. Densifying mechanisms include grain-boundary diffusion, grain-boundary lattice diffusion, and plastic flow. All of these densifying mechanisms involve the source of atoms coming from the bulk of the grain, allowing for particle centres to approach each other leading to densification. Non-densifying mechanisms primarily involve diffusion of atoms along the grain surface which leads to coarsening. These non-densifying or "coarsening" mechanisms include: surface diffusion, lattice diffusion, and vapour transport, with each of these mechanisms taking place at various stages of the process. Crystalline SSS has been modelled in an effort to understand the microstructural changes that are taking place. While a comprehensive analysis of all modelling methods is beyond scope, several popular modelling methods are discussed below.

i) Two-Particle Model

The two-particle model proposed originally by Kingley and Berg still remains as one of the most popular methods for explaining the basic mechanisms of polycrystalline sintering. The model makes the assumption that 2 perfectly spherical particles are in contact, limiting the model to describing the initial stages of sintering, as well as not taking into account asymmetry and rearrangement. It considers the principal radii of the curvature of the neck, the area of the neck surface, and the volume of material transported to the neck. The model assumes that the neck is circular but ignores the boundary energy, further limiting its application.

ii) Simple Pore Model

Coble [141], [142] in 1961 developed an intermediate model of sintering for both pores and grains. The model assumes an ideal system, where each particle was represented by an equally-sized tetrakaidecahedra, with cylindrical pores uniformly positioned at its edges, the

structure of which is shown in Figure 2.7. The uniform distribution of the pores leads to an equal chemical potential across all the particle systems and so non-densifying mechanisms cannot take place. Equally, plastic flow cannot occur as the stresses in the assumed system are not high enough, leaving only lattice and grain boundary diffusion [1].

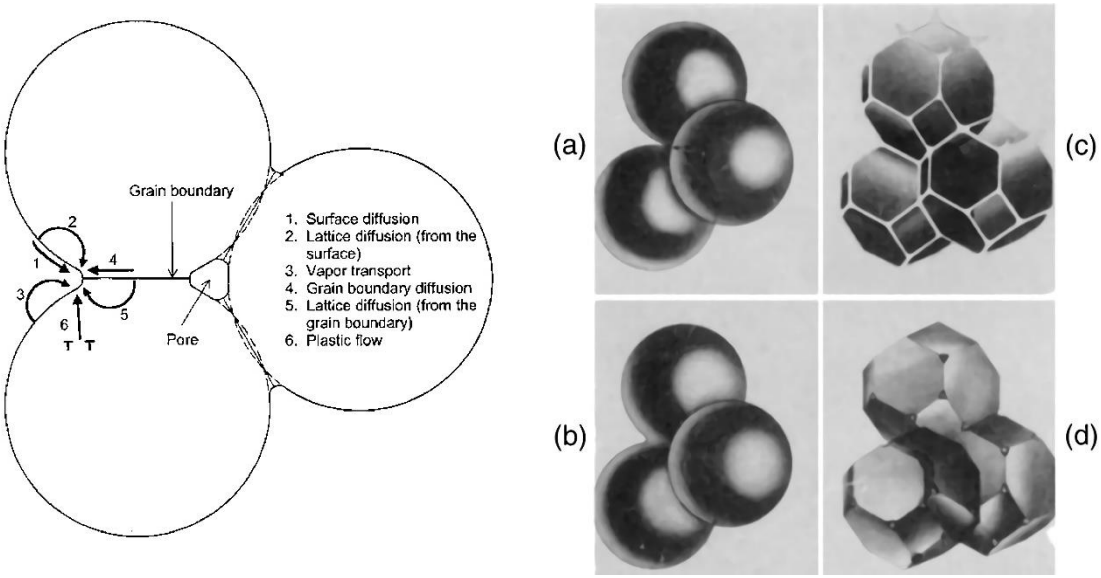

Figure 2.7: Left: Diagram depicting the two-particle model of sold state sintering during the early necking stage. Right: An idealised model of sintering, depicting the two particle and simple pore models in tandem. a-b depict initial particle contact followed by a necking process between the particles (two-particle system), and c-d where necks are assumed to grow to a point where particles can be depicted as tetrakaidecahedron, first with pore-channels along the grain edges, finally being pinched off leaving only pores as tetrahedral inclusions at the corners where the four grains meet (Simple-pore model) [1].

iii) Criticisms of these Models

Despite all of the assumptions made by these models, they are still used in sintering research, as they tend to fit experimental data [143], [144]. However, these models along with many others are heavily criticised by Exner [145], who reviewed a number of the popular methods of modelling SSS. Although it was acknowledged that these methods show excellent fit to most produced data, the large number of assumptions they make gave little to no understanding of the microstructural processes taking place. The difficulty of modelling microstructural mechanisms however, arises from SSS being made up of many different mechanisms which interact and overlap. There have also been other criticisms of the assumptions. Pan [121] discussed that these models ignore surface energy, leading to a number of limitations, such as how Coble's model no longer applies to the sintering of nanosized particles due to high surface energy dominating the driving force.

2.8.3.1.2 Viscous Densification

For amorphous materials, necking still occurs between particles, however, it is a far more complex process with ill-defined material transport paths. This singular densification mechanism is known as viscous flow and takes place across the entire volume of the material. The process is complex and lacks the defined mechanisms of lattice and surface diffusion/sintering. Material flows at a much lower viscosity than its crystalline counterpart and leads to a decrease in free energy, as there is a reduction in the solid-vapour interface. Details of this method of sintering are beyond scope however, modelling viscous flow is a complex matter and often leads to a significant number of assumptions to develop flux equations [1], [146].

2.8.3.2 Liquid Phase Sintering (LPS):

Liquid Phase Sintering is a method of lowering the energy requirements of SSS via the introduction of a secondary phase in which the primary material is soluble and has a T_m within the sintering range. The presence of this secondary phase 'wets' the substrate upon melting and helps to increase mass transport. This can lead to higher final densities and lower sintering temperatures. It also allows for the sintering of materials that traditionally would not be possible via SSS, such as Si_3N_4 and SiC [1], [147].

One of the major disadvantages of traditional LPS is that the liquid phase remains present at the end of the sintering process. This often produces a product with poorer material properties than its solid-state sintered counterpart and thus, can make LPS an unsuitable technique for the densification of certain products, such as those requiring high temperature mechanical strength, or for electronic and magnetic devices.

Choice of secondary phase is critical, with one of the most important aspects of this being the ability to wet the primary phase in its liquid state. Good wetting gives faster densification rates due to higher diffusion and lower viscosity of the liquid phase [3]. An important aspect of the liquid phase is the pressure that it exerts on the grains, which can contribute significantly to the driving force, equivalent to placing the system under hydrostatic pressure. This pressure can be defined as: [1]

$$\Delta p = -\frac{2\gamma_{lv}}{r} \quad (2.15)$$

where γ_{lv} defines the liquid-vapour surface energy, and r the radius of the particles in question. While LPS shares many similarities to SSS, there are some significant modifications, with the 3 stages being rearrangement, solution-precipitation, and Ostwald ripening [1], [137], [3], [148]. A diagram illustrating these stages is given in Figure 2.9.

i) Rearrangement

During this stage, the liquid phase melts and redistributes itself between the particles and into pores via capillary forces. Once sufficient wetting has occurred particles rearrange themselves due to surface tension and any sharp corners and contact points between agglomerated particles dissolve. This lowers the interfacial energy with the knock-on effect of smoothing particle surfaces, allowing for more efficient packing of particles. The higher the volume of liquid phase, the more densification that will take place at this stage. Out of the 3 stages of LPS, rearrangement is by far the shortest and usually only lasts a few minutes.

ii) *Solution-Precipitation*

Once rearrangement within the system slows to a sufficient point, the solution-precipitation mechanism becomes dominant. During this stage, particles at positions of high potential energy are dissolved and their mass is transported through the liquid phase, depositing at positions of low potential energy. Throughout, solution-precipitation coarsening takes place with the amount of liquid phase present affecting the final morphology of the grains. At high liquid concentrations, grains will favour a more rounded shape, but at lower concentrations polyhedral shapes are favoured due to better packing efficiency.

iii) Ostwald Ripening

This stage is the slowest of all the densification stages, due to the large diffusion distances caused by the coarsening of grains. During Ostwald ripening, a rearrangement of the grain-morphology takes place to accommodate better packing efficiency. This can also lead to the liquid phase flowing into any previously isolated pores, increasing density. Polycrystalline materials can also go through a process of secondary rearrangement, which can lead to the breaking up of crystallites to form individual particles.

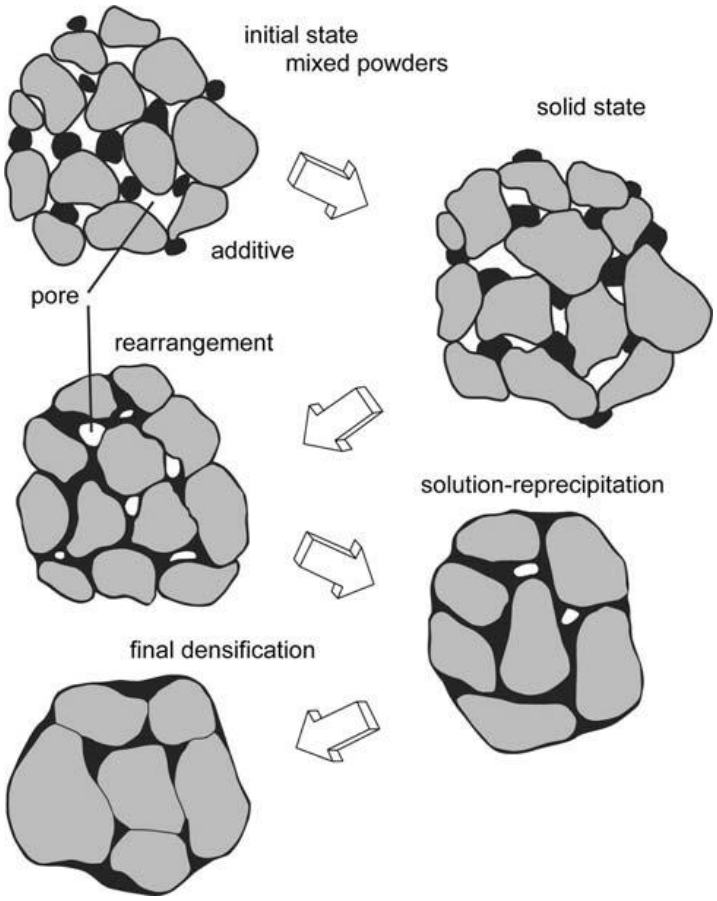

Figure 2.8: A diagram depicting the changes that take place at a microstructural level during LPS, with the black representing the liquid phase melt during the process. Once melted this phase spreads filling pores and allows grain rearrangement to take place [3].

2.8.3.3 Stress-Assisted Sintering

External factors may also be used to increase the driving force of sintering. A common technique is the application of pressure during sintering, such as in hot pressing or hot isostatic pressing. In general, pressure provides significant driving force compared to the surface-vapour interface, and has the advantage of enhancing densifying mechanisms, such that non-densifying mechanisms may be disregarded [1], [148]. There are extra considerations to take into account when hot pressing, in the form of the induced diffusion mechanisms. Lattice and grain boundary diffusion are present just as in SSS and LPS. However, plastic deformation, viscous flow, grain boundary sliding, and particle rearrangement all contribute to increasing density. The calculation of densification rate is also more complex for LPS compared to SSS, and can be expressed as [1]:

$$\frac{1}{\rho}\frac{d}{dt} = \frac{HD\phi^n}{G^m kT} p_a^n \quad (2.16)$$

where H is a constant, D is the diffusion coefficient, G is the grain size, k is Boltzmann constant, T is absolute temperature, and m & n are exponents which are defined by the mechanism of sintering. ϕ is known as the stress intensification factor and accounts for the effect porosity has on the magnification of internal pressure which decreases as density increases:

$$\phi = \frac{1}{1-P} = \frac{1}{\rho} \quad (2.17)$$

where P is the porosity of the solid. However, this equation assumes that all pores are perfectly spherical. Since ϕ is related to the ratio of the external cross-sectional area to internal cross-sectional area, pore shape has a major impact, meaning a more complex approach is required [1]. Traditionally, hot pressing takes place at high temperatures of 1000-2200^{o}C and relatively low pressures of 10-50MPa. Dies are often graphite based to prevent reaction with the ceramic material at such intense conditions [148].

2.8.4 Low Energy Sintering Techniques

2.8.4.1 Spark Plasma Sintering (SPS)

Spark Plasma Sintering (SPS) is a technique that makes use of an applied DC voltage (normally <10V) combined with pressure (50-250kN). This process allows for dense material to be produced at speeds much quicker than traditional techniques, as well as the synthesis of new compounds in a single step [137], [149]. A wide variety of both ceramic and metal materials have been sintered via this method such as alumina, zirconia, and hydroxyapatite [150]. The process involves densification inside a conductive die (graphite) in a controlled atmosphere for both conductive and non-conductive material. Conductive materials are Joule heated via a pulsed DC current which promotes a high sintering rate. Non-conductive materials do not undergo Joule heating, but sintering occurs by efficient heat transfer between from the die [149]. Heating and cooling rates are as high as 1000^{o}C/min which allows the process to be much quicker than traditional sintering techniques [149].

2.8.4.2 Flash Sintering (FS)

Similar to SPS, flash sintering is another field assisted technique that was developed more recently. The primary differences between FS and SPS is that the electric field is much larger (>60Vcm^{-1}) and applied directly to the green-body. When this is combined with sufficient temperature, sintering occurs in less than a few minutes [8]. As FS is still a technique in its infancy, research is still being performed to understand the mechanism and to determine the extent of potential commercial exploitation.

A general procedure for FS involves a green body being pressed into the desired shape (pellet or dog-bone) with electrodes attached to either end. The sample is placed into a furnace with the electrodes in contact with a power supply. The temperature is raised and a large field is applied across the sample. At sufficient temperature and field, a 'flash event' occurs almost immediately densifying the sample. This event involves thermal runaway generated by Joule heating from the field, and there is a significant drop in conductivity, with a sudden bright emission of light [9].

Significant interest has been generated around flash sintering for industrial applications due to the lower temperature and time required for densification. In 2011, Muccillo et al. found that 8YSZ flash sinters at 900^{o}C, ~600^{o}C below its normal sintering temperature [151]. When Nie et al. combined flash sintering with the cold sintering process (CSP), ZnO was found to flash sinter at room temperature [7]. Flash sintering has the ability to densify material with almost no coarsening [8]. Disadvantages of Flash sintering however include: i) it is an autocatalytic process, with very little control once the flash event occurs and ii) heterogeneous current concentration (hot-spots) within components that are larger than a few millimetres leads to anisomorphic properties [8].

2.8.4.3 Cold Sintering Process (CSP)

CSP has been recently developed and has shown to densify materials at significantly lower temperatures than previously thought possible (<300^{o}C). In CSP, the material to be sintered is combined with a small amount (a few wt%) of a transient solvent (often water). The material is placed into a die and put under pressure and heat which leads to densification. This technique has been the subject of significant research due to the potential of not only lowering energy costs, but facilitating the combination of disparate materials (ceramics, polymers and metals) previously not possible due to processing temperature constraints.

2.8.4.3.1 History of Cold Sintering

While cold sintering shows novelty, this technique has a long history of research that has led to its development. Its roots can be found in liquid phase sintering but the most significant milestones leading to its evolution are found in hydrothermal synthesis. The first indications of pressure assisted hydrothermal sintering were shown by Roy et al. in the 1970s, who combined Portland cement with water and hot pressed them at ~250^{o}C, producing material with near theoretical densities and excellent mechanical properties [49], [50]. This was followed by Yamasaki et al. [51], [52] who developed a process known as 'Hydrothermal Hot-Pressing' (HHP) for densifying silica at ~350^{o}C. This process involved the use of a specially designed hot-press, with a plunger design containing a zone for the liquid phase to retreat. Pressure and heat were then applied on the material leading to densification. HHP was then shown to be able to densify a number of other materials such as cement, calcium carbonate, $BaTiO_3$, and cubic zirconia with a subsequent heat-treatment at 1350^{o}C [51], [52].

Other more recent methods of hydrothermal sintering include 'Reactive Hydrothermal Liquid-Phase Densification' (rHLDP) by Vakifahmetoglu et al. [10] In this technique, cold-pressed green bodies of pre-cursor materials are infiltrated by a secondary phase over a time, reacting hydrothermally as the temperature is raised. This technique was demonstrated by using precursors of cold-pressed TiO_2 infiltrated by $Ba(OH)_2$-$8H_2O$ and allowed to react for up to 72 hours at varying temperatures. It was shown that densities of up to 90% theoretical could be achieved, but this came at the cost of a long processing time and the need for the identification of specific pre-cursors.

Concurrently to the publication of the rHLDP method, Pennsylvania State University published their works on the Cold Sintering Process (CSP), inspired by Yamasaki et al's earlier HHP data [51], [52]. In this process, a material is mechanically mixed with a small amount of solvent (usually water) to ensure sufficient coating of particles. This mixture is then placed in a die and hot pressed at <300^{o}C for up to an hour, in which time hydrothermal densification mechanisms take place.

The first studies demonstrated a range of cold sintered materials using water as the solvent, including NaCl, a series of molybdate based materials ($K_2Mo_2O_7$, $Na_2Mo_2O_7$, Li_2MoO_4), and V_2O_5 [11]. However, since initial publication a far broader range of materials has been densified with the use of a larger selection of solvents, as well as minor adjustments to the

technique for some materials (e.g. $BaTiO_3$) [55], [56]. The need for other solvents originates from the lack of solubility of a number of materials in water because, similar to LPS, at least partial dissolution of the material is critical to achieving densification. For some materials such as ZnO, this has included using acetic acid or Zn acetate [15], [16], [19].

To densify some materials, a change in solvents and an extra heat-treatment step is required, often due to the material exhibiting incongruent dissolution. For $BaTiO_3$, the presence of water causes leaching of Ba, leading to passivated layers of TiO_2 combined with non-homogenous distributions of Ba rich zones throughout and little densification. This problem is solved with the addition of a $Ba(OH)_2/TiO_2$ suspension, which forms a glass phase preventing Ba leaching. A final annealing step at ~950^oC removes this glass phase, transforming it into homogenous crystalline $BaTiO_3$ [157]. A similar intermediate-step process has been found to be required to densify other ternary compounds such as $SrTiO_3$. Boston et al. [158] found that cold sintering $SrTiO_3$ at 180^oC, with additions a $SrCl_2/TiO_2$ solution followed by a similar heat treatment at 950^oC, produced material with >96%.

2.8.4.3.2 Mechanism of Cold Sintering

The mechanisms of cold sintering are still under debate, the model proposed by Maria et al. [13] described a 2-stage dissolution-precipitation process, with many similarities to that of LPS.

The first stage of densification was said to proceed via uniaxial pressure assisted by the liquid phase, which increases lubrication between particles. With pressure thought to distribute the liquid phase throughout the green body and help drive solubility, with sharp corners and edges dissolving first to allow for more efficient packing. Over time the pressure aids compaction, re-arrangement, and grain boundary creep within the green body.

Once the temperature has been raised a second stage is described, where the increase in temperature under pressure further raises solubility. This leads to the formation of a supersaturated solution which increases mass transport and rearrangement of particles throughout the material, which combined with the applied pressure leads to densification as pressure centres are driven together.

Over time, as the liquid phase is removed, supersaturation increases which further mass transport. However, as liquid removal progresses, Maria et al. [146] proposed up to 3

mechanisms that can take place: homogenous nucleation, heterogenous nucleation, and formation of metastable intermediate compounds.

In homogeneous nucleation, the dissolved material precipitates onto crystal sites with lower potential energy, producing grain growth and minimising free energy. In heterogenous nucleation, new grains are formed at interstitial spaces between boundaries, Maria et al. [146] noted that this can be observed sometimes in the form of 2 different grain size populations forming within the material. The formation of metastable intermediates is thought to occur via the Oswald-step rule, and only takes place in some materials. This mechanism is used to describe the glassy amorphous phase formed in materials such as $BaTiO_3$ [13], [157]–[159]. The theory of a dissolution-precipitation reaction is further supported by Ndayishimiye et al, whose work on hydrothermal sintering also showed these interactions taking place between the liquid phase and silica [155].

However, other research suggests that there are more mechanisms at play than first thought, especially with regards to the role of the liquid phase, and some even argue that the LPS model is not suitable in describing CSP. Gonzalez-Julian et al. [150] used a combination of FAST/SPS with CSP to densify ZnO with water or 0.5%Zn-Ac solution. By using Kelvin probe force microscopy (KPFM) and impedance spectroscopy to analyse mechanisms. KPFM found high surface potentials in Zn-H_2O samples indicating high defect concentrations, but which were slightly lower for Zn-Ac indicating that acetate assists grain growth. Impedance spectroscopy showed bulk activation energy was significantly lower for both water and Zn-Ac samples. However, grain-boundary energy was higher for water and lower for Zn-Ac, and therefore dissolution by the acetate was proposed to produce defective diffusion pathways on grains. It was concluded that the liquid phase has 5 key roles within cold sintering: i) it provides better initial packing due to lower particle friction, ii) dissolution of Zn^{2+} & O^{2-} on particle surfaces, iii) formation of defects within bulk crystals due to diffusion of H^+ and OH^- into crystals, iv) the formation of highly defect diffusion pathways between grains, and v) the removal of carbonates.

During the experiment, the sintering stress exponents (n) were extrapolated from measurements of densification rate taken during the SPS-CSP method. Unlike SSS or LPS where n would be ~1, much higher values were measured, with 4.55 for ZnO/H_2O and 2.68 for ZnO/Ac-H_2O. These exponents are much closer to that of plastic deformation $(n > 3)$ and

grain boundary sliding ($n = 1\ or\ 2$) and are typically observed during traditional hot pressing. This suggests that there are other more complex mechanisms present, implying that a simple LPS model is not sufficient [150].

In-depth theoretical analysis of CSP done by Biesuz et al. [14] also challenges the initial theories of cold sintering following an LPS-like mechanism. In this analysis, the previously proposed mechanisms by Maria et al. (stages 1 and 2) were broken down and examined, taking account different conditions such as liquid content. During stage 1, Biesuz et al. describes the process as a system of non-contacting particles in a liquid suspension. With support from observations made by Taveri et al. [160], who studied another similar hydrothermal technique called Isostatic cold consolidation. Biesuz et al. states that Ostwald ripening can be assumed to be the only active process. Thus, using a combination of standard coarsening equations and derivations of solubility, sintering equations were proposed for stage 1:

$$\overline{\alpha^2_{(t)}} - \overline{\alpha^2_{(t0)}} = \frac{64}{81}\frac{\beta_T \gamma_{sl} \Omega_s^2}{RT} S_f \times \exp\left(P_{ext}\frac{\Omega_s - \Omega_l}{RT}\right)(t - t_0) \qquad (2.18)$$

$$\overline{\alpha^3_{(t)}} - \overline{\alpha^3_{(t0)}} = \frac{8}{9}\frac{D_l \gamma_{sl} \Omega_s^2}{RT} S_f \times \exp\left(P_{ext}\frac{\Omega_s - \Omega_l}{RT}\right)(t - t_0) \qquad (2.19)$$

where equation 2.18 is for diffusion-controlled coarsening, and equation 2.19 for interface reaction-controlled coarsening. $\overline{\alpha}$ is the average radius of particles, β_T is a transfer constant, D_l is the diffusivity of atoms through the liquid phase, and t is time. P_{ext} represents the external pressure on the system and S_f the solubility of the particle as a flat surface, R is the universal gas constant and T is the absolute temperature.

Ω represents the molar volume of the solid or liquid, with $\Omega_s - \Omega_l$ being positive under normal CSP conditions, usually decreasing with increasing pressure. The importance of the effect of this term is noted, as it is material-solvent dependent. High solubility sintering systems have a high $\Omega_s - \Omega_l$ and so will also be more pressure sensitive, indicating pressure is a more important factor in some CSP systems than others.

Stage 2 is said to start once enough liquid phase has evaporated for the particles to form a rigid skeleton structure. However, distinction is made between systems which have enough liquid phase to fill all pores present and those that do not; as those with the latter are proposed to bypass stage 1 entirely, beginning the sintering process with stage 2. If enough liquid phase is present to fill all of the pores, (which is possible during the early parts of this stage), LPS mechanisms are described as being possible. However, as the liquid phase evaporates, the LPS model is argued to not apply.

The first evidence for this was shown by applying LPS sintering laws to the CSP to see if logical results were produced. By producing a sintering strain (ε) curve for the cold sintering of NaCl using equation 2.20, even when very small values for the geometric factor (k_1) were used, unreasonably high sintering kinetics were produced.

$$|\varepsilon| = (\frac{2K_R S_f k_1 P_{ext} \Omega_s}{\alpha RT} t)^{\frac{1}{2}} \quad (2.20)$$

Evidence for the inapplicability of LPS sintering mechanisms is further shown by focusing on the interparticle liquid film. By modelling the equilibrium thickness (δ_{eq}) in NaCl under CSP conditions, film thicknesses were found thinner than the width of a H_2O molecule, which gives no possibility for the dissolution mass-transport. Biesuz et al. concluded that more investigation is needed into the CSP mechanisms, as current theories were insufficient, further supporting Gonzalez-Julian et al's findings that other mechanisms such as plastic deformation are taking place.

2.9 Cold Sintering of ZnO

ZnO is a material that has been of great interest for cold sintering due to its many applications as well as being useful for studying sintering kinetics, due to its well-known crystal structure and general ease of cold sintering. The first report of cold sintering of ZnO was by Funahashi et al. [17] who showed that sintering was possible with low molarity acetic acid as the liquid phase. Using a range of molarities (0.1, 1, 16.5), pressures (77MPa to 387MPa), and temperatures (25°C to 305 °C), samples of ZnO were cold sintered. Samples showed >90% density at <100°C, and conductivities of samples produced at 300°C were similar to those sintered conventionally at 1400°C. 1 molar acetic acid was found to produce the optimal results and XRD analysis showed no indication of secondary phases.

Kang et al. [16] also performed a comprehensive study of the mechanisms of cold sintering of ZnO. In their study, effects of pH, ion concentration, choice of solvent phase, temperature, pressure, and the effect environmental conditions (such as die sealing) on the quality of pellets were examined. The work generally supported Funahashi et al's earlier findings, but Raman spectroscopy revealed the presence of secondary acetate phases within sintered samples. This indicates that during the process, small amounts of residual phases are possible, however, their effect and methods of removal require further investigation.

Using solvent phases other than acetic acid produced drastically different results. A range of solvents were chosen including: HCl, H_2SO_4, $ZnCl_2$, and $ZnSO_4$. Use of $ZnCl_2$ produced samples with a significant amount of zinc oxychloride secondary phase, with chemically similar secondary phases forming in SO_4^{2-} and NO_3^- samples. These solvents were also found to produce large amounts of die corrosion and densities never exceeded 70-75%.

Investigation into pH and ion concentration showed the material had strong pH independence, indicating it was in fact the presence of Zn^{2+} ions that was the most important factor in achieving high densities instead of dissolution of grains, and thus a recommendation of zinc acetate as the ideal solvent liquid for densification is given.

The effect of pressure on final density showed that a threshold must be reached before significant densification takes place. In the case of ZnO, this is quoted to be >140MPa, but it is noted that significant diminishing returns occur if the pressure is further increased. This finding confirms that the application of pressure is directly linked to the driving force for densification. It is also noted that sufficient sealing of the die had a significant impact on the minimum pressure required, with unsealed dies requiring almost 80% more pressure before significant densification would begin.

Towards the end of this project, work was published by Hong et al. [161] showing the cold sintering of Al-doped ZnO. High densities were achieved using 1.0 molar acetic acid, and a two-step process of heating to 180^{o}C for 60 minutes then 300^{o}C for 30 minutes, on a side-heating press at 300MPa. The highest densities and lowest resistivity were achieved with 2wt% Al_2O_3 additions, with no secondary phases reported via XRD and EDS techniques. However, resistivity showed to be 3 times higher than materials conventionally sintered at

1500°C. The addition of Al into the ZnO system inhibited grain growth, just as in conventional material, with a dramatic decrease in density >2wt% Al_2O_3.

2.10 Cold Sintering of Alumina (Al_2O_3)

Alumina is a material that has remained until recently difficult to cold sinter due to its chemically resistant nature and traditionally high sintering temperature.

2.10.1 Al_2O_3-NaCl Composites

Initial attempts to cold sinter Al_2O_3 involved α-Al_2O_3-NaCl composite by Induja & Sebastian [162]. Their aim was to demonstrate α-Al_2O_3-NaCl as a new type of microwave composite due to alumina's attractive dielectric properties. NaCl moistened with 4% deionised water was mixed with α-Al_2O_3, and hot pressed at 120°C and 200MPa for 50min. This was followed by a heat treatment at 120°C to remove residual moisture. 96% theoretical densities were achieved with no indication of unwanted secondary phases from XRD. SEM images revealed a platelet like microstructure on the fracture surface. (Figure 2.9) Thermal stability of up to 790°C was shown, beyond which NaCl decomposed. Microwave dielectric properties showed a low loss of $2x10^{-3}$ with ε_r = 6.04 at 4GHz with a close to zero temperature coefficient of the resonant frequency. (Figure 2.10 & Figure 2.11)

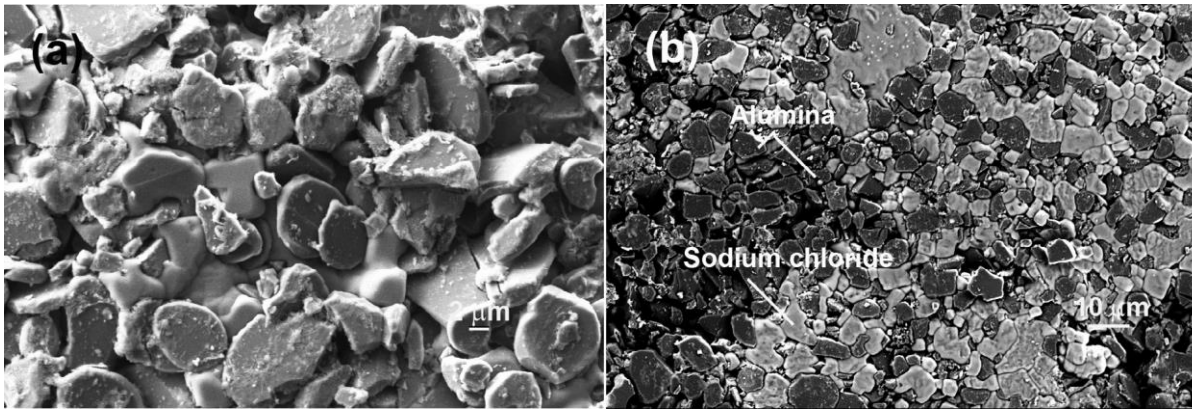

Figure 2.9: a) Fracture surface of the Al_2O_3-NaCl composite (b) Backscattered electron image of the composite sintered at 120°C [162]

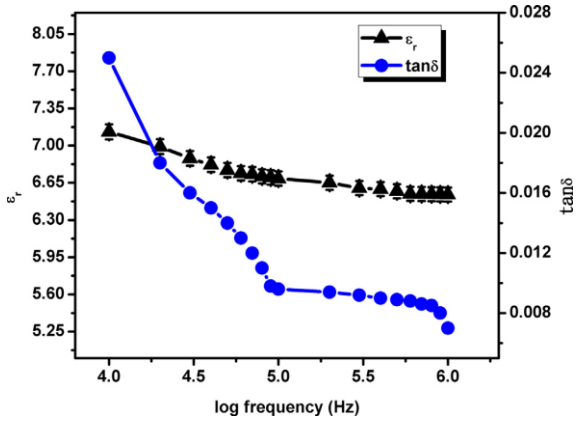

Figure 2.10: Dielectric response of Al_2O_3-NaCl composite sintered at 120°C under radio frequencies [162]

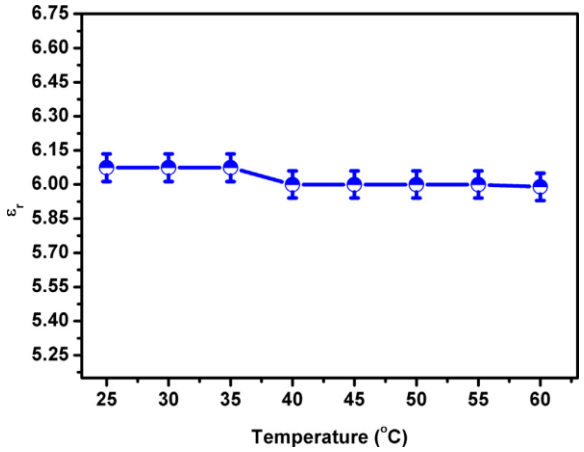

Figure 2.11: Variation in ε_r in Al_2O_3-NaCl composite produced at 120°C at 5GHz across different temperatures [162]

A more in depth study of this composite mixture was performed by Suleiman et al. [163] who investigated the α-Al_2O_3-NaCl as a phase change material (PCM) in thermal energy storage (TES) applications for waste heat recovery applications.

Once again αAl_2O_3 and NaCl were mixed 1:1 ratio but combined with ~11% deionized water. This was then hot-pressed under 3 different sets of conditions. Experimental conditions are shown in Table 2.2.

Table 2.2: A list of the different experimental conditions used by Induja & Sebastian to cold sinter Al_2O_3-NaCl composites [163]

Experiment No.	Temperature (°C)	Pressure (MPa)	Hold Time (Min)	Density (% Theoretical)
1	120	100-500	50	88-98
2	80-140	400	50	97.6-98.6
3	140	400	10, 30, 50, 60, 90	Not Reported

Their findings were similar to those of Induja & Sebastian with higher densities and better mechanical properties achieved at higher pressures. Similarly, the composites showed no signs of secondary phases. However, a significant microstructural difference was noted. Whereas Induja & Sebastian showed a platelet like structure polycrystalline structure (Figure 2.9), Suleiman et al. report zones of encapsulated NaCl with clear boundaries of nano-polycrystalline Al_2O_3 (Figure 2.12). Most notably, they report that the Al_2O_3 grain size is significantly smaller than the starting particle size decreasing from 0.2-0.45µm to 18.9-89nm.

The authors proposed that the reduction is due to chloride ions breaking down oxide bonds in the Al_2O_3 by absorption of Cl^- into the crystal, a process noted to be previously observed by Boxley et al. [164], who studied the dissolution of Al_2O_3 in Cl solutions. Similar to Induja & Sebastian, Suleiman et al. [157] showed high thermal stability up to ~800°C, with no indication of interdiffusion while sintering or during thermal cycling.

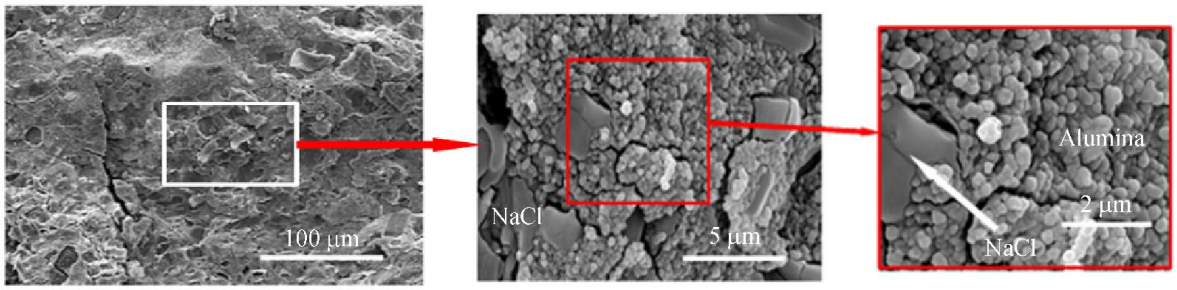

Figure 2.12: Fracture surface of NaCl-Al_2O_3 composite sintered at 120°C and 200MPa for 50min [163]

2.10.2 Cold Sintering of Boehmite Precursor to Produce Sintered γ-Alumina

One of the most recent works into the cold sintering of alumina was performed Beauvoir and Estournès [165]. The pair made use of the commonly found hydrated $Al(OH)_3$, a precursor to boehmite (discussed in 2.7.3.1) which readily transforms into γ-alumina. Hydrated $Al(OH)_3$ was hot pressed at 150°C to 400°C at 500MPa pressure for various dwell times of 30-180min. Post-dwell, the temperature was allowed to naturally reach room temperature before pressure being lowered over 45min to reduce cracking. A subsequent heat treatment at 500°C for 2hrs in air was performed to transform the samples entirely to γ-Al_2O_3.

Initial hot-pressing of the hydrated $Al(OH)_3$ transformed a majority of the material into boehmite, with Raman spectroscopy indicating a small residual amount of amorphous $Al(OH)_3$. After heat treatment, the pellets completely into γ-Al_2O_3 with no indication of secondary phases. (Figure 2.13 & Figure 2.14)

The sintering process described by Beauvoir and Estournes [159] produced translucent pellets whose transparency increased with the volume of γ-Al_2O_3. SEM showed a <100nm needle-like grain structure with an average crystallite size increasing with sintering temperature (3.7nm at 380°C, 5.5nm at 400°C) but with little grain growth during the process. (Figure 2.15a-d) Issues with structural integrity problems of the pellets are mentioned frequently by

the authors caused by the layered boehmite structure. This issue is proposed mitigated by the presence of residual amorphous phase which acts as a binding agent.

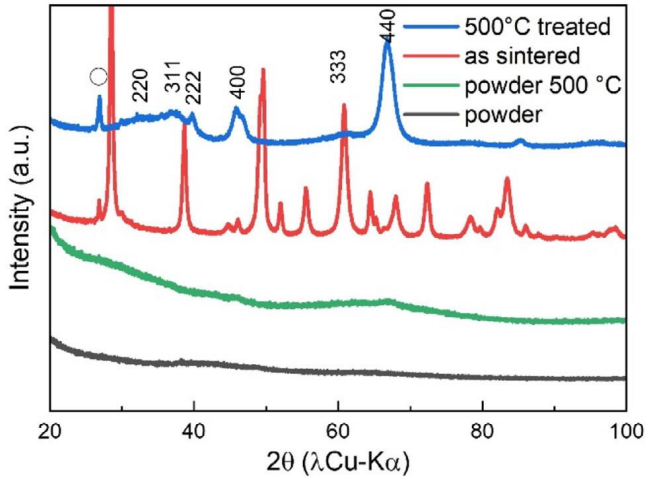

Figure 2.13: XRD pattern of starting hydrated $Al(OH)_3$ powder, sintered at 380°C, and heat treated at 500°C [165]

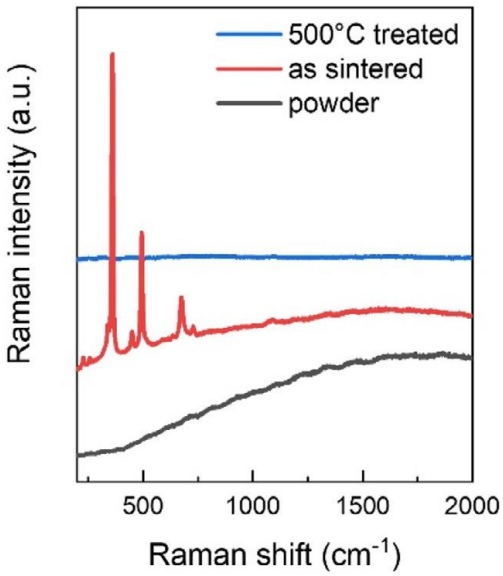

Figure 2.14: Raman spectra of starting hydrated $Al(OH)_3$ powder, sintered at 380°C, and heat treated at 500°C. Note, that Al_2O_3 is Raman inactive which was used as partial indication of its presence and total transformation of other phases [165]

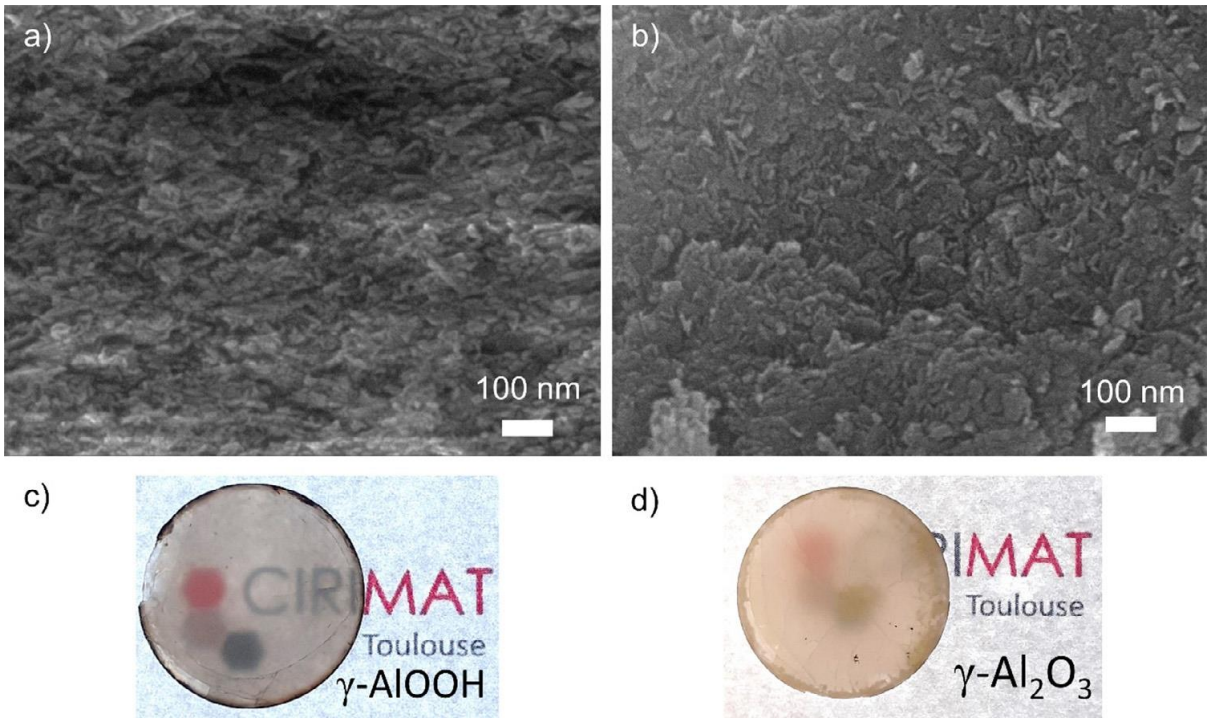

Figure 2.15: Fracture surface SEM images of a) as sintered b) 500°C heat treated $Al(OH)_3$. The corresponding samples c) sintered and d) 500°C heat treated are below each image [165]

2.11 Composite Materials and Device Manufacture via Cold Sintering

One of the first demonstrations of new composite materials by cold sintering was by Guo et al. In their study, they produced 3 examples of different composites by CSP that would not be viable to be co-sintered conventionally due to processing temperature differences. Composites of $(1-x)LM_{-x}PTFE$, $(1- x)LAGP_{-x}(PVDF\text{-}HFP)$, and $(1-x)V_2O_{-x}PEDOT:PSS$ were produced at 120°C with densities of 80-97%. The 3 types of devices showed an improved dielectric, ionic, and electric transport response respectively, with properties predictable by basic mixing laws [166].

Another early example of composites via CSP was by Zhao et al. who produced ZnO-PTFE nanocomposite varistors via CSP. To do this, composites were prepared by adding volume fractions of 0-40% of PTFE to ZnO material and cold sintering at temperatures of 25-300°C and pressures of 100-350MPa. All samples were found to reach densities of >90% theoretical and no significant secondary phases detected via XRD Microstructural analysis showed a network of ZnO surrounded by grain boundary PTFE ranging from 1-10nm. However, samples with a PTFE content >10% produced segregation of ZnO between polymer phases, which contained dispersed and unsintered ZnO powder. In contrast, 0.5-10% PTFE samples showed grains of ZnO with a consistent size. All devices displayed varistor-like behaviour with highest performance at 5-10% PTFE combinations. While commercial level performance was not achieved, proof of concept for device fabrication was demonstrated [167].

More recently, Wang et al. [168] demonstrated a number of different composite materials for microwave dielectric applications with a near-zero temperature coefficient of resonant frequency (TCF), e.g. $Na_{0.5}Bi_{0.5}MoO_4$-Li_2MoO_4 ((1-x)NBMO-X-LMO). Samples were produced by cold sintering varying ratios of NBMO to LMO from 0-100% LMO with 5-10% deionized water at 150°C at 200MPa for 30 minutes. Followed by a drying step for 24hrs at 120°C to remove any residual moisture. Just as with Guo's works, analysis showed little to no chemical interaction between the NBMO and LMO during the sintering process, and properties accurately followed mixing laws. The material showed a near zero-TCF at 20% LMO, with a relative permittivity (ε_r) of 17 and microwave quality factor (Qf) of 8,000 GHz.

Other examples of zero TCF cold sintered ceramic composites by Wang et al. include $(Bi_{0.95}Li_{0.05})(V_{0.9}Mo_{0.1})O_4$-$Na_2Mo_2O_7$ (BLVMO-NMO) composites [169] and $CaTiO_3$-K_2MoO_4 (CTO-KMO) composite [164]. Wang et al. [164] also included the fabrication of a CTO-KMO microstrip patch antenna via cold sintering (Figure 2.16) which achieved a radiation efficacy ~62.0%, and s11 = -14.2dB at 2.51GHz (where s11 is used for determining how much power is reflected from an antenna).

While these examples all gave proof of concept of cold sintering microwave dielectric materials and devices, most involved the use of high concentrations of Mo, a material that is both toxic [170] and expensive [171]. However, Wang et al. [22] recently demonstrated cold sintering of $0.5LiMgPO_4$-$0.1CaTiO_3$-$0.4K_2MoO_4$ (LMP-CTO-KMO) composites as a replacement for low temperature co-fired ceramics (LTCC). The produced material was similar to previous composites and showed no sign of secondary phases or interaction. Near zero-TCF with ε_r = 9.1 and Qf = 8500 was obtained which was also suitable for microwave dielectric applications but with significantly reduced Mo concentration [166].

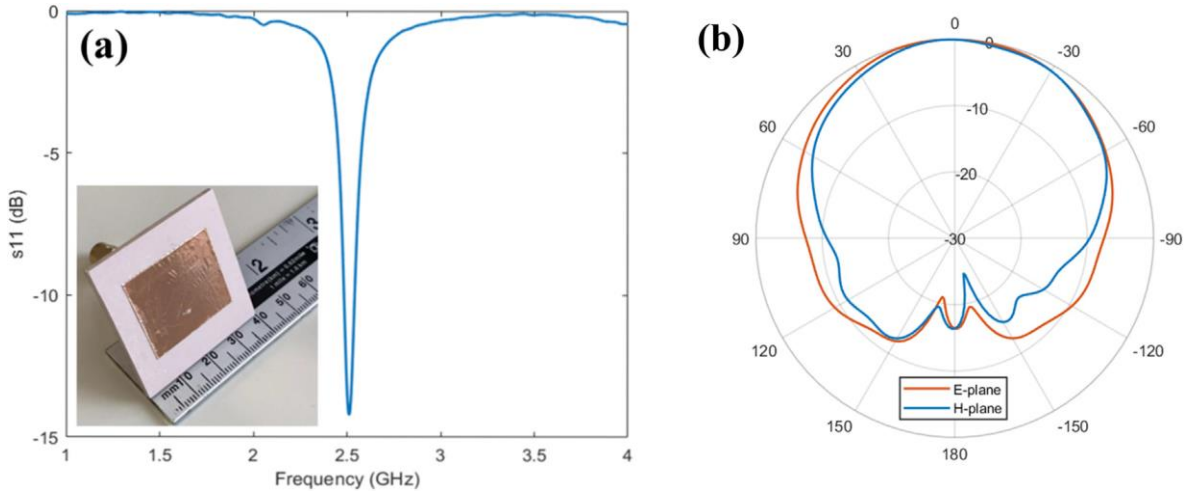

Figure 2.16: a) a graph of the S11 results produced by the microstrip patch antenna depicted in the same diagram. b) The radiation pattern of the CTO-0.92KMO microstrip patch-antenna [172].

2.12 Energy use of Cold Sintering

Energy consumption is an important aspect to consider when studying the viability of cold sintering. In 2017, Heidary et al. [173] performed an analysis comparing and contrasting the energy efficacies of different sintering processes. The energy consumptions of SSS, LPS, Fast-firing, FAST, Laser sintering, and CSP were all considered. To compare energy consumption between the different techniques a new term was developed dubbed 'Normalised Excess Energy' (NEE). NEE is stated as:

$$NEE = \frac{E}{mC_pT_s} \tag{2.21}$$

where E is energy used during the process, m is weight of samples, C_p is the heat capacity, and T_s is the sintering temperature in the conventional processing of the material. A lower NEE indicates a higher energy efficacy. From this equation, the efficiencies were compared using the data extracted from 7 materials and NEE's were plotted for each material being sintered under different sintering conditions. This is shown in Figure 2.17. From this the conventional sintering showed NEE values of ~400 whereas CSP showed a NEE of between ~0.1-10, depending on material and sintering schedule, giving an average of 2.4. The next closest technique in terms of efficiency was laser sintering at ~16.5, significantly higher than many CSP sintered materials.

While CSP is clearly far more efficient than conventional techniques by the data presented by Heidary et al, criticism of the study is justified. In the paper, there is a distinct lack of consideration of the energy required to manufacture the nano-powder required for the CSP. Many techniques do not require nano-powders to densify material, and it may be the case of energy requirements shifting from one step of the process to the other.

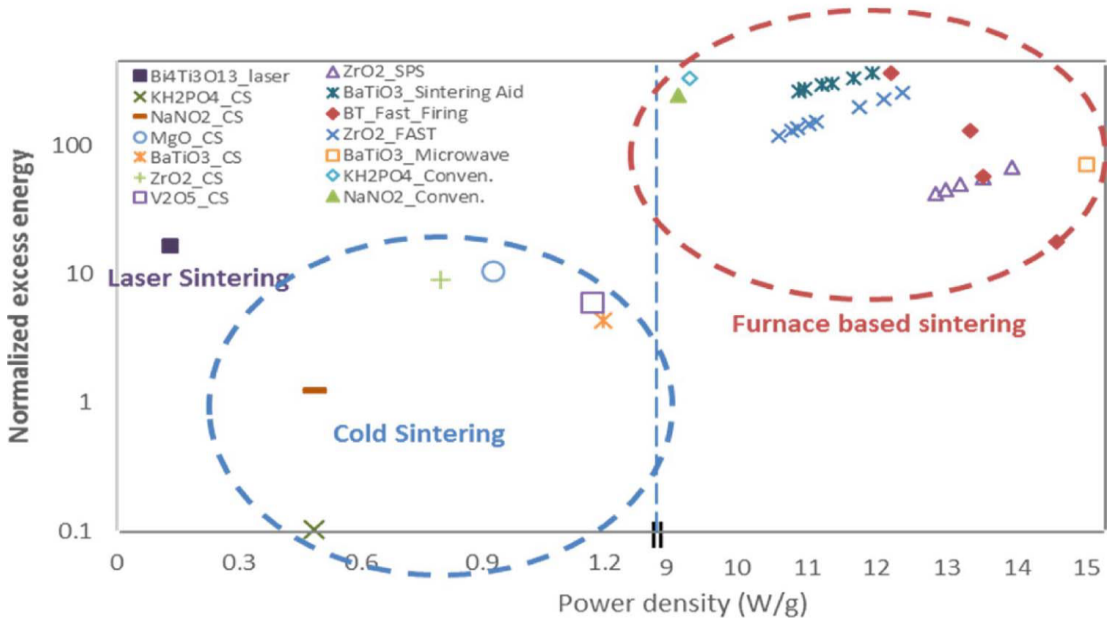

Figure 2.17: A Normalised Excess Energy (NEE) plot contrasting and comparing the energy consumption of different sintering techniques [173].

2.13 Current Challenges and Future Work

Cold sintering is a promising new field of materials densification that has not only opened up the fabrication of many new types of composites, but appears to show new levels of control of the sintering process while remaining highly efficient. However, there are many hurdles that must be overcome before this technique may find its way into large scale commercial manufacture. Some of these hurdles below are discussed.

2.13.1 Scaling-Up

It is as of yet unknown whether this process can be efficiently scaled-up to an industrial level. Current work has focused only on pellet like samples and small-scale devices, all produced on experiment scale hot presses. It is not known if the same quality of manufacture is possible on much larger scale devices. There also may be issues encountered over the requirements of nano-powder and the extra costs this may incur, if these costs prove too high then applications of the process may be more niche than first hoped.

Preliminary studies into scaling have been performed recently by Bang et al. [174] who investigated methods of lowering applied pressure to <50MPa during cold sintering, as well as utilising a custom-made large scale hot-press that allowed for 25cm^2 square sample manufacture. Three ZnO-based composites, $Li_{1.5}Al_{0.5}Ge_{1.5}(PO_4)_3$, and zeolite Y were all cold sintered using this apparatus and analysed. From their analysis, a number of new processing

challenges were identified. For ZnO, high density was achieved, but inhomogeneous grain growth was observed across the sample with some zones showing equiaxed grain growth while other zones showed anisotropic columnar grain growth. This was thought to be explained by randomly localised transient liquid evaporation rates across the sample, which is amplified for larger sample sizes. Zeolite Y showed incomplete densification at the lower applied pressures with incomplete pore-shrinkage shown. Thus, this possibly may indicate the limitations of the types of materials that may be cold sintered under 'industrial' processing conditions.

2.13.2 Secondary Phase

As previously mentioned, there have been several reports of a small amount of secondary phase within materials such as ZnO, especially when the solvent phase is not water [13], [16]. It is not currently known if these phases can be totally removed in an efficient manner, as well as what effect their presence has on the properties of the material.

2.13.3 Materials Properties

One of the other critical factors to determining the industrial suitability of cold sintering is whether the properties of sintered material are equal to or better than those currently available via conventional processing. Early indications imply this is true for many materials, especially with the prospect of new composite materials.

However, this is not the case for all materials. Lowum et al. studied the mechanical properties of cold sintered ZnO via 'ball-on-three-balls biaxial bending'. It was found that cold sintered ZnO showed mechanical strength ~40% lower than conventionally sintered material, and is thought that it may be related to the presence of the residual secondary phase contributing to poor bonding between adjacent grain boundaries [20].

2.14 Challenges to be Addressed

Based on the above review of literature, these works aim to address a number of questions within the cold sintering process.

2.14.1 Questions Addressed in Chapter 4

1. How effective is the cold sintering process at sintering ZnO and do the results align with that of current literature?
2. How does powder size affect the ability to cold sinter ZnO at various temperatures and pressures, and how does the cold sintered material compare to conventional?
3. How much of an effect does the reported secondary acetate phase have on the final properties of the material and these be removed efficiently?
4. Does the introduction of a doping element (Ga) affect the ability to cold sinter ZnO, and is it an effective method for producing material similar or better in properties compared to conventionally sintered material?

2.14.2 Questions Addressed in Chapter 5

1. Is it possible to use cold sintering to directly sinter ZnO onto a polymer layer as demonstration of the ability to use cold sintering as a method of producing a TCO device?

2.14.3 Questions Addressed in Chapter 6

1. Can cold sintering be used to sinter γ-alumina and are those properties similar to conventionally produced material?
2. Further, if possible, can a highly porous γ-alumina material be produced using cold sintering as demonstration of a typical high surface area γ-alumina catalyst/catalyst support?
3. Is it possible to utilise cold sintering to manufacture α-alumina at lower temperatures than conventional techniques?

Chapter 3 – Methodology

3.1 Introduction

This chapter details processing techniques and relevant theory of experimental techniques generally used within this thesis. Specific techniques unique to a material or process are given in the relevant chapters.

3.2 Processing Techniques

3.2.1 Powder Preparation

Powders were ball milled for 2 hours in 10cm diameter PTFE bottles a third full with 10mm diameter alumina media in isopropanol, before being dried at 180^{o}C for 24 hours. Dried powder was then sieved in an 180µm sieve to remove final agglomerates. Nano-powders deemed too small for ball milling to be effective were sieved to remove agglomerates. All processed powder was maintained in a 180^{o}C drying oven ready for use.

3.2.2 Conventional Sintering

Powder was removed from the 180^{o}C drying oven and cold pressed at 250MPa for 1 minute into 10mm pellets ready to be sintered. To prevent cracking, some powders were combined with 5wt% of 5wt% PVA binder solution before cold pressing. Material was then sintered in a conventional furnace with a controlled heating rate, cooling rate, and dwell period. Specific details are given for each material/condition within the relevant sections.

3.2.3 Cold Sintering

The cold sintering process is separated into 2 steps (Figure 3.1), dependent on the material type and the requirement for a post-sintering heat treatment.

3.2.3.1 Mechanical Mixing

A weighed amount of dried powder was mechanically mixed for several minutes in a pestle and mortar to remove any remaining agglomerates. 20-30wt% of 1.0 Molar acetic acid was then added with a pipette. The ideal volume of liquid phase was determined by trial and error for each powder, with nano-materials requiring higher volumes due to increased surface area. Powder and solution were then pestled. During this process the mixture transfers through several observable states. Initial mixing produces a slurry-like liquid, mixing with ease, this is followed by a noticeable increase in resistance in mixing as the slurry begins to thicken and dry from absorption and evaporation of excess liquid phase, leaving a pearl-like coating across

the mortar surface. PTFE film was used to remove the coating on the mortar surface giving agglomerated flakes. Hot-pressing at this stage produces poorly bonded material, thus these flake agglomerates were pestled further until back into a deagglomerated powder. This powder was then transferred into an M2-Tool Steel die ready for cold sintering.

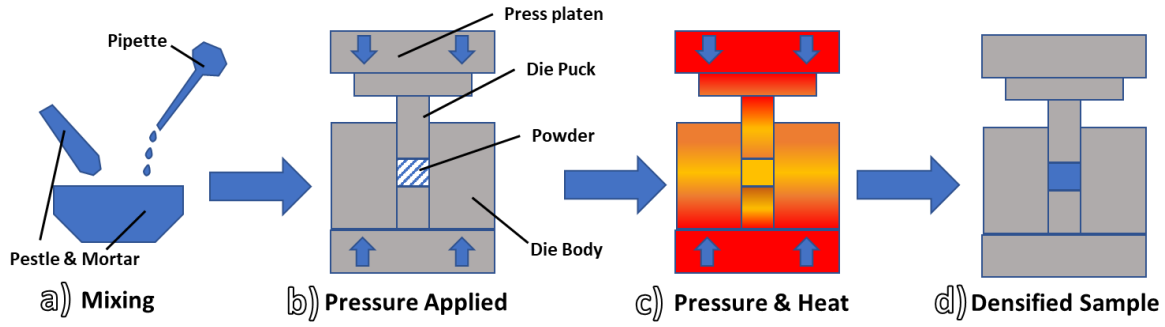

Figure 3.1: Diagram demonstrating the basic CSP process. a) Powder and transient solvent are mixed together in a pestle and mortar, b) Powder is placed into a die and pressed at room temperature, c) While maintaining pressure the temperature is raised (usually <300°C) sintering the sample. d) A densified sample is ready to be removed from the die

3.2.3.2 Cold Sintering

The filled die was placed into a press (Specac Manual Hydraulic Press with Specac Atlas Heated Platens). A set pressure was then applied at room temperature for 10 minutes, allowing for particle rearrangement based on the advice from previous literature [1], [2]. At the end of this stage, any pressure lost during particle rearrangement was reapplied, and heating from the top and bottom, the temperature was raised to 125, 200, or 300°C for 1 hour. Control of heating and cooling rate was not possible due to apparatus setup, but heating rate varied between 20-40°C/min. Dependent on experiment, cooling was allowed to occur ambiently or was assisted using a 20mm fan.

3.2.4 Tape Casting

Full experimental details of the tape-casting of ZnO are given in Chapter 5. The following is a more general description of the technique.

Tape casting is a slurry-based casting process used to deposit a thin-layer onto a flat surface before sintering, and is widely used in the mass-manufacture of functional devices such as capacitors [2], [3].The process is achieved by mixing the desired material to be sintered with a number of components to produce a slurry of the correct consistency for successful casting. The most common slurry components and their role is given in Table 3.1. The slurry is then carefully spread over the surface of a material using a doctor-blade, allowing for thicknesses from 1-3000 µm to be produced. Once the tape has been cast it is dried, allowing the tape to

be utilised for binder burnout and densifying stages [1], [177]. A diagram of this process is given in Figure 3.2.

To achieve maximum density other considerations must be made with regard to the quality of the powder matrix. Final particle packing is affected by particle size, size distribution, particle shape, and the "solids loading" [1]. Particle size distribution and shape are well known factors that affect how efficiently a material will pack. Traditionally the ideal system for tape-casting was deemed to be a powder of small (<1μm), mono-sized, spherical particles [1]. However later work has shown that correctly sized bimodal powders are preferred giving better packing, reducing defect sizes, maximising contact between particles, and avoiding sintered regions with extreme packing density [178], [179], [180].

The solids loading is the ratio of the solid matrix phase to the total volume of the slurry. This affects final density, as well as impacting its flow behaviour. A high solids loading theoretically leads to a higher final green density, but raising solids loading leads to a poor flow behaviour [181], [182]. Thus, there is a complex balance to achieve high enough solids-loading for a high green density, but low enough to allow good flow behaviour for casting.

Traditionally tape cast material (once dry) is often then stacked allowing for the manufacture of multi-layer devices such as capacitors, or can be left unstacked for single-layer applications. A binder burnout step then takes place over a long period to minimise porosity development and allow for total binder removal. Sintering then takes place to produce fully densified material.

Table 3.1: Table listing the most common components of a tape-casting slurry and a brief description of their primary function

Slurry Component	Role
Binder	A low glass-transition temperature (T_g) polymer that holds the tape-cast system together, whilst giving required flexibility to the tape.
Defoamer	Reduces gas bubbles within the system improving tape quality by lowering tape porosity.
Dispersant	Breaks up and disperses matrix particles improving distribution throughout the slurry.
Matrix	The material to be densified and primary component of a slurry (nZnO in this case)
Plasticiser	Further lowers the T_g of the binder component to improve the final flexibility of the tape.
Solvent	The medium in which all of the slurry components are dissolved in. The chosen solvent must be able to dissolve all components of the slurry effectively.

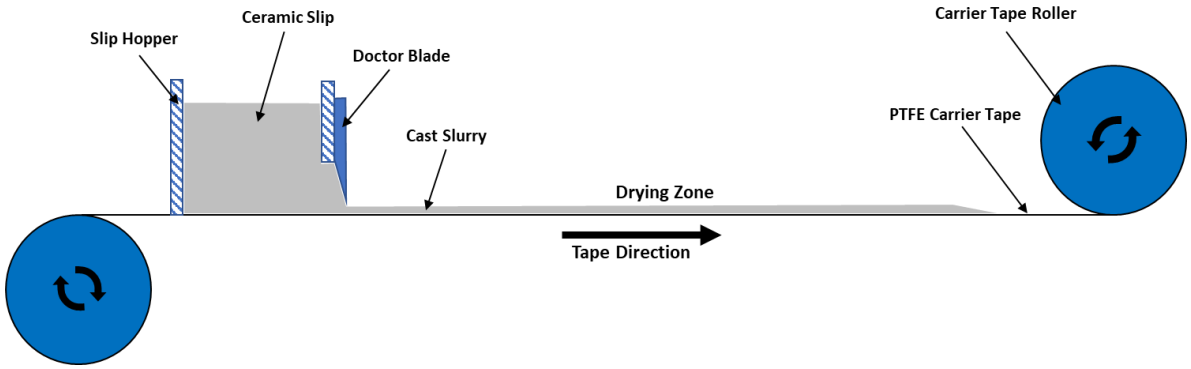

Figure 3.2: A simple diagram showing the basic setup of the tape-casting process

3.3 Analysis Techniques

3.3.1 Density measurement

3.3.1.1 Archimedes Density

Archimedes density measurement makes use of Archimedes principle of buoyancy. The sample is weighed in air, and then in a liquid of a known mass and density. The following equation is then applied to determine density:

$$\rho_b = \frac{w_a \rho_l}{w_a - w_w} \tag{3.1}$$

where w_a is the weight of the sample in air, w_w is the weight of the sample in water, ρ_l is the density of the liquid phase, and ρ_b is the bulk density. Due to the water sensitivity of ZnO samples were measured in ethanol. Measurements were performed on a Toledo XPR404S balance with Archimedes density apparatus. Three measurements were taken of each sample and an average is calculated from these 3 measurements.

3.3.1.2 Density by Volume

For samples not suitable for the Archimedes density technique, a volumetric method was used. The volume of samples was measured using Mitutoyo 500-196-20 ABSOLUTE Digimatic Callipers, and mass taken. Density was then calculated via:

$$\rho_b = \frac{m}{v} \tag{3.2}$$

where m is mass in grams and v is volume in m^3. Calculated density was then divided by theoretical and multiplied by one-hundred to calculate percentage density. Each sample was measured three times and an average taken.

3.3.2 X-ray Diffraction (XRD)

XRD uses X-rays to determine the crystal structure of a sample. Monochromatic K_α X-rays are fired from a source directly at a sample across a range of angles, with a detector recording the intensity of X-rays diffracted off of the sample. Constructive interference (and thus peaks) can only occur at integer-multiples of the X-ray wavelength (λ). In combination with the angle of the incident X-rays, the hkl d-spacing can be solved for by using Bragg's Law:[183]

$$n\lambda = 2d_{hkl} \sin\theta \tag{3.3}$$

Where n is an integer, λ is wavelength of X-rays used, d_{hkl} is the d-spacing which is the distance between the two crystallographic planes being diffracted off, and θ is the angle between the incident X-ray beam and the surface being studied [183].

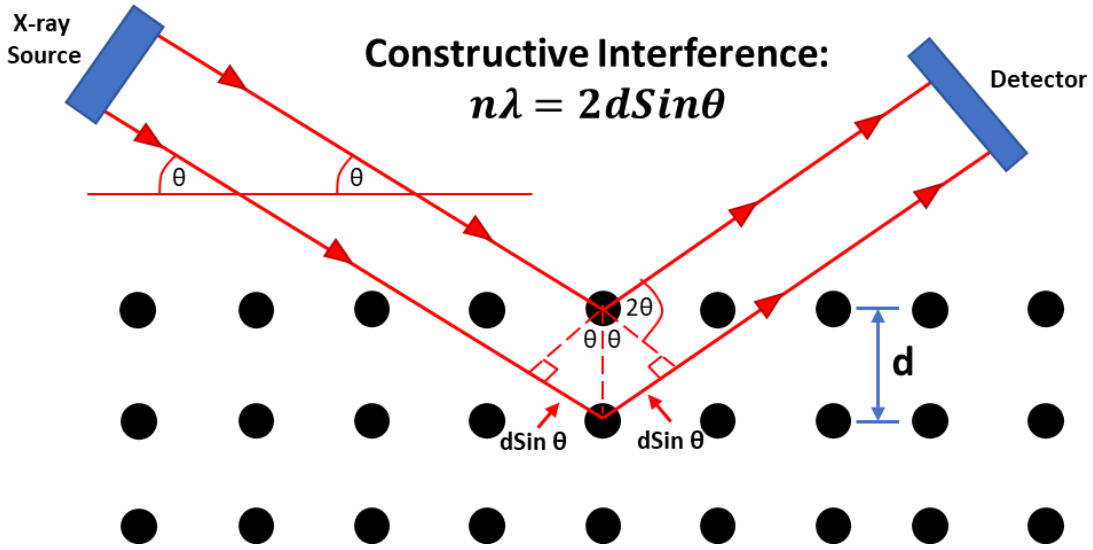

Figure 3.3: Diagram showing the geometric proof for Bragg's Law; the basis for X-ray Diffraction analysis

XRD analysis was performed using CuK_α (λ = 1.5419Å) radiation on a Bruker D2 Phaser. This technique was used across all experiments to study the phase structure present, any phase changes, and presence of any secondary phases.

3.3.3 Raman Spectroscopy

Raman spectroscopy takes advantage of the Raman effect or shift. When photons are absorbed by electrons of certain energy states, they are promoted to a higher virtual energy state. From this unstable energy state, the electron then relaxes to a lower vibrational energy state. In nearly all cases this relaxation is to the original vibrational state emitting a photon of the original wavelength. This is called Rayleigh scattering and is not useful. However, in about $1x10^{-7}$% of cases [2], the electron relaxes to a different energy state and emits a photon of a different wavelength which is known as the "Raman effect". If the produced energy state is higher than the original this is defined as Stokes scattering giving longer wavelength emissions. A lower final energy state is called Anti-Stokes scattering giving shorter wavelength emissions [2], [184]. To account for the extremely low occurrence of Raman scattering and accurately measure change in wavelength during analysis, a monochromatic laser is used. Knowing the wavelength of the analysis laser and the series of Raman modes produced by different materials leads to a "molecular fingerprint". The intensity of the peaks produced can also be used to determine the concentration of a particular molecule in a sample, allowing

for a semi-quantitative analysis [2]. However, not all excitation modes are visible. For Raman scattering “modes” to be visible on a spectrograph (Raman-active), the excitation must cause a change in the polarizability of the molecule. Symmetry plays an important role in this, as in molecules with a centre of symmetry, Raman-active modes are Infrared-inactive and vice-versa [184].

Raman spectroscopy in this work was performed on a Renishaw InVia Raman microscope, using a 514.5nm green laser at 10-20MW. At least three measurements were taken on the surface and internally of each sample.

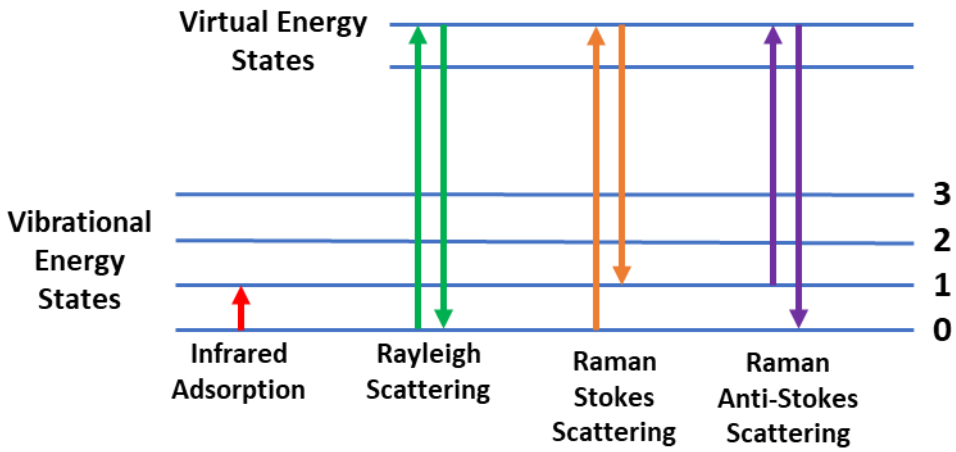

Figure 3.4: Diagram demonstrating the different excitation states that can occur and which ones correspond to a Raman scattering mode. (Diagram adapted from: [185])

3.3.4 Scanning Electron Microscopy (SEM) & Electron Probe Micro-Analysis (EPMA)

SEM uses a stream of electrons to allow for high resolution imaging and elemental analysis of a sample. EPMA on the other hand is used specifically for elemental analysis. A sample is placed into an analysis chamber which has atmosphere removed to a sufficient vacuum for electrons to pass freely from the electron gun to the sample. Electrons are emitted by the heating of a thermionic cathode or a field emission gun. These electrons are given initial direction by a cathode ring with a strong positive charge, which is then focused down into a primary beam using electromagnetic condenser lenses and a raster scan generator, which gives the final primary beam strong direction to allow for raster image production. For each raster scan point, the detection strength is recorded, which produces a brighter pixel [186].

When the primary electron beam hits the sample, an interaction zone is produced (Figure 3.5). This interaction produces a number of different responses; however, these works only utilised three: Secondary electron (SE), Back-scattered electron (BSE), and Characteristic X-rays used either for Energy Dispersive X-ray Analysis (EDX) or Wavelength-dispersive X-ray spectroscopy (WDS) [187], [188].

Secondary electron analysis is the primary imaging method used to study microstructure, and is the most analogous to light-microscopy. It is produced by the primary beam knocking a shell electron out of a sample atom. This ejected electron is known as a secondary electron and scatters into the vacuum chamber where it is attracted to an anode attached to a detector. For each raster scan point, the secondary electron intensity is recorded, which produces a pixel with increased intensity. Combination of these elements allows for a geometrical 3D image to be produced of the sample [187], [188].

Backscattered Electron imaging is a qualitative technique that makes use of the elastic scattering of primary electrons interacting with the sample material. Electrons with insufficient energy to remove or replace shell electrons are reflected back from the sample surface. Elements with a higher 'atomic number' (Z) are able to deflect electrons better due to their larger nuclei. Thus, on imaging, heavier elements appear brighter, and lighter elements darker [187], [188].

EDX analysis uses high energy electrons that cause non-elastic scattering with inner shell electrons, resulting in an electron hole. The instability of this hole leads to higher energy electrons from another shell lowering in energy to fill this vacancy, and the lost energy is emitted as X-rays of the same wavelength as the energy change. Measurement of these X-ray wavelengths and intensities allows for quantitative elemental analysis [187], [188], [189].

Characteristic X-rays may also be used to perform WDS, another elemental analysis method similar to EDX. However, the produced characteristic X-rays collide with a crystal specimen of a known d-spacing at a range of angles, making use of Bragg's Law. These X-rays then diffract to a detector, where X-ray counts can then be used quantitatively to measure the amount of each element in a given volume [189].

The advantages of WDS over EDX include a higher accuracy, better sensitivity, and better analysis of lighter elements. However, it is more expensive, requires more specialised

equipment, takes longer to perform, and being a diffraction method makes it highly sensitive to sample topography [189], [190]. EPMA primarily makes use of WDS, but can also include EDX analysis simultaneously.

SEM in this project was performed on an FEI Inspect F50 at 10kV, spot size of 3.5, and working distance of ~10mm. Bulk samples for fracture-and top-surface analysis were fixed to a mount with conductive silver paste and coated in either gold or carbon to perform SE, BSE, and EDX analysis. Samples for cross-sectional analysis were mounted in epoxy resin, before being ground with 400, 800, 1200, 2000 grit paper, and polished with 6, 3, and 1µm diamond paste to achieve a mirror finish.

EPMA was performed by Johnson Matthey PLC, using EDX and WDS on a JEOL JXA-8500F electron probe microanalyser.

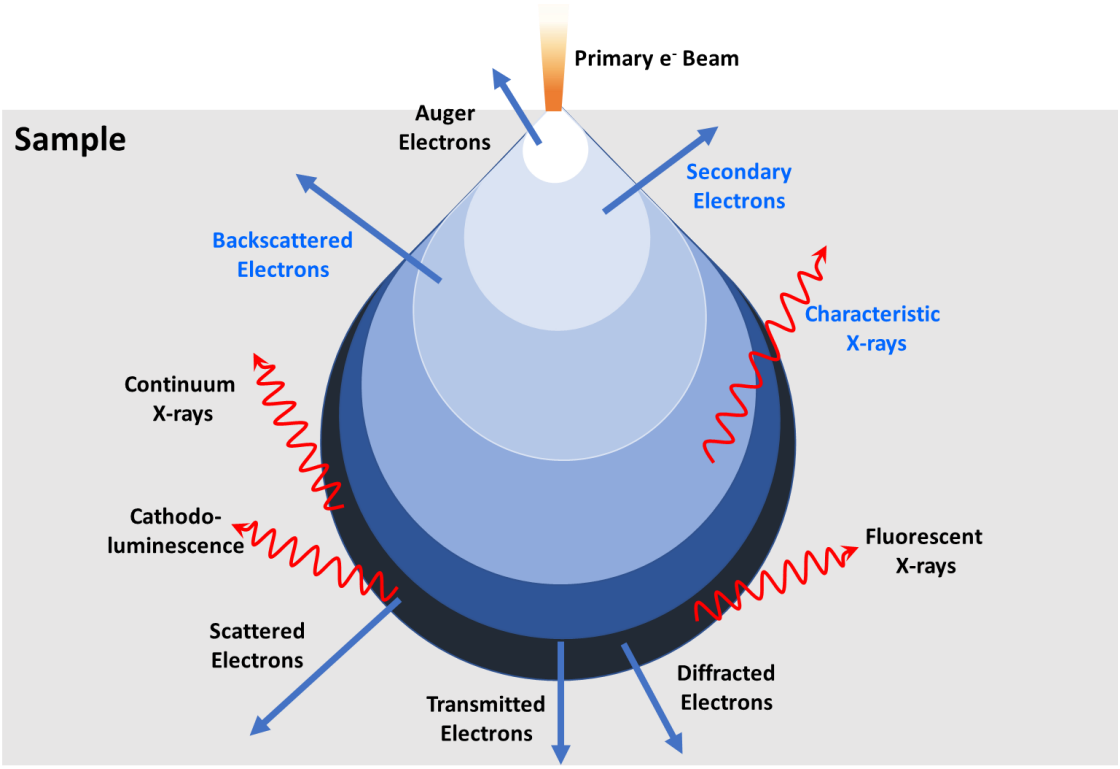

Figure 3.5: Diagram demonstrating an interaction volume of an SEM beam against a bulk sample. The 3 interactions used in analysis of these works are highlighted in blue. Higher voltage and atomic number directly impact the size of the interaction volume. A high atomic number sample would lead to a more semi-spherical shaped interaction volume instead of tear drop. Image adapted from: [191]

3.3.5 Impedance Spectroscopy

Impedance spectroscopy is a versatile non-destructive technique that allows for analysis of the electrical properties of a broad range of materials by measuring the impedance response. It allows for the deconvolution of the impedance response (made up of resistive and reactive components) into separate individual effects e.g. bulk, secondary phases, grain boundary effects, surface layers, and electrode-effects [192].

In this technique, characterisation is performed by measuring the electrical relaxation time (time constant, τ) of a material across a wide range of AC frequencies (often 10^{-2}-10^{7}Hz). These relaxation times can be defined by individual parallel RC elements defined by:

$$\tau = \mathrm{RC} \tag{3.4}$$

$$\omega_{max} RC = 1 \tag{3.5}$$

$$\textit{where } \omega_{max} = 2\pi f_{max} \tag{3.6}$$

where R is resistance, C is capacitance, ω_{max} is maximum angular frequency, and f_{max} is maximum frequency. Because of equation 3.5, both the R and C elements can be decoupled from equation 3.4 to extract both of their values [192].

Experimentally the impedance (Z) is directly measured on an LCR meter. This is split into real in-phase ($Z' = |Z|Cos\theta$) and imaginary out-of-phase ($Z" = |Z|Sin\theta$) parts. This can be represented as [193]:

$$Z^* = Z' + jZ" \tag{3.7}$$

Where Z* is total impedance, and $j = \sqrt{-1}$. From this the electric modulus (M*) is extracted:

$$M^* = j\omega C_0 Z^* \tag{3.8}$$

Plots of Z' vs Z" (Debye plot), Z" & M" against frequency (ω) are then made. Separate peaks on each of these graphs can then be interpreted as individual RC elements which can relate to different electrical components within the material. Typically, Z" components relate to grain boundary effects, and M" bulk component effects. However, depending on the response this is not always the case [192]. Using equation 3.5, R and C can then be extracted. For Z":

$$R_{Z"} = 2Z"_{Max} \tag{3.9}$$

$$\textit{And } C_{Z"} = \frac{1}{\omega R_{Z"}} \tag{3.10}$$

and for M":

$$C_{M"} = \frac{1}{2M"_{Max}} \quad (3.11)$$

$$And\ R_{M"} = \frac{1}{\omega C_{M"}} \quad (3.12)$$

From this conductivity ($\sigma = \frac{1}{R}$) is calculated, and its log is plotted against $\frac{1000}{T}$ for each identified RC element. The gradient of each plotted element is taken and multiplied by 0.1986 to give the activation energy in eV. This conversion factor to is derived from Arrhenius law:

$$\sigma = Ae(\frac{-E_a}{kT}) \quad (3.13)$$

$$\ln \sigma = \ln A - \frac{E_a}{kT} \quad (3.14)$$

$$Where\ by\ y = mx + c \text{ gradient is } -\frac{E_a}{k}$$

where E_a activation energy in Joules, k is Boltzmann constant and A is constant. However, due to plotting convention in these works, $\ln \sigma$ is converted to $\log_{10} \sigma$. Where:

$$\ln \sigma = 2.303 \log_{10} \sigma \quad (3.15)$$

Dividing $-\frac{E_a}{k}$ by 2.303 and dividing by 1000:

$$m = \frac{-E_a}{2303\ k} \quad (3.16)$$

$$E_a = -m2303k \quad (3.17)$$

Multiplying by k $$E_a = -m(3.181 \times 10^{-20}) \quad (3.18)$$

Converting to eV $$E_a = -0.1986m \quad (3.19)$$

Thus the 0.1986 multiplier is produced, where m is the gradient of the RC element plot.

3.3.6 Compression Testing

Compression testing involves placing a material under increasing load at a certain rate to assess its compressive properties. A specimen of known dimensions is placed into a compression tester (Figure 3.6a) and placed under load. The applied force (F in Newtons) and load cell displacement over time are recorded during testing. From this data, Stress (σ) and Strain (ε) are calculated via:

$$\sigma = \frac{F}{A} \quad (3.20)$$

$$\varepsilon = \frac{-\Delta l}{l_0} \tag{3.21}$$

where A is the top surface area of the specimen, Δl is the change in specimen length, and l_0 is the starting length. Note that $-\Delta l$ is negative as the length is decreasing. Calculated σ and ε values are plotted against each other, allowing for extraction of a number of materials properties including: Young's Modulus (E), Yield Strength, and Ultimate Compressive Strength (UCS).

Compression testing in this project was performed on a Hounsfield H100KS tensile tester with a Tinius Olsen 100kN strain gauge.

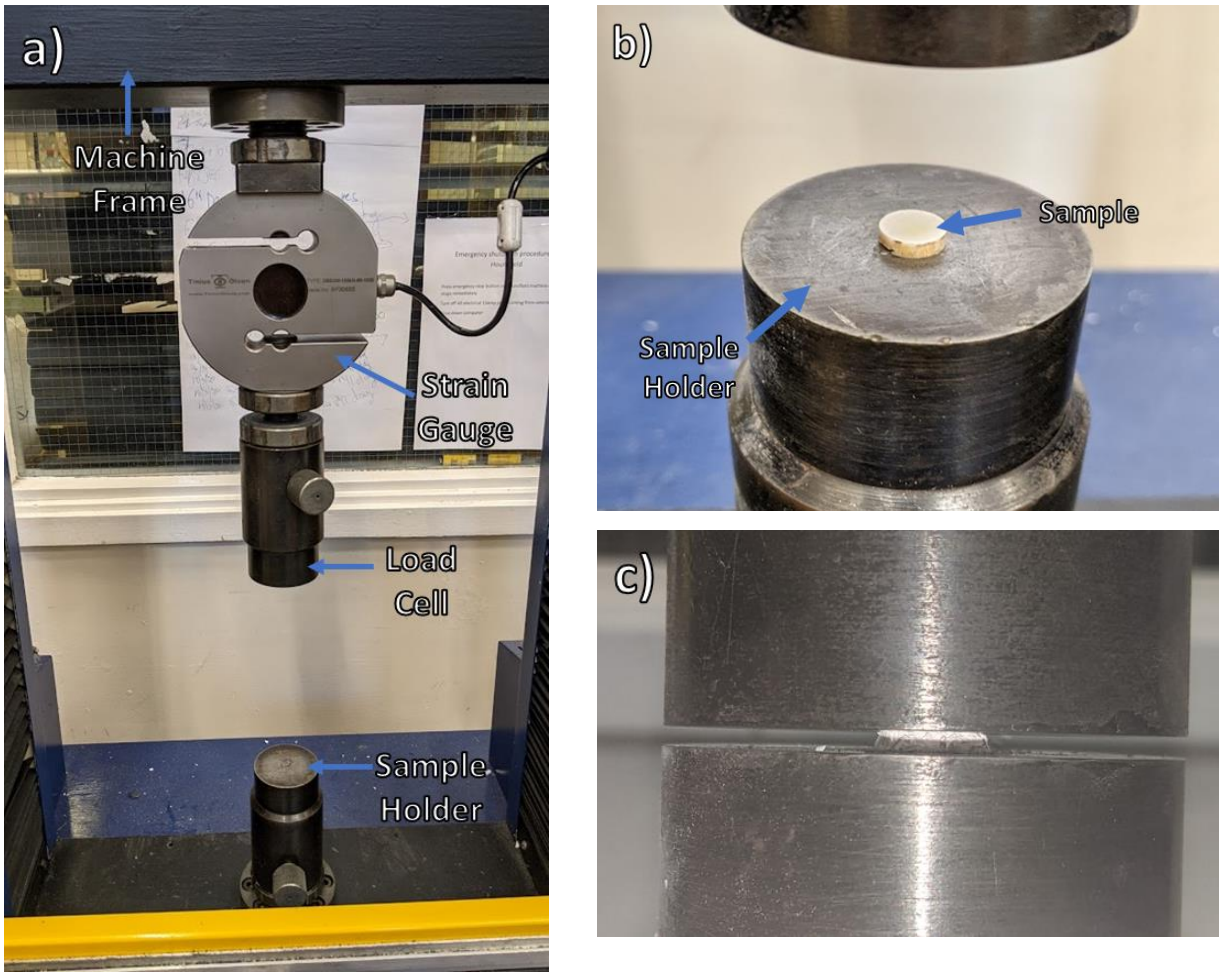

Figure 3.6: Images of the compression tester (a) and compression testing of alumina pellets (b,c)

Chapter 4 – The Cold Sintering of ZnO and $Ga_{0.02}Zn_{0.98}O$

4.1 Introduction

4.1.1 Motivation for the Cold Sintering of ZnO and Gallium Doped-ZnO

The densification of ZnO has been a topic of significant focus within cold sintering research since its development. As discussed in section 2.6, ZnO has promising applications as a replacement for ITO in TCO applications, and cold sintering has potential to densify powders on the surface of polymers at low temperature, one possible way of achieving this goal. To date, recent papers have focussed on the most effective way to cold sinter ZnO and have often used it as an ideal material to study its mechanism [15]–[17], [21], [167], [194], [195]. However, if cold sintering is to achieve commercial applications, a number of processing questions still need to be answered such as the role of particle size [1] and whether doped (e.g. Al and Ga) as well as undoped ZnO can be cold sintered.

4.1.2 Aims

The aims of this chapter were to answer the following questions:

- How effective is the cold sintering process at sintering ZnO and do the results align with that of current literature?
- How does powder size affect the ability to cold sinter ZnO at various temperatures and pressures, and how does the cold sintered material compare to conventional?
- How much of an effect does the reported secondary acetate phase have on the final properties of the material and these be removed efficiently?
- Does the introduction of a doping element (Ga) affect the ability to cold sinter ZnO, and is it an effective method for producing material similar or better in properties compared to conventionally sintered material?

4.2 Methodology

4.2.1 Choice of Materials

4.2.1.1 Coarse-ZnO (cZnO), Nano-ZnO (nZnO) and $Ga_{0.2}Zn_{0.98}O$ (GZO)

High purity ZnO powders were chosen for these experiments to avoid complications associated with unwanted impurities. “Coarse” ZnO was 99.9% pure (Sigma Aldrich) and

quoted with a <5µm particle size but which was 90-250nm after ball-milling. Nano-ZnO was >99% pure (US Research Nanomaterials Inc), quoted with a 10-30nm mostly spherical particle size but was measured as having 40-80nm. 2% Ga doped into nano-ZnO was provided by the group of Darr from University College London and was produced using a continuous hydrothermal flow process with particle size 25-40nm. Figure 4.1 shows SEM images of the cZnO, nZnO.

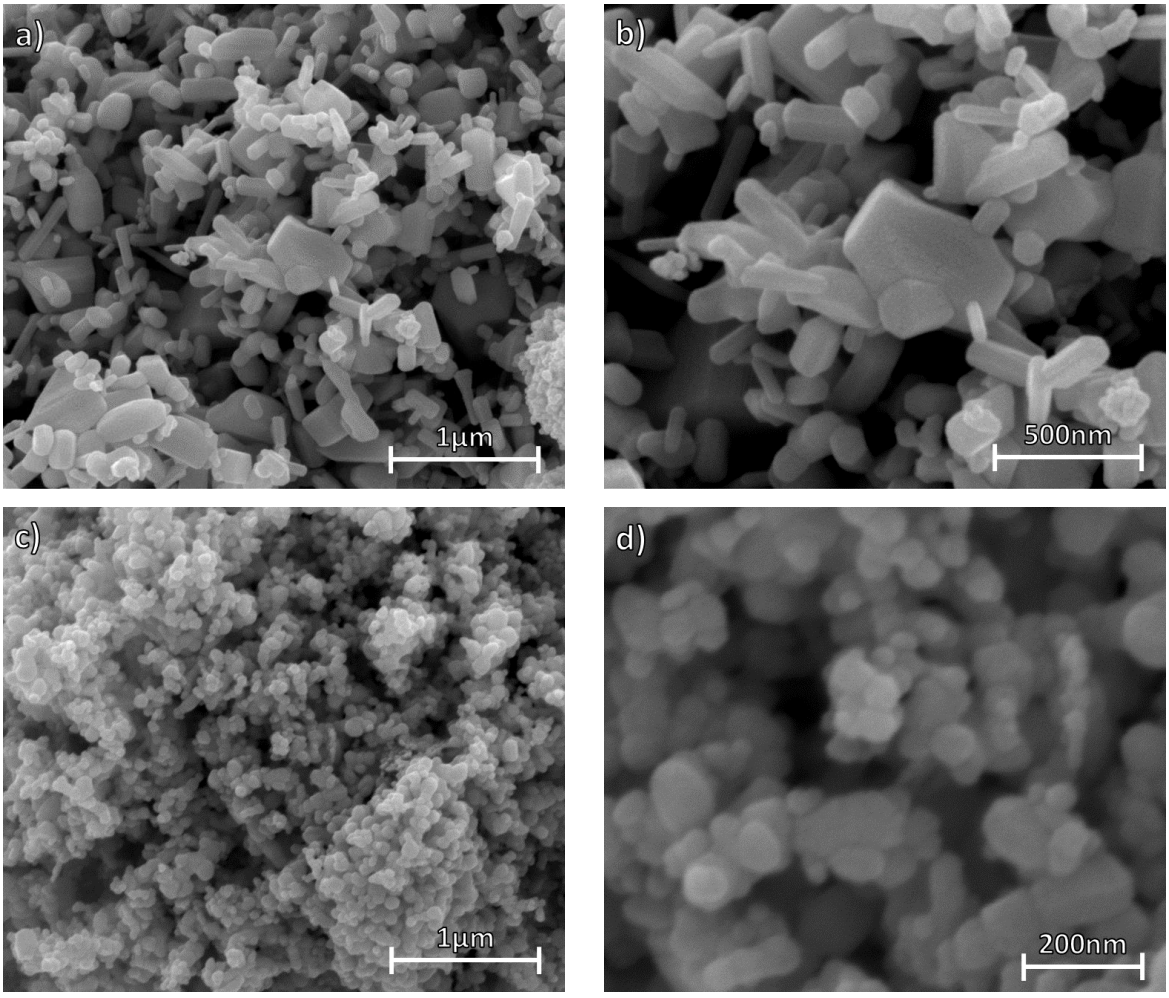

Figure 4.1: Secondary SEM micrographs of the cZnO (a-b) and nZnO (c-d) starting powders used in this chapter

4.2.2 Cold Sintering of cZnO & nZnO & $Ga_{0.2}Zn_{0.98}O$

4.2.2.1 Powder Preparation of Course ZnO (cZnO), Nano-ZnO (nZnO) & $Ga_{0.2}Zn_{0.98}O$ (GZO)

cZnO was ball-milled in isopropanol with 5mm cylinder alumina media overnight. The powder was dried and sieved before being placed into a 180°C drying oven and kept there until used. Particle sizes of GZO and nZnO were too small to be affected by ball milling. Thus, only sieving was used to break up larger agglomerates with the powders kept at 180°C before being used.

4.2.2.2 The Cold Sintering Process

All powder was cold sintered via the same processing route, with variation only in the volume of acetic acid. 0.5g of ZnO powder was combined with ~20wt% (cZnO), or ~30wt% (nZnO, GZO) 1.0 molar Acetic acid, and mixed continuously in a pestle and mortar until a slurry-like rheology was obtain followed agglomeration. Mixing was performed until all agglomerates were broken up a leaving a fine powder.

Mixed powder was poured into a 10mm die and pressed at either ~190, 250, or 375 MPa at room temperature for 10 minutes. While maintaining pressure, the temperature was raised to either 125, 200, or 300 ^{o}C, and held 1 hr before being cooled using a small 20mm fan to room temperature. Heating and cooling rate was not controlled but was estimated to be between 20-40^{o}C/min. Some samples were heat treated for 8hrs at 500^{o}C in air with a 5^{o}C/min ramp to remove residual acetate groups. Figure 4.2 shows final cold sintered ZnO material and its colour variation discussed in section 4.3.1.3 (a,b,&d), as well as the hot pressing equipment used in the process (c).

4.2.2.3 Conventional Solid-State Sintering (SSS)

cZnO and GZO powder were placed into a 10mm die and cold pressed 125MPa for 1 minute, and sintered at 1500^{o}C for 8hrs in flowing air, with a ramp and cooling rate of 5^{o}C/min.

To prevent cracking of nZnO, 5wt% of a 5wt% PVA binder solution was mixed into the powder with a pestle and mortar and cold pressed 1 min, at 250MPa. Binder burnout was performed at 500^{o}C for 2 hours before the temperature was raised to 1500^{o}C for 8hours at 3^{o}C/min. The temperature was lowered at 2^{o}C/min to 900^{o}C where it was held for 2 hours before being lowered to room temperature at 5^{o}C/min. This more careful cooling process such as holding at 900^{o}C was to further assist in preventing cracking by helping normalise the pellet before a faster cooling rate as per the advice of a colleague.

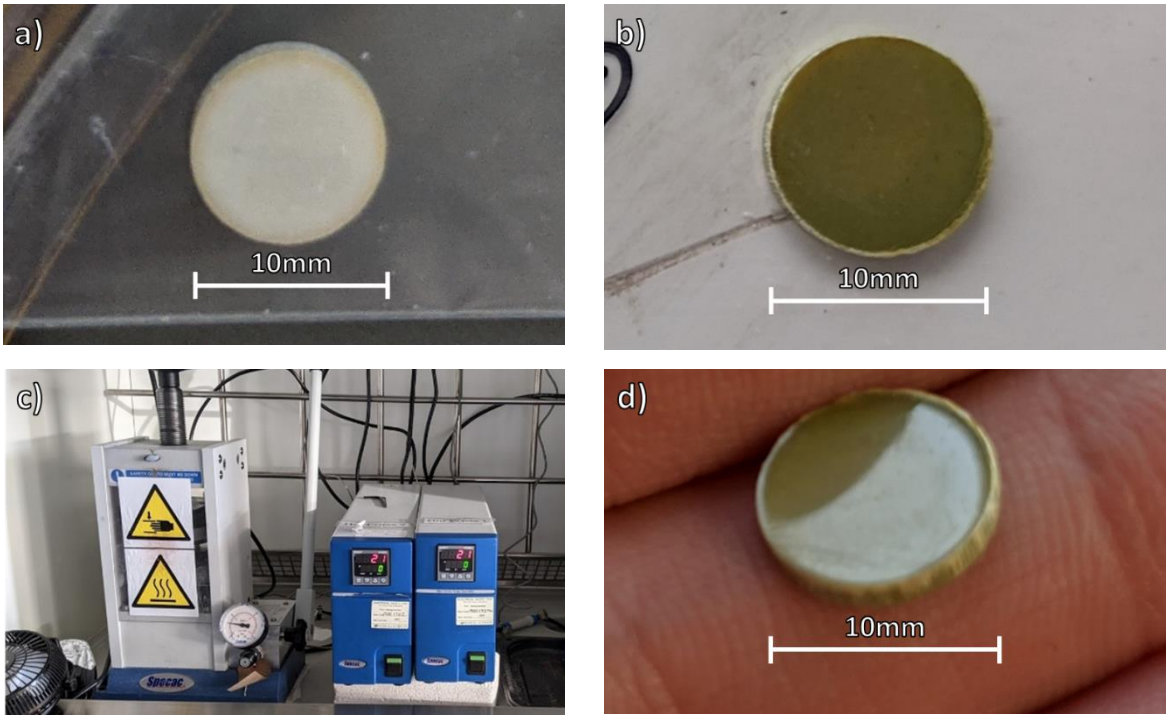

Figure 4.2: Photos of the pellets produced from cold sintering and of the hot press used. a&b) Pellets produced at 125°C 190MPa and 300°C 375MPa respectively. Distinct colour change to green occurred at 300°C. c) Presses used for cold sintering. d) Photo of the result of using mirror-finish dies to produce ultra-flat pellet surfaces.

4.2.3 Analysis

4.2.3.1 Density Measurement

Density was measured using the Archimedes method in ethanol. An average was taken from 3 measurements.

4.2.3.2 Structural and Microstructural Studies

X-ray diffraction was performed in a Bruker-D2 phaser, with a 0.3 second step time, 0.02° step, 1mm diffraction slit, 3mm air-scatter gap, from 2θ = 10-90°.

Raman spectroscopy was carried out on a Renishaw InVia Raman microscope, using a 514.5nm green laser at 20MW, 15 second scans, with 3 data accumulations. Scans were performed on fracture surfaces so that bulk rather surface effects could be studied.

Samples for SEM were coated in either gold or carbon and analysed using an FEI Inspect F50 at 10kV and 3.5 spot size. Secondary electron and backscattered electron images were obtained from top and fracture surfaces of the pellets. Images presented are not representative of pressing orientation and was not accounted for when images were taken.

SEM images using ImageJ were also used to analyse grain size, and grain size distribution, but measurements were limited to fracture surfaces due to COVID restrictions thus only general

trends can be taken from the gathered data. Using fracture surface images, measurement was calibrated using the scale-bar on the taken images using ImageJ's length calibration tool. A minimum of 500 grains were measured across each image with a minimum of 2 separate zones being measured. 4 diameter measurements were taken from each grain and an average was calculated. Grains where no dimension was over 2.5x others of taken of that grain (aka not elongated grains) were taken in a criss-cross pattern. Elongated grains on the other hand had 2 measurements taken length ways, and 2 width ways and an average taken. Samples where elongated grains were measured are noted when data is provided as these measurements are of much lower accuracy. From the data collected from each sample the average, standard deviation, and median were calculated.

To determine the Ga distribution of cold sintered $Ga_{0.2}Zn_{0.98}O$, electron probe microanalysis was performed on a sample fabricated at 300°C and 375MPa. Analysis was performed externally at Johnson Matthey Technology Centre, Sonning Common courtesy of H. Zheng.

Sample sections were mounted in epoxy resin and polished on a sectional mount. Grinding with 800, 1200, 2500 grit was performed followed by polishing with 5,3, and 1µm diamond polish to achieve a mirror finish.

The polish face was vacuum carbon coated and analysed using a JEOL JXA-8500F electron probe microanalyser with wavelength dispersive spectrometers and one silicon drift diode (SDD) EDX detector. Matrix corrections used either ZAF or Phi-Rho-Z. The ZAF or Phi-Rho-Z algorithm utilized was Armstrong/Love Scott. The 'LINEMU Henkie (LBL, 1985) <10KeV / CITZMU >10 kV' dataset for mass absorption coefficients was used. Where required interference corrections were applied.

4.2.3.3 Impedance Spectroscopy (EIS)

An AC-EIS sweep from 1Hz-1MHZ were taken using an Agilent E4980A Precision LCR Meter. Sweeps were performed from 50-312K on a 10mm diameter nano-ZnO pellet cold sintered at 300°C 375MPa pre-and-post-heat treatment at 500°C in air. The pellet was polished with 6,3 and 1µm diamond paste before being coated with In-Ga eutectic electrodes to ensure an Ohmic contact.

Data taken was processed in ZView. A correction factor based on the pellet based on $\frac{Area}{Thickness}$ was used to normalise for pellet size. Maximum frequency (F_{max}) measurements were taken

to find the maximum modulus (M''_{max}) and maximum impedance (Z''_{max}) of any peaks (defined in Chapter 3). From this, conductivity ($\sigma = \frac{1}{R}$) and angular frequency ($\omega = 2\pi F_{max}$) were extracted. σ was plotted against 1000/T in kelvin and the gradient was taken and multiplied by 0.1982 (explained in section 3.3.5) to extract the activation energies of each component of the material. ω was then used to calculate capacitance of where $C_{Z''} = \frac{1}{\omega 2 Z''_{max}}$ and $C_{M''} = \frac{1}{2M''_{Max}}$ for Z" and M" respectively.

4.3 Results & Discussion

4.3.1 General Discussion

4.3.1.1 Sample Fabrication

Samples were successfully densified across all tested temperatures and pressures but results were initially difficult to repeat, with final densities and mechanical integrity sensitive to temperature and humidity of the cold sintering environment. However, repositioning of the cold sintering press to a fume-cupboard with constant airflow greatly improved reproducibility.

4.3.1.2 Mechanical Stability

Mechanical stability varied significantly for initial samples which were often fragile and crumbled if not handled carefully. However, samples produced later in the project were of a much higher quality with superior handling characteristics. The mechanical properties of cold sintered ZnO have been addressed in detail by Lowum et al.[20] who described similar findings which they also attributed to changes in atmospheric conditions on a daily basis within their laboratory.

4.3.1.3 Sample Colour Change

Samples showed a distinct colour change from yellow/white to dark green (Figure 4.2) with increasing temperature, especially between 200 and 300^{o}C. This colour may indicate a high concentration of oxygen vacancies produced by reduction during the sintering process, resulting in F-centres [196], [197] that favour reflection of primarily green light. This agrees well with the findings of Gonzalez-Julian et al. [15] who found oxygen vacancies were prevalent in cold sintered ZnO and proposed them as a key factor in the mechanism of densification.

4.3.2 The Effect of Powder Size on the Cold Sintering of ZnO

4.3.2.1 Powder Analysis

SEM images (Figure 4.1) showed notable differences in morphology as well as particle size between the cZnO and nZnO, 171nm(±81) and 59nm(±21) respectively. cZnO particles had a mostly elongated morphology with only a few pseudo-spherical particles whereas nZnO (Figure 4.1c-d) consisted of pseudo-spherical particles.

4.3.2.2 Crystal Structure

XRD of cZnO and nZnO (Figures 4.3 and 4. 4, respectively) each showed dominant (101), (100), and (002) peaks, consistent with polycrystalline Wurtzite ZnO [198]–[200]. Little peak narrowing is observed in cold sintered cZnO or nZnO in comparison to raw powder, with all cold sintered samples showing very similar patterns. However, both powders' XRD show evidence of peak splitting, consistent with change in grain size discussed in section 4.3.2.3.2. All observed results agree well with available literature [15]–[17].

No peaks associated with secondary phases were observed in XRD traces. However, as confirmed and discussed in 4.3.1.6, a zinc acetate mode is often observed in Raman spectra. Its absence in XRD traces suggests that the volume fraction of residual zinc acetate is below the detection limit of the Bruker D2 diffractometer under the conditions of operation described in section 4.2.3.2.

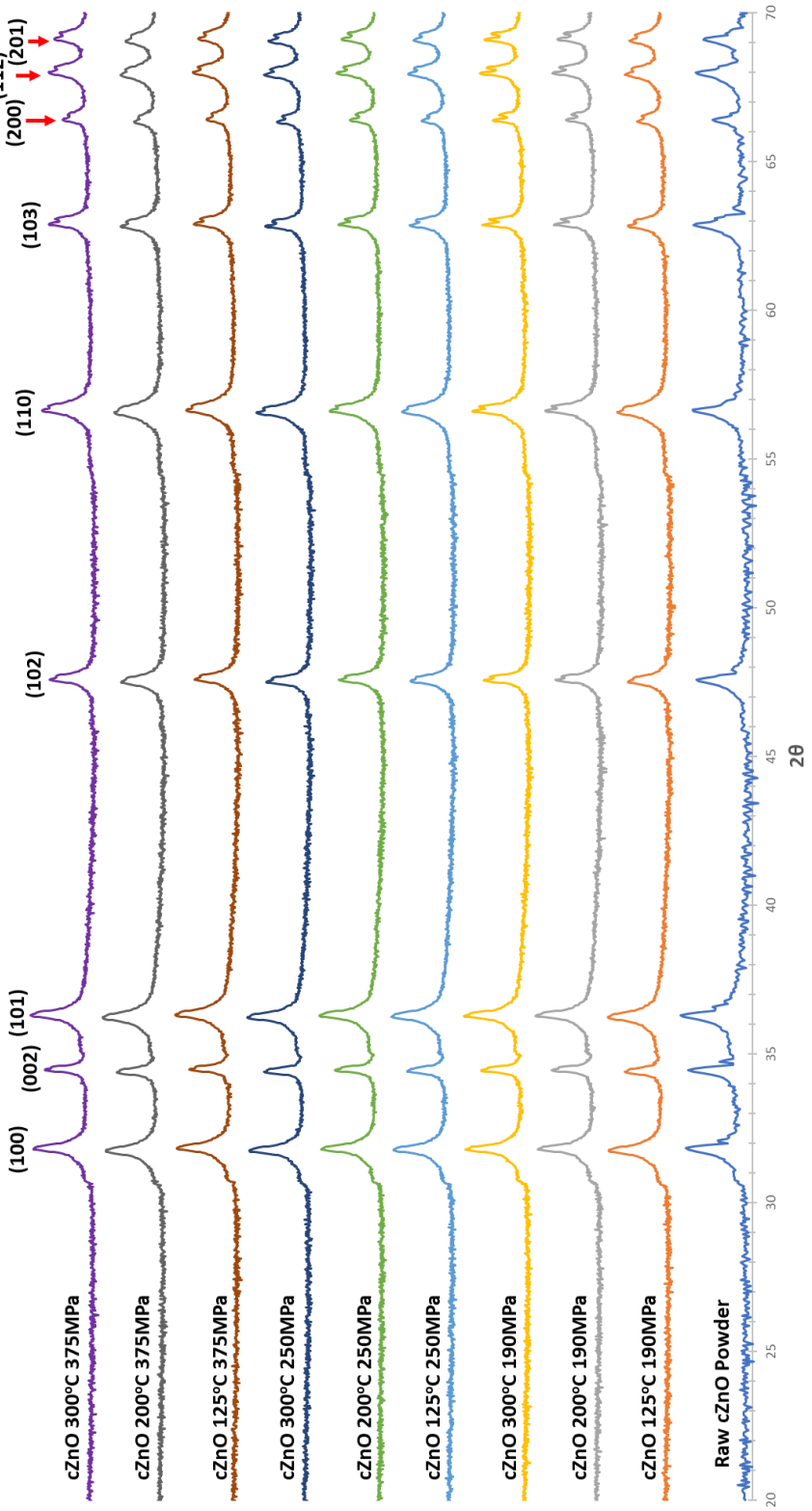

Figure 4.3: Log-linear XRD spectra of cZnO cold sintered at increasing temperature and pressure, compared to unsintered powder.

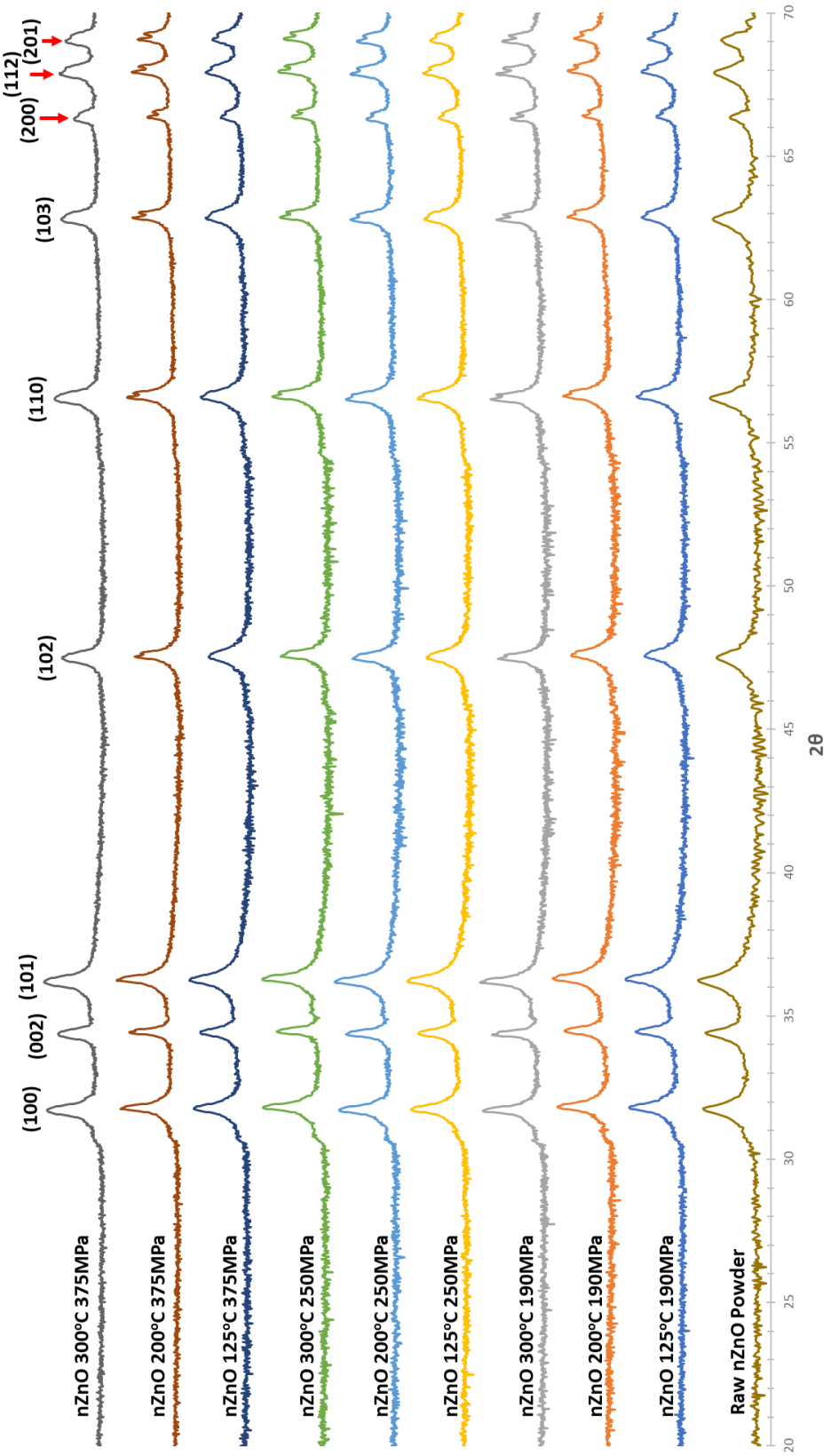

Figure 4.4: Log-linear XRD spectra of nZnO cold sintered at increasing temperature and pressure, compared to unsintered powder

4.3.2.3 Grain Growth and Densification

SEM images (Figure 4.6-4.9) compare the top surfaces and fracture surfaces of both nZnO (Figure 4.6 & 4.7 respectively) and cZnO (Figure 4.8 & 4.9 respectively). Images are arranged into a picture-graphs to visually compare the effects of cold sintering pressure and temperature on microstructure. Measurements of average and median grain sizes, and grain size distribution using a range of SEM images are displayed on Figure 4.10. Raw data from Figure 4.10 is given in Table A.1 in the appendix.

4.3.2.3.1 Density

>90% density was achieved for nearly all samples, as reported in Figure 4.5. At 200^{o}C, all samples were >92% relative density, and >95% from for samples cold sintered at 300^{o}C and >250MPa. At 125^{o}C, densities varied ranging from 84% and upward. The sensitivity to external conditions (e.g humidity) appears more prevalent at lower temperatures with high temperatures achieving more reproducible and higher densities. cZnO consistently showed higher density than nZnO, similar to observations reported by Serrano et al.[201] Densities observed for cZnO matched those of Funahashi et al.[17] who employed powder with a similar particle size (~200nm) [17]. SEM images (Figures 4.6-4.9) revealed fracture surfaces consistent with a high relative density. The top surfaces also have a microstructure consistent with a high theoretical density although some small pores (90-300nm) are apparent (Figures 4.6 and 4.8 - arrowed).

Although the higher surface area/energy of nZnO compared with cZnO creates a greater driving force for the sintering, it also leads to greater agglomeration. Agglomerates cause loss of grain contact and encourage pore formation [202]. Cold sintering at higher temperature and pressure forces agglomerates together and encourages their dissolution within the liquid phase [11], generally leading to higher densities.

Conventionally-sintered nZnO powder samples also suffered from agglomeration and which, as discussed in section *4.2.2.3* required a carefully controlled sintering process for the fabrication of dense samples. In contrast, cZnO routinely achieved near theoretical density when conventionally sintered.

The cold sintering temperature had a greater impact on final density compared to pressure [16], [17], which had little effect on the density of cZnO and nZnO at 125^{o}C or 200^{o}C. At 300^{o}C

however, a modest increase in density with increasing pressure is noted in nZnO and may relate to the large grain size distribution at this temperature (section 4.3.2.3.2).

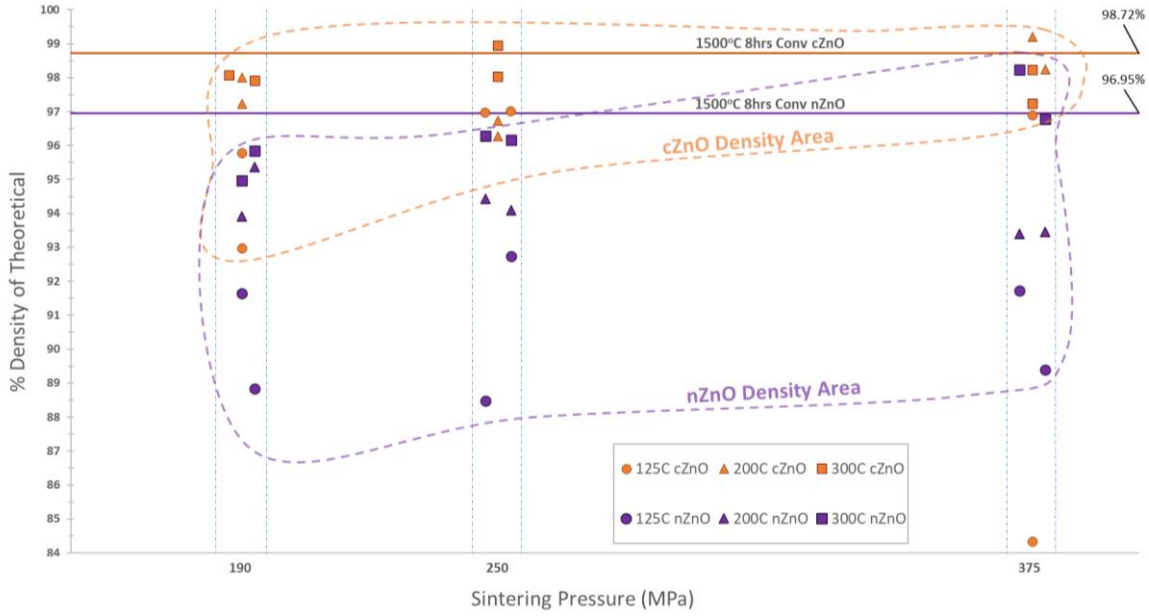

Figure 4.5: Graph comparing densities of nZnO (purple) and cZnO (orange) conventionally-sintered and cold sintered at various temperatures (125, 200, 300°C) and pressures (190, 250, 375MPa).

4.3.2.3.2 Grain Growth, Size Distribution and Morphology

Grain Size & Grain Size Distribution

For nZnO, increase in temperature increases in grain size at all pressures. However, pressure increases only promote a notable effect on grain size at 300°C. At 125°C and 200°C, a slight increase in grain size is seen from 105nm(±42) to 127nm(±46), respectively, at 190MPa, and 68nm(±26) to 196(±98), respectively, at 375MPa. However, at 300°C grain growth is far more significant and has a much larger grain size distribution; with sizes of 408nm(±155), 786nm(±874), and 1.1µm(±0.73), at 190MPa, 250MPa, and 375MPa respectively. Two grain size populations of larger and smaller grains are also observed in SEM images (Figure 4.7; arrowed).

cZnO follows a similar pattern to nZnO (Figure 4.10). At 125°C 190MPa, no grain growth is observed, however densification has occurred, with SEM images showing intergranular contact (Figure 4.9). As temperature increases, (similar to nZnO) grain size increases but to a lesser degree, with a narrower grain size distribution. Grain size increases to 285nm(±154) at 300°C 190MPa, and increases further to 505nm(±330) when pressure is raised at 300°C to

250MPa. However, the average grain size increase slows with further pressure increase to 375MPa to 538nm(±458), but with a wider grain size distribution.

As with nZnO, the mean becomes much larger than the median grain size, indicating a greater population of larger grains and a more inhomogeneous microstructure. For both materials, median grain size remains relatively close to the mean for nearly all conditions. However, at 300^{o}C 375MPa the mean becomes much larger than the median indicating greater numbers of very large grains.

The grain size distribution (Figure 4.10), increases with temperature for both cZnO and nZnO with pressure having a limited effect at lower temperature. However, at 300^{o}C, grain size and distribution increase at higher pressures particularly for nZnO, (733nm, 300^{o}C and 375MPa) compared to 458nm for cZnO under the same conditions.

The centre of cZnO and nZnO pellets (Figure 4.7) show no signs of anisotropic grain growth. However, the surfaces of both materials showed increased grain growth in plane, especially at higher pressures (Figure 4.6 & 4.8). This is attributed to a "constrained sintering" effect, and a common feature of other hot-pressing sintering techniques [8], [202], [14]. These results clearly show the impact of starting grain size on cold sintering with respect to temperature and pressure. Similar to XRD, the presented results for cZnO compare well with Funahashi et al.[17] and Kang et al.[16] who used starting powders of a similar starting size. However, the presented nZnO results deviate from literature findings with a greater impact of higher pressure than previously described [17], [16], especially with grain size distribution. A number of factors may have caused the large observed distribution at the highest pressures and temperatures such as pressure gradients causing higher levels of homogeneous nucleation [16], [17] and higher pressures increasing the role of plastic flow [18], thereby promoting grain boundary sliding.

The higher free surface energy available in the nZnO powder is the likely cause of the explosive grain growth and large grain size distribution compared to cZnO. Taking the average grain size of each powder particle and treating them as spherical, nZnO has a surface area ~3x that of the cZnO powder. Explosive grain growth and broad grain size distributions are a common problem in the sintering of nano-powders and are very sensitive to sintering conditions such as heating rate [202], which was uncontrolled in this study. If cold sintering is

to reach commercial status, much better control of processing conditions will be required for controllable and repeatable results.

As discussed in 4.2.3.2, the method of grain size measurement means that the grain size and grain size distribution values will not be entirely representative of the actual sample as they were taken from fracture surfaces. However, as measurements were taken consistently cross each fracture and top surface of the samples analysed, clear trends can be concluded based on the presented and discussed data with regards to the effects of starting grain size, applied pressure, and temperature. Further analysis using conventional cross-sectional grain size analysis would be required for more accurate results.

Grain Morphology

Pressure and temperature also showed clear effects on grain morphology for both powders. This is most clearly demonstrated in nZnO (Figures 4.6 & 4.7), which at the lowest pressure remains pseudo-spherical until 300^{o}C. At 250MPa grain growth occurs at 200^{o}C with the formation elongated grains. In contrast, cZnO (Figures 4.8 & 4.9) only develops elongated grains at 300^{o}C.

Elongated growth of ZnO is energetically favourable due to the ideal stacking ABABAB in the c-axis direction and is the most common morphology for ZnO powders and is reported in many cold sintering and conventionally-sintered studies [15], [17], [186], [203]. If a spherical grain structure is desired, grain growth must be limited through control of pressure and temperature.

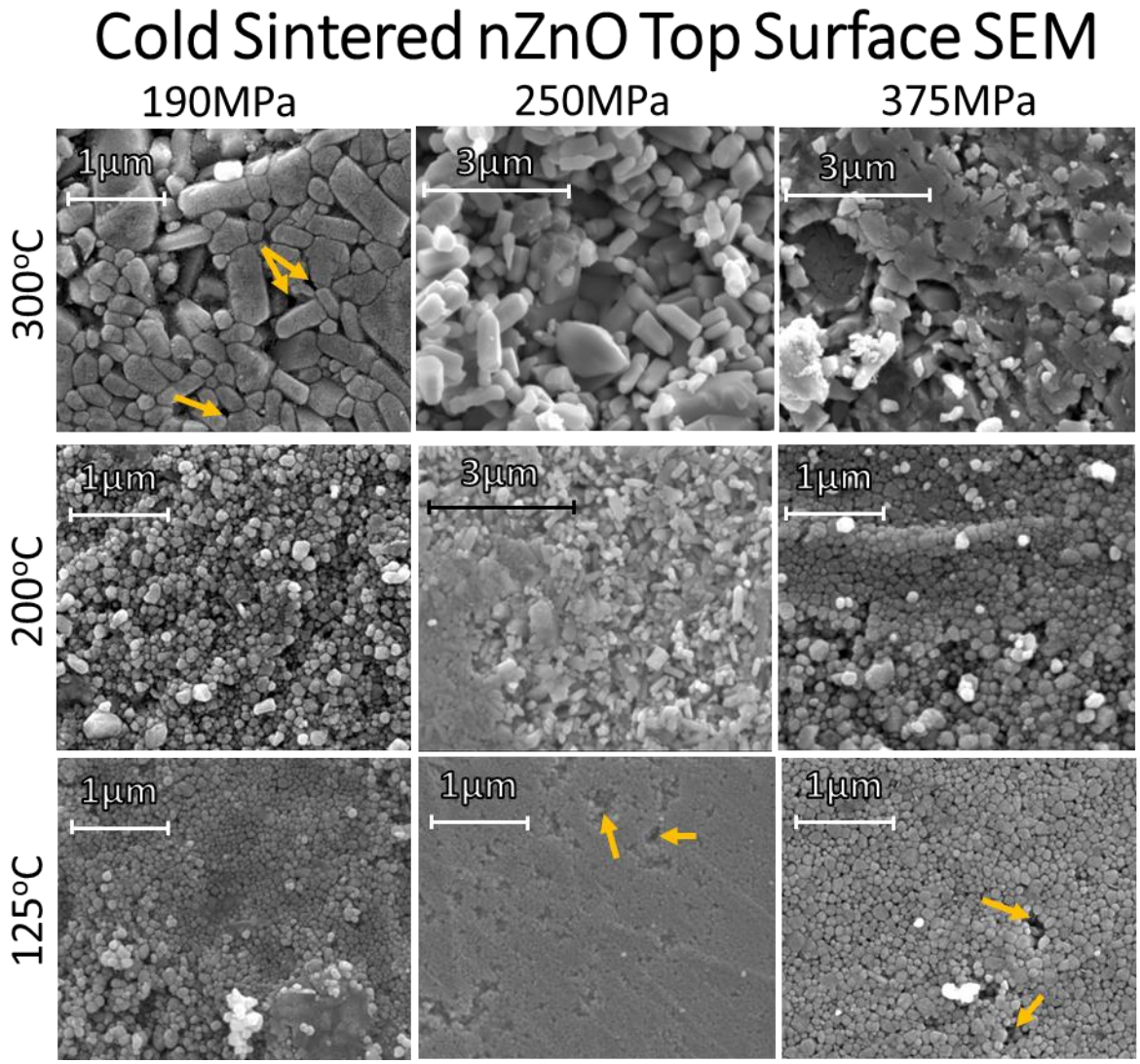

Figure 4.6: SEM micrographs of the top surfaces of nZnO cold sintered at 125, 200, & 300°C and 190, 250, & 375MPa. Arrows on images indicate pores (~2-300 nm) visible on the sample surfaces.

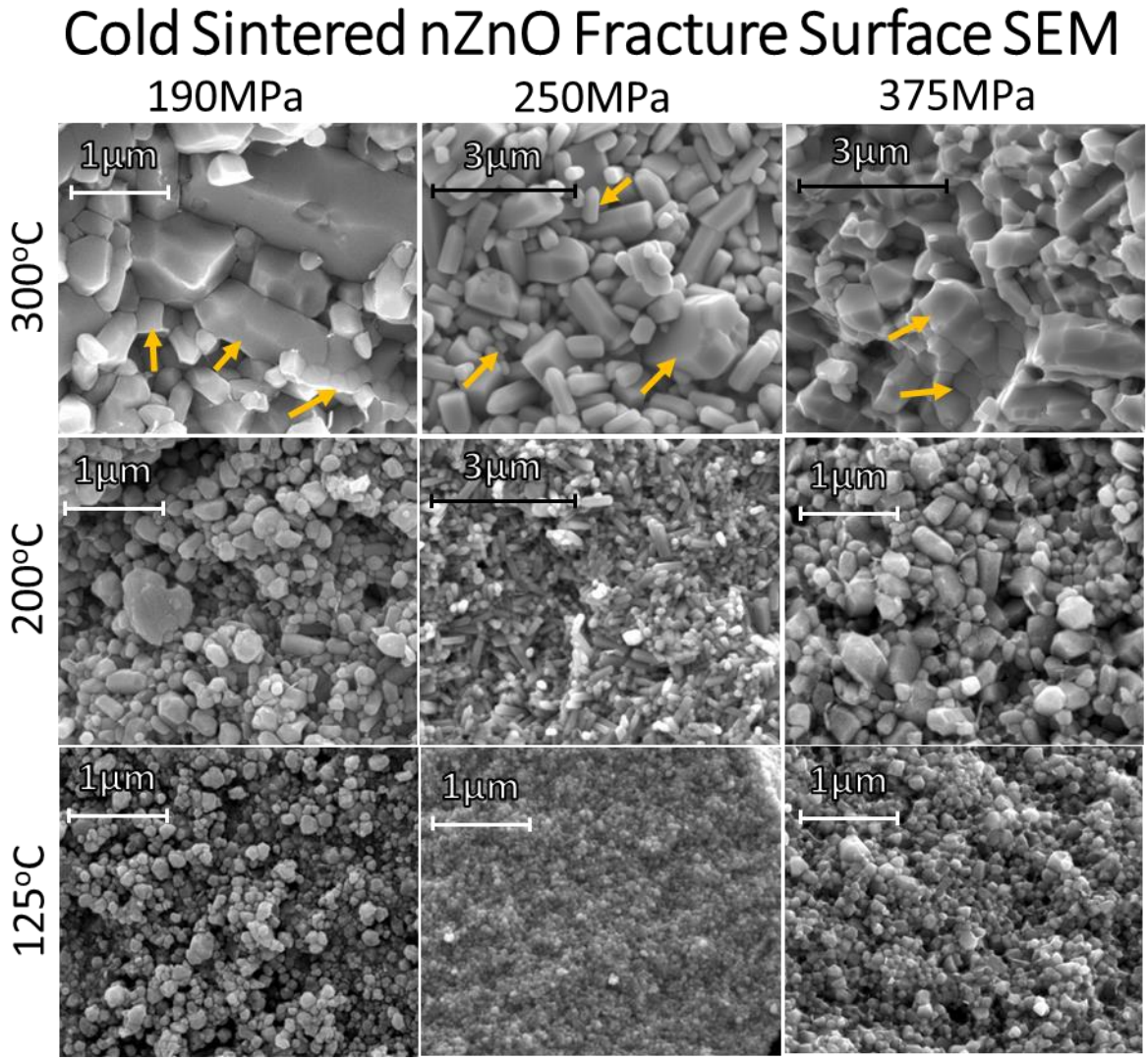

Figure 4.7: SEM micrographs of the facture surface of nZnO cold sintered at 125, 200, & 300°C and 190, 250, & 375MPa. Arrows on images indicate the 2 different grain size populations observed after cold sintering at 300°C (all pressures).

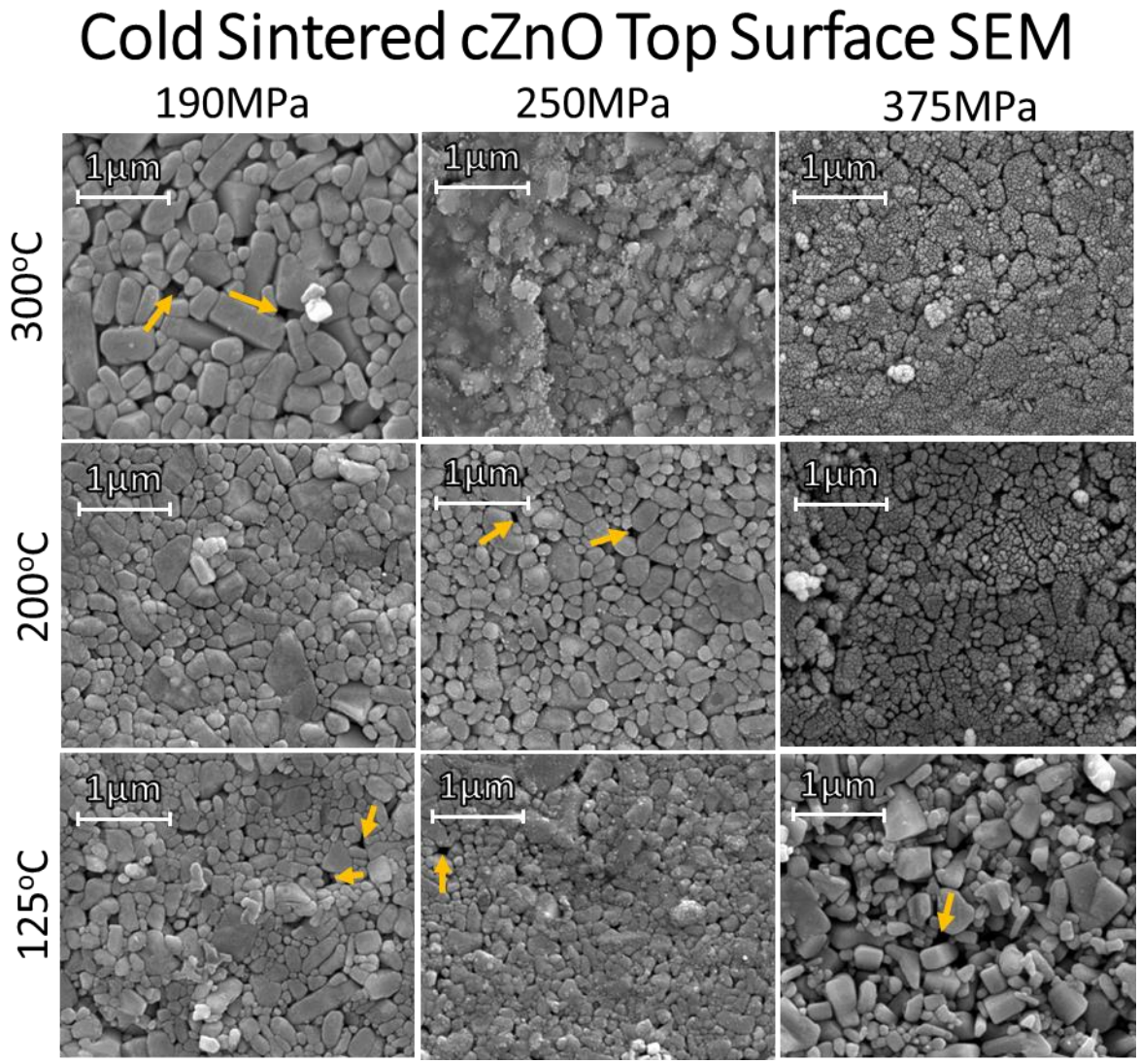

Figure 4.8: Secondary SEM micrographs of the top surface of cZnO cold sintered at 125, 200, & 300°C and 190, 250, & 375MPa. Arrows on images indicate some surface pores.

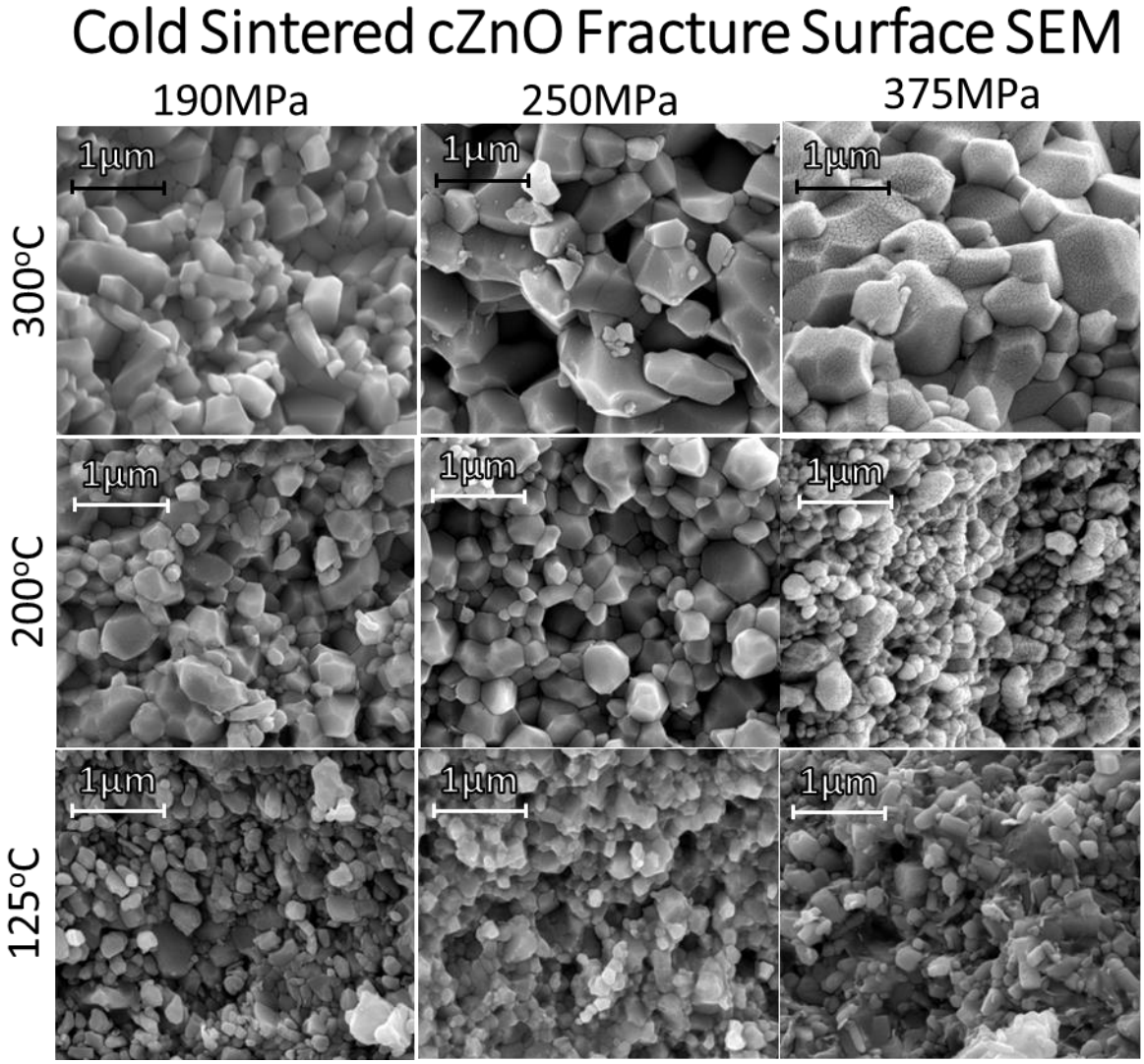

Figure 4.9: Secondary SEM micrographs of the facture surface of cZnO cold sintered at 125, 200, & 300°C and 190, 250, & 375MPa.

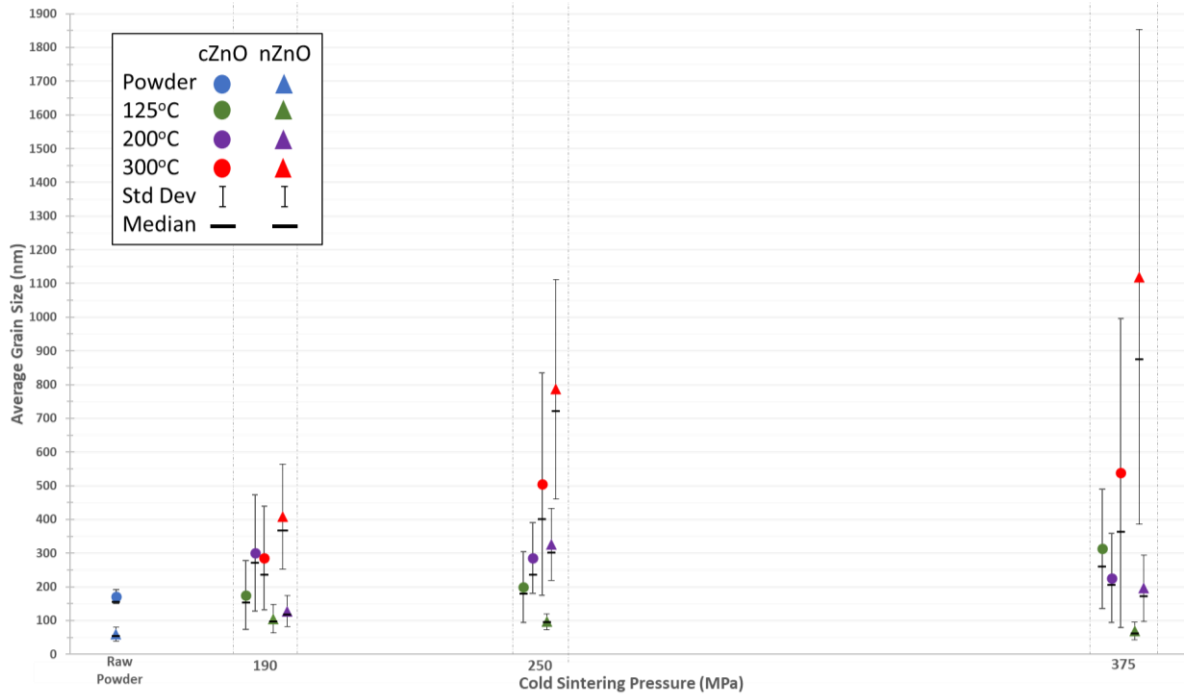

Figure 4.10: Graph comparing the increase in grain size with temperature and pressures between cZnO and nZnO. Standard deviation indicating grain size distribution, and median grain size are also given.

4.3.2.3.3 Comparison with Conventional Sintering

Cold sintered and conventionally sintered microstructures for both cZnO and nZnO show substantial differences (Figure 4.11). Conventionally-sintered cZnO consisted of closely packed elongated grains (18-20µm, large intergranular pores of 1-3µm, and sparse intra-granular pores of 300-600nm. nZnO also showed a continuous and dense microstructure with a wider grain size distribution of 5-20µm, and intragranular porosity from 100-500nm diameter. These grain and pore sizes are several orders of magnitude larger than cold sintered ZnO and it is not known if they are achievable via cold sintering, as it would likely require starting powders with particle sizes comparable to the final microstructure. Such large particle size may not densify well using cold-sintering.

This result may be seen as an advantage or disadvantage of cold sintering [173]. If small grain sizes are desired then the advantages are clear, as maintaining a very small grain size while achieving high density conventionally is a challenging task for conventional sintering [202]. If a large grain size is desired, then other sintering techniques may have to be utilised.

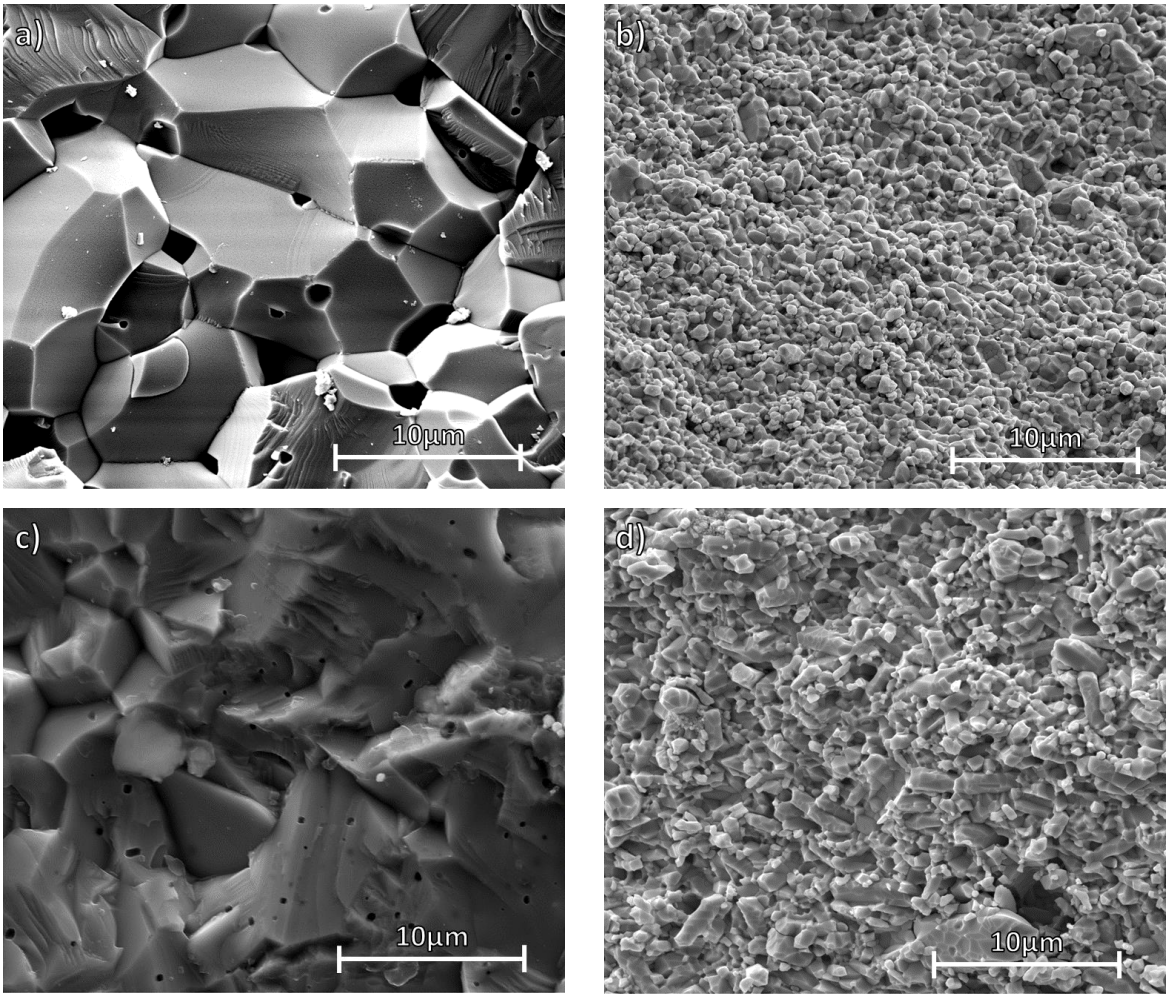

Figure 4.11: Secondary electron SEM fracture surface images comparing conventionally-sintered (1100°C) (a) cZnO and (c) nZnO to cold sintered (b) cZnO and (d) nZnO at 300°C 375MPa. Cold sintered material shows significantly less grain growth than conventionally-sintered.

4.3.2.4 Abnormal Microstructural Features

Although a homogenous grain structure was consistently observed for nearly all pellets, a minority would produce some abnormal features (Figure 4.12).

4.3.2.4.1 Zones of Abnormal Grain Growth (Figure 4.12 a-b)

Abnormal grain growth is a well-known to occur in sintering and is detrimental to the final properties of a material. It is frequently observed when grains in specific locations grow faster than the rest, leading to a bimodal grain-size distribution. Causes of abnormal grain-growth vary [1]. Two kinds of abnormal growth occurred in cold sintered samples. Either as zones of grains larger than the rest of the bulk (Figure 4.12a), or as singular 'super-grains' (Figure 4.12b) within the structure that were orders of magnitude larger than the rest of the grain structure.

Causes of the zones of larger grains (Figure 4.12a) may be caused by inadequate mixing of the liquid phase into the powder phase, as many of these zones were scattered throughout the sample. Another cause may be zones of highly porous grains acting as liquid reservoirs which leads to zones of higher liquid content. These zones of higher liquid phase concentration upon heating experience and increased amount of mass transport and thus densify better and experience increased grain growth. Comparable zones of abnormal grain growth were observed by Bang et al. [174] whose investigation into the upscaling cold sintering ZnO experienced inhomogeneous grain growth, blaming localised evaporation of the transient phase. 'Super grain' formations (Figure 4.12b) are thought to have been caused by insufficient breaking up of powder agglomerates before the cold sintering process. Thus, these agglomerates with better pre-compaction experience accelerated growth. Hynes et al. [199] observed similar grain formations.

These two examples highlight the need to properly prepare the starting powder, and carefully control sintering conditions to avoid inhomogeneous microstructures. This is demonstrated in Figure 4.12a, where the arrowed zone of larger grains is thought to have been the cause of the large crack shown in the image.

4.3.2.4.2 Grain Boundary Nano-Grain Formation (Figure 4.12c-d)

The second kind of anomaly appeared as ultra-high concentrations of homogeneous nucleated nano-grains at the grain boundaries, forming a 'pebbled' or 'cobbled' appearance. This was most commonly observed at the sample surface (Figure 4.12c) but occasionally appeared in the bulk (Figure 4.12d). As discussed in section 2.8.4.3.2, upon evaporation, homogenous nucleation leads to formation of nano-grains at interstitial sites between grains [13]. The significantly higher concentration of nano-grains found at the sample surface are possibly due to the highest volumes of super-saturated solution evaporating from the surface where the highest temperatures occur. This causes significantly more dissolved material to be deposited, leaving a pebbled or cobbled appearance. This microstructural feature was never observed homogenously across the sample surface suggesting uneven liquid evaporation. Exact conditions to initiate this surface grain growth are unclear and this phenomenon requires further investigation.

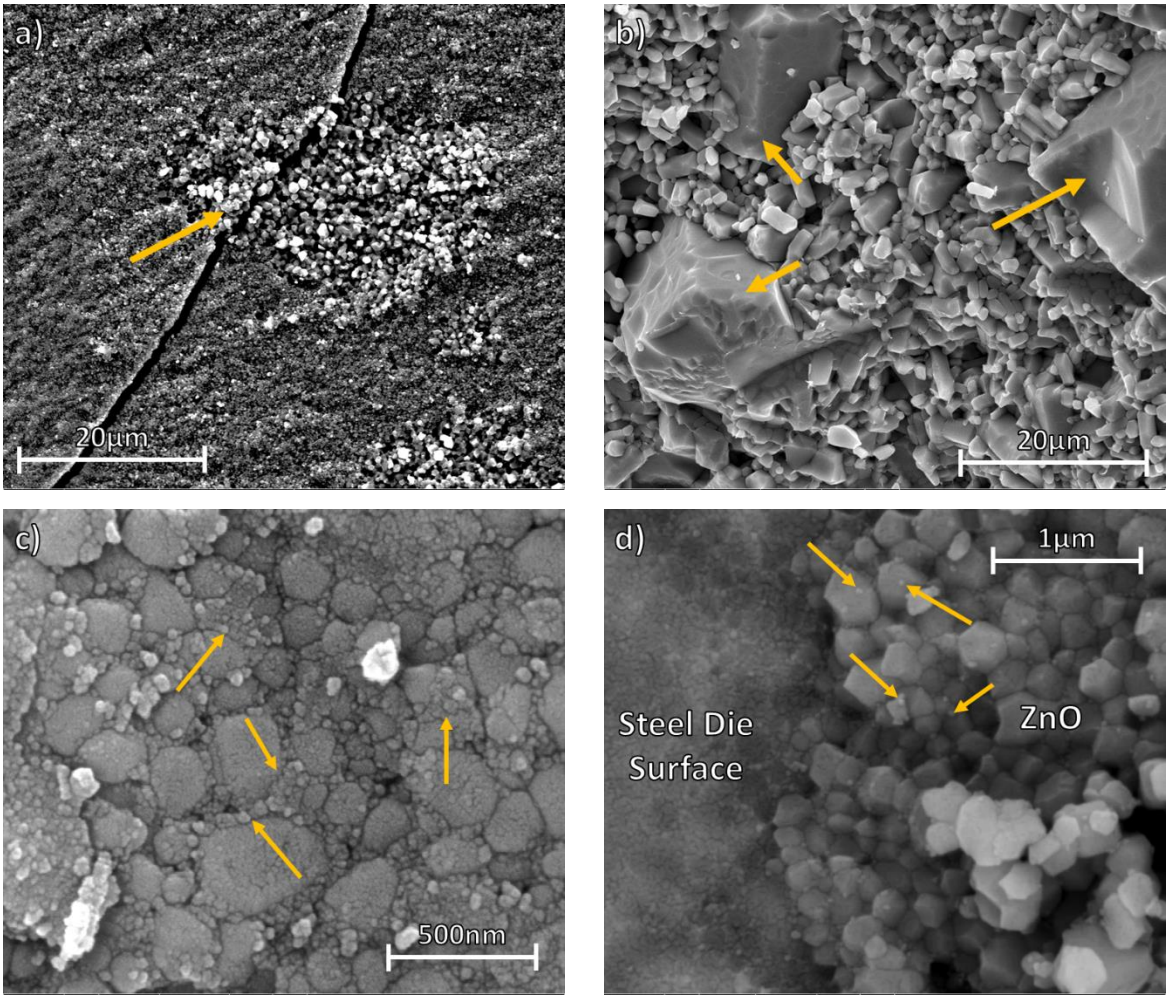

Figure 4.12: Secondary electron SEM images showing several of the abnormal grain growth features that sometimes occurred across both powders at varying pressures and temperatures. a) Fracture surface image of a suspected "hot-spot" (arrowed) zone where significantly more grain growth occurs compared to the rest of the bulk material, this is thought to have caused the crack formation seen in the same images. b) Fracture surface image of formation of "super-grains" (arrowed) that could sometimes be found in some samples, this is although thought to be from a hot-spot formation during hot pressing. c) Top surface image of "nano-grains" or "pebbling" (arrowed) that sometimes formed at grain boundaries in large quantities, especially at sample surfaces. d) Fracture surface image of nano-grain grain boundary "pebbling" sometimes observed internally (arrowed).

4.3.2.5 Raman Spectroscopy and Secondary Acetate Phase

As discussed in section 2.5.1, the hexagonal wurtzite structure of ZnO belongs to the $P6_3mc$ space group, made up of 2 group units per unit cell. The irreducible symmetry representation is given by:

$$\Gamma^{P6_3mc} = A_1 + E_1 + 2E_2 + 2B_1 \qquad (4.1)$$

where only the A_1 and E_1 polar modes and E_2 modes are Raman active [204], [205].

Raman spectra from cold sintered sample agree with available literature across (Figure 4.13) [16], [201], [205], and compares well with conventionally sintered ZnO (Figure 4.14). Intense modes at ~99 and 438cm^{-1} correspond to E_2^{low} and E_2^{high} respectively. E_2^{low} is influenced by Zn sublattice vibrations, and E_2^{high} by oxygen vibration [204]. Several modes are prescribed to second-order modes, including the E_2/A_1 at 328cm^{-1}, A_1(TO) at 372cm^{-1}, A_1 at ~541cm^{-1}, $A_{1(LO)}$ at ~569cm^{-1}, and $E_{1(LO)}$ at ~585cm^{-1}. The last 2 of these modes dominantly arise from second-order background, but can be influenced by impurities, particularly [204] $E_{1(LO)}$ [206]. Two modes form one extended broad peak at 1094cm^{-1} and 1146cm^{-1}. The former is a TO+LO mode at M and L Brillouin points. The latter is a combination of $2A_1$(LO), $2E_1$(LO), and 2LO modes occurring at the centre point (Γ) of the Brillouin zone [206].

A single weak secondary acetate phase was observed previously [16], [19], [207] in Raman studies with 3 modes caused by symmetric stretching of C-C bonds at ~950cm^{-1}, C-O at ~1600cm^{-1}, and C-H at ~3000cm^{-1}. From available decomposition data [208], [209], acetate was expected to be removed from samples at 300°C, above its decomposition temperature. However, acetate was repeatedly observed in 300°C samples possibly due to the limited time not allowing for total acetate decomposition. A successive heat treatment at 500°C (Figure 4.14) completely removed the acetate. However, treatment also caused increased expression of second order A_1 and E_1 modes at ~580 and ~586cm^{-1} respectively. These oxygen dominated responses relate to z-axis Zn-O bond vibrations, and are affected by oxidation during the conventional sintering, and heat treatment. This behaviour suggests that the lattice re-oxidises at 500 °C, hinting that cold-sintered samples may contain comparatively high concentrations of defects.

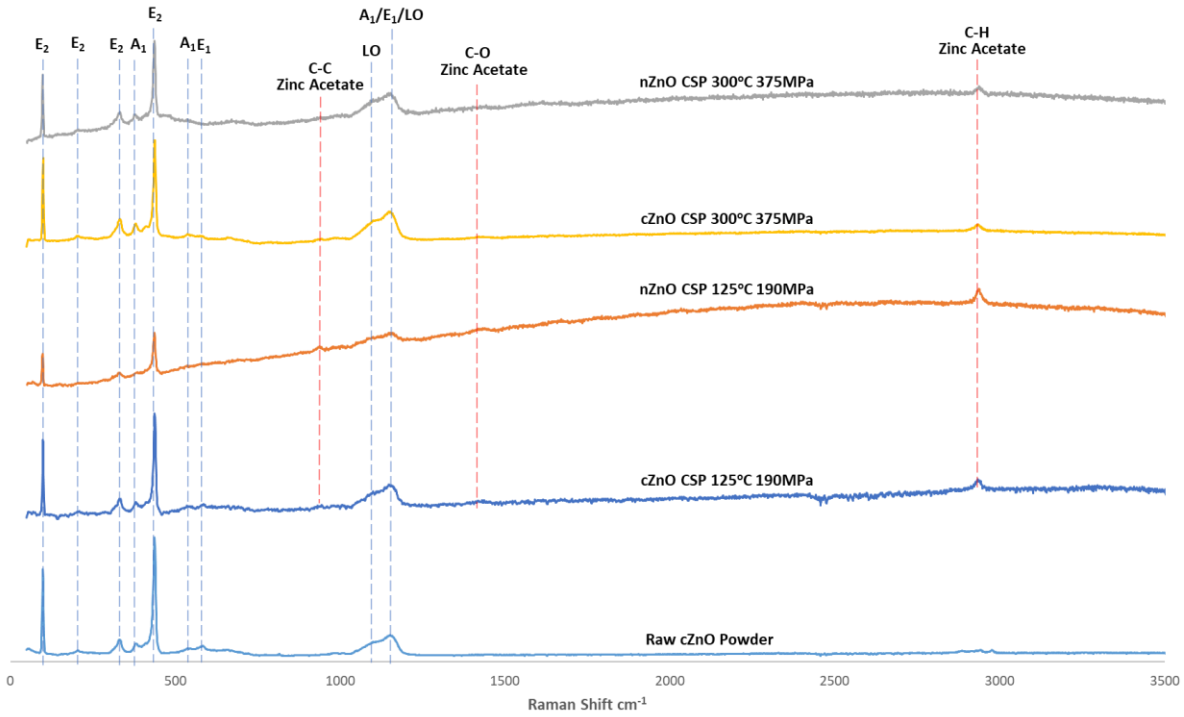

Figure 4.13: Raman Spectrograph (normalised) comparing nZnO and cZnO cold sintered at the lowest temperature and pressure, with the highest temperature and pressure. This is all compared against a scan of unsintered cZnO powder. The active Raman modes of ZnO observed in these works are denoted by the blue lines. The secondary acetate phase only observed in cold sintered material is given by the red lines.

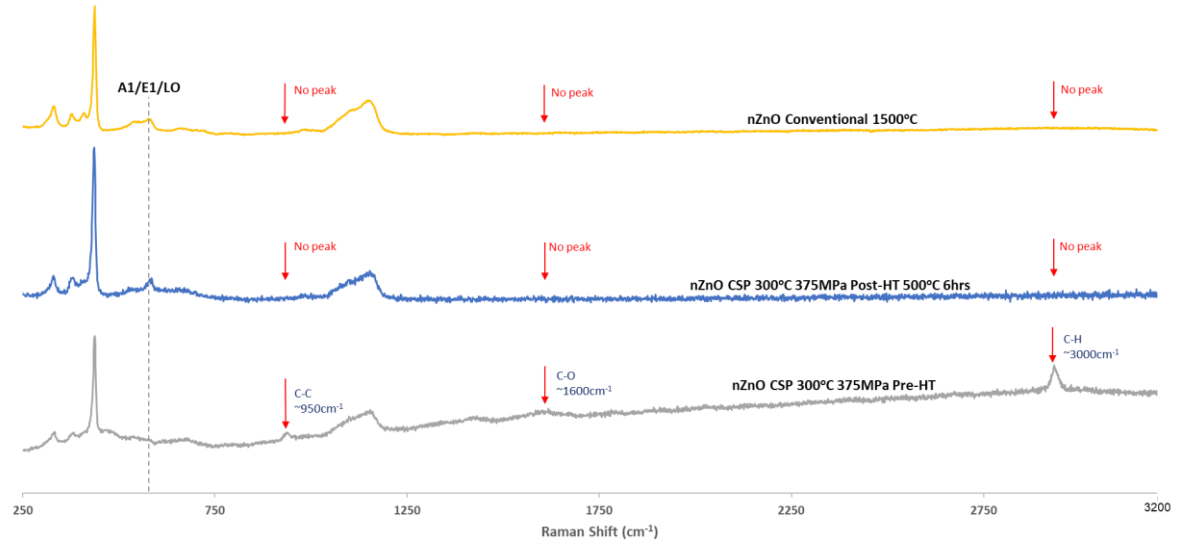

Figure 4.14: Raman spectra (Normalised) showing the effective removal of acetate phase from cold sintered (300°C 375MPa) ZnO via heat treatment at 500°C

4.3.2.6 Impedance Spectroscopy

Due to the impact of COVID and ongoing equipment issues, only preliminary electrical impedance measurements could be performed. Results support previous suggestions that the presence of water during the sintering process as well as the secondary acetate phase may impacting the conductivity of cold sintered ZnO [15], [210].

The presence of two M" (M"$_A$ and M"$_B$) and one Z" peaks (Figure 4.15) was observed both pre-and post-heat treatment. Based on activation energy, M"$_B$ likely corresponds to standard slow cooled ZnO [30]. The activation energy of this phase was unchanged by heat treatment but showed a slight reduction in conductivity. However, total conductivity of the sample increased post-heat treatment from $5.44x10^{-9}$ to $4.78x10^{-8}Sm^{-1}$ at 290K, as seen by the decrease in Z* (Figure 4.16 – Arrowed)**.** The remaining M"$_A$ and Z" responses are suspected to be a singular homogenous response for several reasons:

- identical activation energies (0.15eV) prior to heat treatment (Table 4.1)
- inhabiting in the same frequency domain pre-and-post heat treatment (10^2Hz and 10^3Hz respectively) (Figure 4.15 - arrowed)
- occupying similar conductivity ranges of between -8 to $-7.5\Omega m^{-1}$ pre-heat treatment and increasing by the same order to ~$-7\Omega m^{-1}$ post heat treatment (Figure 4.17)
- showing capacitances in the order of 10^{-12} indicating a bulk response [192].

This result also indicates that neither of these responses are caused directly by the secondary acetate phase. Post-heat treatment however, the activation energy of Z" slightly increased to 0.18eV. Reasons for this change requires further investigation but may indirectly relate to the removal of the acetate phase.

Based on the collected data and literature from Dargatz et al. [4] and Gonzalez Julian et al. [2], a defect-based core-shell structure is hypothesised. The ZnO grains are proposed to be composed of a highly defective outer-grain structure producing the Z" and M"$_A$ response, and a standard low defect ZnO core structure responsible for the M"$_B$ response (Figure 4.15). A diagram of this proposed structure is shown in Figure 4.18.

Explanation for this proposed structure originates from discussion by Gonzalez-Julian et al. [15] who describe the manufacture of highly defective grains, caused by proton and hydroxyl diffusion from the acetic acid solution diffusing into the crystal structure during cold sintering.

The limited diffusion of H^+ into the crystal structure leads to donor doping of the outer shell, lowering the activation energy and increasing the overall conduction. It is likely this mechanism is made even more favourable due to the observed reduction that takes place during cold sintering at 300°C (section 4.3.1.3), as H^+ will act as a donor both at interstitial (H_i^+) and oxygen (H_o^+) sites [84], [211]. A decrease in activation energy leads to an increase in defects via equation 4.2 [15]:

$$\frac{N_d}{N} = \exp\left(\frac{-Q_p}{KT}\right) \quad (4.2)$$

where N_d is the number of defects, N is the number of potential defect locations, Q_p is the activation energy, K is a constant, and T is temperature in Kelvin.

The increase in conductivity after heat treatment at 500°C in air matches that of Jing et al.[194]. However, their conclusions that V_o and Zn interstitials are responsible for conduction are improbable, as V_o in ZnO are deep donors [81], [82], and Zn interstitial formation is unlikely [82], [72], [74], as discussed in depth in section 2.5.3.

Jing et al. also discuss increase in crystallinity is also pointed to as a reason for the conduction increase. The oxidative atmosphere of the heat treatment may have reduced the number of V_o at grain boundaries, increasing the activation energy. Although the secondary acetate phase was not detected under impedance, it was confirmed by Raman spectroscopy and would likely be detrimental to conductivity even if not detected. These reasons given for conductivity change, however, do not explain the slight decrease in conductivity observed in the M''_B post-heat treatment, and warrants further investigation.

Table 4.1: Calculated activation energies of conduction in electron volts (eV) for nZnO cold sintered at 300°C 375MPa before and after heat treatment at 500°C in air.

nZnO CSP 300°C 375MPa	**Activation Energy (eV)**		
	Z''	**M''_A**	**M''_B**
Pre-HT	0.15	0.15	0.33
Post-500°C HT	0.18	0.15	0.33

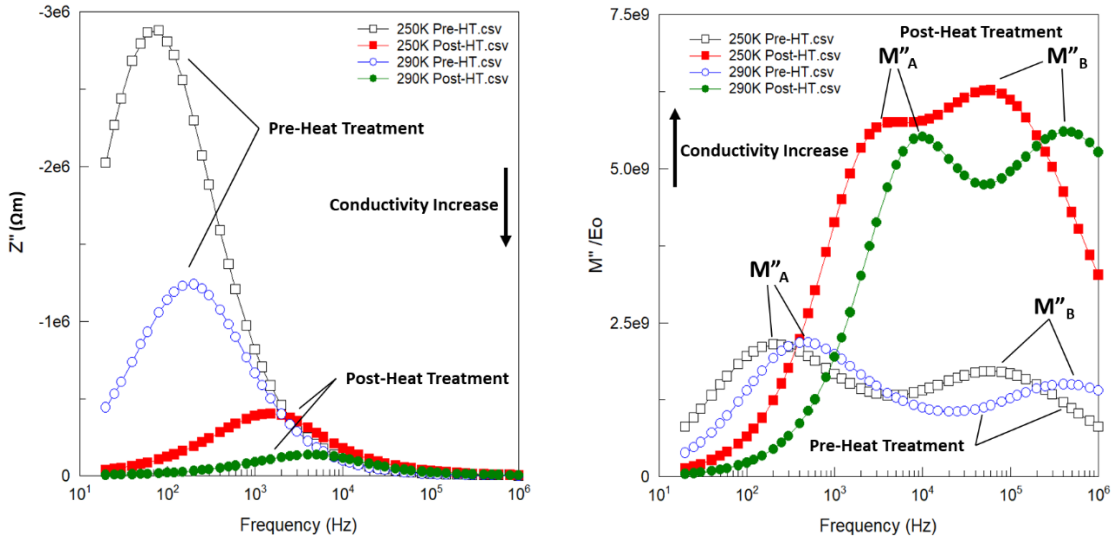

Figure 4.15: EIC Z" and M" responses at 250K and 290K of a nZnO cold sintered at 300°C 375MPa before and after heat treatment at 500°C in air. 3 responses are recorded in total. The Z" and M"$_A$ are likely from the same response indicating a core-shell type structure with a highly defected homogenous outer grain structure and a more standard ZnO core. Conductivity also shows to increase dramatically after heat treatment

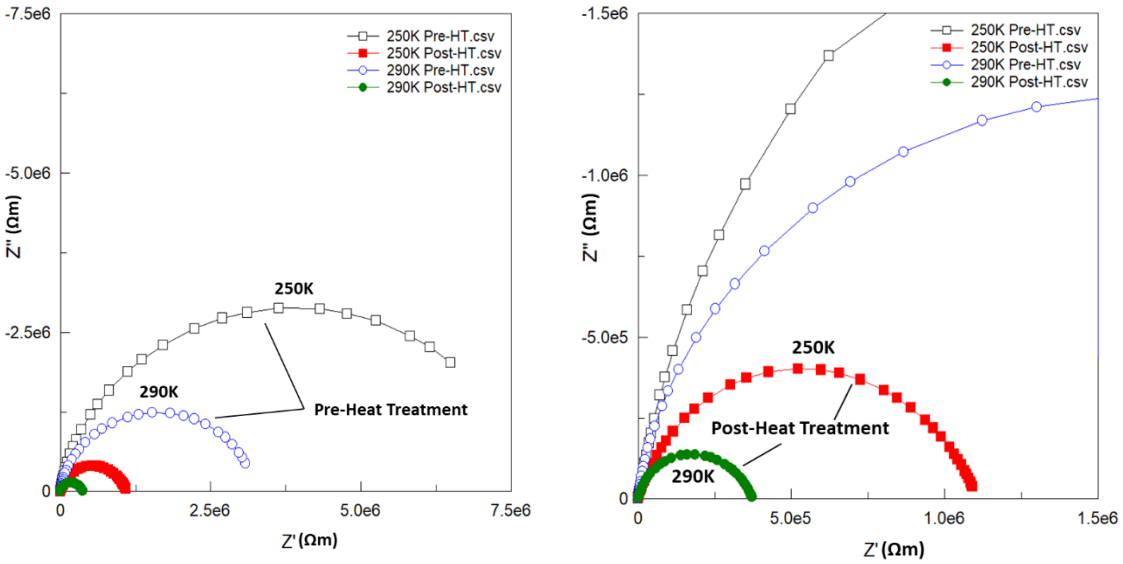

Figure 4.16: EIC Z impedance diagrams of responses at 250K and 290K of a nZnO cold sintered at 300°C 375MPa before and after heat treatment at 500°C in air. Post heat treatment shrinkage of the arcs give a clear indication of increased conductivity. A near-spherical arc is observed, with the slight stretching possibly indicating overlapping of the grain boundary and bulk response.*

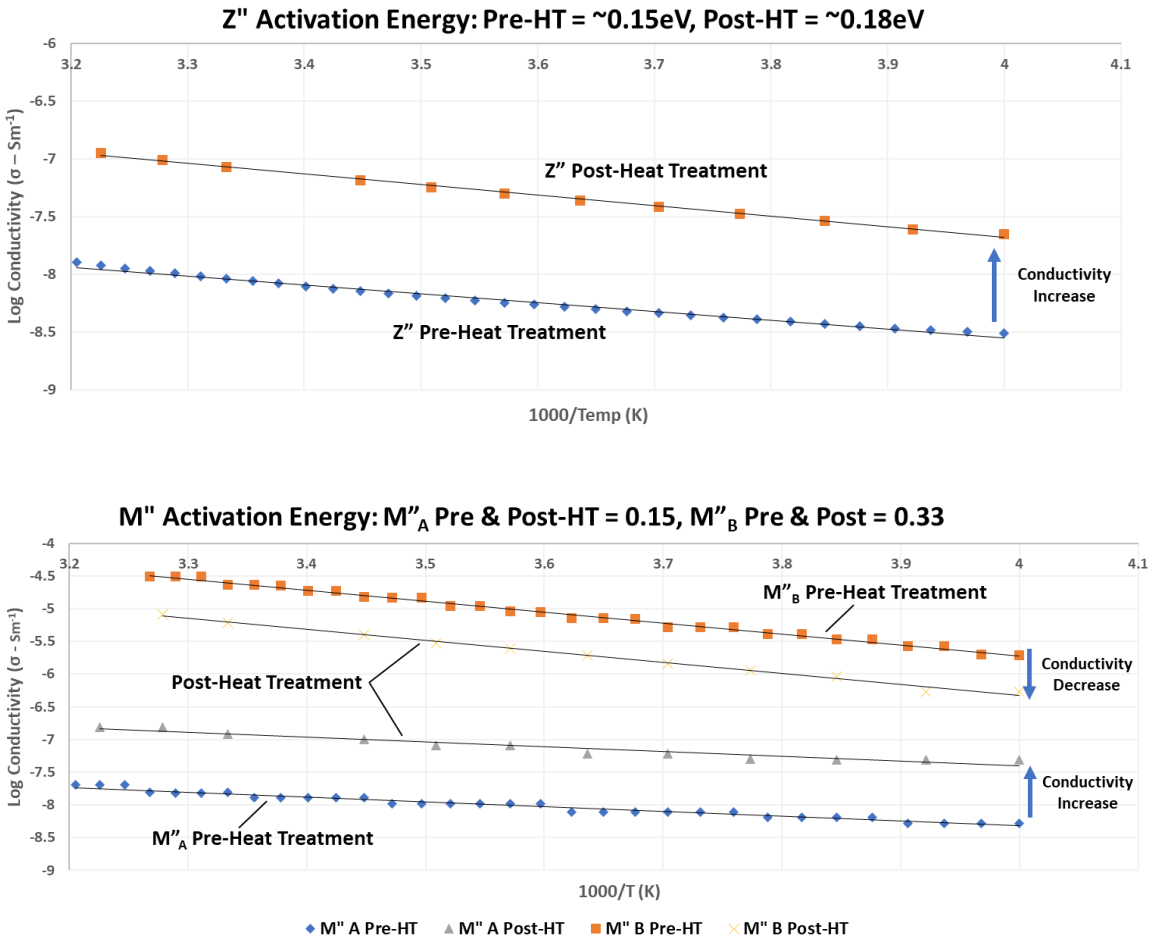

Figure 4.17: Conductivity graphs from EIC data of Z" (Top) and M" (Bottom) *nZnO cold sintered at 300°C 375MPa before and after heat treatment at 500°C in air. Heat treatment shows to increase conductivity in Z" and M"$_A$ and a slight decrease in conductivity of M"$_B$ but little to no change in activation energy.*

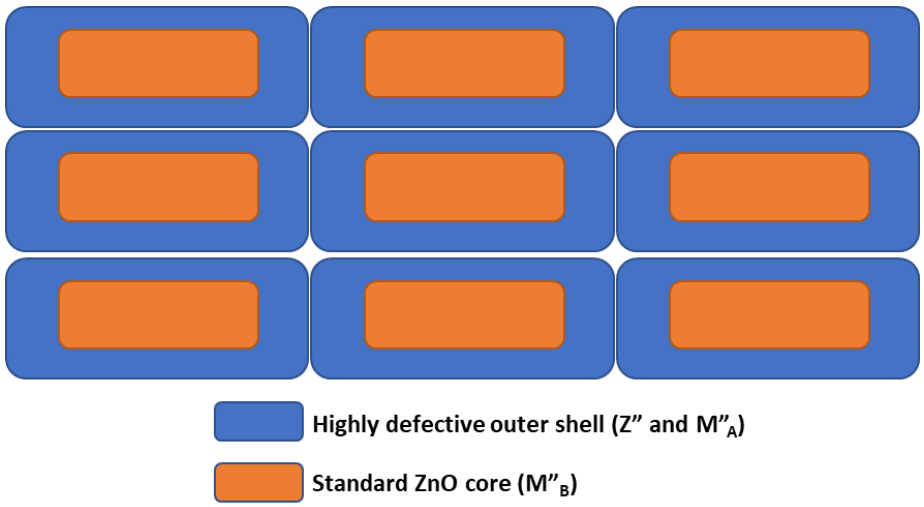

Figure 4.18: Diagram showing the proposed defect-based core-shell structure produced via cold sintering ZnO based on preliminary EIS work presented.

4.3.3 The Cold Sintering of 2% Gallium Doped ZnO

4.3.3.1 Powder Analysis

The 2% GZO Powder provided by UCL analysed via SEM revealed that it has smallest grain size and narrowest grain size distribution of the 3 powders (Figure 4.19) investigated, with an average grain size of 31nm, median of 30nm and standard distribution of +/-7nm. An almost entirely near-spherical morphology was observed throughout.

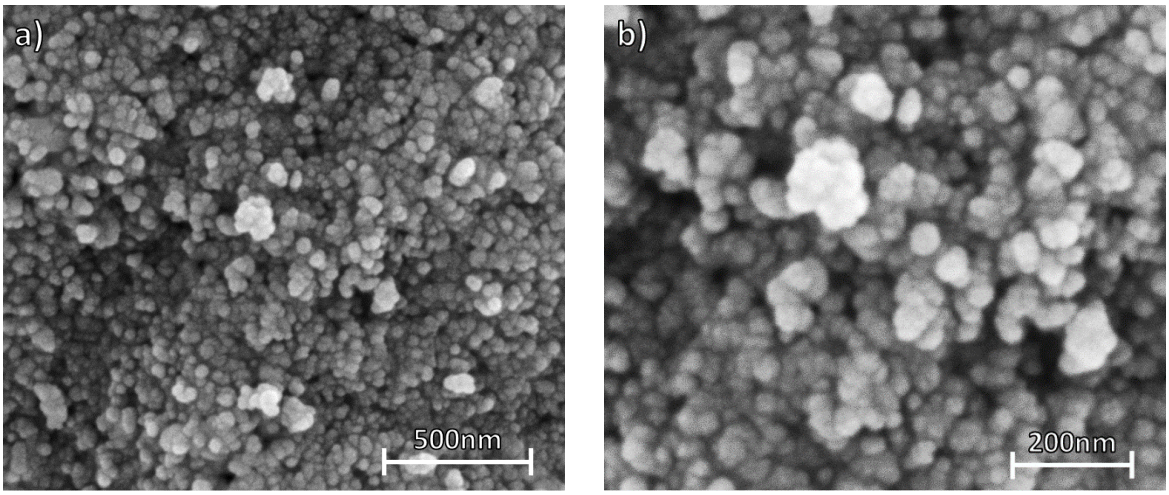

Figure 4.19: Secondary Electron images of $G_{0.02}Zn_{0.98}O$ (GZO) powder used for cold sintering.

4.3.3.2 Crystal Structure

All cold sintered GZO showed the expected spectra for wurtzite ZnO (Figure 4.20) [212]–[214]. Samples sintered below 300°C showed little-to-no peak narrowing or splitting consistent with a lack of crystallite growth. However, material sintered at 300°C showed distinct narrowing and high angle peak splitting above 55°, clearly indicating crystallite growth.

4.3.3.3 Zinc Gallate ($ZnGa_2O_4$) Secondary Phase

When presented in log-linear form, possible indication of a minor secondary phase could be observed under XRD of some cold sintered samples (Figure 4.20). However, this secondary phase is more prominent in conventional material when compared (Figure 4.21). This peak is likely associated with zinc gallate ($ZnGa_2O_4$). Further analysis using a high-resolution XRD spectrum though showed the presence of small volume fraction of zinc gallate in a 300°C 500MPa sample of cold sintered GZO (Figure 4.22).

Zinc gallate ($ZnGa_2O_4$) is a well-known secondary phase that often forms in Ga-doped ZnO between from ~500°C and is stable up to ~1100°C. Its effect on the properties of GZO is still debated and not fully understood [88]. However, due to its very wide bandgap of ~5eV, and evidence showing it does not couple with conduction band electrons [215], [216], it is

assumed to be detrimental to the conduction properties. Even if it is not directly detrimental, its formation reduces the amount of Ga able to contribute to donor doping in the ZnO lattice.

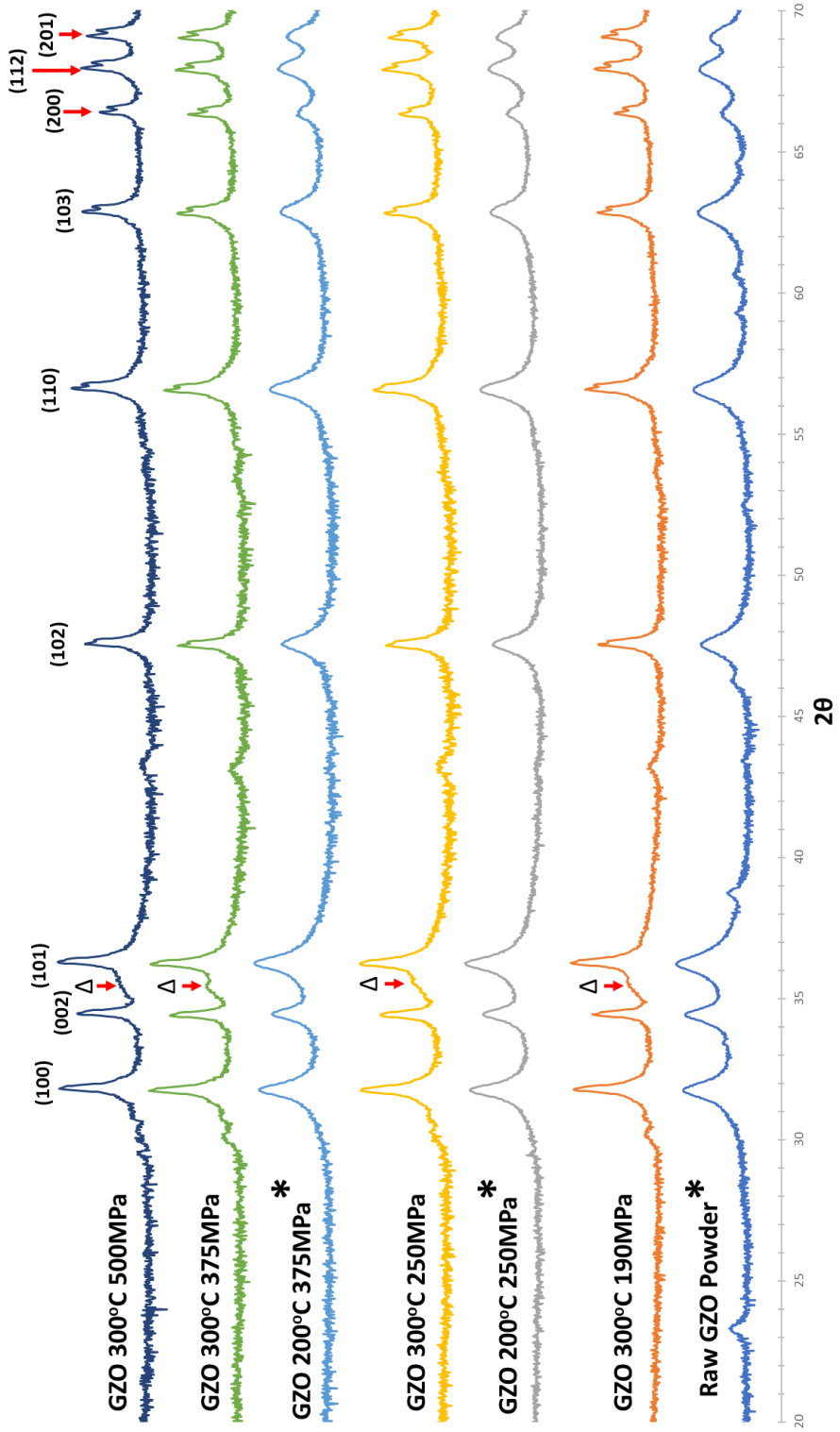

*Figure 4.20: Log-linear XRD spectra of $Ga_{0.2}Zn_{0.98}O$ cold sintered at various temperatures and pressures, compared to unsintered powder. An * denotes spectra that remained very similar to that of the raw powder with little to no peak narrowing. Δ symbols indicate possible indication of a small amount of Zinc Gallate as a minor secondary phase.*

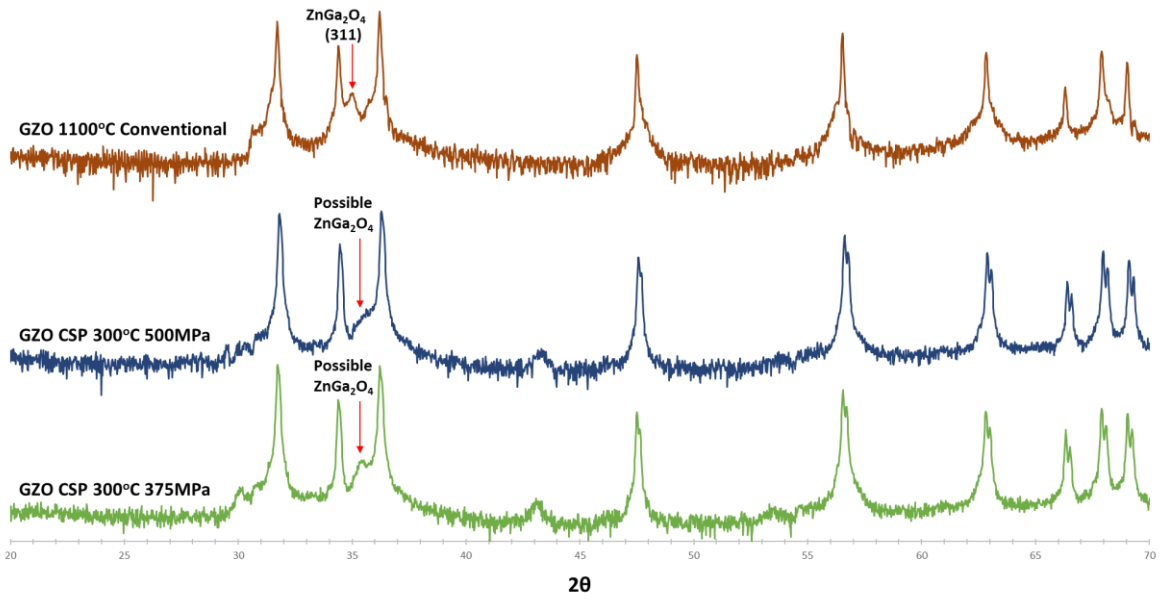

Figure 4.21: Log-linear XRD comparing $Ga_{0.02}Zn_{0.98}O$ conventionally-sintered at 1100°C to cold sintered at 300°C and 375 & 500MPa and the lack of the (311) Zinc Gallate ($ZnGa_2O_4$) peak in cold sintered material. This is due to the concentration being below detection limits of the Bruker D2 as seen in Figure 4.22.

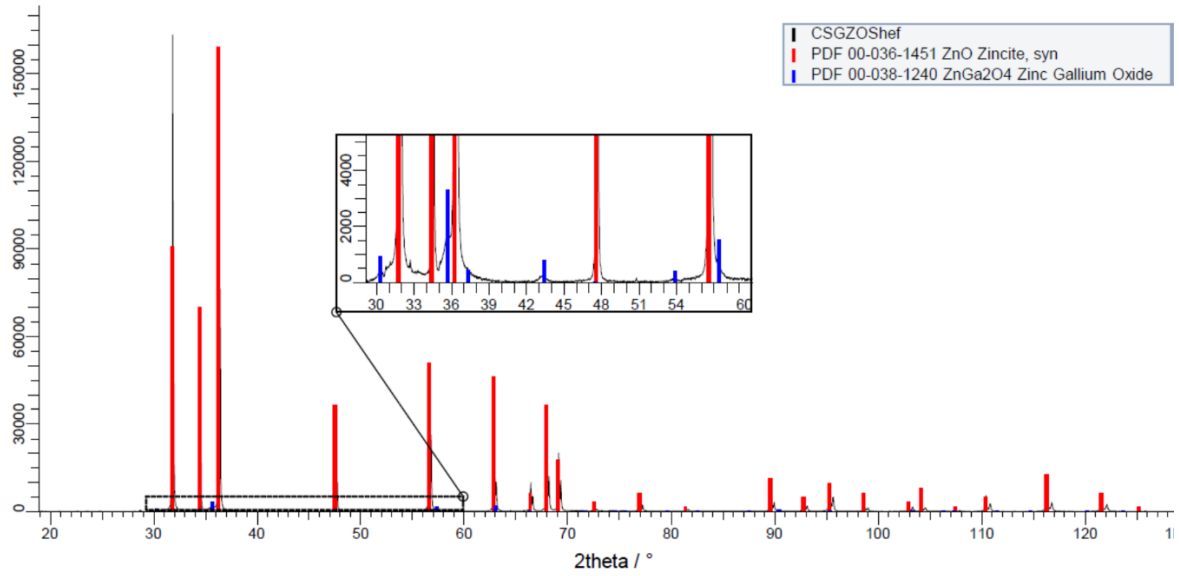

Figure 4.22: High-resolution XRD of 300°C 500MPa $Ga_{0.02}Zn_{0.98}O$ showing the presence of a small amount of secondary Zinc Gallate ($ZnGa_2O_4$) phase. (Analysis and figure courtesy of Johnson Matthey)

4.3.3.4 Densification and Grain Growth Suppression

4.3.3.4.1 Density

$Ga_{0.2}Zn_{0.98}O$ proved more difficult to cold sinter than undoped ZnO, with lower sintering temperatures producing undensified samples. Only pellets sintered at >250MPa at 200°C, or sintered at 300°C (all pressures) densified. Sintered material consistently attained 89-96% relative density (Figure 4.23).

4.3.3.4.2 Grain Size and Morphology

SEM images in Figure 4.25 and 4.26 compare the top surfaces and fracture surfaces, respectively, of cold sintered GZO, (Figure 4.26), sintered at various temperatures and pressures. Conditions that did not sinter are greyed out and presented only to give a better overview to compare to undoped pellets. Separate results for GZO cold sintered at 625MPa are shown in Figure 4.27. As before, measurements of average and median grain sizes, and grain size distribution, using SEM images are displayed on Figure 4.24.

All material cold sintered at 200°C showed no noticeable grain growth, maintaining an average grain size of ~30nm and median of ~29nm. At 200°C 250MPa, pellets were poorly sintered, with the consistency of a very densely packed powder. At 375MPa, a comparatively densely packed nano-structure was observed but with no evidence of grain growth.

At 300°C however, there is a dramatic change in the microstructure at all pressures. Both surface and internal grain structure was composed of two primary populations: surface elongated grains (0.5-1µm) with larger radial grains and a nano-grain structures decorating larger grain surfaces (Figure 4.26 - Arrowed), similar to the “pebbling” discussed in 4.3.2.4.2. (Figure 4.25). Internal grain morphology was even more variable, with an inconsistent mixture of elongated and pseudo-spherical grains 70-600nm diameter with nano-grains across all larger grain surfaces (Figure 4.26 - arrowed). Much better control on microstructure formation is therefore required achieved to consistent and reproducible mechanical and electrical properties.

Average grain size at 300°C was 244, 224, and 218nm at 190, 250, and 375MPa, respectively. Full details are given in appendix Table A.1. Grain size and distribution for all GZO samples lower than those found in cold sintered nZnO under the same sintering conditions (Figure 4.24).

Once again as discussed in sections 4.2.3.2 and 4.3.2.3.2, these measured values are of limited accuracy due to the grain size and grain size distribution measurement method. However, very clear general trends can be taken from these measurements on the effects of pressure and temperature.

4.3.3.4.3 Effects of Ga Introduction

Grain growth and densification inhibition in these samples is likely caused by the introduction of Ga, which is known to cause Zener pinning in conventional sintering [8], solute drag effects [40], and increase the number of nucleation centres [41], leading to the observed microstructures. During cold sintering, higher 'energy barriers' have likely inhibited grain boundary motion, hence grain growth and densification do not occur until ≥200^{o}C.

When pressure was raised to 625MPa, abnormal grain growth was observed in the radial direction, producing elongated grains 2.5-4μm in length, surrounded by a smaller elongated grain structure of <1μm (Figure 4.27). This effect is likely relates to restricted sintering often observed in hot-pressing [13]–[18]. Wilkinson and Cáceres [19] suggest a strain-rate dependent grain growth mechanism, where grain boundary migration is induced by grain-boundary sliding at triple points leading to accelerated grain growth. Other authors have suggested that other mechanisms also occur to cause grain growth, inducing: grain-switching, grain-rotation, diffusion, and dislocation motion [20]–[23]. Ratzker et al. [24] described a rotational grain boundary sliding grain growth mechanism for pressure induced grain growth in alumina during high-pressure spark plasma sintering. They suggested at higher strain rates, defected regions form between grains via grain boundary sliding enhancing grain growth leading to coalescence.

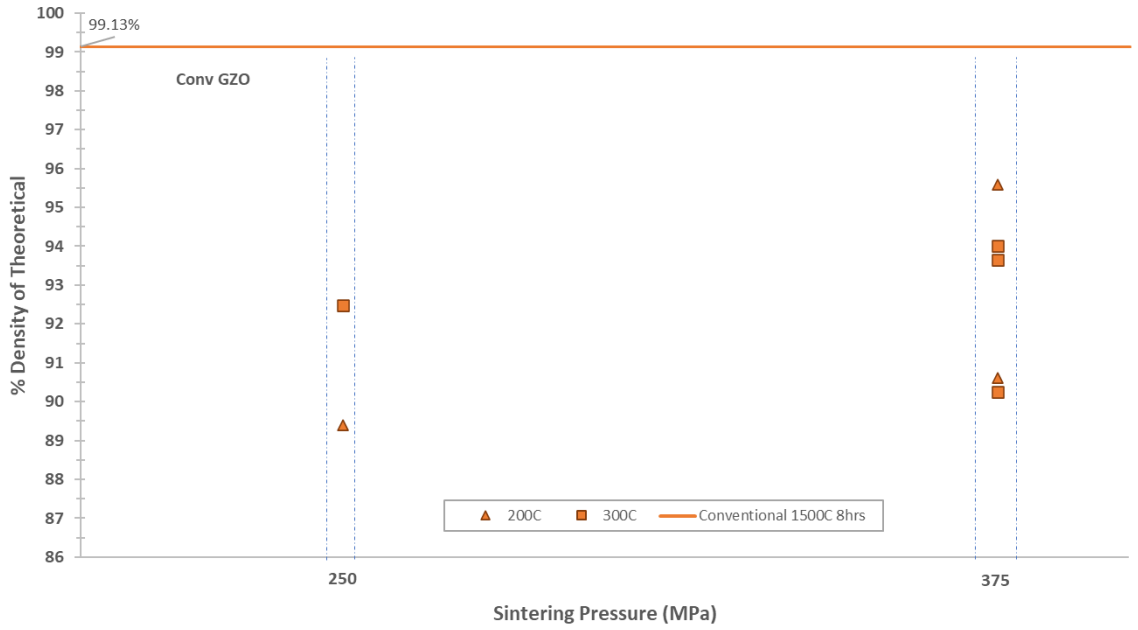

Figure 4.23: Graph of densities of $Ga_{0.02}Zn_{0.98}O$ cold sintered at 200-300°C at 250MPa and 375MPa vs Conventionally sintered at 1500°C (orange line)

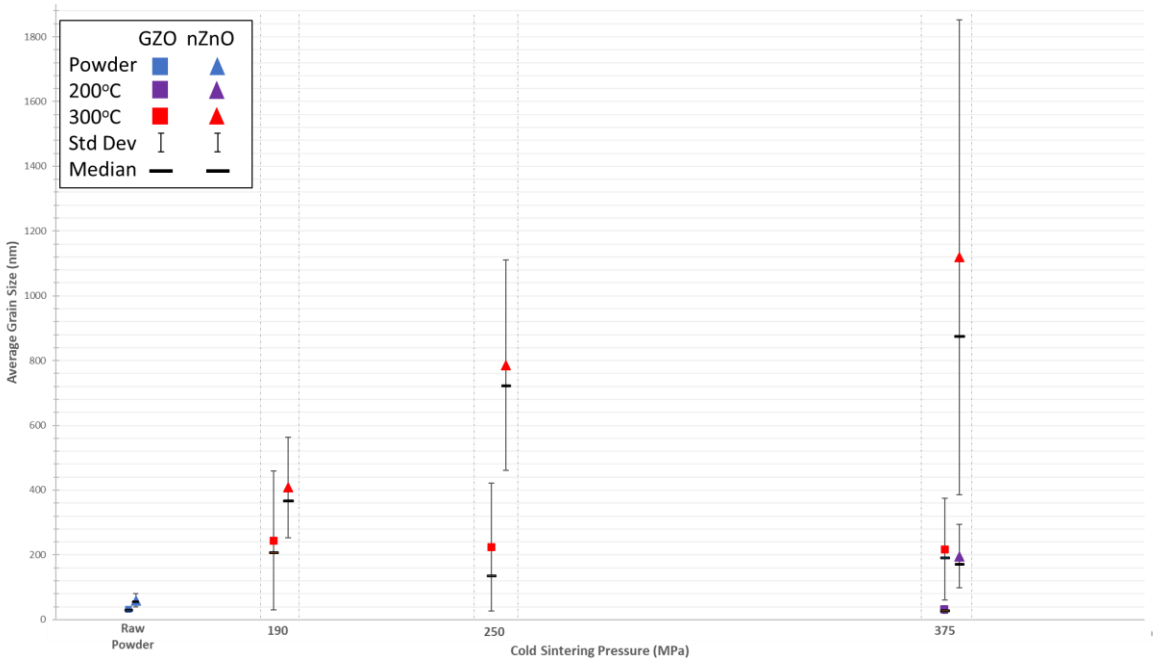

Figure 4.24: Graph comparing the change in grain size and grain size distribution of GZO and nZnO over temperature and pressure. Standard deviation indicating grain size distribution, and median grain size are also given.

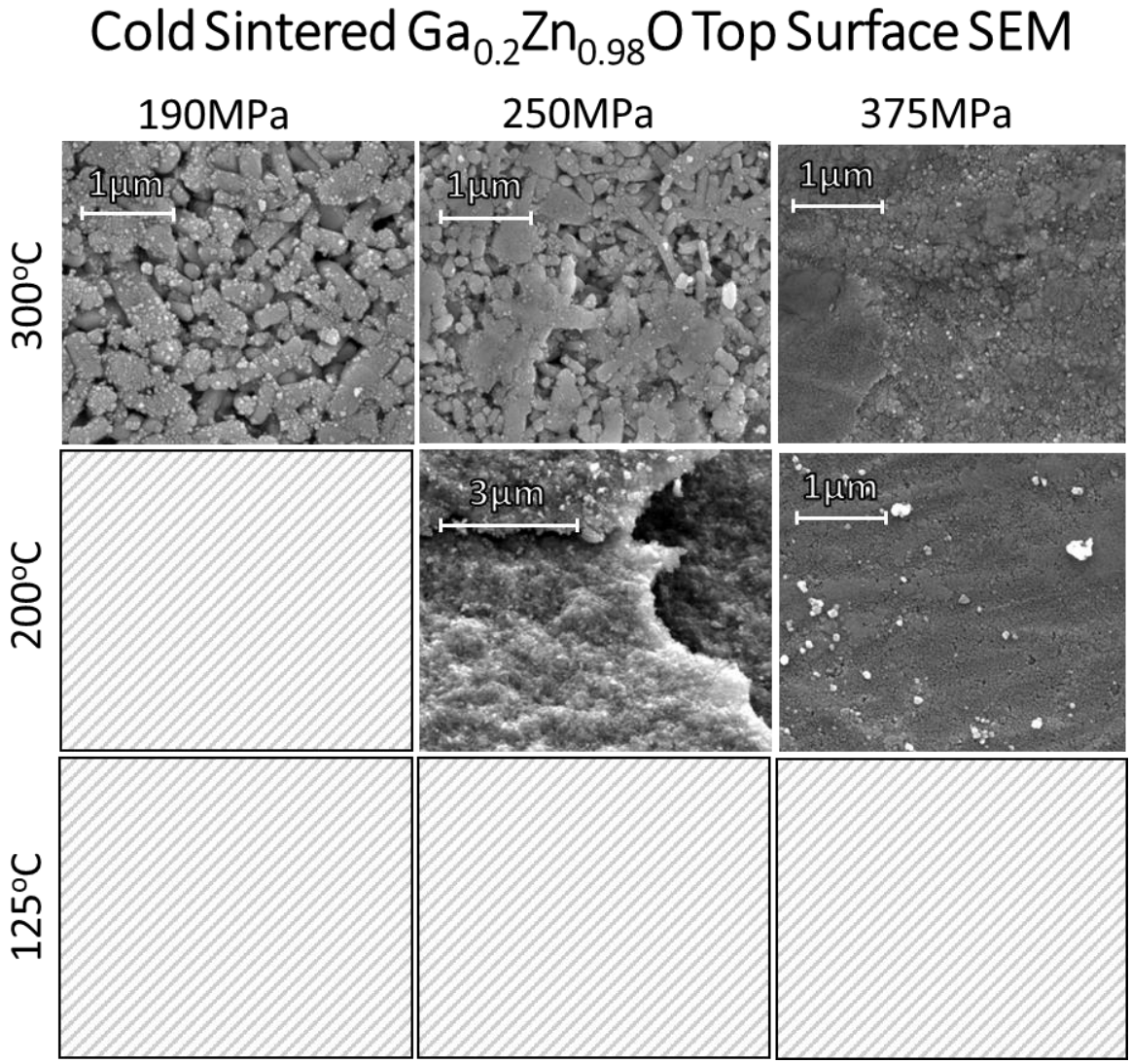

Figure 4.25: Secondary SEM micrographs of the top surface of $G_{0.02}Zn_{0.98}O$ cold sintered at various temperatures and pressures. A number of conditions did not successfully sinter and are marked by the greyed-out squares. These blank spaces have been left in to illustrate the progression of sintering with temperature and pressure.

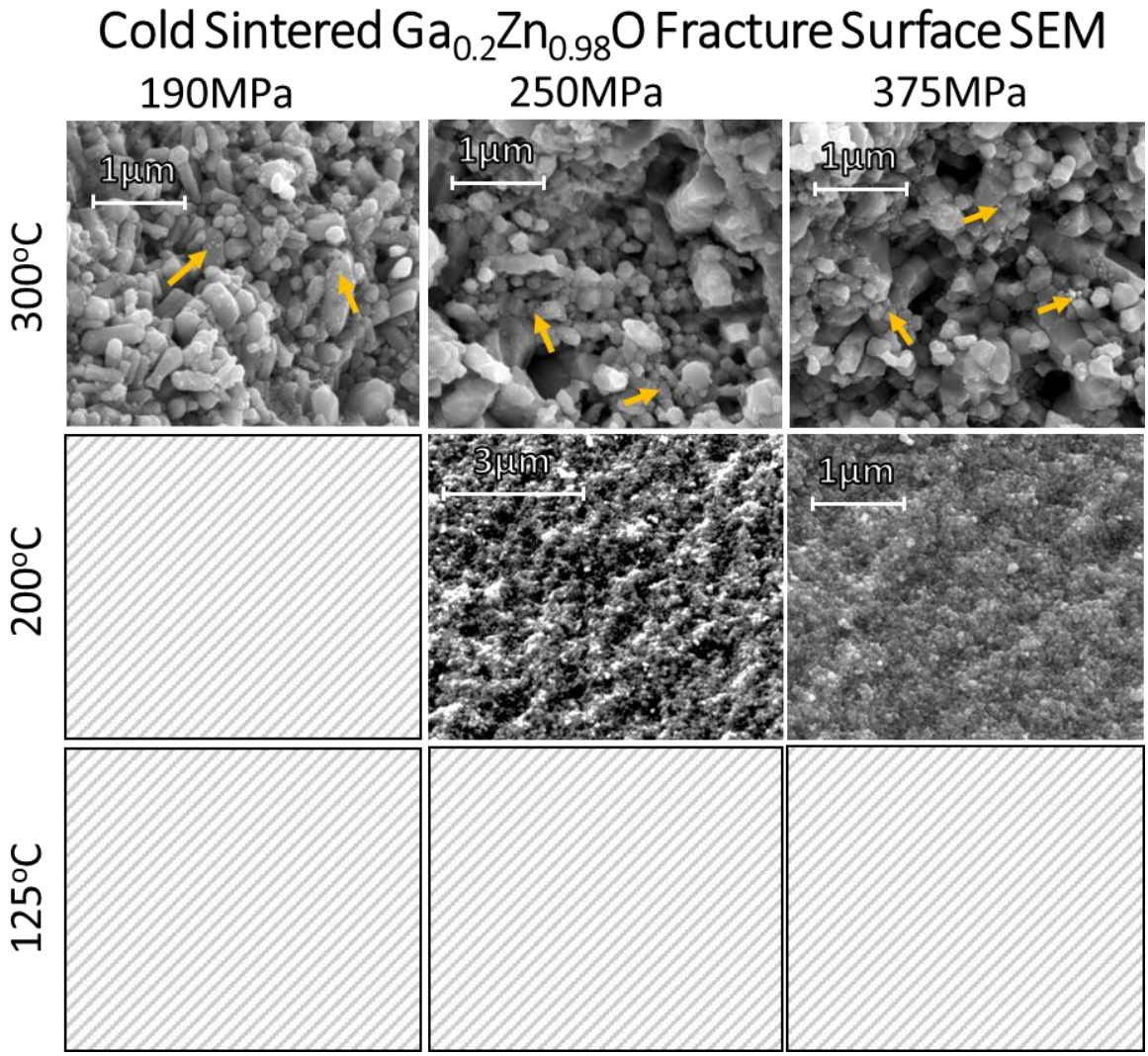

Figure 4.26: Secondary SEM micrographs of the fracture surface of $G_{0.02}Zn_{0.98}O$ cold sintered at various temperatures and pressures A number of conditions did not successfully sinter and are marked by the greyed-out squares. These blank spaces have been left in to illustrate the progression of sintering with temperature and pressure. Arrows point to some of the many nano-grains that formed on grain surfaces of the bulk material.

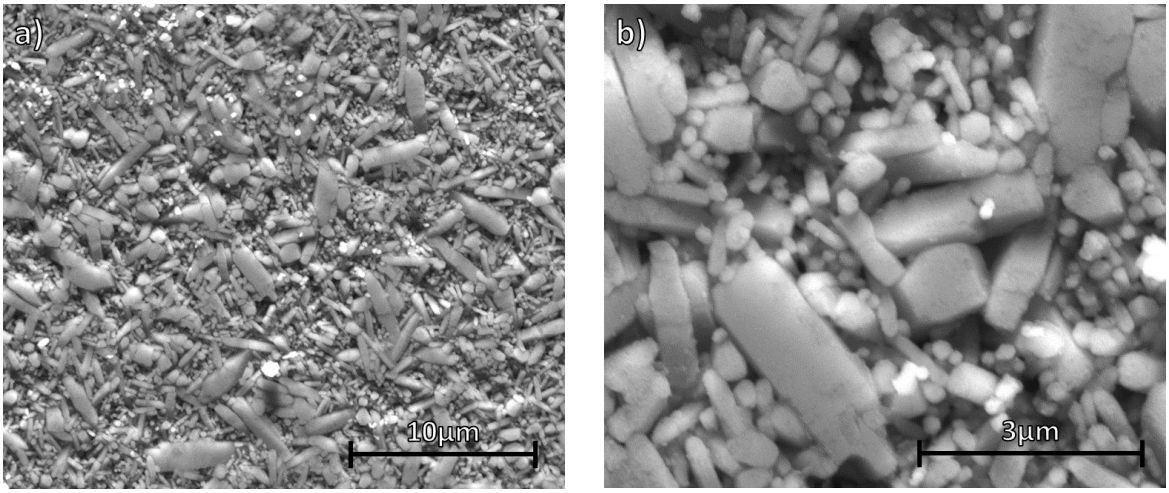

Figure 4.27: SEM top surface images of $Ga_{0.02}Zn_{0.98}O$ post-cold sintering at 300°C 625MPa. Images indicate high pressure has induced significant grain growth in a limited population of grains. Elongation and greater size in the planer direction may relate to restricted sintering mechanisms.

4.3.3.5 Distribution of Ga in Cold Sintered $Ga_{0.02}Zn_{0.98}O$

EPMA analysis (Figure 4.28) was utilised to explore the Ga distribution within a GZO sample. Ga was distributed across the sample, but localised areas of high Ga concentration (arrowed) were sometimes observed. It is not known if these higher concentrations of Ga are from $ZnGa_2O_4$ or if there are other mechanisms at play.

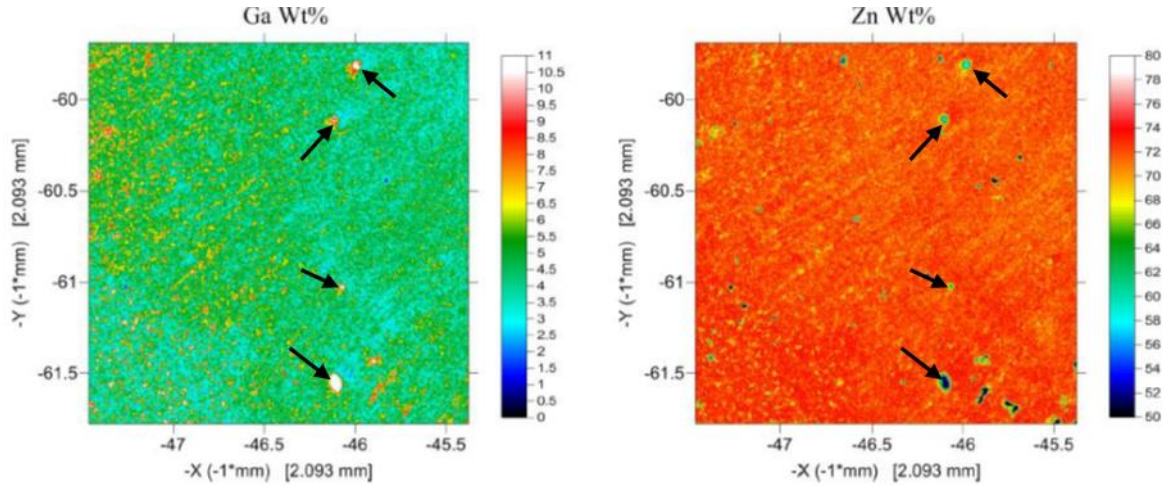

Figure 4.28: EPMA scans across a 2.093mm² area showing the distribution of Ga in $Ga_{0.02}Zn_{0.98}O$ cold sintered 300°C 500MPa. Good Ga coverage is observed but localised zones of varying concentration are present (Arrowed Left: Zones of high Ga concentration, Arrowed Right: Zones of simultaneous Zn deficiency). (Analysis and images courtesy of Johnson Matthey)

4.3.3.6 Chemical Analysis

Raman spectra of GZO (Figure 4.29) revealed modes associated with ZnO and the known secondary acetate phase, as described in 4.3.2.5, as well as 4 new modes. A new mode at ~635cm^{-1} indicates incorporation of Ga into the ZnO crystal [217], [71]. A second possible indicator of Ga substitution might be observed at ~485cm^{-1} as a $2B_{1(Low)}$ mode, but is more likely to be caused by a ZnO A_1 mode, caused by L-A overtones along the M-K Brillouin zone [206]. It is unclear as to why this mode only appears in cold sintered material.

A 3rd response at 586cm^{-1} only appears in 200°C 375MPa, and in conventionally-sintered samples. The peak corresponds to an exaggerated E_1(LO) mode indicating a higher oxygen lattice defect concentration compared to other samples [204]. The cause of its appearance in only one cold sintered condition is uncertain.

The 4th mode at ~715cm^{-1} which is only seen in conventional material, is typical of the A_{1g} modes of cubic spinel $ZnGa_2O_4$ [218], furthering evidence that it is in much lesser quantities in cold sintered material. It must be noted that even though at least 3 scans for each sample were performed, the little $ZnGa_2O_4$ present in samples may have been missed since EPMA data (section 4.3.3.5) possibly indicates $ZnGa_2O_4$ is present in small concentrated zones.

Although Figure 4.29 is normalised, visual comparison of peak heights is not possible due to the florescence experienced by cold sintered material compared to conventional, leading to visual exaggeration of low angle modes.

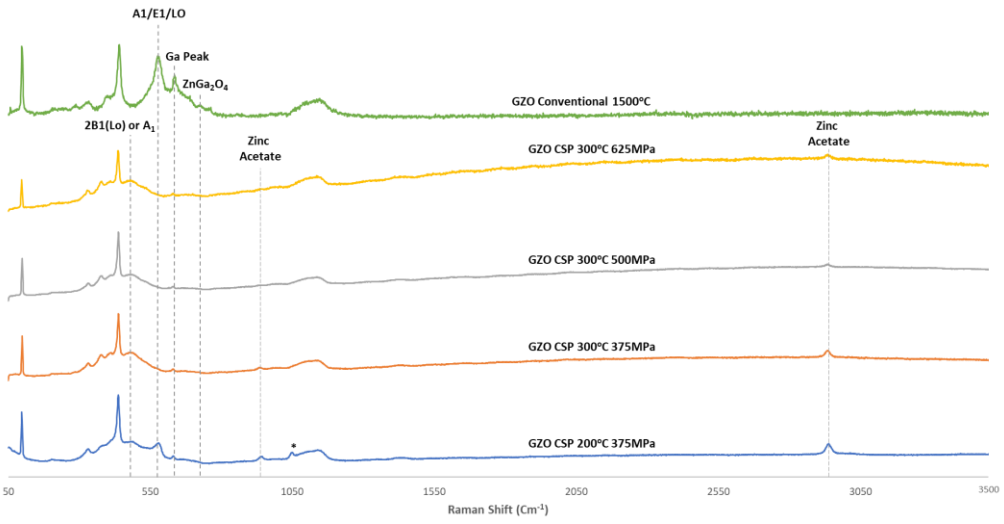

*Figure 4.29: Raman of $Ga_{0.02}Zn_{0.98}O$ cold sintered at 200-300°C and 375-625MPa and conventionally sintered at 1500°C showing the presence the expected secondary acetate phase as well as modes relating to Ga incorporation. The peak labelled with a * is unknown and suspected contamination. Due to significant florescence of cold sintered samples, peak size ratio distortion is significant even once normalised and visual intensities are misleading.*

4.4 Conclusions

4.4.1 Effects of Starting Powder on Cold Sintering

Two powders of different size were cold sintered at a range of temperatures and pressures, and were analysed and compared. The cZnO results agree closely with current literature, with temperature having the largest impact on densification.

nZnO was more difficult to densify. It produced a more controlled grain size distribution at lower temperatures (<200^{o}C), but as temperature increased to 300^{o}C, uncontrolled grain growth became prevalent, with increase in pressure (125-375MPa) exacerbating the issue.

Increase in pressure consistently resulted in radial grain growth, presumably as a result of a restricted sintering mechanism. Increase in temperature and pressure encouraged elongated grain-growth throughout the material.

Zinc acetate phase was observed throughout all samples, but could be removed with a 500^{o}C heat-treatment.

Preliminary impedance analysis indicated the presence of a defect-based core-shell structure. With grain outer shells being highly defective, encasing a central more traditional ZnO core. Heat treatment in air at 500^{o}C increased overall conductivity, and matched that observed in the literature. However, the reasons for this conductivity change given in literature are questionable and instead we propose a proton-donor type mechanism based on analysis here and information from other researchers.

4.4.2 Cold Sintering of Ga-doped ZnO

$Ga_{0.02}Zn_{0.98}O$ nano-powder was successfully cold sintered. Compared to undoped samples however, higher temperatures and pressures were required to achieve densification, with notable grain growth not occurring until 300^{o}C. This is likely due to Ga inhibiting grain growth and densification through a Zener-like pinning model, solute drag, and increasing number of nucleation centres.

At 300^{o}C grain growth was uncontrolled producing fewer large grains (up to 400nm) respective to a smaller (~200nm) population. All of these grains were decorated with large numbers of nano-grains on their surface. Extremely high pressures (500-625MPa) showed an exaggerated stress-induced grain growth mechanism giving large abnormal elongated grains as 2.5-4μm in length relative to the normal grain population.

Raman spectroscopy of GZO showed similar spectra to pure-ZnO but with extra modes that indicate the incorporation of Ga into the crystal structure. Oxygen defect concentrations may be lower in 300°C CSP GZO, as evidenced by the absence of a mode at 586cm^{-1}. A secondary acetate phase was also observed in cold sintered GZO.

Zinc gallate concentrations were reduced in cold sintered compared with conventional samples. EPMA analysis revealed an even distribution Ga throughout the crystal, but some zones of higher concentration, potentially indicating the location of $ZnGa_2O_4$.

4.5 Future Work

Future works based on this chapter include:

- A more comprehensive investigation into the conductivities of cold sintered ZnO and GZO, looking at the effects of processing temperature and pressure.
- Investigation into the effect of heat treatment on the conductivity and microstructure of cold sintered ZnO and GZO.
- Testing the hypothesis of the proposed core-shell defect model proposed.
- More detailed study into how various parameters affect densification in cold sintering, and how they can be controlled to better control grain growth, especially in nano-materials.
- Seeing how adjustments of Ga concentration affect the ability to cold sinter ZnO.
- Understanding the cause of the zones of high Ga concentration that were observed in EPMA analysis.

Chapter 5 – ZnO-Kapton® Thick Film layers and Multilayers

5.1 Introduction

5.1.1 Motivation for the Development of a Cold Sintered Multilayer Device

With the ability to cold sinter ZnO and 2% Ga-doped ZnO illustrated in Chapter 4, Chapter 5 explores the possibility of producing a transparent layer of ZnO on a polymeric substrate with the goal of demonstrating a multilayer device/component. ZnO was therefore directly cold-sintered on the surface of a polymer sheet (Kapton®) which not only demonstrated the ability to produce ceramic-polymer layered composites at ultra-low temperatures, but also that such components could be transparent.

Attempts to manufacture ceramic-polymer layer and multilayers through conventional technology are limited due to incompatible temperatures and thermal expansion coefficients during processing. The only previous direct densification method for thick films was achieved using aerosol deposition in which near fully dense material were deposited onto a polymer surface at room temperature [219]. This however leads to an extremely small crystalline size (~5-20nm), and requires annealing far above the melting/decomposition temperature of the polymer to initiate sufficient grain growth to achieve the desired properties [220].

Several authors have demonstrated ZnO-polymer composites, mostly based on PTFE, either within a ceramic matrix [167], or as a multilayer device [21]. However, to date, no authors have demonstrated direct sintering of ZnO onto a thermoset polymer to produce a transparent multi-layer ceramic composite. The aims of this chapter therefore are:

- To cold sinter a layer of ZnO directly onto the surface of a polymer.
- To produce a multilayer ZnO-polymer composite using cold sintering.

5.1.2 Overview

5.1.2.1 Outline of Chapter

This chapter discusses the key aspects of the development of polymer-ZnO layers and multilayers. A full discussion and analysis of single and multi-layer composites is given, issues that remain unresolved are discussed and future work is proposed to advance their performance to create a potential functional device.

5.1.2.2 Choice of Materials

5.1.2.2.1 Starting ceramic powder

The nano-ZnO (nZnO) (US-Research Nanomaterials Inc) powder used in Chapter 4 was the ceramic powder of choice since it cold sintered to a high density and large quantities were readily available. The subsequent preparation of layers and multilayers with GZO rather than ZnO was curtailed due to the impact of COVID19.

5.1.2.2.2 Polymer

HN-Kapton®, or poly(4,4'-oxydiphenylene-pyromellitimide) (Figure 5.1), is a temperature stable (-269 to +400^{o}C) polyimide film developed in the 1960s by DuPont. It has good chemical resistance, mechanical properties, is stable at high temperatures (~300 ^{o}C), and is transparent, albeit orange in colour [221]. It is therefore an ideal substrate upon which to attempt to cold sinter layers of ZnO.

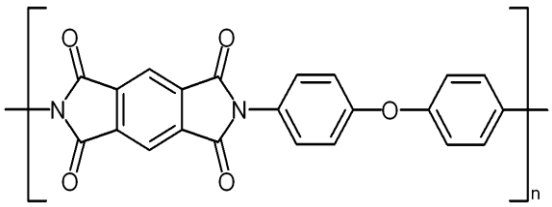

Figure 5.1: A monomer of Poly-oxydiphenylene-pyromellitimide (Kapton®) [222]

5.1.2.2.3 Tape-Casting

In later trials, tape-casting was used to produce continuous layers of ZnO for cold sintering. A low-temperature burnout, water-based tape casting system was chosen from Polymer Innovations Inc. Its low temperature removal allows binder burnout to take place on top of the Kapton® permitting maximum surface contact for sintering. This system consisted of PL005 plasticiser, DS001 dispersant, DF002 defoamer, WB4104 binder, distilled water as the solvent, and nZnO powder.

5.2 Fabrication

5.2.1 Direct Sintering of Powder onto Kapton®

5.2.1.1 Experimental

Initial attempts to produce a Kapton®-ZnO composite broadly follow the descriptions in sections 4.2.1 and 4.2.2. However, a Kapton® sheet was additionally introduced into the die either, underneath, on top, or between powder layers depending on the desired layer/multilayer geometry. Cold sintering was initially performed at 250MPa and 300^{o}C before being lowered to 200^{o}C when it was recognized that Kapton® thermally decomposes at 300^{o}C under pressure.

5.2.1.2 Results & Discussion

Initial trials highlighted challenges such as lack of adhesion of ZnO to Kapton®, Kapton® adhering the die puck, and the decomposition of Kapton® under pressure which is not reported in the supplier guidelines. The following section describes how these problems were overcome to achieve proof of concept.

5.2.2 Mixing Acetic Acid and Powder Directly on Kapton®

5.2.2.1 Experimental

Due to the lack of adhesion shown by Kapton® to the ZnO, a simple test was performed to see if any adhesion of ZnO to Kapton® could be achieved by direct cold sintering. Mixing of the acetic acid (1M) and ZnO was therefore performed directly on the Kapton® sheet. This produced an uneven layer that adhered to the polymer surface. Before the layer could totally dry, the sample was placed in a die and hot pressed at 150^{o}C & 250MPa. To protect the Kapton®, a thin layer of graphite was placed underneath the Kapton®. Samples pre- and post-cold sintering were analysed using XRD, before being sectioned and gold coated for SEM.

5.2.2.2 Results

Discontinuous zones of dense ZnO were adhered to the surface of the Kapton® sheet, translucent to the naked eye and in optical images (Figure 5.2).

SEM images comparing pre- (Figure 5.3a,c,e) and cold sintered material (Figure 5.3b,d,f) shows clear evidence of densification. Pre-sintered material is composed of loosely packed nano-powder on the surface of the Kapton® whereas, post cold sintering a discontinuous dense sintered sheet of ZnO formed. The sintered ZnO sheets showed evidence of contact and necking between grains, with some grain growth. Grain size was in the range of 60-

200nm, with an equiaxed morphology. The grains, when compared to bulk samples under similar conditions in Chapter 4, are larger but do not show elongated growth. Figure 5.3 shows no indication of interaction between the ZnO and Kapton® or any secondary phases.

XRD (Figure 5.4) reveals broad peaks corresponding ZnO with no secondary crystalline phases. The 3 distinct amorphous peaks at $2\theta = 14^{o}$, 22^{o}, and 26^{o} match that for Kapton®. The peak at 26^{o} is the strong (002) peak typical of graphite from the protective layer placed underneath the Kapton® during the cold sintering. The graphite layer stuck to the Kapton® and left visible residue, Figure 5.2a. XRD shows no evidence of an acetate peak sometimes observed at ~12^{o}. The presence of acetate phases was confirmed by Raman spectroscopy in bulk cold sintered samples but due to the extreme florescence caused by Kapton®, this was not possible for ZnO layers.

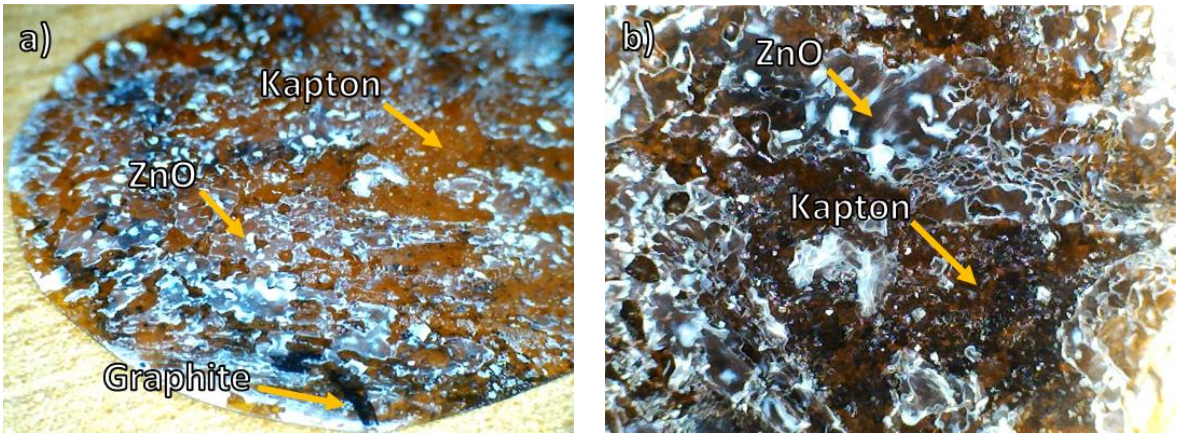

Figure 5.2: Low magnification optical images of ZnO directly sintered to the surface of at 20mm diameter sample of Kapton® at 150°C & 250MPa a) Surface of the discontinuous ZnO with transparent regions and residual graphite. b) Top-down view of the ZnO layer illustrating some transparent regions. Scale-bars not available for these images. Images meant for illustration purposes only.

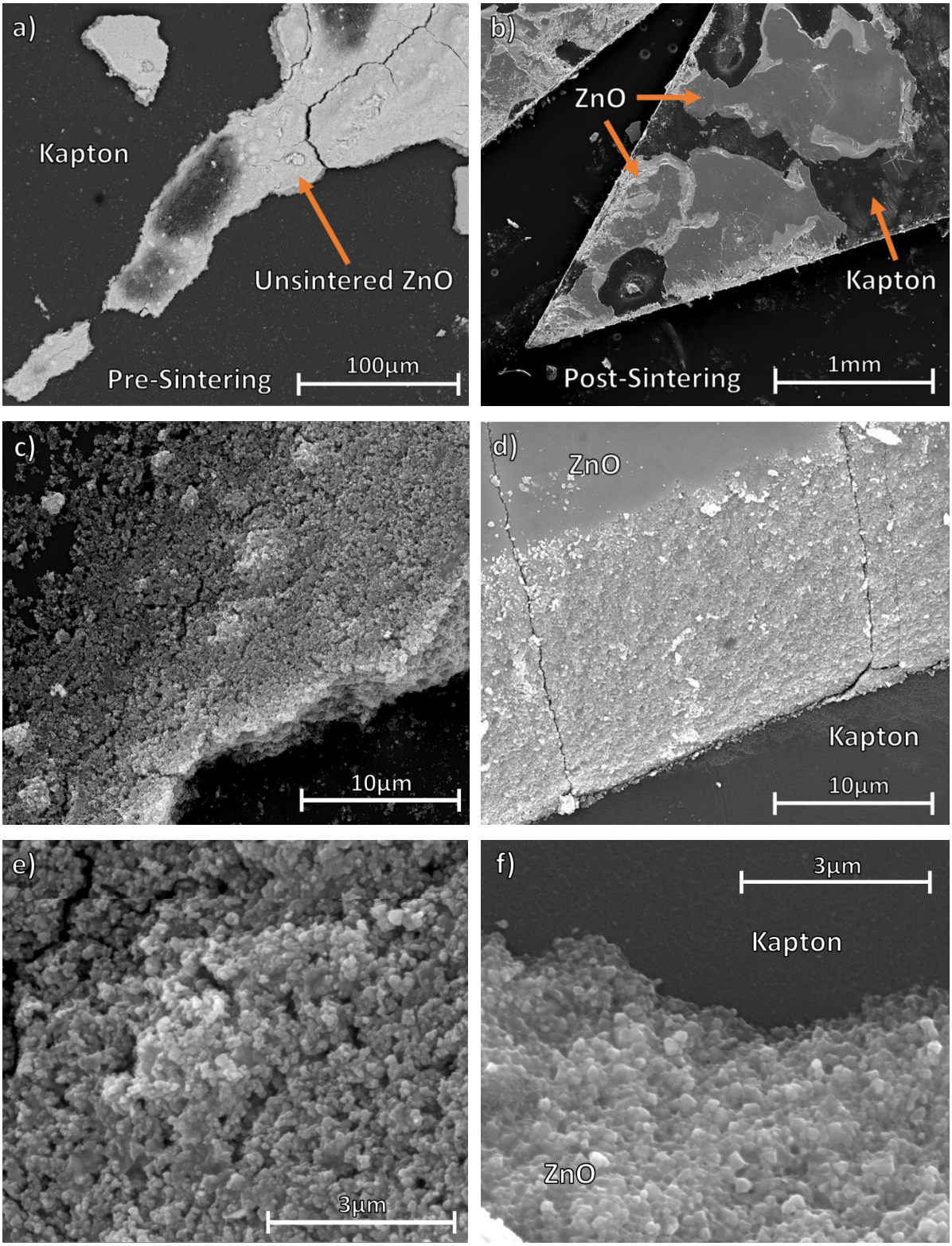

Figure 5.3: SEM images of ZnO directly mixed onto Kapton® pre-cold sintering (a,c,e) and post-cold sintering (b,d,f) at 150°C & 250MPa. Pre-cold sintered ZnO powder has low density and loose compaction whereas, post sintered layers are well adhered to the Kapton® surface and dense. e) shows the small grain size and low density of pre-sintered samples. Charging has partially distorted this image.

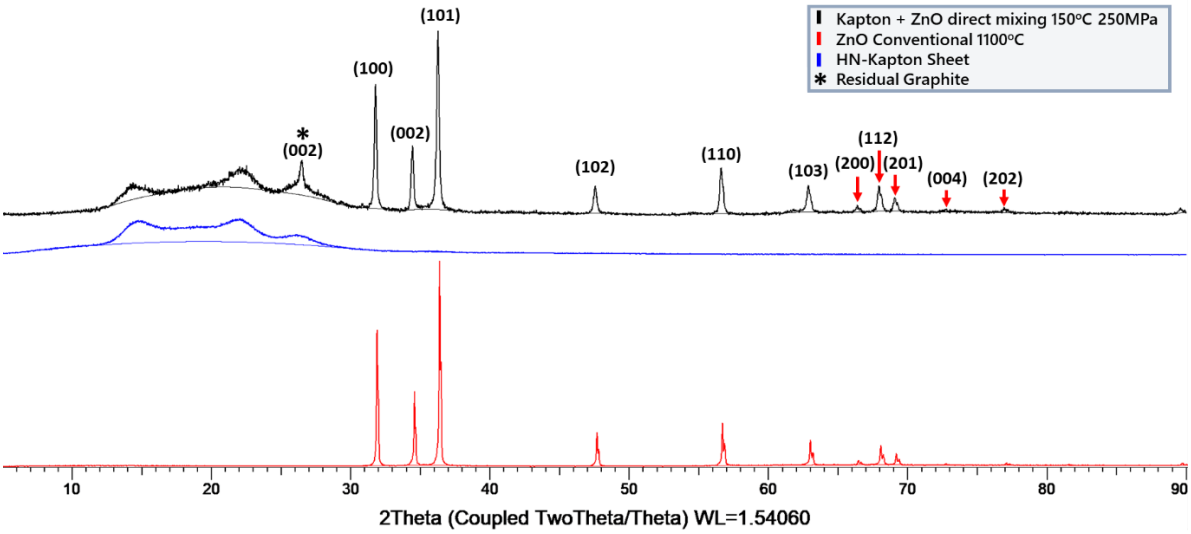

Figure 5.4: XRD of ZnO cold sintered on Kapton® at 150°C & 250MPa by direct mixing compared with a Kapton® sheet, and conventionally sintered ceramic.

5.2.3 Tape Casting

Tape casting was undertaken in preference to screen printing to highlight the potential for multilayering using a cold sinter process.

5.2.3.1 Experimental

A water-based system from Polymer Innovations Inc. (section 5.1.2.2) was used for tape casting. Table 5.1 shows the optimised quantities of plasticiser (PL005), dispersant (DS001), defoamer (DF002), binder (WB4104) and solvent (distilled water) with a solid loading of approx. 40-50% nano ZnO.

Table 5.1: Table of the final quantities of each constituent in the tape cast slurry

Binder constituent	Final quantity (wt%)
WB4104 Binder	11.399
DF002 Defoamer	0.1247
DS001 Dispersant	1.705
nZnO Matrix	6.540
PL005 Plasticiser	0.9833
Distilled H_2O Solvent	79.247

Solvent, dispersant, defoamer, and plasticiser were combined with nZnO powder and ball-milled 24 hours. The solvent, defoamer and binder were periodically added to the mixture during milling. The mixture was speed-mixed for 5, 4-minute cycles at 800rpm to give the

ideal consistency for tape casting. The slurry was sieved to remove milling media and any remaining agglomerates, before being left overnight to de-gas. The tape was cast onto a mylar carrier film with a blade height of 80µm. The tape was then dried in air at room temperature for 48 hours before use.

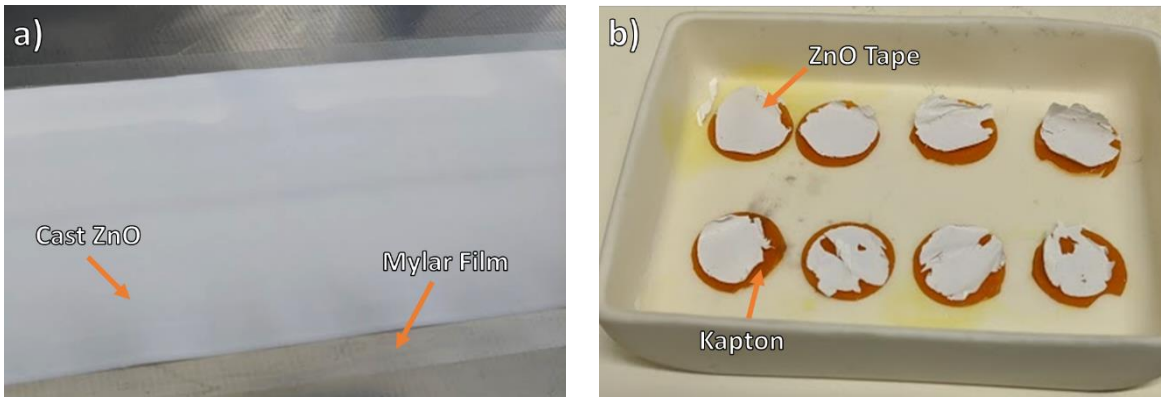

Figure 5.5: a) Optical image of dried cast ZnO tape on Mylar film. Although the tape was imperfect with zones of inconsistent distribution, it was determined strong enough for initial tests, with samples taken from zones of the highest quality. b) Cut ZnO tape mounted pre-binder burnout on the surface of 1" diameter circles of Kapton® film. Tape would often tear and curl when removed giving poor contact to the Kapton® surface. Tearing was due to experimental limitations but curling was unavoidable and solved only when a direct tape cast method was employed in subsequent trials.

The initial tape quality was imperfect and suffered from scattered porosity due to a disproportionately high concentration of solvent. However, tape strength, and quality were sufficient to initiate preliminary tests of the cold sintering process. 1" circles were cut from the tape, ZnO was then peeled off the carrier film and placed onto 1" circles of Kapton® sheet. Samples were then put into a furnace to burnout the binder. Although the recommended binder removal temperature of the system is 450°C for 1h (above the temperature resistance of Kapton®), TGA data of the binder system from the manufacturer (Figure 5.6) indicated that it could be removed at 300°C if done over a long period. Thus, a time of 20 hours with a ramp rate of 0.1°C/min was chosen. After binder burnout, 25µl of 1.0molar acetic acid were pipetted onto the surface of the samples before placing in a die, sandwiched between either a PTFE or cellulose film to prevent sticking, followed by cold sintering 1 hour at 200°C and 250MPa.

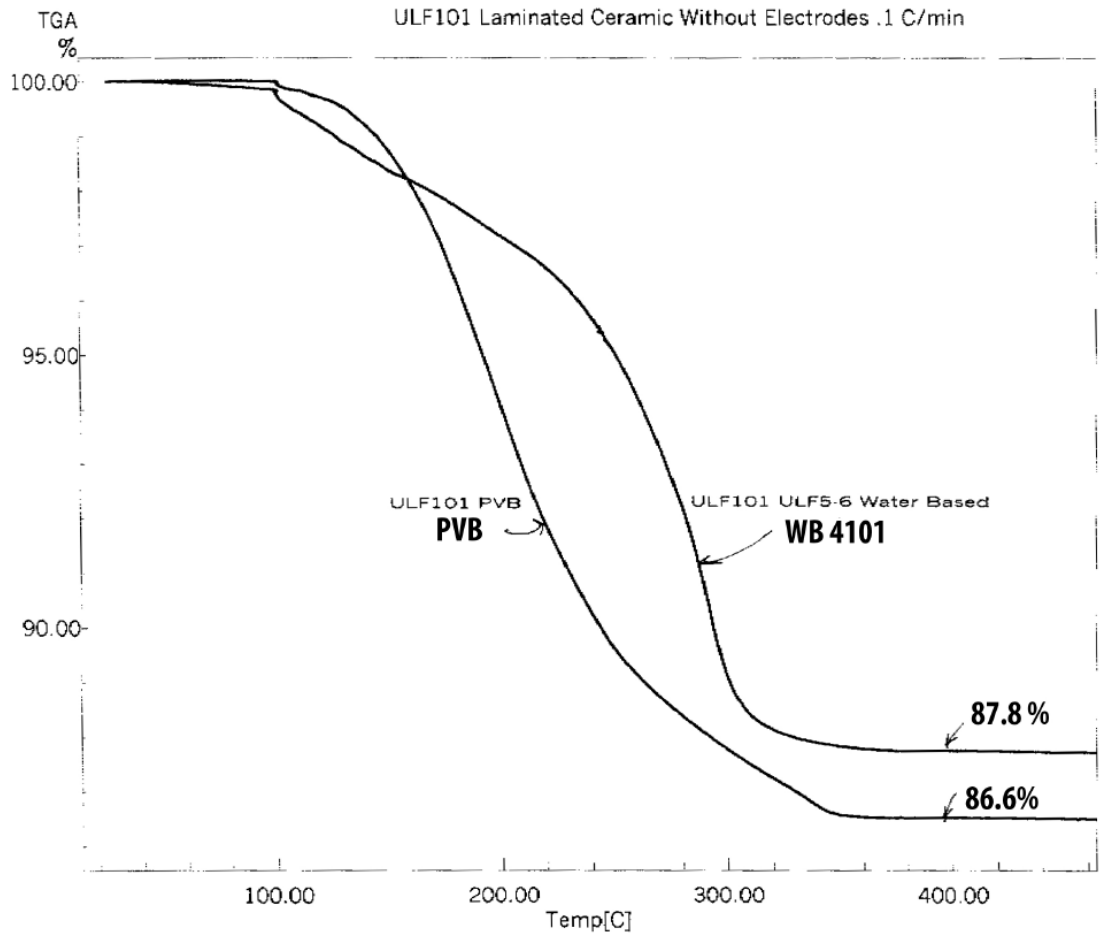

Figure 5.6: TGA provided by the manufacturer (Polymer-Innovations Inc) of the water-based binder system (WB4101) used in the tape-casting of this project. This indicated that a long burnout at 300°C could be used to remove the binder system effectively whilst protecting the Kapton.

5.2.3.2 Results and Discussion

These trials highlighted a number of issues: i) transfer of the tape to the surface of Kapton® circles was difficult with the tools available, with tape often curling up at the edges and tearing. (Figure 5.5); ii) ZnO would often adhere to the die, with the Kapton® sheet suffering from heat damage even at these low temperatures. (Figure 5.7a) and iii) the cellulose thermally decomposed at a lower temperature than expected whereas with PTFE film adhered to the surface of the composite, removing the ZnO layer when peeled off.

Given the partial success of directly mixing the ZnO and acetate on the surface of Kapton, it was decided to improve further protocols by directly tape casting powder onto the surface of the polymer film to maximise adhesion and alleviate transfer problems. In addition, a superior spacer/barrier (5mm thick PTFE pucks) was required to protect the Kapton® from heat damage.

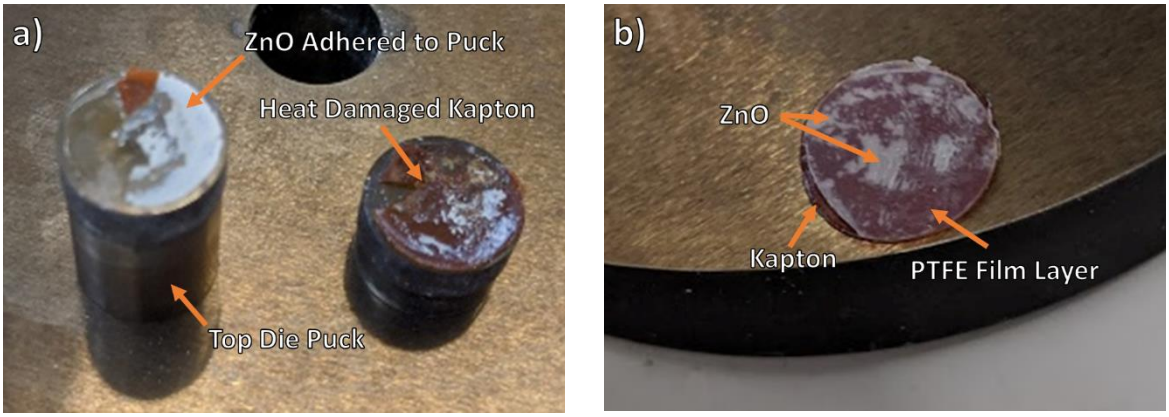

Figure 5.7: a) Image of a sample cold sintered at 200°C 250MPa after removal from the die without any barrier layer. Kapton® sheet has become heat damaged, with a layer of ZnO adhering to the die piece instead. b) Sample post sintering with a barrier layer. ZnO has sintered to the Kapton® but the PTFE has become stuck to it. Removal of the PTFE would remove the ZnO layer with it.

5.2.4 Tape Casting Directly Onto the Kapton®

5.2.4.1 Experimental

To enable direct tape casting onto Kapton, the tape cast slurry formulation and preparation process was modified as follows: Suitable amounts of plasticiser (PL005), dispersant (DS001), defoamer (DF002), binder (WB4104), solvent (distilled water), were combined with nZnO. This mixture was placed into a speed mixer for 5 minutes at 1000rpm, 2 minutes at 1200rpm, and 4 minutes at 1400rpm, to produce a slurry of the correct consistency. The slurry was then placed into a vacuum chamber for 2 hours to de-gas, before being cast over the surface of an A4 sheet of 50µm thick Kapton® film and allowed to dry. (Figure 5.8a)

Table 5.2: Table of the final quantities of each constituent in the tape cast slurry

Binder constituent	Final quantity (%)
WB4104 Binder	31.055
DF002 Defoamer	0.329
DS001 Dispersant	3.294
nZnO Matrix	17.786
PL005 Plasticiser	2.635
Distilled H_2O Solvent	44.901

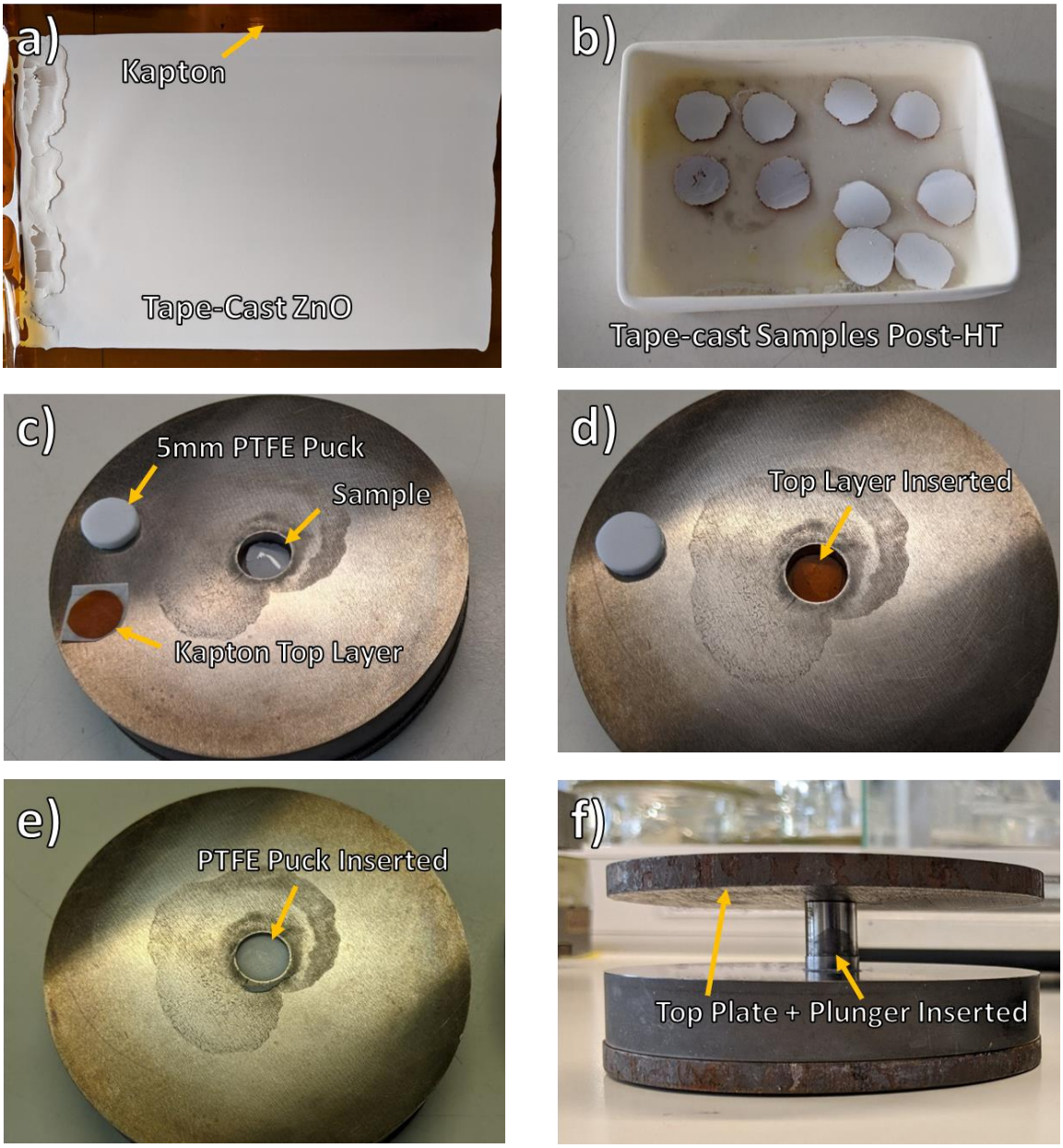

Figure 5.8: a) The final cast tape onto a sheet of HN-Kapton, b) 1" diameter samples of the tape on Kapton® post-300°C heat treatment ready for use. c) 1" sample placed in a 1" die on top of a 5mm puck (not visible) after addition of 25µl of 1.0molar acetic acid. d) The top layer of HN-Kapton® placed on top of the ZnO layer in the die. e & f) The top PTFE puck is placed into the die followed by the die plunger and top plate ready for hot pressing.

1" circular sections of the tape/Kapton were cut out. These were then placed in a furnace to burnout the binder as described in 5.2.3.1. Post-binder burnout, 25µl of 1.0molar acetic acid was pipetted onto the surface of the samples before being placed into a die. 5mm thick PTFE pucks were positioned on top and underneath the sample in the die to protect the Kapton® from heat damage. Images illustrating this process and the final setup ready for cold sintering (200°C and 250MPa for 1 hour) are shown in Figure 5.8.

5.2.4.2 Results & Discussion

Direct tape-casting onto the Kapton coupled with the use of 5mm PTFE spacer pucks to protect from damage during the cold sintering, facilitated reproducible, transparent samples (1-2 layers) with up to 4 layers of ZnO. (Figure 5.9)

Single layer devices showed high transparency, note the orange colour is from the Kapton not the ZnO. As expected however, transparency decreases with an increase in the number of layers, with the device becoming totally opaque by 4 layers. (Figure 5.9) The loss of transparency is thought to be not only due to the increase in thickness but also to a decrease in the density as the number of layers increases. Adhesion of the ZnO varied from sample to sample and flexing resulted in cracking of the ZnO layer. Some samples however, were well adhered, often tearing the Kapton® before detaching from the ZnO, Figure 5.9d. To fully explore adhesion of ZnO to Kapton, systematic scratch [223] peel, [224] and pull [225] tests would be required.

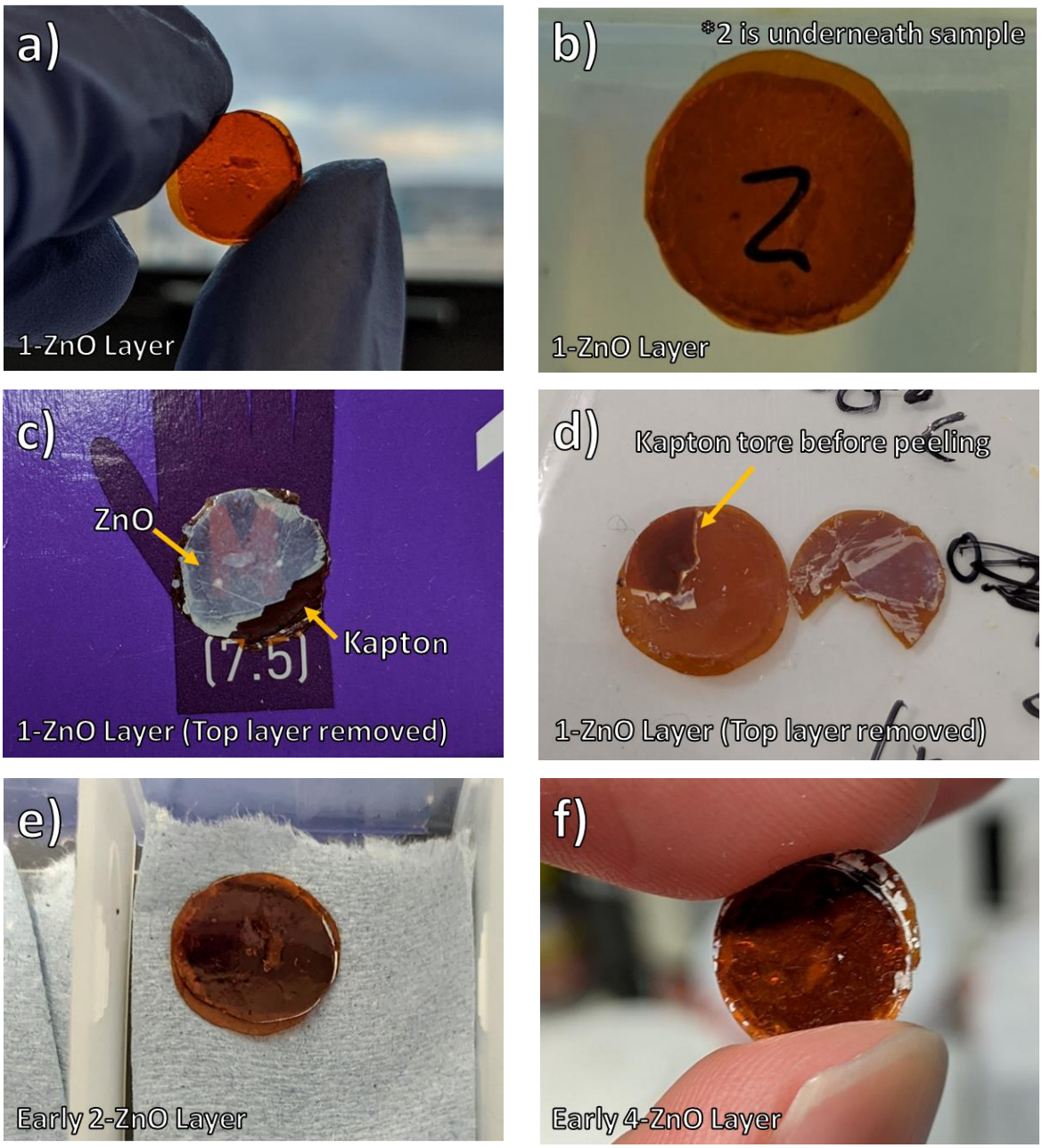

Figure 5.9: Images showing 1-, 2-, and 4-layer samples cold sintered at 200°C 250MPa and the transparency of the deposited ZnO layer. a&b) First successful transparent single layer sample. c) Single layer sample, with the top layer removed revealing a translucent sheet of ZnO on the Kapton. d) Single layer separated illustrating strong to the Kapton® which results in tearing before peeling. e-f) Early 2-, and 4-layer samples in which the transparency decreased with increasing number of layers

XRD (Figure 5.10) revealed the expected wurtzite structure for ZnO [58], [226] for 1-, 2- and 4-layer devices with greatest intensities for (101) and (100) peaks. Peak widths increased with the number of layers. Narrow peaks in the 1-layer sample lead to splitting at higher angles due to the separation of the $K\alpha_1$ and $K\alpha_2$, previously observed in Chapter 4 and suggesting a high degree of crystallinity. As the number of layers increases, however, $K\alpha_1$ and $K\alpha_2$ merge, confirming that grain growth is suppressed as the number of layers increases, which is consistent with the loss of transparency. Broad intensities are observed at ~14°, 22°, and 26° from the amorphous Kapton®, Figure 5.3 with 5.4. No secondary phases such as the acetate peak sometimes seen in cold sintered ZnO were observed [16]. Previously in ceramics, the secondary acetate phase was detected using Raman spectroscopy but florescent interference from the Kapton® sheet produced a bleaching response hiding any useful information. A much lower wavelength UV laser would be required to avoid fluorescence.

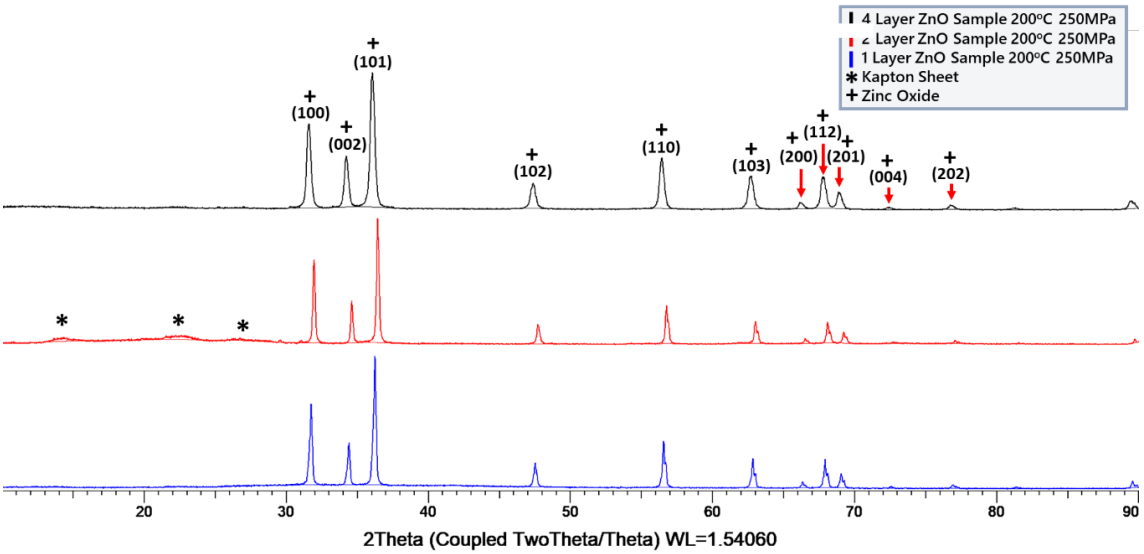

Figure 5.10: XRD patterns of 1-, 2-, and 4-layer ZnO-Kapton® samples cold sintered at 200°C 250MPa normalised to the (100). All scans showed expected ZnO Wurtzite character with a small residual background from the Kapton® film. No secondary phases are noted. As the number of layers increases, the peak width increases indicating less crystallite growth.

Figure 5.11 shows SEM images of the top and delamination surface grain structure of the 1-layer sample, top-surface of a 2-layer sample, and delamination surface of a 4-layer sample. Grains were mostly equiaxed with a few elongated but the grain size notably decreased with an increase in the number of layers, consistent with the loss of transparency and broadening of the XRD peaks. Delamination surfaces of 1- and 4-layer samples (Figure 5.11b,e,f) show a stark contrast, the former showing a higher density with a much stronger evidence of particle coalescence and the formation of a clear grain structure and necking. The 4-layer composites showed a more porous structure with more loosely packed grains, poorer particle contact and less necking. The lower density explains why the ZnO layer in a 4-layer sample separates to reveal a delamination surface instead of the top of a layer.

The ZnO in all samples appeared to form sharp interfaces with the Kapton® surface with striations in the 2-layer samples (Figure 5.11d) caused by ZnO sintering to the shape of defects/scratches on the Kapton® sheet. Cross-sections of samples also revealed good contact between layers and highlight the continuous sheets of sintered ZnO sandwiched between Kapton® film with evidence of interdiffusion. Several zones with poor adhesion were observed, (Figure 5.12e&f), but it is not known if this was caused by the SEM sample preparation process. Detachment occurred more frequently from the top-layer of Kapton® (Figure 5.12f) with the most likely cause being poor preparation of the top layer before sintering. This was later resolved by cleaning the top Kapton® surface before placing in the die. The ZnO layer thickness varied from ~22-33µm. Some vertical cracks were also observed within sintered layers. (Figure 5.12c). Cracks were not observed in bulk films and could be due to either faults within the tape before pressing, pressing flaws caused during cold sintering, damage during handling of the specimens or during the SEM sample preparation process.

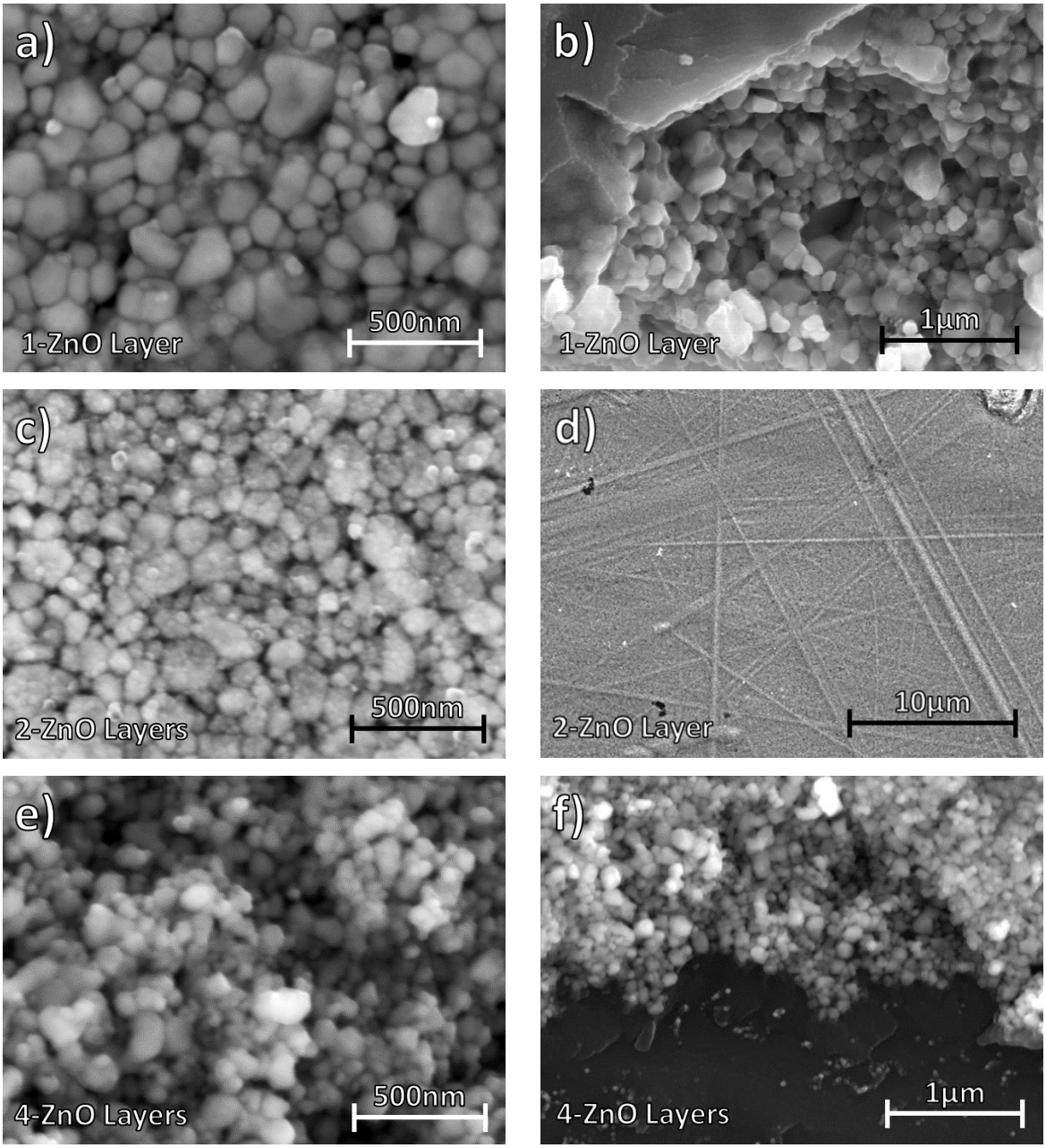

Figure 5.11: SEM of 1-,2-, and 4-layer samples cold sintered at 200°C 250MPa. a&b) Top and delamination surface images respectively of a 1- ZnO layer sample, showing grain growth and microstructure similar to bulk material. c) Top surface images of 2-ZnO layer samples with less grain growth was observed than in 1-layer. d) A low magnification image shows how ZnO mirrors defects in the Kapton® sheets. e&f) Delamination surfaces of 4-ZnO layer samples illustrating that 4-layer samples have the smallest grain/particle size and ZnO conforms to the Kapton® surface.

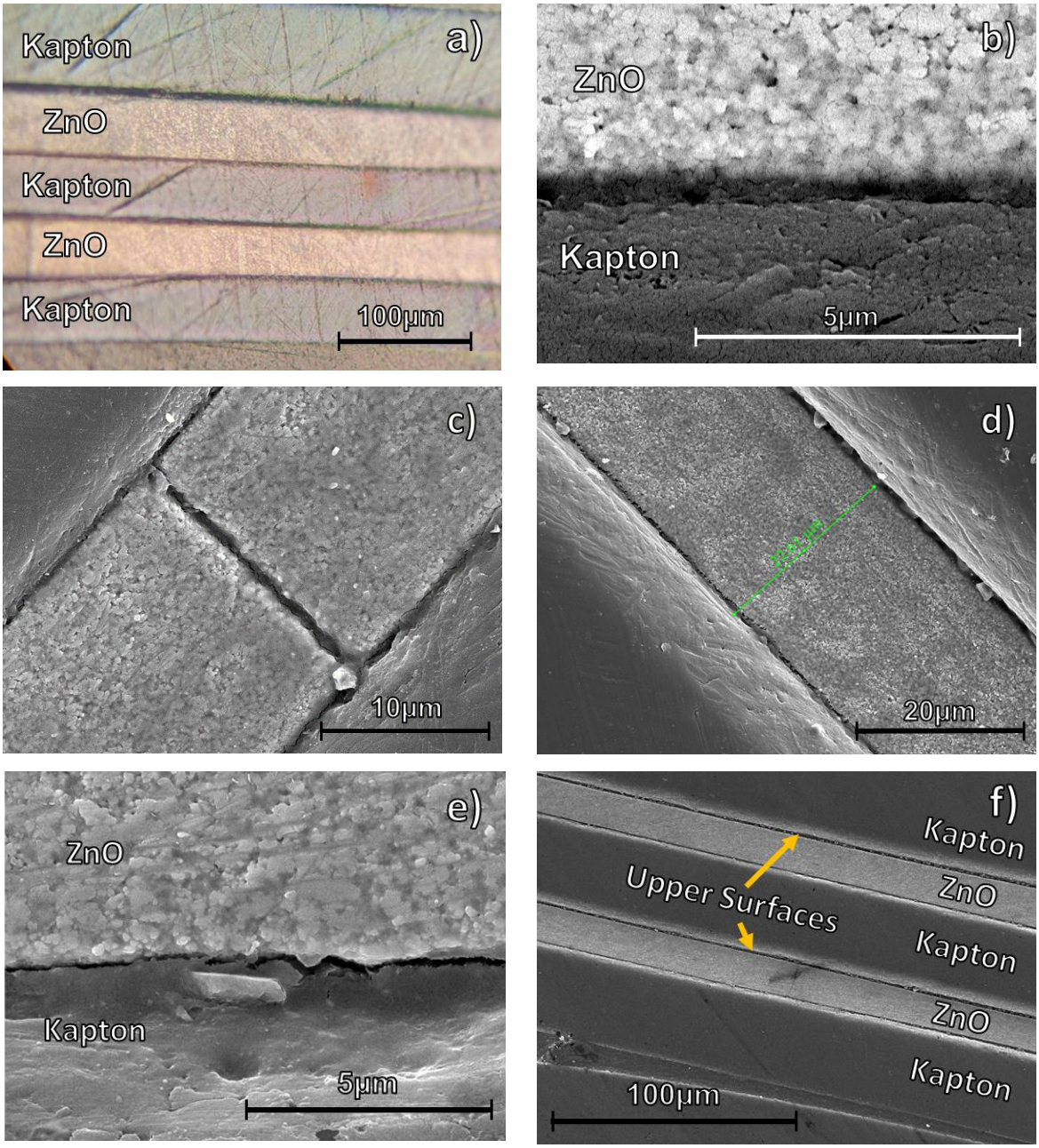

Figure 5.12: Cross-section optical and SEM images of 2-layer ZnO-Kapton® samples cold sintered at 200°C 250MPa. a) Optical imags showing the sandwich structure of the layers. b) SEM image of the interface between Kapton® and ZnO. c) SEM image of 1 of several cracks observed in some samples. d) measurements of ZnO layer thickness (~22-33µm). e) detactchment area of layered sample. f) Image showing detachment from ZnO by upper surface.

5.2.5 Conclusions and Future Work

Transparent thick layer samples comprised of ZnO directly cold sintered onto Kapton® sheets were produced. These were sintered either as a single layer or stacked in a ZnO-Kapton® arrangement up to 4 layers. Optical transparency decreased with increasing number of layers contiguous with a decrease in density and grain/particle size. No secondary phases or interaction between the Kapton® and ZnO were observed. Adhesion between the ZnO and Kapton® varied from sample to sample with quantitative testing still required. Although proof of concept is demonstrated several issues still need to be solved.

- Secondary acetate phase removal will prove critical if high conductivities are to be achieved for, e.g. TCO applications. A heat treatment at 300^{o}C may be possible but it is not known how this would affect the overall sample quality,
- Adhesion is not reproducible and requires optimisation. Better control of sintering conditions such as a purpose-built die and a better spacer material than PTFE, which deforms, are needed,
- Reproducing the results using doped ZnO is critical to achieve the desired conductivity for TCO applications. It is noted that although GZO was more difficult to cold sinter compared with undoped ZnO, good densities were obtained (section 4.3.3).

Chapter 6 – The Cold Sintering of Boehmite to Produce γ-and α Alumina

6.1 Introduction

6.1.1 Motivations

As discussed in Chapter 2, alumina is a ceramic widely used in many industries. It has a broad range of polymorphs, all of which are utilised for their unique properties. The focus of this chapter is the sintering of γ-alumina and α-alumina from boehmite with the assistance of a cold sintering process.

γ-alumina is widely used as both a catalyst and catalyst support. However, its relatively low temperature formation window (500-800^{o}C) [101] makes it is difficult densify via conventional solid-state methods which require samples to be heated to 80%T_m (~1600^{o}C) to achieve high density [1]. α-alumina is the most stable polymorph and has the highest formation temperature (>1000^{o}C) [101]. Undoped α-alumina has high chemical resistance and operating temperature but to achieve sufficient densification, it requires >1500-1800^{o}C in many industrial processes [227]. As well as the high energy cost, these temperatures require specialised furnace equipment such as $MoSi_2$ heating elements.

Cold sintering is therefore, perceived as a way of overcoming these issues and potentially reduce manufacturing and energy costs for densifying γ and α-alumina. Beauvoir and Estournès [165] demonstrated the ability to use cold sintering using an in situ reactive sintering process with a heat treatment to form γ-alumina, but pellets suffered from mechanical instability. In this contribution, a similar method of sintering using boehmite and acetic acid is proposed but with the additions of a PVA binder to help stabilise the pellet, leading to improved mechanical stability of the γ-alumina pellet.

6.1.2 Aims

- To use cold sintering to densify γ-alumina while maintaining a porous microstructure for potential catalytic substrate applications.

- To use cold sintering to reduce densification temperature of α-alumina using boehmite, achieving a pellet with high final density.

6.2 Method

6.2.1 Choice of Materials

6.2.1.1 Pseudo-Boehmite

Although it is possible to use aggressive solvents such as high molarity aqueous HCl to partially dissolve alumina, this approach was deemed unfeasible for both health and safety reasons and the lack of suitable equipment. Moreover, using such aggressive chemicals negates the environmental advantages of cold sintering. Pseudo-boehmite was therefore seen as the ideal alternative feedstock to α alumina as it readily dissolves in acetic acid [228] and transforms into the two desired polymorphs (γ & α) upon heat treatment [101]. Other advantages include its low cost and worldwide abundance.

6.2.1.2 PVA Binder

Mechanical stability of the pellets to create adequate handling characteristics was a continuous issue throughout this study. 5% PVA binder solution was thus added to the pseudo-boehmite powder prior to cold sintering since it is low cost and it burns out at a similar temperature to the transformation to the γ-alumina phase (500^{o}C).

6.2.2 Experimental Method

6.2.2.1 Producing a Stable Cold Sintered Boehmite Pellet

Pseudo-boehmite powder (Johnson Matthey >99.7% pure) was ball-milled in isopropanol for 24 hours to break up agglomerates. This powder was then dried, sieved and maintained at 180^{o}C. 5wt% PVA solution was produced by dissolving the appropriate mass of PVA in distilled water at 60^{o}C for 24h. 1.0 molar acetic acid (pH 2.38) was produced by diluting glacial acetic acid (Honeywell) with distilled water.

Cold sintering of the boehmite was performed by combining 0.5g of pseudo-boehmite with 0.3ml (27wt%) of 1.0 molar acetic acid and mixing in a pestle and mortar. The solution was mixed to slurry-like state before it returned to a powdered appearance. Any agglomerates were broken up during the final stages of mixing. A further addition of 0.1-0.5ml (11-38wt%) of 5wt% PVA solution was used in later fabrication procedures, following the same mixing process.

Due to the highly adhesive nature of boehmite mixed with acetic acid, a high temperature resistance graphite lubricant (Holts Graphite Spray) was applied to the surface of all die components. The mixed powder was then placed into the die and to be cold sintered. The die

within the press was first raised to 250-625MPa before the temperature was increased from to 125°C, 200 °C, or 300°C for 1 hour with a heating rate of 20-40°C/min, followed by unassisted cooling to room temperature.

6.2.2.2 Manufacture of Densified γ-Alumina

Pellets of cold sintered pseudo-boehmite were placed in a still air furnace at 500°C for 6-10 hours, with a ramp rate of 0.5°C/min heating and 2.5°C/min cooling to simultaneously burnout the PVA binder and facilitate the transformation to γ-alumina.

6.2.2.3 Manufacture of Densified α-Alumina

Cold sintered pellets of pseudo-boehmite were placed in a furnace whose temperature was first raised to 500°C with a ramp rate of 0.5°C/min before holding for 6-10 hours to remove the PVA binder. The temperature was further raised to 1100-1400°C with a ramp rate of 2.5°C and held 8 hours to densify to encourage the transformation to α-alumina. The final sample was cooled in the furnace at 5°C/min.

6.2.2.4 Structural and Microstructural Characterisation

Density measurements were performed via the volumetric method and compared against theoretical densities from the scientific literature. X-Ray diffraction was carried out on a Bruker D2 Phaser, with a 1mm divergence slit, 3mm air-scatter gap, step scan time of 0.3s, and a step size of 0.02°. Crystallite size for γ-alumina was calculated via the Scherrer method via equation 6.1:

$$\tau = \frac{K\lambda}{\beta Cos\theta} \tag{6.1}$$

Where τ is the average crystallite size, λ is x-ray wavelength, β is the line broadening via full-width half maximum (FWHM), θ is the Bragg angle, and K is the dimensionless shape-factor taken as 0.9 for these experiments.

SEM was performed on a FEI-Inspect F50 microscope at 10kV with a spot size of 3.5. Samples were sputter-coated to prevent charging in either gold or carbon. SEM Images presented are not representative of pressing orientation and was not accounted for when images were taken. Raman spectroscopy was performed with a Renishaw InVia Raman microscope setup, using a 514.5nm green laser.

6.2.2.5 Mechanical Testing

Compression testing was performed on a Hounsfield H100KS tensile tester with a Tinius Olsen 100kN strain gauge at a test speed of 1mm/min. Compression testing was not able to be performed on samples with the requisite dimensions of 2.5 height to diameter ratio due to available die geometries.

6.3 Results & Discussion

6.3.1 Cold Sintering of Boehmite

6.3.1.1 General Discussion

Following the procedures describe in section 6.2, densified samples of cold sintered boehmite were obtained. Whilst levels of translucency reported by Beauvoir and Estournès [165] were never reached, PVA-free samples would appear translucent in thinner sections. However, samples had poor mechanical stability and were difficult to produce defect free, an issue also reported by Beauvoir and Estournès [165]. The fragility of the cold sintered boehmite is likely related to its layered structure of out of plane H-bonds [229]. The highly adhesive nature of the boehmite when cold sintered made removal from the die difficult compounding the fragile nature of the samples.

When removed from the die, (even if done very slowly), the samples produced audible high-pitched cracking and, in many cases, completely shattered (Figure 6.1a) or resulted in a highly microcracked microstructure that crumbled easily when handled (Figure 6.1b).

5wt% PVA binder solution increased sample stability. 0.3ml (27wt%) PVA gave the best stability but produced a colour change at the cost of translucency, eventually becoming totally opaque above a certain wt%. Importantly, the addition of PVA allowed samples to be removed more easily from the die.

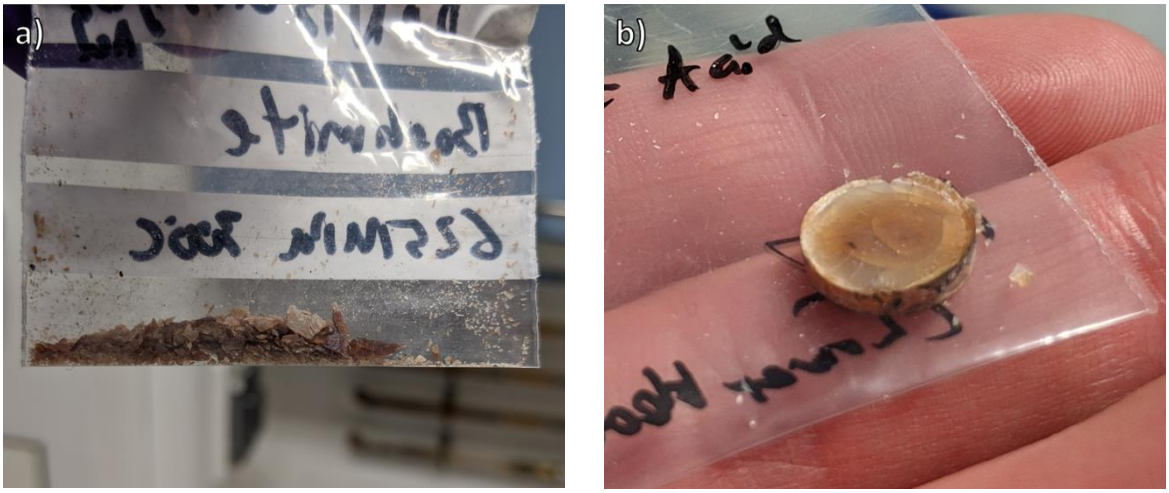

Figure 6.1: Images of early unsuccessful samples cold sintered at 300°C 625MPa. a) A sample that crumbled into shards upon die removal. b) A sample removed very slowly from the die but still had a shattered top surface and a large number of visible defects throughout

A number of further adjustments to the cold sintering procedure allowed for consistent production of defect-free samples with good mechanical stability, Figure 6.2. A list of these minor adjustments is reported in Table 6.1. Strong adhesion to the die-puck was nonetheless sometimes observed, requiring mechanical impact methods, followed by grinding and polishing to completely remove residual boehmite (Figure 6.3). Adhesion to the die requires further investigation but is not considered as completely negative and may point at the ability of cold sintering to be used in the fabrication of boehmite coatings on the surface of metal. The strong adhesion may be purely topotactic but equally chemical bonding may occur under the harsh cold sintering conditions. According to Castet et al. [228], at 200°C in a 2.38pH environment, 3 dissociated species will occur in order of dominance: $Al(OH)^{2+}$, $Al(OH)_2^{+}$, and Al^{3+}. This concentration increases significantly under hot-pressing conditions due to the super-saturated solution in the cold sintering process [11], [12]. Alumina is known to strongly bond to Al and Fe interfaces [230] and boehmite has been demonstrated a number of times as a coating material on various metals [231][232][233]. Thus, it is possible that at 200°C Al/Fe-O(H) bonds form [234] between the puck and the boehmite.

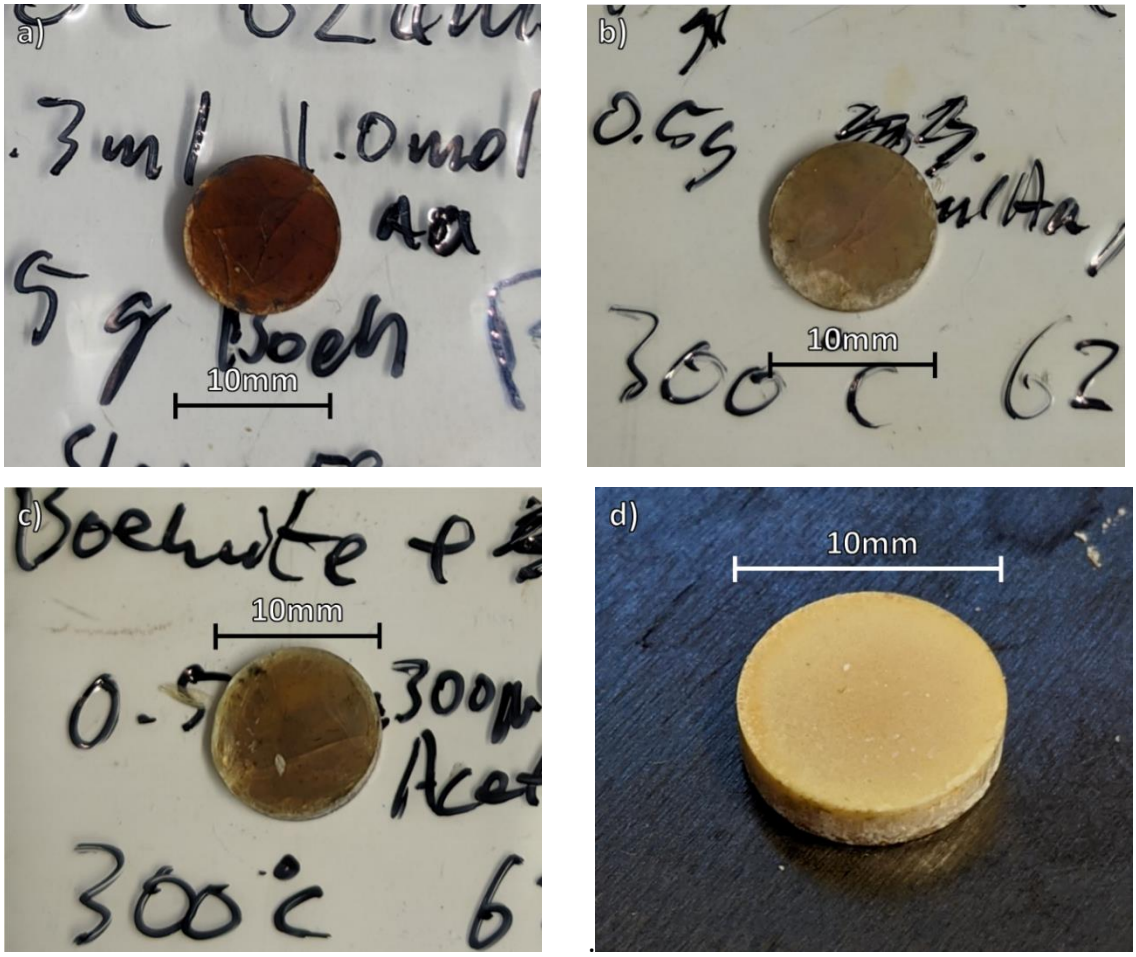

Figure 6.2: Photos of cold sintered boehmite with various volumes of 5wt% PVA solution introduced. a) 0%, b) 5%, c) 10% d) 27%. It must be noted that the image d) shows a high quality sample post lowering of sintering temperature and pressure to 200°C and 250MPa down from 300°C and 625MPa shown in a-c

Table 6.1: Details of measures taken to increase sample quality during the cold sintering of boehmite

Measure Taken to improve stability	Reason for action taken
Sintering pressure lowered to ≤250MPa	High pressure would damage/crush samples once densified causing defects. Lowering pressure prevented this. Is thought pressure could still be successfully lowered further.
Sintering temperature lowered to ≤200°C	Prevented binder burnout occurring during sintering (PVA boiling point = 228°C). Increasing sample stability reducing defects.
Rate of cooling slowed	Help significantly slow pressure reduction based on findings by Beauvoir and Estournès [165]. Reduced instances of sample failure and defects within the sample.
Graphite lubricant applied to die surfaces before sintering	Helped lower sample removal pressure and lowered occurrences of sample adhesion to die pucks.

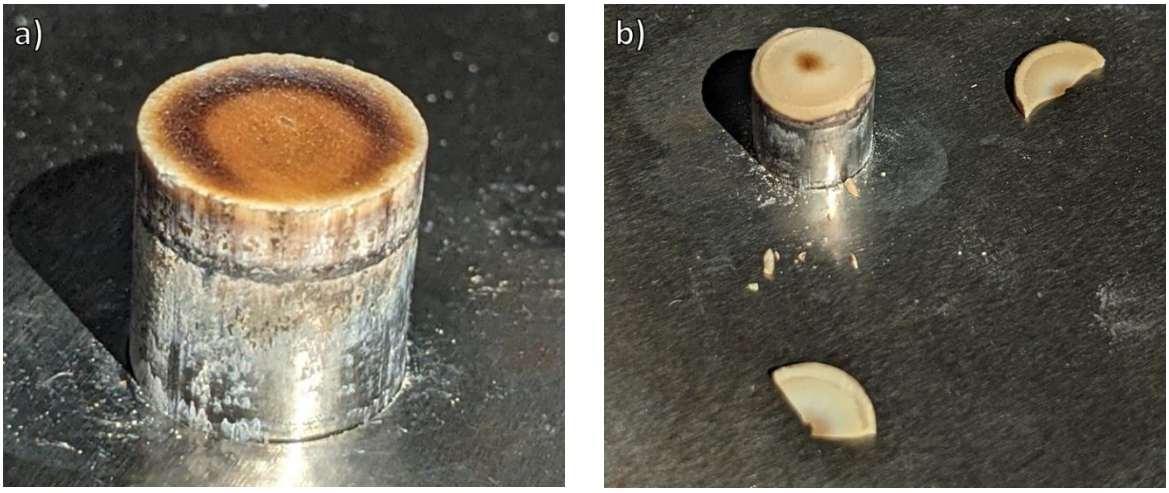

Figure 6.3: Example of a post-cold sintered boehmite pellet strongly adhered to the surface of a die puck, a) before attempts at mechanical removal, b) after of attempt mechanical impact removal.

6.3.1.2 Crystal Structure

XRD (Figure 6.4) of cold sintered pellets illustrated that the boehmite phase was retained with no indication of secondary phases. However, as the cold sintering temperature and pressure increased, the boehmite peaks narrowed and the broad (051/220) peaks split, consistent with an increase in crystallite size. This is commensurate with SEM images, the results from which are listed in Table 6.2 which show an increase in grain size at 300°C 625MPa, a more limited increase for 300°C 375MPa and no discernible increase for 200°C 250MPa.

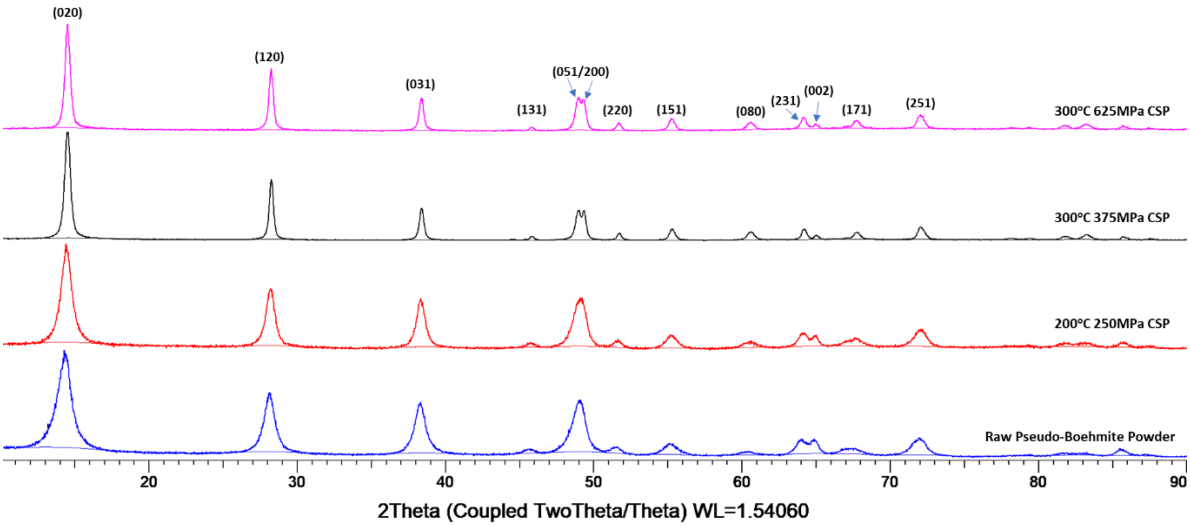

Figure 6.4: XRD of unsintered pseudo-boehmite powder compared with pseudo-boehmite cold sintered at various temperatures and pressures.

Table 6.2: Table of average grain sizes measured from SEM images

Sample	Average grain size (nm)	Standard Deviation (nm)
300°C 625MPa	46	19
300°C 375MPa	28	7
200°C 250MPa	21	4
Raw Pseudo-Boehmite Powder	24	7

Boehmite cold sintered at 250MPa showed a more densely packed microstructure than unsintered but still with evidence of porosity. However, pellets cold sintered at 625MPa (Figure 6.5d) showed a more closely packed structure with larger, flatter grains of up to ~100nm. Low pressures in hot pressing are known to suppress grain growth, since its introduction inhibits all non-densifying mechanisms [1]. However, at high pressures, grain growth is enhanced [235]–[240]. The reason for grain growth is still highly debated with many different proposed mechanisms. Wilkinson and Cáceres [241] suggest a strain-rate dependent grain growth mechanism, where grain boundary migration is induced by sliding at triple points leading to accelerated grain growth. Others suggest mechanisms relating to grain-switching, grain-rotation, diffusion, and dislocation motion [242]–[245]. Ratzker et al. [246] propose a rotational grain boundary sliding grain growth mechanism when observing pressure induced grain growth in alumina during high-pressure spark plasma sintering. They suggest at higher strain rates, defective regions form between grains via grain boundary sliding enhancing grain growth and leading to grain coalescence.

How well these processes can be applied to the unique hydrothermal conditions of cold sintering is open to debate but Gonzalez-Julian et al. [15] and Biesuz et al. [12] discussed grain boundary sliding and plastic deformation as pivotal to cold sintering.

Samples cold sintered at 625MPa may also exhibit restricted sintering as previously observed in many of the ZnO samples in Chapter 4. The effect of pressure on the microstructure is also evident with lateral grain growth normal to the pressing direction in contrast to lower pressure samples in which a spherical morphology is retained.

The observed microstructures in the SEM images match the measured densities (Table 6.2) which, discounting cracked and defective samples (visual to the naked eye) were consistently ~65-70% theoretical, with temperature appearing to have little effect on final density (Table 6.3).

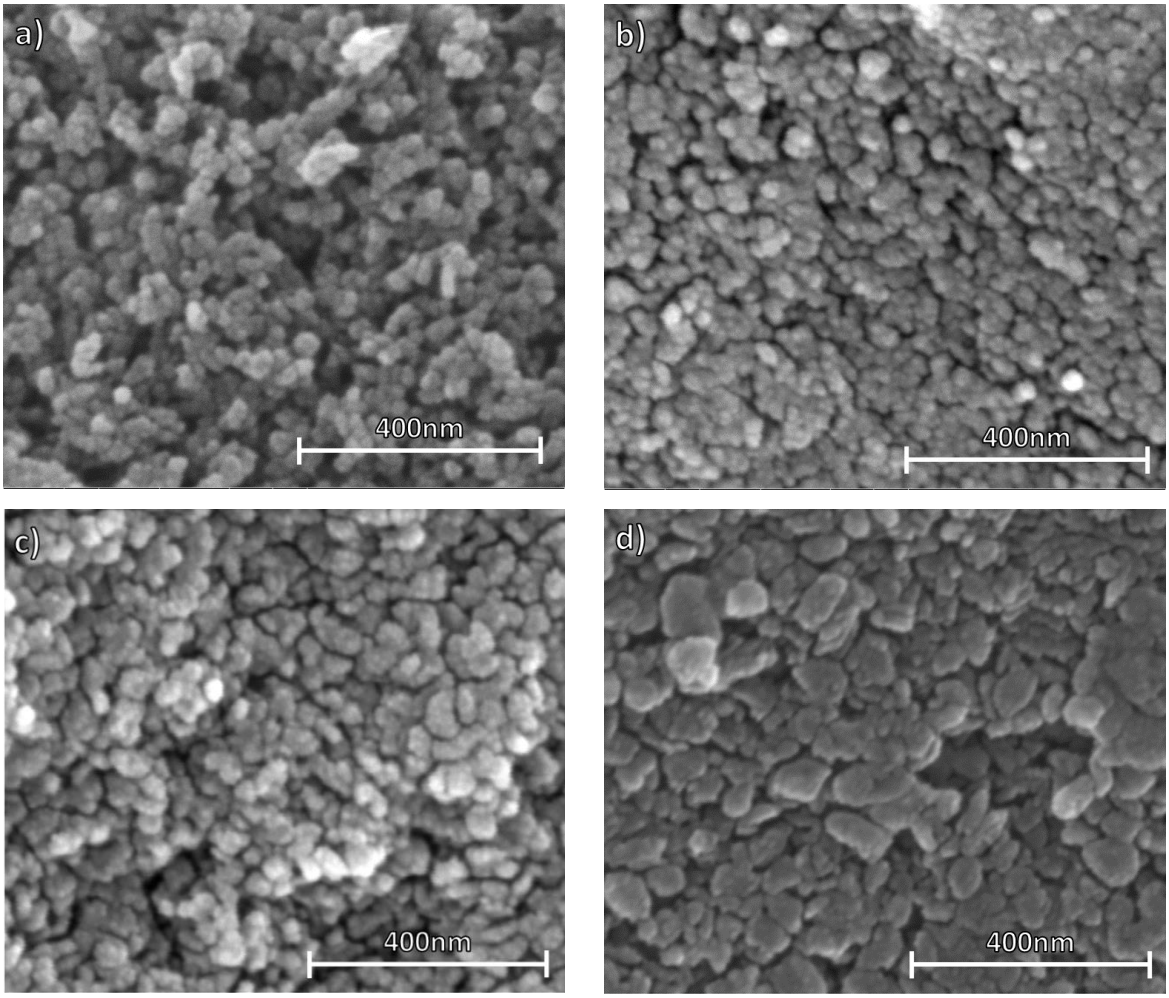

Figure 6.5: Secondary Electron SEM top-surface images of pseudo-boehmite pre and post cold sintered at various conditions a) Unsintered Powder, b) 200°C 250MPa, c) 300°C 250MPa, d) 300°C 625MPa

Table 6.3: Table of recorded densities of post-cold sintered boehmite.

Sample	Relative Density (%)
125°C 250MPa	65.7
125°C 250MPa	62.25
200°C 250MPa	67.18
200°C 250MPa	69.22
200°C 250MPa	69.98

6.3.1.3 Chemical Analysis

As discussed in Chapter 2**,** boehmite has 4 known polymorphs but Noel et al. [247] showed that the ground state arrangements are best described by either orthorhombic $Cmc2_1$ (N°. 36) or monoclinic, $P2_1/b$ (N°. 14) space group symmetries. Although the permitted Raman

modes from these 2 space-groups differ slightly, none of these differences were observed in the experimental data. $Cmc2_1$ orthorhombic was arbitrarily chosen whose irreducible representation is:

$$\Gamma^{Cmc2_1} = 8A_1 + 4A_2 + 8B_1 + 4B_2 \quad (6.2)$$

of which all 24 modes are Raman active [247]. In practice however, far fewer of these peaks are commonly observed, due to their low intensity. In this study (Figure 6.6), 6 low wavenumber modes (<800cm^{-1}) [165], [247]–[250] were observed from those permitted with no extraneous bands from secondary phases. The 2 strongest peaks at 360 and 495cm^{-1}, and a very weak response at 234cm^{-1} are caused by Al-O vibrational modes. The 234cm^{-1} A_2 mode significantly decreases in intensity in cold sintered pellets, possibly due to florescence, but strengthens in post annealed cold sintered samples. The broad mode observed at 674cm^{-1} is caused by OH vibrations relating to deformation and translation of Al-OH bonds, and skeletal flexing of Al-O-Al bonds [249]. Bands at ~340 and ~450cm^{-1} are thought to be caused by OH^- deformation modes. The 340cm^{-1} peak is only observed in the CSP 300^{o}C 625MPa material. The appearance of this peak may be caused by an increase in crystallinity, as evidenced by peak splitting in XRD and a larger grain size, for samples cold sintered at 625MPa [251].

High angle modes that exist for boehmite (1000-3500cm^{-1}) were not resolved due to bleaching from florescence. The origin of the strong fluorescence is not known but in principle could be alleviated by the use of an UV rather than visible light laser.

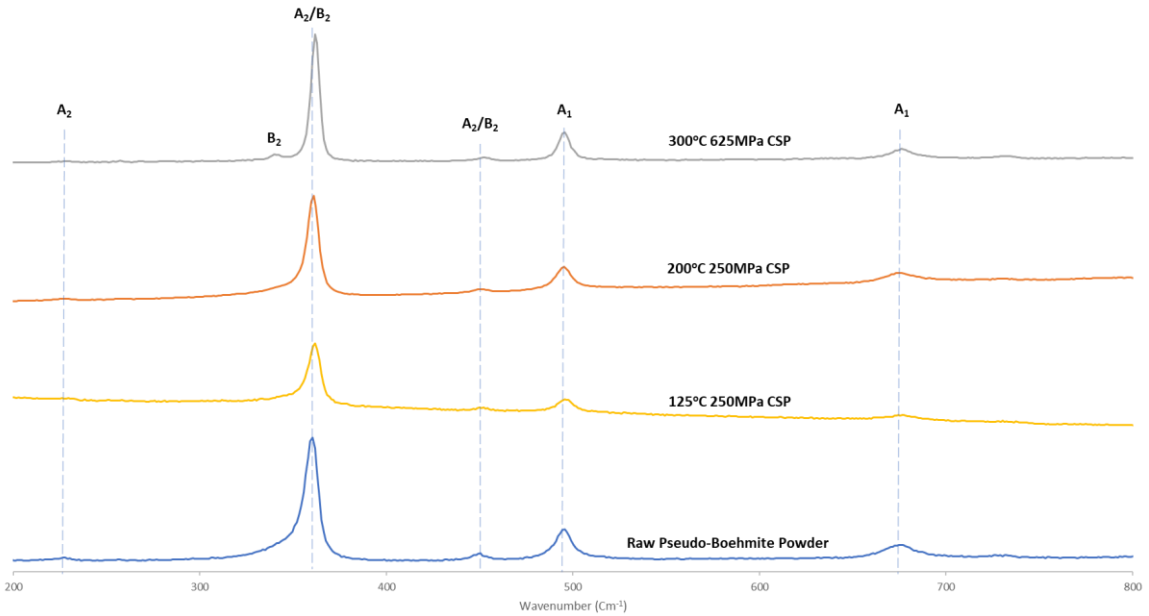

Figure 6.6: Graph showing the comparison of the Raman spectra of cold sintered boehmite under various temperatures and pressures, with unsintered pseudo-boehmite. No other peaks to indicate secondary phases were observed.

Table 6.4: Table containing a comparison of literature modes and those appearing in this study. All peaks fit well with current literature.

Literature Peak (cm^{-1})	These Works (cm^{-1})	Raw Powder	125C 250MPa	200°C 250MPa	300°C 625MPa
228	225-227	Yes	Weak	Weak	No
340	340	No	No	No	Yes
362	360-361	Yes	Yes	Yes	Yes
448	447-453	Yes	Yes	Yes	Yes
495	493-496	Yes	Yes	Yes	Yes
675	674	Yes	Yes	Yes	Yes

6.3.2 Conversion of Cold Sintered Pseudo-Boehmite to γ-Alumina

6.3.2.1 General Discussion

Cold sintered pellets heat treated at 500°C became an opaque white colour (Figure 6.7a-b). Some minor brown discolouration was observed on the surface of some samples due to lubricant residue. Samples rarely showed visual cracking from the transformation process and were mechanically stable. This is in stark contrast to both non-PVA and PVA conventional pellets which maintained a loose white-powder texture, showed little to no shrinkage, and were mechanically fragile (Figure 6.7c-d).

The contrast between cold and conventional samples is further demonstrated through density measurements (Table 6.4). Cold sintered samples gave ~53% relative density compared to the ~37% and ~32-34% for PVA and non-PVA conventionally heat treated material respectively.

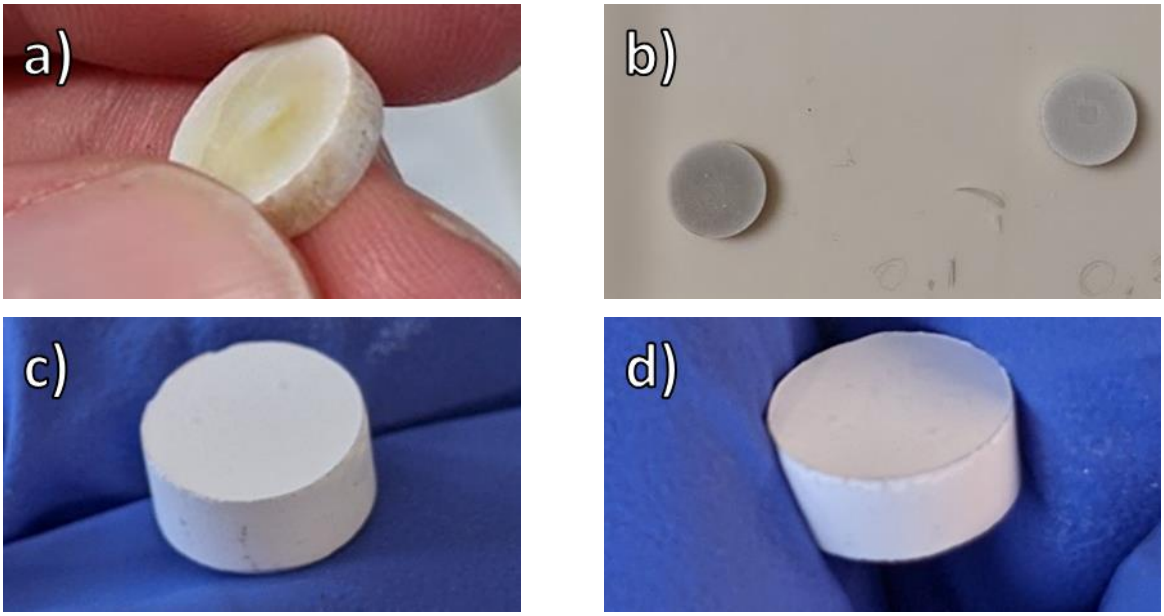

Figure 6.7: (a & b) Photographs of γ-Alumina from boehmite cold-sintered at 200°C 250MPa and heat treated at 500°C (c & d) Boehmite cold pressed at 250MPa and conventionally heat treated to form γ-Alumina without using and with PVA binder respectively

Table 6.5: Table of the densities measured of produced gamma alumina material

Sample	Relative Density (%)
CSP 200°C 250MPa A1	53.2
CSP 200°C 250MPa A2	52.7
Conventional with PVA A	37.08
Conventional with PVA B	37.2
Conventional no PVA A	32.4
Conventional no PVA B	34.3

6.3.2.2 Crystal Structure

All heat-treated samples showed complete transformation to γ-alumina with no secondary phases or residual boehmite evident in the XRD patterns. The lack of secondary phases is further supported by Raman analysis. However, samples cold sintered at higher temperatures and pressures XRD (Figure 6.8) revealed splitting and narrowing of the (400) peak as the cold

sintering pressure and temperature increases, consistent with the grater crystallite size in the as cold sintered boehmite. Analysis of the peak's width via the Scherrer method suggested a typical γ alumina crystallite size of 4-6nm but due to the low intensity and noisy background of the γ alumina XRD patterns, crystallite measurement accuracy may be low.

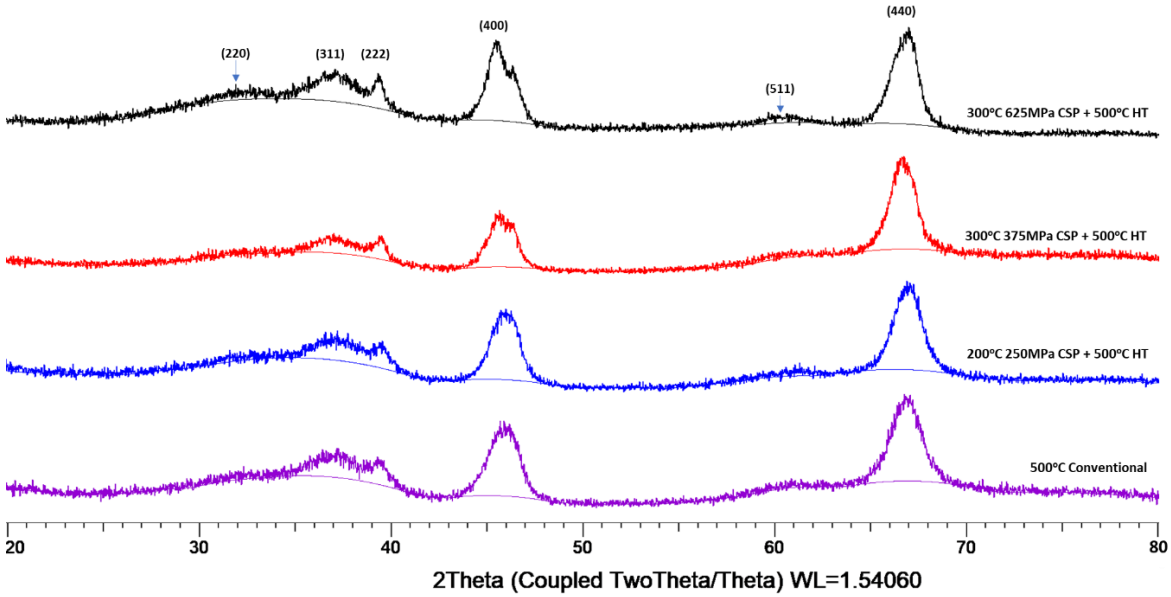

Figure 6.8: XRD pattern of cold sintered boehmite after a 500°C heat treatment compared to cold pressed and conventionally heat treated at 500°C.

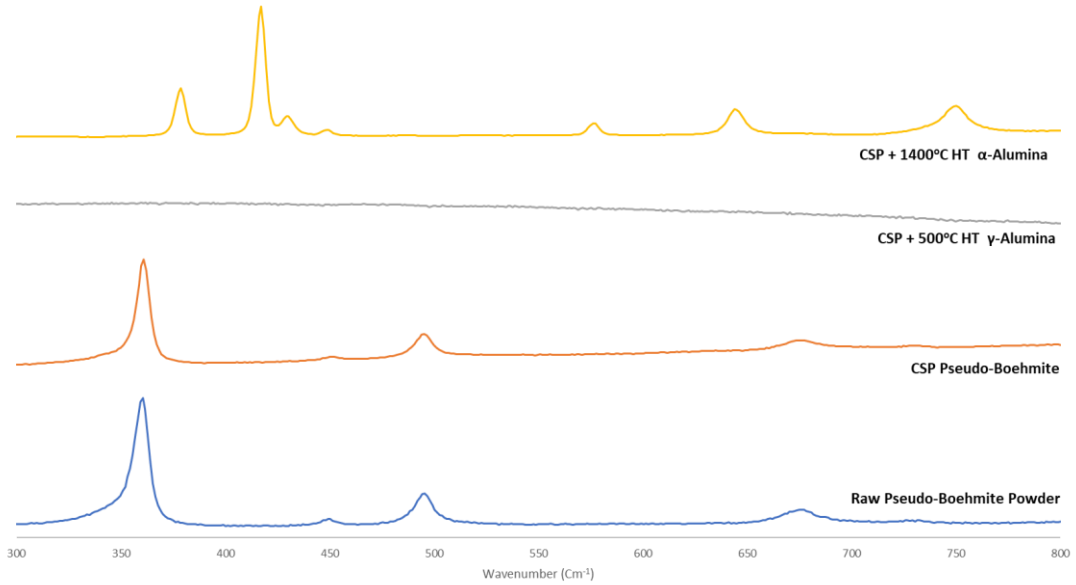

Figure 6.9: Graph showing the compared Raman responses of unsintered Pseudo-boehmite powder, cold sintered: Pseudo-boehmite, γ-alumina, and α-alumina

A number of authors have previously concluded that γ-alumina has no active Raman modes due to its high symmetry (Fd3m) and spinel structure [165], [252], [253] (higher symmetries do not have phonon modes in which polarisation changes asymmetrically. This is one of the

fundamental principles of Raman shift [254]) with some researchers reporting few if any modes visible above background. No modes were observed in our study Figure 6.9, consistent with some previous reports [165], [252], [253] but also indicating the absence of secondary phases. However, Shebanova and Lazor [255] however, have shown some active Raman modes exists and first principles calculations by Liu et al. [256] give a predicted Raman spectra. Liu et al. suggested the irreducible representation of γ-alumina should be split into spinel and non-spinel components due to its unique crystal structure:

$$\Gamma_{optical-spinel} = 25A_u + 35B_u + 34A_g + 23B_g \quad (6.3)$$

$$\Gamma_{optical-nonspinel} = 25A_u + 32B_u + 34A_g + 26B_g \quad (6.4)$$

A total of 57 spinel (34 A_g and 23 B_g), and 60 non-spinel (34A_g and 26B_g) Raman-active modes are therefore predicted which were confirmed experimentally by Jbara et al. [257] in γ-alumina nano-powder. We postulate therefore that a combination of florescence, small crystallite size and non-optimised analysis conditions have inhibited the appearance of Raman modes in this study. Florescence was a consistent issue and could have been resolved with a UV-laser but would not eliminate the problem associated with the small crystallite size [165], [252], [253] [251], [258]. The detection of active modes also depends on the analysis conditions, with laser power and exposure time all affecting intensity and which were not fully optimised within this study.

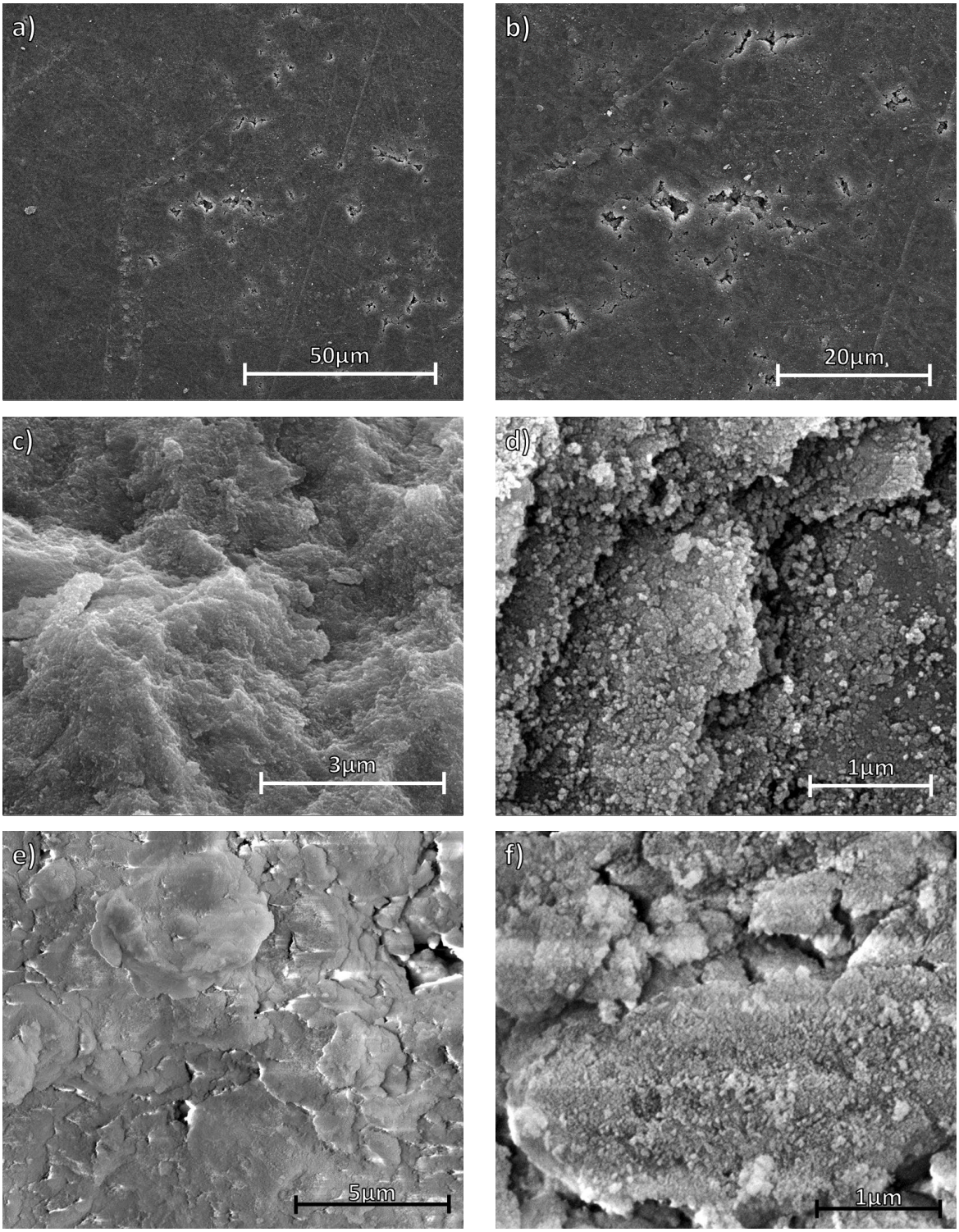

Figure 6.10: γ-Alumina produced from pseudo-boehmite via a-d) 200°C 250MPa Cold sintering + 500°C HT Top surface (a,b) & fracture surface (c,d). e-f) Fracture surface of cold pressed boehmite with PVA binder + 500°C conventional sinter

SEM images show a clear difference between heat-treated samples with and without a cold sintering step. Cold sintered samples (Figure 6.10a-d) have a continuous dense structure of extremely small grains (<50nm), indicating little to no grain growth during the heat treatment process. However, the surface of the cold sintered material also shows scattered clusters of

surface porosity (Figure 6.10a-b). In contrast, the top and fracture surface of samples fabricated without a cold sintering step reveal only poorly packed powder of low density which easily charged in the electron beam, Figure 6.10e-f.

6.3.2.3 Mechanical Properties

Stability of handling was improved with a cold sintering step in the fabrication process. Pellets were unable to be broken with bare hands, and if accidentally dropped did not show damage in contrast to conventional samples, which were fragile and easily crumbled when handled. The results from preliminary compression testing are shown in Figure 6.11 and Table 6.5. CSP pellets have a Young's modulus ($\boldsymbol{E}$) approximately twice that of conventional samples and the crushing strength ($\boldsymbol{CS}$) improved a factor of 12 over conventionally heat treated samples. The conventional pellets showed a failure mechanism typical of compacted powder, with flatter compression curves, and shallower post CS, suggesting necking between grains occurred during cold but not conventional sintering [259]. Moreover, cold sintered pellets exhibit a distinct crushing strength point, indicating brittle failure. The continued curve and increase in pressure after the initial fracture is due to incomplete failure of the pellet, with a central portion remaining intact. The crushing strength for this portion could not calculated due to the unknown residual dimension of the pellet. The non-standard sample geometry must also be taken into account. Under standard conditions sample height (h) is recommended to be 2.5x that of diameter, as below this the failure mode will begin to transfer from a cracking to a crushing mode [260]. However, due to manufacturing constraints diameter was up to 5x sample height, meaning crushing failure mode will have been the primary mechanism.

Comparison with literature data is not only difficult due to the non-standard testing conditions and sample geometry, but also due to the limited literature studying the mechanical properties of γ-alumina. Samimi et al. [261] studied the mechanical strength of γ-alumina catalyst supports which suggests that cold sintered samples produced in this study have ~5x to 6x that reported. It is noted however, that more samples are required to give statistically meaningful data and the testing conditions need to modified so that results can be more readily compared with previous work. These results however, are extremely encouraging and hint at potential commercial exploitation for cold sintering in the fabrication of γ alumina components.

Table 6.6: Table of the mechanical properties recorded for compression testing of γ-alumina

Sample	E (MPa)	CS (MPa)
CSP 200°C 250MPa + 500°C	960	597
Conventional with PVA 500°C	390	49
Conventional 500°C	580	15

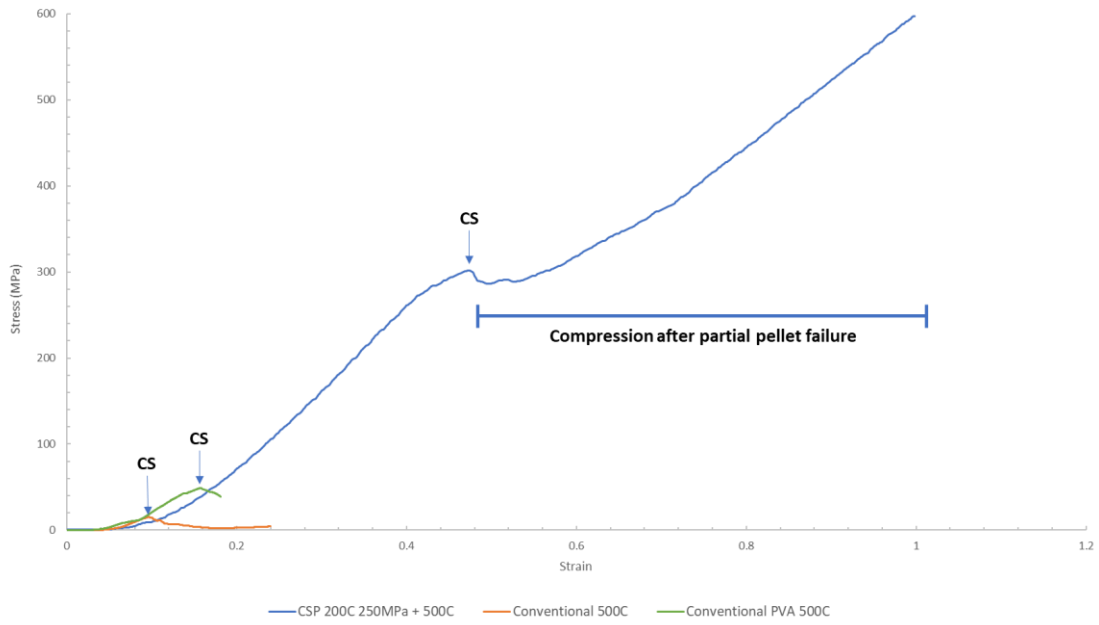

Figure 6.11: Graph showing the results of compression testing of boehmite cold sintered at 200°C 250MPa and heat treated at 500°C to form γ-alumina, and conventionally cold-pressed boehmite followed by heat-treatment at 500°C to form γ-alumina.

6.3.3 Conversion of Cold Sintered Pseudo-Boehmite to α-Alumina

6.3.3.1 General Discussion

All samples heat treated between 1100-1400°C successfully transformed to α-alumina with a consistent white colour. Any slight discolouration of samples relates to residual lubricant from the cold sintering process (Figure 6.12).

Samples heat treated at 1100-1200°C were mechanically stable with no visible cracks. However, cold sintered samples, heat-treated at 1400°C often showed cracking due to shrinkage (Figure 6.12b), indicating that the increase in temperature is leading to greater densification. In contrast, conventional samples showed little shrinkage and were mechanically unstable.

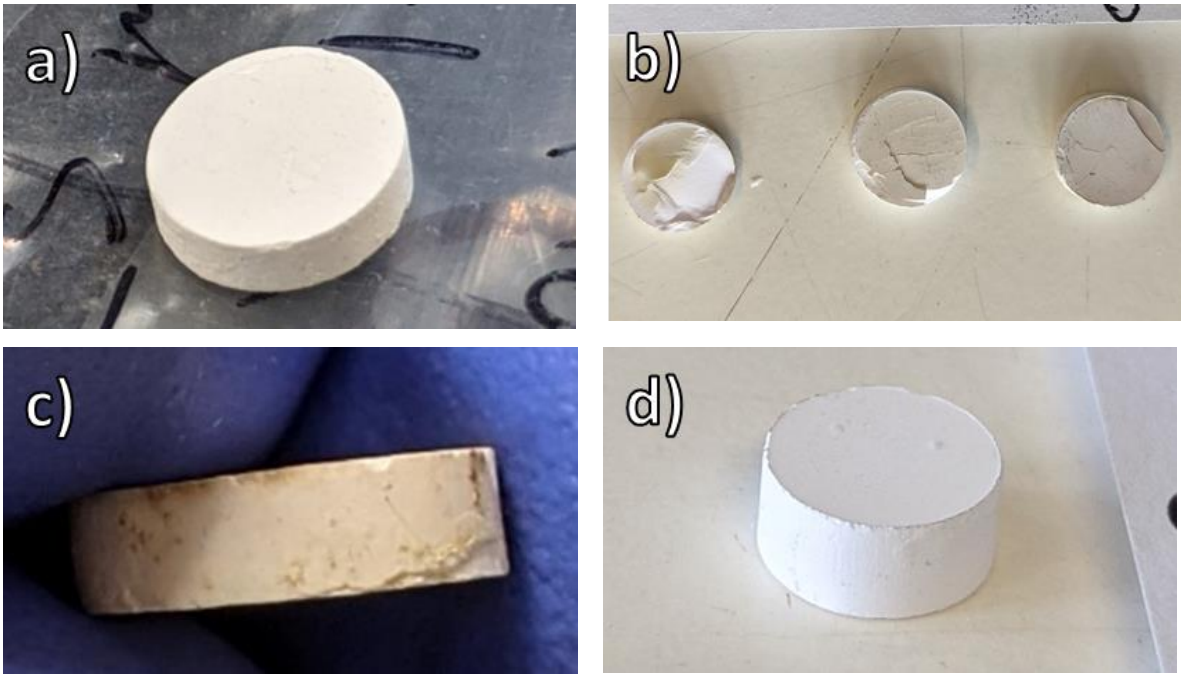

Figure 6.12: Photographs of Cold Sintered Boehmite samples heat treated to α-alumina at a) 1200°C, b&c) 1400°C. Image d) shows Boehmite conventionally sintered at 1400°C with no PVA binder

6.3.3.2 Crystal Structure

X-ray diffraction patterns (Figure 6.13) from samples heated above 1100°C showed no evidence of unwanted secondary phases with peak profiles and intensities similar to those of conventional α alumina. Both conventional and CSP alumina sintered at 1400°C showed an increase in high angle peak splitting with respect to 1200°C due to growth in crystallite size. No texturing is observed in either cold sintered or conventional samples.

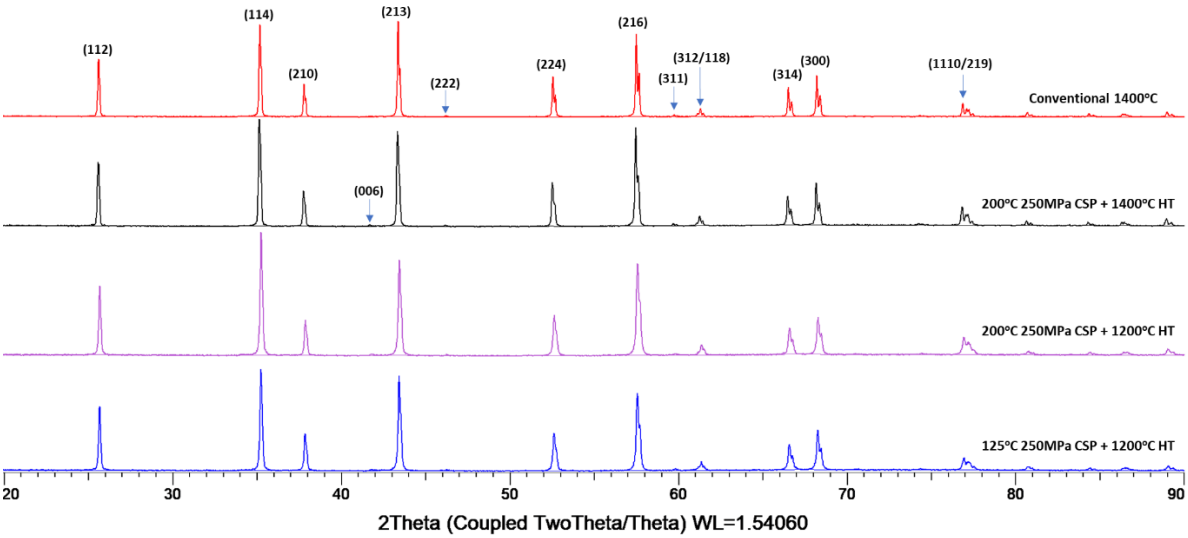

Figure 6.13: XRD spectra comparing α-alumina from conventionally sintered boehmite at 1400°C to cold sintered boehmite heat treated at 1200 and 1400°C

α-alumina is described by the R3c space-group [262], [263], the irreducible representation pf which gives 18 optical modes [264], [265]:

$$\Gamma^{D_{3d}} = 2A_{1g} + 2A_{1u} + 3A_{2g} + 2A_{2u} + 5E_g + 4E_u \qquad (6.5)$$

with only the 2 A_{1g} and 5 E_g modes Raman active [265]. These 7 phonon modes appear (Figure 6.14) at ~379, ~418, ~431, ~450, ~578, and ~750 cm^{-1} and all spectra are in good agreement with reports in the literature, Table 6.7 [264]–[266]. A small consistent peak shift in all modes is observed from 1200°C to 1400°C. It is unclear whether this represents small changes in the frequencies of the phonon modes or a systematic error in recording the spectra.

For most samples, no secondary phases were detected, however, at 1100cm^{-1} in samples sintered at 1200°C a mode ascribed to Li_2CO_3 peak is observed (Figure 6.15). This mode disappears in samples annealed at 1400 °C, is thought to be due to contamination from the furnace and is discussed further in 7.3.3.3.

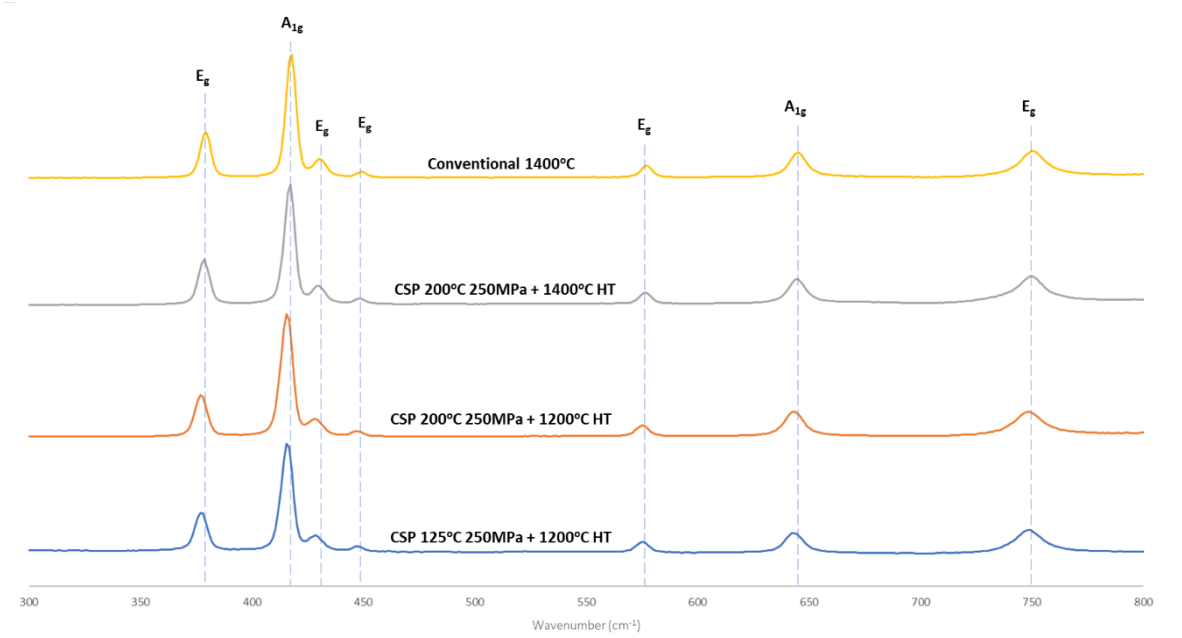

Figure 6.14: Raman spectra comparing α-alumina from conventionally sintered boehmite at 1400°C to cold sintered boehmite heat treated at 1200 and 1400 °C

Table 6.7: Comparison of wavenumbers recorded for each alumina sample compared to the corresponding literature value, as well as the phonon mode they correspond to.

Literature Peak Position[264]–[266] (cm^{-1})	125°C CSP + 1200°C HT (cm^{-1})	200°C CSP + 1200°C HT (cm^{-1})	200°C CSP + 1400°C HT (cm^{-1})	Conventional 1400°C (cm^{-1})	Phonon Mode
379	378	378	378	379	**E_g**
418	415	415	417	417	**A_{1g}**
431	426	426	431	431	**E_g**
478	447	447	448	448	**E_g**
450	575	575	576	576	**E_g**
578	643	643	643	644	**A_{1g}**
750	748	748	750	750	**E_g**

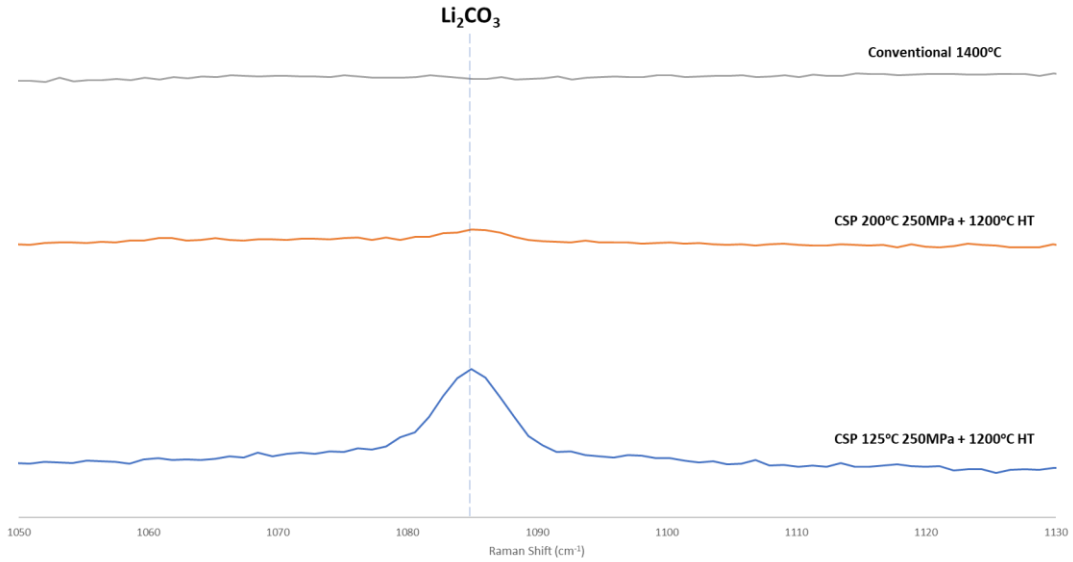

Figure 6.15: Raman spectra showing the presence of suspected Li2CO3 contamination in cold sintered Al_2O_3

Cold sintered samples showed higher densities than conventional, irrespective of the use of a PVA binder (Table 6.8) but the cold sinter temperature appears to have no effect on the final density of α-alumina. Due to cracking when sintered at 1400°C, Archimedes and geometric density measurements were not considered to represent the sintering process at a granular/particulate level. Despite repeating the process multiple times, crack-free pellets could not be obtained. Hence, to better assess the coalescence of particles and the general

sintering process, porosity within the microstructure was determined using Image J software and will be discussed in more detail in section 6.3.3.6.

SEM images of cold sintered pellets showed higher density than conventional samples at 1400^{o}C (without PVA). All pellets exhibited evidence of densification and grain growth with increasing temperature and were homogenous in non-cracked regions. Higher porosity was noted at the surface compared to the interior for some samples.

For cold sintered samples annealed at 1100^{o}C (Figure 16a-b), necking between grains is observed but densification is incomplete, with no section of the sample beyond the intermediate stage [1]. Large networks of pores between grains are seen, but close-packed networks of necked grains are observed. Grain size is difficult to calculate due to continuous necking but is no larger than 300nm. Grain size and morphology are uniform with a mixture of semi-elongated and elongated grains.

In contrast, conventional samples pressed with a PVA binder (Figure 6.17) showed more porosity and necking and coalescence had progressed only to the late-initial/early-intermediate stages [1]. Grain growth however, is greater. Precise grain boundaries are once again difficult to determine due to continuous necking between grains, but the grain diameter is estimated to be between ~0.5-1µm. Imaging of non-PVA samples was impossible due to excessive charging which indicates that the particles are isolated with little interconnection.

*Table 6.8: Percentage density by volume of cold sintered and conventionally sintered boehmite to alpha alumina between 1100-1400°C. Measurements with * were found to be erroneous or unsuitable for conventional measurement, due to structural defects. This is discussed further in 7.3.3.6.*

Sample	Relative Density (%)
CSP Boehmite 125°C 250MPa + 1100°C	55.6
CSP Boehmite 125°C 250MPa + 1200°C	60.5
CSP Boehmite 125°C 250MPa + 1200°C	60.0
CSP Boehmite 125°C 250MPa + 1200°C	64.5
CSP Boehmite 200°C 250MPa + 1200°C	64.3
CSP Boehmite 200°C 250MPa + 1400°C – X	Not measurable due to cracking*
CSP Boehmite 200°C 250MPa + 1400°C – Y	72.4*
CSP Boehmite 200°C 250MPa + 1400°C – Z	70.3*
CSP Boehmite 200°C 250MPa + 1400°C - θ	81.4*
Conventional 1400°C with PVA - A	59.0
Conventional 1400°C with PVA - B	58.0
Conventional 1400°C without PVA	51.9
Conventional 1400°C without PVA	49.6

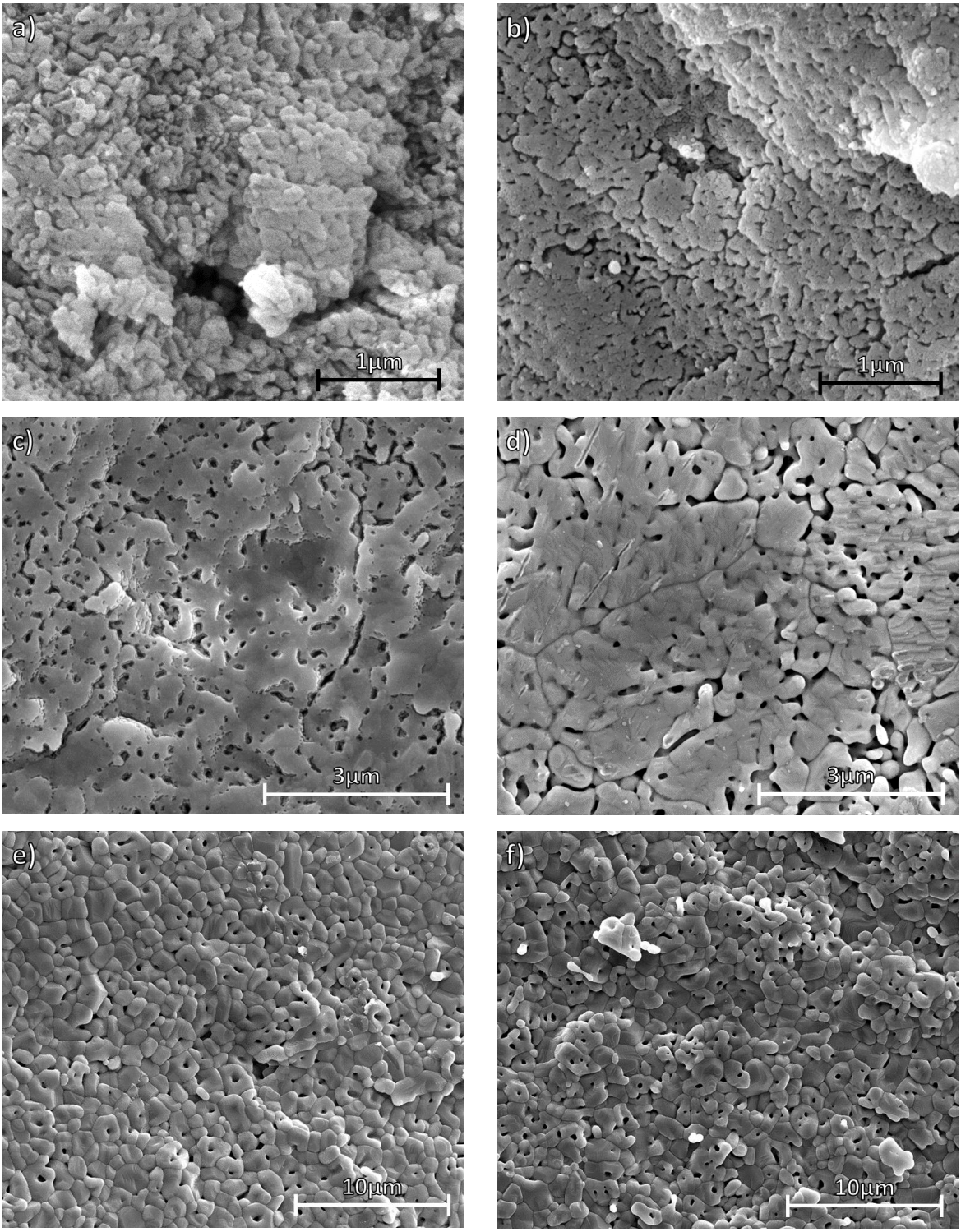

Figure 6.16: SEM images of boehmite, cold sintered and heat treated to form α-alumina. Left column shows fracture surfaces, right column shows top surfaces. a-b) CSP 1100°C HT, c-d) CSP 1200°C HT, e-f) CSP 1400°C HT.

Grain surfaces are decorated with a 'giraffe-skin' pattern which is likely to result from contamination from Li_2CO_3 (and the subsequent formation of $LiAlO_2$) during sintering. Initial evidence of Li_2CO_3 as discussed is observed in Raman data (Figure 6.15). This was also observed in certain areas of cold sintered samples, revealing itself as a network of nano-pores across the surface of grains (Figure 6.18). This is discussed in more detail in 7.3.3.5.

Cold sintered samples heat treated at 1200-1400°C are shown in Figure 6.16c-d & 6.16e-f, respectively. At 1200°C, similar to 1100°C, a continuous network of necked grains is observed, but with higher density, some closed-porosity, closer packing of grains and larger grain size. Grain boundaries are difficult to distinguish, with intra-granular to inter-granular porosity hard to differentiate.

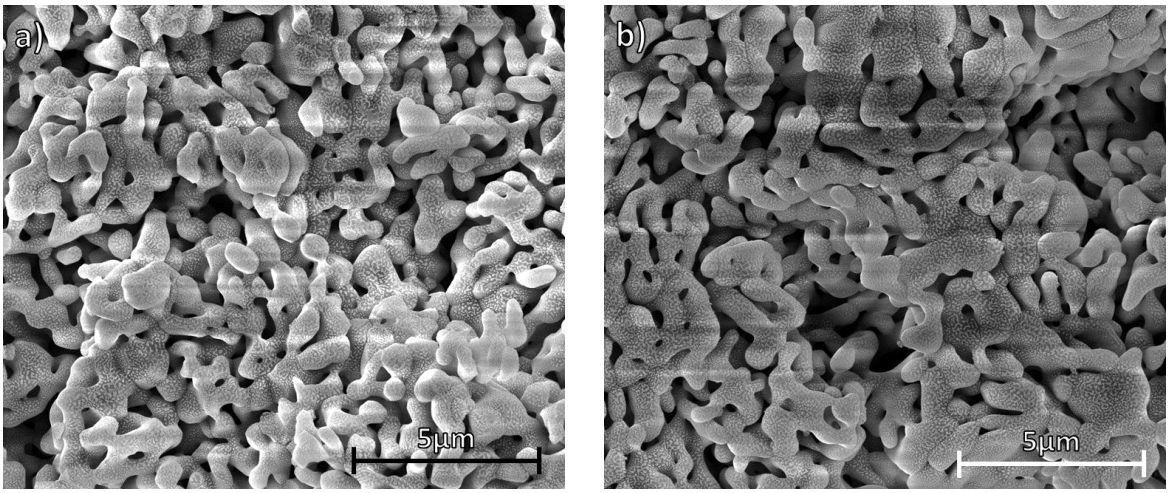

Figure 6.17: SEM images of boehmite conventionally sintered with PVA binder at 1400°C to form α-alumina. a) fracture surface, b) top surfaces

At 1400°C (Figure 6.16e-f), cold sintered samples have a microstructure close to full density. Densely-packed grains are observed, with few inter-granular pores and 120° contact angles at triple junctions (Figure 6.18a). Intra-granular porosity is observed throughout but (Figure 6.18b) with higher volume fractions at the surface. Proposed reasons for this pore formation are discussed in 6.3.3.4. Two grain size populations are observed: a larger 2.5-3µm elongated-like structure, and a smaller, more spherical secondary population of <1µm.

For CSP samples heat treated at 1400°C, there is an obvious discrepancy between the visual density in the SEM images (approaching full density) and the values measured either by the Archimedes or geometric methods, (Table 6.8) which is attributed to the presence of

microcracks caused by shrinkage. A digital density estimate, presented and discussed in 6.3.3.6, was therefore performed using SEM images processed with Image J software.

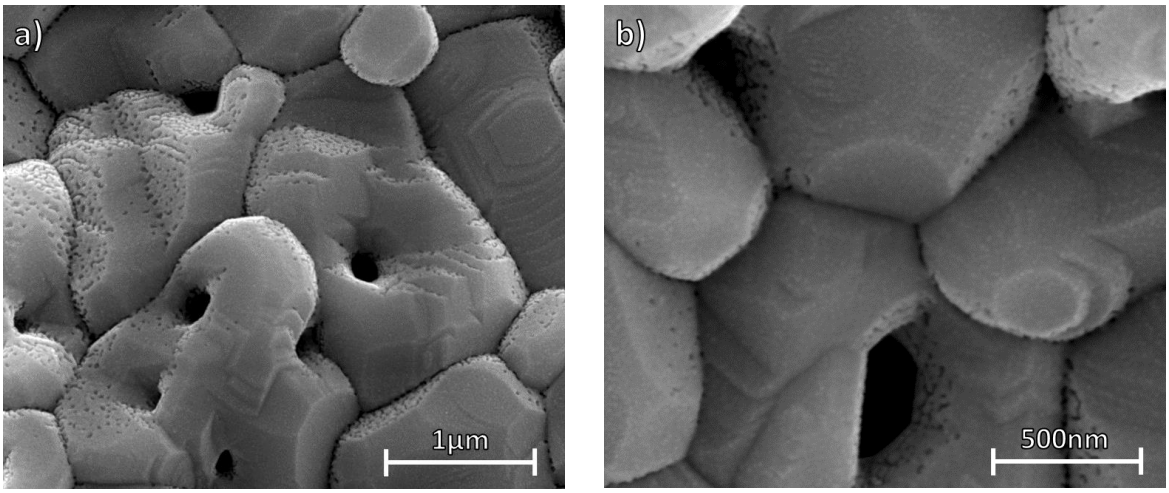

Figure 6.18: SEM images of a sample cold sintered 200°C 250MPa + 1400°C heat treatment. a) image demonstrating the common intra-granular porosity found throughout the samples, b) image demonstrating the triple-point grain contact consistently observed throughout the sample.

6.3.3.3 Cause of Higher Density in Cold-Sintered Material

Densification is significantly greater for the same annealing/sintering temperature in cold sintered compared to conventional samples. However, cold sintering prior to annealing restricts grain growth. The higher green density of boehmite pellets could be assumed as the sole reason for the higher density, as it requires >1600°C to reach full density due to pores that form during the α-alumina transformation [31], [32]. However, green density >40% theoretical has been previously shown only to affect the sintering rate, having no effect on the final densification [267], [268]. Due to the nucleation process inherent in the growth of α-alumina from boehmite, [31], [32], [269] we propose that a secondary effect is responsible for the lower densification temperatures.

Microstructures observed in this study replicate those reported for α-alumina 'seeding';[31], [32], [269] a process whereby small amounts (1-10wt%) of pre-transformed α-or-γ alumina powder are introduced into boehmite. The α-alumina particles act as epitaxial nucleation sites, leading to reduced sintering temperatures. Pach et al. [269] found that without seeding components, natural nuclei will most likely appear in zones of dense hexagonal packing where the coordination number is at its highest. The close packing of the cold sintered boehmite leads to much larger volumes of these favourable nucleation points, as well as more rapid transformation and grain growth. Evidence for this is found from the avoidance of large pores

in conventional samples, as well as the formation of intra-granular pores, often linked to rapid grain growth. A more detailed discussion of intra-granular pore formation is given in 7.3.3.4. Figure 6.19 illustrates the effect close packing will have on transformation.

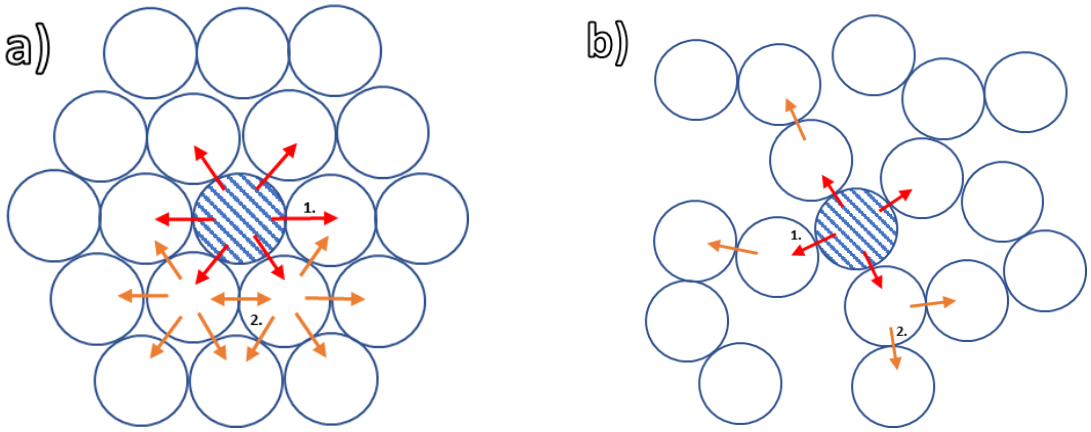

Figure 6.19: Schematics demonstrating the effect of higher green density on a-alumina transformation from a nucleation point (lined circle). a) high green density allowing for faster transformation from good contact. b) low green density with pores affecting transformation rate.

6.3.3.4 Intra-Granular Porosity

Intragranular porosity is observed throughout 1400°C CSP samples, an effect commonly reported by several researchers [270]–[275]. Most often this is caused by the rate of grain-growth being faster than that of densification, leading to the boundary moving past the pore and isolating it in the interior. A diagram of this process is shown in Figure 6.20. This method of intragranular pore formation relates to how pore and grain boundary motion occurs during sintering [1]. The velocity of a pore (v_p) and grain boundary (v_b) respectively can be described by the equations:

$$v_p = M_p F_p \quad \& \quad v_b = M_b F_b \tag{6.6}$$

where M_p and M_b are the pore, and boundary mobility respectively. F_p and F_b describe the driving force that is enacted upon the pore and boundaries, respectively. For intragranular porosity to occur, the following condition must be met in equation 6.7:

$$v_p < v_b \tag{6.7}$$

Once this occurs, pores will detach from the grain boundary migrating into the grain structure becoming an intragranular. Detachment is also closely related to the ratio of pore size to grain size. This can be visualised using a diagram developed by Brook, Figure 6.21. As a consequence, during heat treatment, grain growth takes place significantly faster than pore

shrinkage leading to the continuous zones of intragranular porosity. How this may be controlled through adjustment of processing conditions requires further consideration.

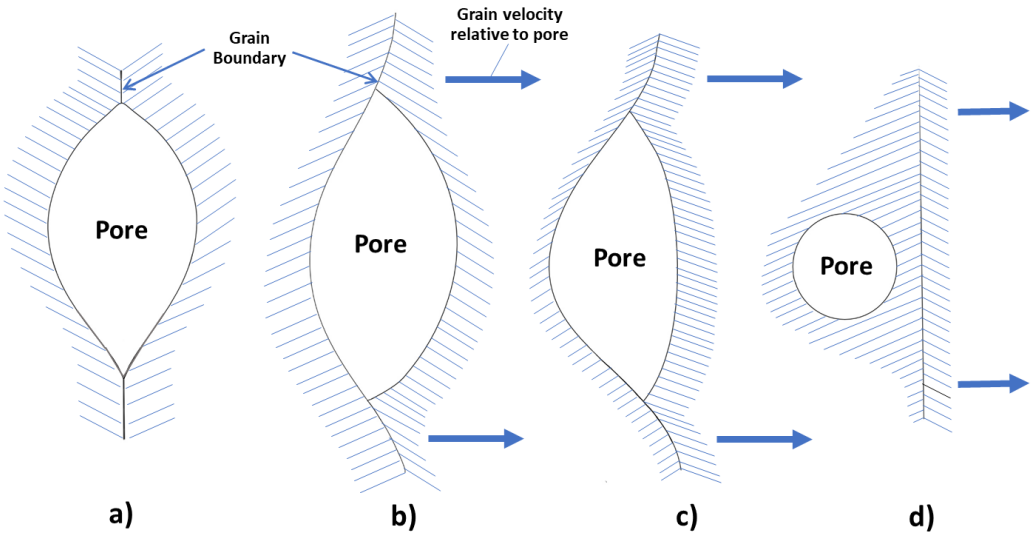

Figure 6.20: Diagram illustrating the process of pore separation from a grain boundary [276]. *a) The pore and grain boundary maintain an even velocity, b-c) As the velocity of the grain boundary exceeds that of the pore, it creates drag across the pore surface causing distortion in its shape. d) Eventually the boundary drag-forces become too high leading to pore breakaway, isolating it in the grain interior. The isolated pore lowers its surface energy by taking on a spherical shape.*

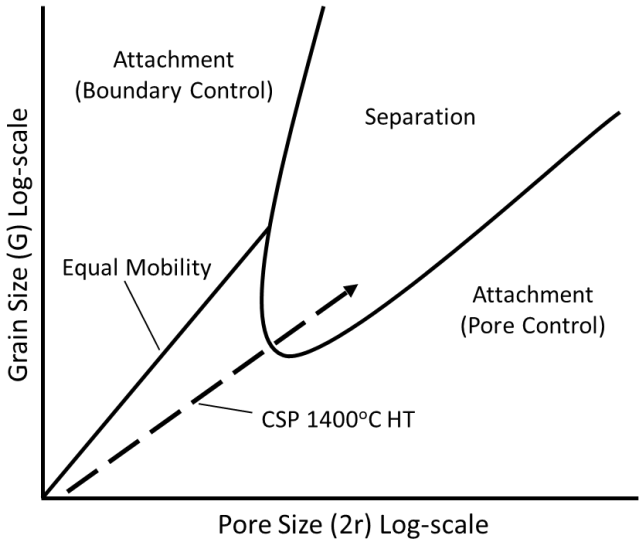

Figure 6.21: Diagram developed by Brook [1], [277]*, visualising the requirements for pore separation to occur related to pore-size. An arrow depicts the approximate path likely followed during the α-alumina formation in cold sintered samples at 1400°C.*

6.3.3.5 Contamination of Samples by Li to Form Suspected $LiAlO_2$

As discussed in 6.3.3.2, SEM images (Figure 6.22) revealed secondary phase on grain surfaces which is related to the presence of a characteristic mode of Li_2CO_3 at ~1090cm^{-1} in Raman spectra (Figure 6.15). This secondary phase appears extensively throughout the grain structure of 1100-1400^oC sintered material. It is noted that the phase within the microstructure is unlikely to be Li_2CO_3 as this decomposes ~725^oC [278] but rather a reaction product with the Al_2O_3 to give $LiAlO_2$. It is proposed that lithium aluminate forms at the grain surface, below the detection limit of XRD but after exposure to air, Li_2CO_3 forms on the surface resulting in a characteristic mode appearing in the Raman spectra. Although EDS analysis (Figure 6.23) revealed carbon throughout all affected samples and may be evidence of lithium carbonate, surface contamination within the SEM cannot be eliminated as a potential source this element. It is noted that the Z of Li is below the detection limit of the EDS detector within the SEM. Thus, the presented Raman spectra (Figure 6.15) is by far the strongest evidence of Li_2CO_3 being present.

Li contamination is thought to have occurred during sintering from a tube contaminated by a previous user. However, a repeat of the 1400^oC cold sintered sample using a fresh uncontaminated tube (Figure 6.24) revealed a similar grain structure with no 'giraffe-skin' patterns decorating the grain surfaces. It is concluded therefore the Li contamination had little or no impact on the sintering of samples. $LiAlO_2$ has a melting temperature > 1600^oC and therefore would not induce a liquid phase assisted densification mechanism [279], [280], [3]. The absence of grain growth or abnormal grain growth is further circumstantial evidence that a there is no liquid phase sintering within the Al_2O_3 samples [1], [3].

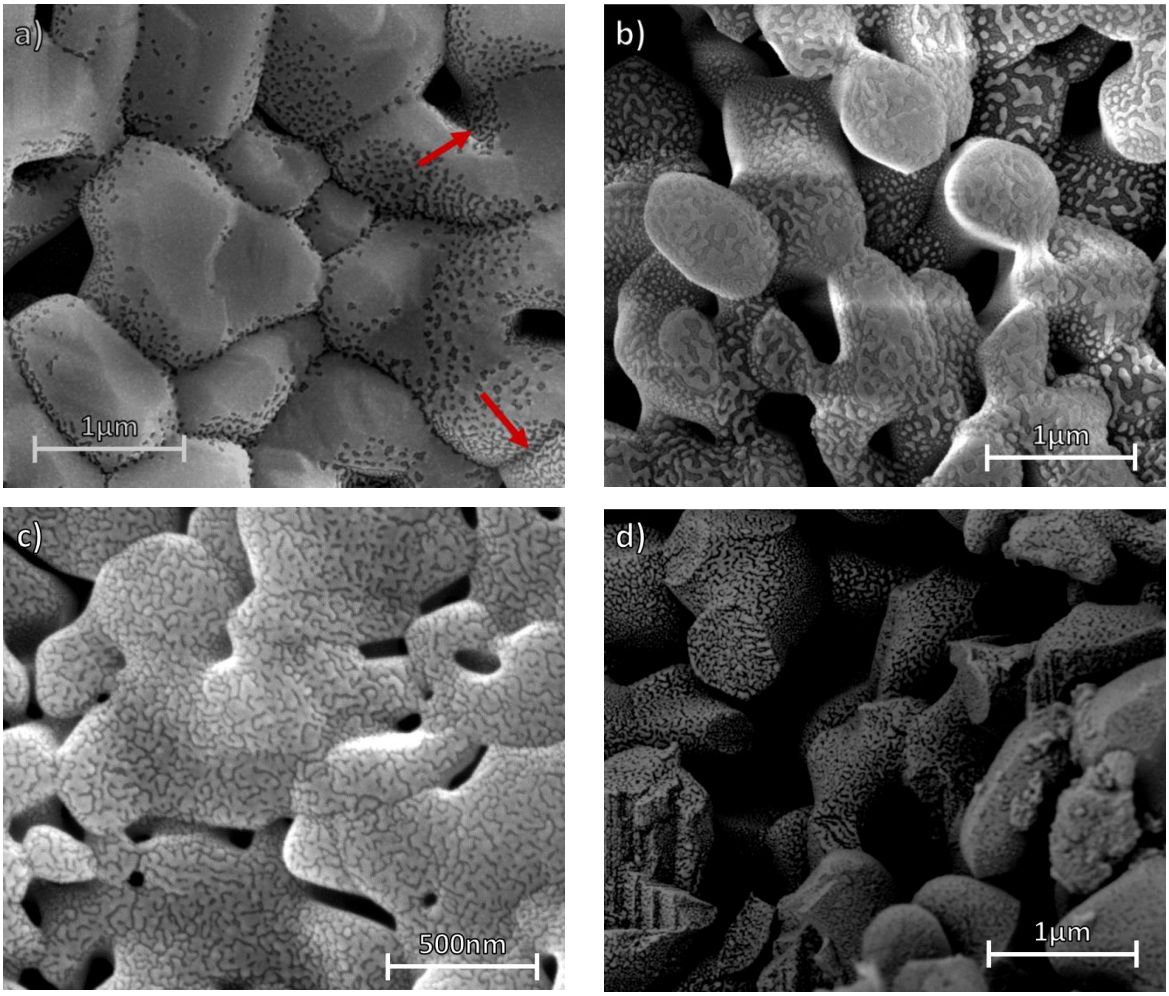

Figure 6.22: SEM Secondary Electron (a-c), Backscatter (d) showing visible evidence of suspected Li_2CO_3 contamination of cold sintered + post-sintering (a - 1400°C , c – 1200°C , d – 1200°C) and conventionally sintered (b - 1400°C) material due to the "giraffe skin"-like texture on grain surfaces.

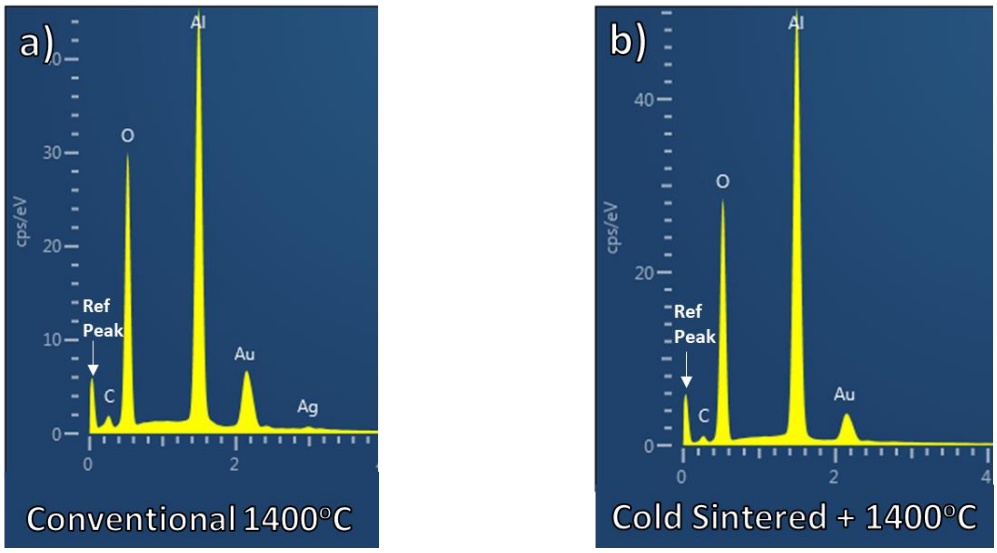

Figure 6.23: EDS spectra of (a) conventional 1400°C and (b) cold sintered + 1400°C HT material. Carbon is detected thought to be indication of a Li_2CO_3 phase. Li was not detected but does not discount its presence. Au and Ag detected are coating elements for SEM analysis. No other secondary elements were detected.

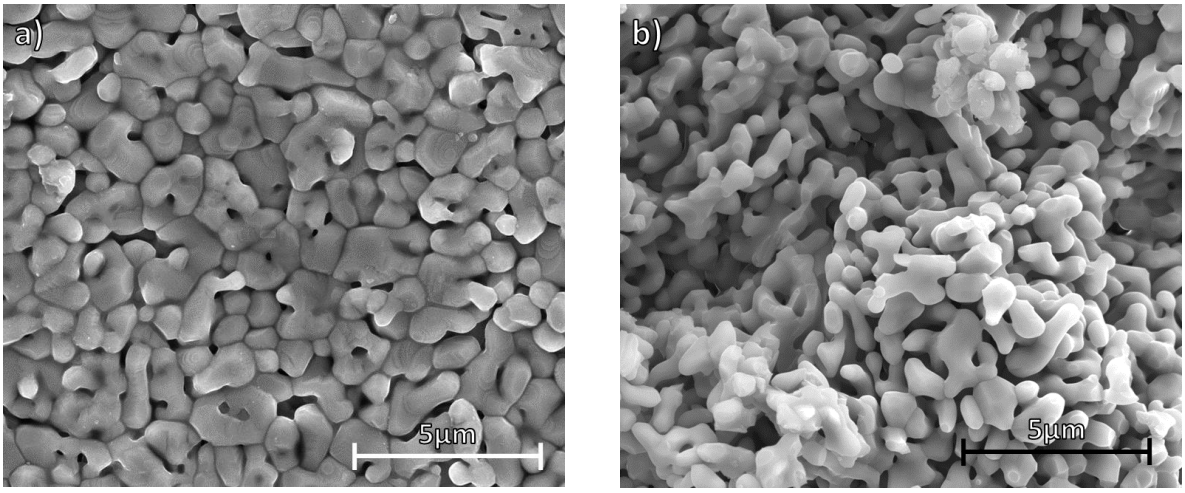

Figure 6.24: Contamination free repeats of a) Cold sintered (200°C + 250MPa) + post-sinter (1400°C), and b) conventionally sintered (1400°C) material showing Li contamination has had no reportable effect on results

6.3.3.6 Using SEM-BSE Imaging to Estimate Density

Although microcracking of high purity α Al_2O_3 has been resolved in industry, insufficient time was available to further research this issue for 1400°C CSP samples. A visual inspection of the microstructure in the SEM images suggests that the density is far greater than measured by either the Archimedes or geometric methods. Hence, an estimate of the sintered density between microcracks was obtained using Image J software applied to SEM images.

6.3.3.6.1 Measurement Process

Images were chosen that were as flat as possible and best represented the microstructure. These images were processed using ImageJ using the 'Threshold' imaging tool, which uses contrast to detect variation (Figure 6.25). Using differences in contrast from pores to grains, the total area of the pores was measured, and percentage density was calculated by comparison to the total area of the image:

$$\left(\frac{A_{total}-A_{pores}}{A_{total}}\right)x100 \qquad (6.8)$$

where A_{total} is the total area of the image and A_{pores} is the total area of the measured pores. An average density was then taken from images of the bulk and surfaces. As it is not clear how deep surface porosity travels into the bulk, a simple average of bulk and surface would be inappropriate. Thus, these numbers are presented separately.

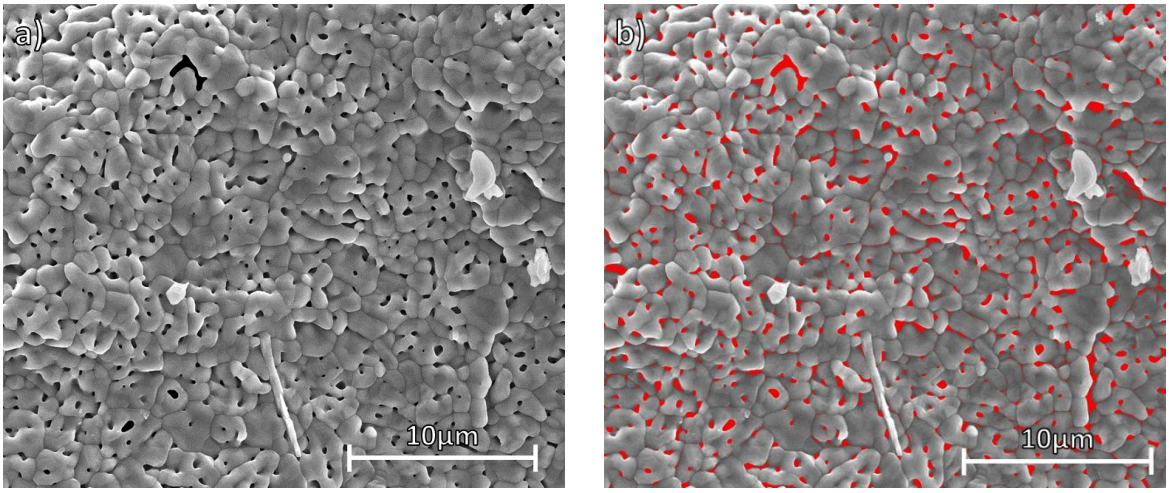

Figure 6.25: Images showing before (a) and after (b) pores have been highlighted in the ImageJ software

To establish the accuracy of this technique, images from Bae & Baik [275] were utilised. Their images are from α alumina samples with a known density. Several of their presented images were analysed by the same method and compared against reported densities (Figure 6.26). Because of contrast issues with these test images, the centres of pores were painted white in editing software to allow for easier detection.

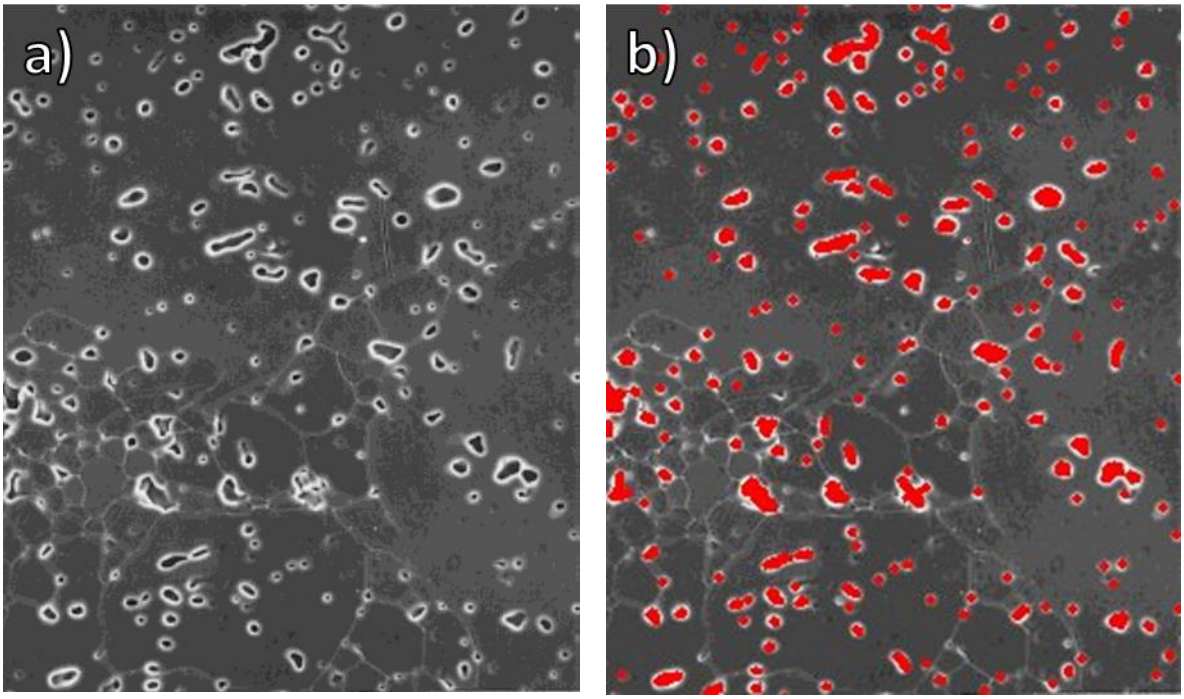

Figure 6.26: Images of conventionally sintered alumina presented in work by Bae & Baik [275] *used to test density estimation from pore size measurement. a) the original image, b) image (a) after pores have been highlighted by the ImageJ software.*

6.3.3.6.2 Assumptions and Limitations

This estimation method assumes that non-pore areas are 100% dense and pores are cylindrical and not spherical. This can lead to an overestimation of porosity, as a cylinder has an ~50% larger volume than a sphere for the same diameter. Defects not visible in the images are neglected and the visible pore diameter is taken as its maximum. Perspective distortions from non-flat samples also lead to errors as pores viewed at different angles have distorted diameters. The method also assumes the samples are homogenous with accuracy increased by taking multiple measurements of both bulk and surface.

As measurements are based on a contrast imaging technique, there are several other sources of error. Definition of pore-edges is challenging, especially where soft-sloped edges are present and pores with significant boundary charging could lead to overestimation of pore size. Unintended variation in contrast across an image could also cause problems, with artifacts occurring where no pore is present, leading to an underestimation of pore density.

6.3.3.6.3 Findings

Initial tests of the technique against published literature proved successful (Table 6.9), with measured values falling within ~4% of those reported and the technique was thus considered suitable to give a general estimate of density.

Table 6.9: Table comparing densities quoted in work by Bae & Baik [275] *and estimated densities using imaging area method*

Literature Sample [275]	**Quoted Density (%)**	**Image Analysis Density (%)**	**Difference (%)**
300ppm Si (A) NGG	~92	~91	1
300ppm Si (B) AGG	~94	~94	0
500ppm (C) NGG	~90	~94	4
1000ppm (F) AGG	~91	~95	4

Of the 4 cold-sintered samples heat treated at 1400°C, only 3 (X, Z, θ; Table 6.8) were found suitable for measurement. Sample Y was found unsuitable due to poorly defined contrast and the angle at which images had been taken which distorted pore sizes. Measured samples showed densities >90% theoretical, significantly above those taken by volume. Density was lowest at sample surfaces where more porosity was observed, however, this was still >90%. Sample X showed the highest density with both surface and bulk showing similar densities of ~97%. Sample Z and the repeat Sample θ showed lower average densities of 96% and 95%

bulk, and 90% and 92% top surface density respectively. Measurements remained consistent across images with densities falling within 1% of each other. Outliers only occurred when unique surface features were present, such as an unusually large pore. Estimated densities using the ImageJ software are shown in Table 6.10 and are much higher than those obtained from equivalent geometric methods. Despite the caveats discussed above concerning the accuracy of this method, the estimated densities based on the SEM images warrant greater focus on the use cold sintering of boehmite as a precursor step in the fabrication of α alumina and could, if the results are reproduced by other workers, represent a considerable energy saving over conventional processing.

Table 6.10: Table comparing the original measured densities of samples vs the estimated densities from SEM imaging. Note, an original density for X was not possible due to significant shrinkage cracking across the sample.

Sample (CSP 1400°C HT)	**Original Measured Density (%)**	**Estimated Surface Density (%)**	**Estimated Bulk Density (%)**
X	N/A	97.3	96.7
Z	70.3	90.2	95.6
θ	81.4	91.6	94.7

6.3.3.7 Mechanical Properties

All samples (Figure 6.27 & Table 6.11) showed similar stiffness, with conventional (1400 °C) having a Young's modulus within 2GPa of cold sintered (annealed at 1200 °C) samples. 1400°C cold sintered samples were not measured as these suffered from microcracking on cooling. The value of Young's modulus in α alumina relates to necking between grains which increases in the initial stages of sintering [259].

Similar to the γ-alumina results (section 6.3.2.3), the crushing strength of cold sintered showed significant improvement over conventional pellets. Cold sintered pellets had CS 2-2.5x higher than conventional with PVA binder, and ~7-8x higher than conventionally sintered samples without binder. The higher density of the cold sintered pellets will contribute to this improvement but alone is unlikely to cause such a dramatic increase in strength, as measured densities of 1200°C CSP and conventional PVA pellets fall within 5% of each other. Therefore, it is proposed that the increase in crushing strength is due to the smaller grain and pore size of the cold sintered pellets resulting in fewer flaws to initiate failure [186].

One cold sintered sample partially failed before continuing to resist compression until total further failure. As with cold sintered γ-alumina (section 6.3.2.3), CS is taken at the first fracture point since there was a significant change in sample diameter after this, making calculation inaccurate. It is interesting to note however, that resistance to compression continued after partial failure with a second elastic region before final collapse. Just as discussed in 6.3.2.3, comparison to literature is once again difficult due to the use of non-standard pellet aspect ratio, pellet sizes, non-standard testing conditions, and very limited sample numbers.

Table 6.11: Table comparing the Young's Modulus and Crushing Strength of 1200°C Cold Sintered Material vs Conventional 1400°C

Sample	E (GPa)	CS (GPa)
CSP 125°C 250MPa + 1200°C B	14.85	8.20
CSP 125°C 250MPa + 1200°C C	14.80	7.37
Conventional with PVA 1400°C	16.06	2.98
Conventional 1400°C	12.56	0.94

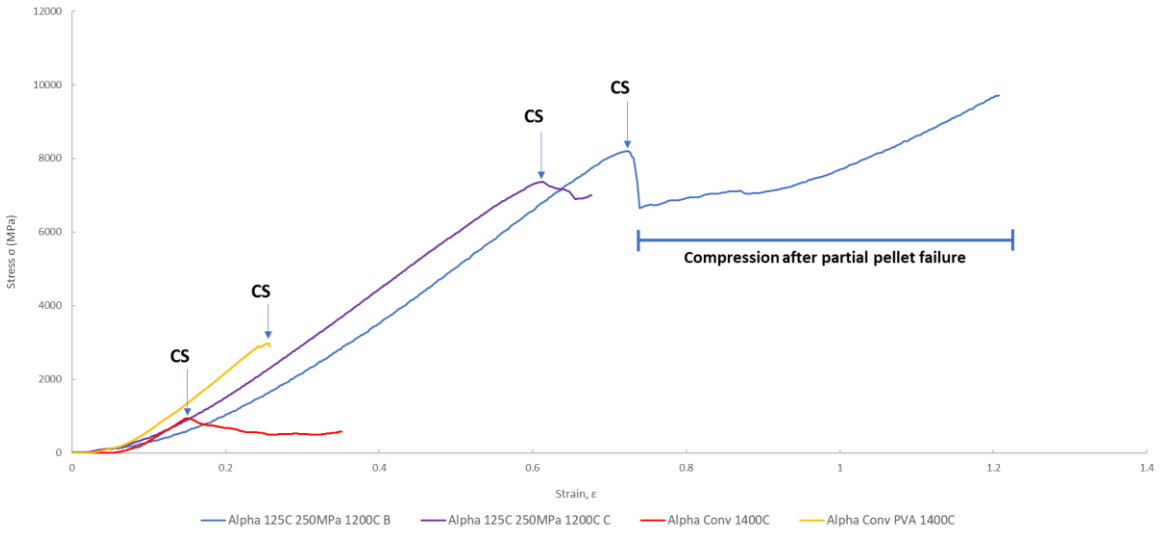

Figure 6.27: Graph illustrating compression tests comparing α-alumina pellets formed from either boehmite conventionally sintered at 1400°C, or cold sintered boehmite heat treated 1200°C heat treatment.

6.4 Conclusions & Future Work

6.4.1 Conclusions

In this chapter cold sintering has been utilised to assist the densification of both γ-alumina, and α-alumina from pseudo-boehmite. No direct comparison to any published literature is known.

6.4.1.1 Using cold sintering to assist with the densification of γ-alumina

The sintering of γ-alumina is known to be difficult due to the low temperature at which it forms and the fact it is stable only to temperatures significantly below that required for densification. Consequently, γ-alumina catalyst/catalyst supports have poor mechanical properties [261] which limits their usage. Using cold sintering as a supporting manufacturing method may broaden applications of γ-alumina, and improve the reliability of existing technology. A previously published study [165] has demonstrated the ability to use cold sintering to help densify γ-alumina from hydroxide precursors. Although samples were translucent, good mechanical properties of the final γ-alumina were difficult to obtain, with the authors stabilised pellets through adjusting the ratio of a glass-ceramic to ceramic phase. Work reported in this chapter simplifies and improves on this process, particularly with respect to mechanical stability with the use of a small amount of PVA binder. More work however, is needed to fully understand the properties of cold sintered γ-alumina and further optimisation of the process is required. These future steps are described in 6.4.2.

6.4.1.2 Consequences of using Cold Sintering to Assist with the Densification of α-Alumina

Lowering the sintering temperatures of α-alumina has been demonstrated many times via the uses of dopants,[99], [281] nano-powders,[282], [283] and other techniques [246], [284]. Utilising cold sintering is the newest in this list. However, undoped boehmite (without the use of seeding [31], [32], [274], [285]) has always required temperatures of >1600^{o}C for densification due to the formation of porosity. Cold sintering inhibits the formation of porosity, allowing dense microstructures at temperatures similar to seeded structures. However, more work is needed to fully understand and optimise this process, in part due to the unfortunate contamination that was only discovered in the final weeks of the project.

6.4.2 Future Work

*6.4.*2.1 *Cold sintering of Boehmite*

- Further optimise the sintering process to lower sintering temperature and reduce required pressure to <100MPa, making the process more attractive for commercial applications
- Repeat work to develop a better understanding of the cold sintering mechanism and to ensure reproducibility of the process

6.4.2.2 *Densification of γ-Alumina*

- Perform more mechanical testing with samples of standard geometry to create a statistically meaningful data set.
- Optimise the densification process with different pellet geometries to determine if fabrication to net shape is feasible for scale-up.

*6.4.*2.3 *Densification of α-alumina*

- Repeat works free of contamination, to confirm presented results. It is particularly important to establish a method of cooling cold sintered samples, annealed at 1400^{o}C to avoid microcracking. In this manner, the true E and CS of cold sinter/annealed α alumina can be determined.
- Investigate if sintering temperature may be further lowered, possibly by seeding a distribution of nano α alumina in the boehmite prior to cold sintering. If successful, this may yield a high purity nano-structured α alumina at ~1400 ^{o}C, a considerable saving in energy and furnace costs with respect to conventional processing.
- The use of boehmite in the cold sintering of refractory bricks based on Al_2O_3-SiO_2 to achieve suitable handling characteristics prior to shipping. This is normally achieved using a pre-sinter step at high temperature.

The whole process of cold sintering boehmite and its transformation to γ and α alumina requires extensive study using advanced analytical electron microscopy to better understand the mechanisms of densification and the transition between polymorphs.

Chapter 7 – The Capabilities and Challenges of Cold Sintering

7.1 Introduction

Cold sintering is a promising new sintering technique, which opens-up new opportunities in advanced ceramics previously not attainable. As discussed in depth in Chapter 2, it has a number of advantages including significant energy savings and ability to co-sinter previously incompatible materials. However, it is a technique still in its infancy, with a significant amount of work is still taking place to understand its capabilities and limitations, and before upscaling of the process can be fully realised, there are still a number of key issues that must be solved.

This Chapter briefly discusses the advantages of cold sintering, before briefly covering some of the important issues still to be solved to allow successful upscaling and adoption by industry.

7.2 The Capabilities of Cold Sintering Demonstrated in these Works

7.2.1 Densification while Material Maintaining a Very Small Grain Size

Densifying ZnO whilst maintaining grain sizes of <100nm has previously been challenging [286]. Cold sintering of ZnO nano-powder at lower temperatures has shown that maintaining a small grain size and narrow grain size distribution is possible. This could allow for easier methods of producing dense nano-grain material.

7.2.2 Densification of Doped ZnO is Possible

These works showed that cold sintering of doped material is possible and, while several challenges arose with the addition of Ga that need to be overcome, cold sintered ZnO for electronic applications is possible with the caveat that conductivity would need to be optimised to match existing materials and products.

7.2.3 Development of Transparent Polymer-Ceramic Composites

One of the key requirements for a good TCO material is high transparency, which was critical to demonstrate if cold sintering is to have potential for use as TCO. This was clearly shown in this work, which not only demonstrated transparency but that sintering directly onto a polymer surface was possible. The ability to create transparent thick-layer sheets directly

sintered onto a polymer surface is a capability almost entirely unique to cold sintering and is a clear demonstration of possible new ceramic coating methods.

7.2.4 Cold Sintering Allows for Significantly Stronger γ-Alumina Manufacture

As discussed in Chapter 6, densification of γ-alumina from boehmite is often a serious issue due to the small sintering window in which it remains stable, well below temperatures needed for the high diffusion rates in solid state sintering. Conventional sintering therefore, leads to a material that is fragile and difficult fabricate. Cold sintering has demonstrated much higher density γ-alumina, with preliminary tests showing crushing strength ~5-6x higher than conventional.

7.2.5 Lower Temperature Sintering of α-Alumina with Cheap and Abundant Starting Material

The ability to achieve high density α-alumina conventionally at temperatures <1500^{o}C has been previously achieved. However, as discussed, it requires either the use of dopants [99], [281], highly specialised nano-powders [282], [283], or low yield specialist techniques [246], [284].

The process developed using cold sintering in these works has shown that near full densification can be achieved at 1400^{o}C (according to microstructural analysis using ImageJ software) with significantly cheaper and more abundant starting material. With further process optimisation, this temperature could be lowered further.

7.3 Current Challenges Preventing Process Upscaling

7.3.1 Factors that Affect Sintered Material Quality

7.3.1.1 Environmental Conditions

To date, published literature has not assessed systematically the effects of the environment (lab temperature and humidity) on the ability to cold sinter various materials. However, as briefly mentioned in section 2.9, environmental conditions have a significant impact on sintering results.

While never quantitatively investigated during this project, lab temperature/humidity were considered the primary cause of inconsistent results and unsuccessful sintering runs during the early-mid stages of the project. Cold sintering presses were originally positioned in an uncontrolled laboratory environment (temperature/humidity). This especially proved an

issue in prolonged spells of high ambient temperature, during which no ZnO samples were successfully cold sintered. This issue was resolved when the cold sinter press was transferred to the more controlled environment of a fume-hood leading to consistent and repeatable results.

This problem has wider implications for potential upscaling, due to extra restrictions it places on machinery designed for large scale manufacture. More conventional sintering processes are less sensitive to ambient temperature/humidity due to their high temperatures. The possible requirement for a more controlled manufacturing environment for cold sintering will likely incur extra setup and maintenance costs, either to control the ambient conditions around the machinery or require the design of a cold-sintering press where these conditions are controlled internally.

7.3.1.2 Powder Quality

As clearly demonstrated in Chapter 4, as with other sintering techniques, powder quality has a significant effect on density and microstructure [1]. However, the complex mechanical and chemical processes occurring mean [14], [15] [11], [13], that more in-depth analysis is required to sufficiently understand how powder size, size-distribution, and morphology effect cold sintering. For example, certain conditions result in very large grain growth in ZnO with only minor changes retaining a nano-crystalline microstructure.

7.3.1.3 Solvent Choice and Secondary Phase Removal

The solvent is one of the most critical aspects to achieving a high-quality outcome in cold sintering. It is not only important to choose a solvent in which partial dissolution is achieved, but one that does not produce unwanted secondary phases [16].

Water and weak acids such as acetic acid have proven to work in many cases [13]. However, as demonstrated early on and discussed in Chapter 2, materials like $BaTiO_3$ or $SrTiO_3$ suffer from incongruent dissolution and require more complex solvent and processing solutions [159][287]. This increase in complexity for some materials may reduce the attractiveness of cold sintering as a commercial technique.

In cases like ZnO, the solvent leads to a residual secondary phase that must be removed by heat treatment (>400 ^{o}C), and some of the advantages of cold sintering are lost, e.g. compatibility with polymers. Chapter 5 demonstrated transparent layers of ZnO on Kapton

and shows the key advantage of cold sintering but secondary acetate removal, if required, would likely prove a significant issue in exploitation.

7.3.1.4 Solvent Effects on Grain Structure

As shown by previous literature [15], [286], and explored in this study, the liquid phase has a significant effect on grain boundaries, where the proposed defect core-shell is produced. The full extent of its effect on electrical properties of ZnO is not known. Jing et al. [194] showed significantly increased conductivity in cold sintered ZnO once heat treated in argon, a much better understanding of the apparent defect structures cold sintering produces is required to attain conductivities suitable commercial applications.

7.3.1.5 Heating Rate and Cooling Rate Effects

For ZnO (including these works), an broad range of heating rates (~5-40^{o}C/min) has been reported [15]–[17], [174], [194], [201]. However, little attention has been paid to its influence on grain growth, densification, solvent removal and properties. In all other sintering techniques heating rate is controlled with great care, however the same has not been so with cold sintering. Current literature also makes little mention of cooling rates. Although successful densification of ZnO has been achieved with rapid cooling using a fan, ZnO's electrical properties are affected by cooling rate [288]. Cooling rate also affects the mechanical stability of cold sintered boehmite samples, as described by Beauvoir and Estournès [165].

While generally laborious, this kind of groundwork is essential if cold sintering is to become a commercially viable and adopted sintering technique, as it is the critical information that industry will require for large scale processing.

7.3.1.6 Effects and Interactions of Impurities/Dopants

Dopants and impurities within ceramic materials are well known to inhibit grain growth and in these works the same effects have shown to be true in cold sintering of GZO, with higher temperatures required to produce densification and grain growth. In materials where higher temperatures are required, the ultra-low temperature co-sintering compatibility with, e.g, polymers may be lost.

7.3.1.7 Sample Size Effects

The effect of sample size also requires more investigation as, to date, nearly all cold sintering papers focus on the manufacture of small pellets or thick/thin layer materials. Only recent

published works by Bang et al. [174] have looked at scaling up and its effects. Achieving a homogenous microstructure at a larger scale proved challenging due to suspected variations in liquid phase evaporation rates.

Total removal of the solvent phase may also prove problematic for thicker materials with the significant increase in diffusion path lengths. The same issue would occur in systems that require a residual phase removal step.

7.3.2 Longevity of Mixed Material

Works to date have assumed that sintering is carried out directly after mixing. If mixed powder were found to have a reasonable 'shelf-life' in ambient conditions when correctly stored, it could significantly increase the flexibility of the cold sintering process at an industrial scale. This may allow for outsourcing of pre-prepared powders for cold sintering performed by specialist manufactures, instead of the end-user having to invest in equipment and expertise mixing powders on site. This could facilitate reduction in costs and engender less risk to the end user.

7.3.3 Lowering of Current Required Pressures

Current pressures of cold sintering are typically >100MPa, with some ZnO at >700MPa [201]. While these pressures are achievable with small 10mm pellets and hand-presses, any increase in surface area requires increase force to achieve the same pressure. Larger industrial components will therefore require pressures of <100MPa. Some studies have attempted to solve this issue directly [174], with others adopting techniques such as die sealing to lower the required pressure [16]. However, this is one of the current primary barriers to upscaling.

7.3.4 Current Lack of Ideal Solvent Ratio Calculation Methods

The ideal solvent:powder ratio is attained empirically, sometimes requiring many trials to achieve the best result. The ratios reported in the literature also vary significantly. For ZnO a broad range of solvent volumes is quoted of from 5-40wt% [15], [16], [19], [21], [167], [201], and in Chapters 4 and 5, a higher volume of solvent was required to cold sinter nano-powders.

Since the solvent:powder ratio relates to total surface area of the powder, development of reliable calculation methods, similar to slurry calculations in tape-casting, would be of great assistance to the upscaling. However, significantly more work is needed to fully understand

the role of the liquid phase, how it's interaction changes at scale, and how these estimations would change with solvent and material.

7.3.5 Grain Size Limitations

Cold sintering to date in materials like ZnO has often utilised nano to sub-micron powders to achieve densification, with grain sizes often quoted as remaining similar to the starting powder to grains of a couple of microns [12], [13]. However, for applications where very large grain sizes are essential, other sintering techniques will likely be needed. Understanding the range of achievable grain sizes for each material will help apply the process to the correct applications.

7.3.6 Understanding the Limitations of the Cold Sintering Process

During the continued development of the cold sintering process, its limitations must be continuously considered if adoption by industry is to be achieved successfully, making sure that the process is not oversold. This not only maximises the efficiency of the research conducted, but also maintains realistic expectations of the process, as wasted investment from oversold promises has too often led lost time and revenue.

7.4 Summary

There are many challenges that still to be solved to achieve full scale-up of the cold sintering process. However, with the significant number of advantages and unique capabilities of the process discovered thus-far, investment into solving these problems is worthwhile with some applications such the fabrication of γ alumina showing great promise.

Chapter 8 Conclusions

Conventional sintering techniques often require temperatures of >1000°C to achieve full densification. These high temperatures lead to high energy usage and significant limitations on materials that may be co-sintered. Cold sintering is a new ultra-low temperature (<300°C) sintering technique that tackles both of these issues, making use of an evaporating solvent phase and pressure to achieve densification. This technique may have commercial potential, but there are significant barriers that must be overcome to allow for upscaling of the process.

8.1 Zinc Oxide for Applications in Transparent Conducting Oxides (TCOs)

TCOs are an important conducting part of many components from LCDs to photovoltaic cells. The most popular TCO, Indium-Tin Oxide, needs replacing due to environmental, cost, and health concerns. Doped ZnO is discussed as being a possible low cost, non-toxic replacement for ITO. 3 separate studies were conducted on ZnO to determine if cold sintering could be a useful tool in the manufacture of ZnO TCOs.

8.1.1 Effect of Powder Size on Cold Sintering (Chapter 4)

Results from cZnO agree closely with current literature, with densities of >90% achieved for all samples. nZnO proved more difficult to densify with all samples ≥200°C achieving >90% density. Temperature had the greatest effect on grain growth, and grain growth distribution, but at 300°C increase in pressure had dramatic effect on grain size distribution particularly on nZnO (105 to 1119nm and 176 to 538nm for nZnO and cZnO, respectively). Grain growth was greater in the radial direction at the surface due to restricted sintering. For cZnO, grains were pseudo-spherical with some elongated grains. nZnO however showed a dominant pseudospherical morphology at lower temperatures which became elongated at higher temperatures and pressures. Cold sintered microstructures were very different to conventionally sintered, with grain sizes orders of magnitude smaller. Abnormal grain growth was observed in some samples but its exact cause requires further investigation.

Raman spectroscopy revealed a secondary residual acetate phase present at all temperatures, in contradiction to some literature that reports its total removal at 300°C. Samples post-heat treated at 500°C however, showed no Raman modes associated with the acetate phase.

Preliminary impedance analysis of cold sintered nZnO indicated the presence of a defect (possibly H^+) core-shell microstructure consisting of a highly defective outer shell, and a more conventional core. Heat treatment in air increased conductivity by an order of magnitude from ~$5x10^{-9}$ to ~$5x10^{-8}$ Sm^{-1}.

8.1.2 Effect of 2% Ga doping on ability to cold sinter ZnO (Chapter 4)

The effects of 2% Ga introduction on ability to cold sinter ZnO with 1.0 molar acetic acid at between 125°C-300°C and 190MPa-375MPa were investigated. $Ga_{0.2}Zn_{0.98}O$ nano-powder (25-40nm) showed to be more difficult to sinter than undoped powder due to well-known grain growth inhibition mechanism caused by Ga.

Temperatures below 200°C did not densify, and notable grain growth not occurring until 300°C. All microstructures at 300°C showed uncontrolled grain growth, with a dual-population of fewer (up to 400nm) larger grains, and smaller (~20nm) nanograin structure at grain boundaries. Like undoped material, at 300°C, grain size distribution exaggerated at pressure. At very high pressures (500-625Mpa) very large abnormal micron sized grains could be observed 2.5-4µm in length.

Raman spectroscopy confirmed the incorporation of Ga into the crystal structure, as well as the expected secondary zinc acetate phase.

Concentrations of zinc gallate were significantly lower in cold sintered material compared conventional. EPMA analysis revealed a good distribution of Ga throughout the crystal, but detected some small zones with high Ga concentration which may indicate the presence of $ZnGa_2O_4$.

8.1.3 Transparent Thick-Layer ZnO-Kapton® Polymer Composites (Chapter 5)

The ability to directly cold sinter transparent thick-layers of ZnO to Kapton® polymer sheet was investigated, and a proof-of-concept process developed.

Successfully sintered samples showed optical transparency that decreased with increasing number of layers. This coincided with a decrease in grain size and density. No secondary phase/interactions were observed between the Kapton and ZnO, but a secondary acetate phase was observed. Adhesion between the ZnO and Kapton varied significantly between sample from very good to poor. Reproducibility of good adhesion proved challenging. Due to the sandwich-like layered arrangement of the samples, acetate removal would likely prove

difficult, thus a better solvent phase may have to be found. Based on the GZO results from Chapter 4, sintering at 200°C may prove difficult if TCO conductivities are desired.

8.2 Cold Sintering of Boehmite to Improve Final Properties of γ-Alumina, and Lowering the Sintering Temperature of α-Alumina (Chapter 6)

γ-alumina is a polymorph with important applications as a catalyst support, and α-alumina has broad applications across industry. However, the stability window (500-800°C) of γ-alumina falls well below conventional sintering temperatures for alumina leading to poor-mechanical properties. α-alumina on the other hand requires high sintering temperatures 1500-1900°C to achieve full densification. Lowering its sintering temperature is possible but requires either doping or the use of expensive nano-powders.

8.2.1 Cold sintering of Boehmite

Cold sintering of boehmite proved difficult due to its layered structure leading to mechanical failure and cracking. This was solved with the addition of a 5wt% PVA binder solution, but samples lost translucency. Strong adhesion to die pieces sometimes occurred. No sign of secondary phases or significant grain growth was observed.

8.2.2 Heat treatment of Cold Sintered Boehmite to Form γ-Alumina

γ-alumina from cold sintered boehmite was produced with a 500°C heat treatment. Mechanical properties of cold sintered materials were superior to conventional with compressive strength ~12-40x and a Young's modulus ~1.7-2.5x higher. Densities were ~13-20% higher than conventional at ~52-53% and SEM images showed well densified regions surrounding pores.

8.2.3 Heat Treatment of Cold Sintered Boehmite to Form α-alumina

Cold sintered boehmite pellets heat treated between 1100-1400°C were compared with conventional sintered ceramics at 1400°C. Cold sintered material showed evidence of grain growth and necking as low as 1100°C, in contrast to conventionally sintered ceramics at 1400°C. At 1400°C, SEM images of cold sintered samples showed fully formed grains with ~120° triple point contacts with a density estimated from the microstructure of >90%. Intra-granular porosity was evident throughout, linked to rapid grain growth. However, microcracking was present in the 1400°C cold sintered samples. Mechanical properties of

1200°C cold sintered samples were found to be ~2.5-8.7x higher than conventional, but with a similar Young's modulus.

8.3 General Conclusions

While this project is only a part of the puzzle in developing commercially scalable cold sintered products, it has demonstrated some of the unique advantages that cold sintering has to offer, e.g. cold sintering has shown it may be an excellent method of maintaining a very small grain size whilst achieving high densities. However, doping inhibits densification and causes an inhomogeneous microstructure in dense pellets. This must be solved before cold sintered doped ZnO can considered for TCOs and other high-conductivity applications. While significantly more work is required, the fabrication of transparent ZnO on Kapton demonstrates the significant co-sintering advantages of the process.

The cold sintering of boehmite showed perhaps the biggest potential for applications during this project. The resulting γ-alumina pellets had better mechanical properties than those commercially available. The decrease in sintering temperature from cold sintered boehmite also points to potential energy/cost savings in the manufacture of high purity dense Al_2O_3.

Chapter 9 Future Work

While discussed at the end of each chapter. The suggested future work is reiterated below:

9.1 The Cold Sintering of ZnO and $Ga_{0.02}Zn_{0.98}O$ (Chapter 4)

- A more comprehensive investigation into the conductivities of cold sintered ZnO and GZO, looking at the effects of processing temperature and pressure.
- Investigation into the effect of heat treatment on the conductivity and microstructure of cold sintered ZnO and GZO.
- Testing the hypothesis of the proposed core-shell defect model proposed.
- A more detailed study into how various parameters affect densification in cold sintering, and how they can be controlled to better control grain growth, especially in nano-materials.
- Seeing how adjustments of Ga concentration affect the ability to cold sinter ZnO.
- Understanding the cause of the zones of high Ga concentration that were observed in EPMA analysis.

9.2 ZnO-Kapton® Thick Film Layers and Multilayers (Chapter 5)

- Work investigating method of removing/preventing secondary acetate phase formations. Heat treatment at 300^{o}C may be possible but it is not known how this would affect the overall sample quality.
- Optimisation of the process to ensure that good adhesion is reproducible. This would involve better control of sintering conditions such as purpose-built dies, better spacer materials than PTFE, and more control of heating/cooling rates and times.
- Work to demonstrate similar results with doped ZnO, as this would be critical to achieve the desired conductivity for TCO applications. Modifications to the technique are likely since sintering of GZO was shown to be more difficult.

9.3 The Cold sintering of Boehmite to Produce γ- and α-alumina (Chapter 6)

9.3.1 Cold Sintering of Boehmite

- Further optimise the sintering process to lower sintering temperature and reduce required pressure to <100MPa, making the process more attractive for commercial applications
- Repeat work to develop a better understanding of the cold sintering mechanism and to ensure reproducibility of the process

9.3.2 Densification of γ-Alumina

- Perform more mechanical testing with samples of standard geometry to create a statistically meaningful data set
- Optimise the densification process with different pellet geometries to determine if fabrication to net shape is feasible for scale-up

9.3.3 Densification of α-Alumina

- Repeat works free of contamination to confirm presented results. It is particularly important to establish a method of cooling cold sintered samples, annealed at 1400^{o}C to avoid microcracking. In this manner, the true E and CS of cold sinter/annealed α-alumina can be determined.
- Investigate if sintering temperature may be further lowered, possibly by seeding a distribution of nano α–alumina in the boehmite prior to cold sintering. If successful, this may yield a high purity nano-structured α alumina at ~1400 ^{o}C, a considerable saving in energy and furnace costs with respect to conventional processing.
- The use of boehmite in the cold sintering of refractory bricks based on Al_2O_3-SiO_2 to achieve suitable handling characteristics prior to shipping. This is normally achieved using a pre-sinter step at high temperature.

References

[1] M. N. Rahman, *Ceramic Processing and Sintering*. New York: Marcel Dekker Inc., 1995.

[2] D. D. Furszyfer *et al.*, “Decarbonizing the ceramics industry : A systematic and critical review of policy options , developments and sociotechnical systems,” *Renew. Sustain. Energy Rev.*, vol. 157, no. December 2021, p. 112081, 2022, doi: 10.1016/j.rser.2022.112081.

[3] R. M. German, P. Suri, and S. J. Park, “Review: Liquid phase sintering,” *J. Mater. Sci.*, vol. 44, no. 1, pp. 1–39, 2009, doi: 10.1007/s10853-008-3008-0.

[4] B. Dargatz, J. Gonzalez-Julian, M. Bram, Y. Shinoda, F. Wakai, and O. Guillon, “FAST/SPS sintering of nanocrystalline zinc oxide-Part II: Abnormal grain growth, texture and grain anisotropy,” *J. Eur. Ceram. Soc.*, vol. 36, no. 5, pp. 1221–1232, 2016, doi: 10.1016/j.jeurceramsoc.2015.12.008.

[5] J. Langer, M. J. Hoffmann, and O. Guillon, “Electric field-assisted sintering and hot pressing of semiconductive zinc oxide: A comparative study,” *J. Am. Ceram. Soc.*, vol. 94, no. 8, pp. 2344–2353, 2011, doi: 10.1111/j.1551-2916.2011.04396.x.

[6] D. V. Dudina and A. K. Mukherjee, “Reactive spark plasma sintering: Successes and challenges of nanomaterial synthesis,” *J. Nanomater.*, vol. 2013, 2013, doi: 10.1155/2013/625218.

[7] J. Nie, Y. Zhang, J. M. Chan, R. Huang, and J. Luo, “Water-assisted flash sintering: Flashing ZnO at room temperature to achieve ~ 98% density in seconds,” *Scr. Mater.*, vol. 142, pp. 79–82, 2018, doi: 10.1016/j.scriptamat.2017.08.032.

[8] M. Biesuz and V. M. Sglavo, “Flash sintering of ceramics,” *J. Eur. Ceram. Soc.*, vol. 39, no. 2–3, pp. 115–143, 2019, doi: 10.1016/j.jeurceramsoc.2018.08.048.

[9] C. E. J. Dancer, “Flash sintering of ceramic materials,” *Mater. Res. Express*, vol. 3, no. 10, 2016, doi: 10.1088/2053-1591/3/10/102001.

[10] C. Vakifahmetoglu *et al.*, “Reactive Hydrothermal Liquid-Phase Densification (rHLPD) of Ceramics – A Study of the BaTiO3[TiO2] Composite System,” *J. Am. Ceram. Soc.*, vol. 99, no. 12, pp. 3893–3901, 2016, doi: 10.1111/jace.14468.

[11] J. Guo *et al.*, “Cold Sintering: A Paradigm Shift for Processing and Integration of Ceramics,” *Angew. Chemie - Int. Ed.*, vol. 55, no. 38, pp. 11457–11461, 2016, doi: 10.1002/anie.201605443.

[12] S. Grasso *et al.*, “A review of cold sintering processes,” *Adv. Appl. Ceram.*, vol. 119, no. 3, pp. 115–143, 2020, doi: 10.1080/17436753.2019.1706825.

[13] J. P. Maria *et al.*, “Cold sintering: Current status and prospects,” *J. Mater. Res.*, vol. 32, no. 17, pp. 3205–3218, 2017, doi: 10.1557/jmr.2017.262.

[14] M. Biesuz *et al.*, “A theoretical analysis of cold sintering,” *Adv. Appl. Ceram.*, vol. 119, no. 2, pp. 75–89, 2020, doi: 10.1080/17436753.2019.1692173.

[15] J. Gonzalez-Julian *et al.*, “Unveiling the mechanisms of cold sintering of ZnO at 250 °C by varying applied stress and characterizing grain boundaries by Kelvin Probe Force Microscopy,” *Acta Mater.*, vol. 144, pp. 116–128, 2018, doi: 10.1016/j.actamat.2017.10.055.

[16] X. Kang, R. Floyd, S. Lowum, M. Cabral, E. Dickey, and J. P. Maria, “Mechanism studies of hydrothermal cold sintering of zinc oxide at near room temperature,” *J. Am. Ceram. Soc.*, vol. 102, no. 8, pp. 4459–4469, 2019, doi: 10.1111/jace.16340.

[17] S. Funahashi *et al.*, “Demonstration of the cold sintering process study for the densification and grain growth of ZnO ceramics,” *J. Am. Ceram. Soc.*, vol. 100, no. 2, pp. 546–553, 2017, doi: 10.1111/jace.14617.

[18] J. Guo *et al.*, “Cold Sintered Ceramic Nanocomposites of 2D MXene and Zinc Oxide,” *Adv. Mater.*, vol. 30, no. 32, pp. 1–6, 2018, doi: 10.1002/adma.201801846.

[19] R. D. Floyd, S. Lowum, and J. P. Maria, “Cold sintering zinc oxide with a crystalline zinc acetate dihydrate mass transport phase,” *J. Mater. Sci.*, vol. 55, no. 31, pp. 15117–15129, 2020, doi: 10.1007/s10853-020-05100-9.

[20] S. Lowum, R. Floyd, R. Bermejo, and J. P. Maria, “Mechanical strength of cold-sintered zinc oxide under biaxial bending,” *J. Mater. Sci.*, vol. 54, no. 6, pp. 4518–4522, 2019, doi: 10.1007/s10853-018-3173-8.

[21] S. Funahashi *et al.*, “Cold sintering and co-firing of a multilayer device with thermoelectric materials,” *J. Am. Ceram. Soc.*, vol. 100, no. 8, pp. 3488–3496, 2017, doi: 10.1111/jace.14852.

[22] D. Wang *et al.*, “Cold sintered LiMgPO4 based composites for low temperature co-fired ceramic (LTCC) applications,” *J. Am. Ceram. Soc.*, vol. 103, no. 11, pp. 6237–6244, 2020, doi: 10.1111/jace.17320.

[23] D. S. B. Heidary, J. Guo, J.-H. Seo, H. Guo, R. Rajagopalan, and C. A. Randall, “Microstructures and electrical properties of V_2O_5 and carbon-nanofiber composites fabricated by cold sintering process,” *Jpn. J. Appl. Phys.*, vol. 57, no. 2, p. 025702, 2018, doi: 10.7567/JJAP.57.025702.

[24] R. A. Afre, N. Sharma, M. Sharon, and M. Sharon, “Transparent conducting oxide films for various applications: A review,” *Rev. Adv. Mater. Sci.*, vol. 53, no. 1, pp. 79–89, 2018, doi: 10.1515/rams-2018-0006.

[25] J. Liu *et al.*, “Investigation of aluminum-gallium co-doped zinc oxide targets for sputtering thin film and photovoltaic application,” *J. Alloys Compd.*, vol. 575, pp. 174–182, 2013, doi: 10.1016/j.jallcom.2013.04.075.

[26] “Gallium Price,” *Strategic Metal Investments Ltd*, 2014. http://strategic-metal.com/products/gallium/gallium-price/ (accessed Sep. 16, 2020).

[27] “Aluminium Commodity Price Live,” *Business Insider: Markets*, 2020. https://markets.businessinsider.com/commodities/aluminum-price (accessed Sep. 16, 2020).

[28] T. Homma, T. Ueno, K. Sekizawa, A. Tanaka, and M. Hirata, “Interstitial pneumonia developed in a worker dealing with particles containing indium-tin oxide,” *J. Occup. Health*, vol. 45, no. 3, pp. 137–139, 2003, doi: 10.1539/joh.45.137.

[29] M. A. Badding *et al.*, “Pulmonary toxicity of indium-tin oxide production facility particles in rats,” *J. Appl. Toxicol.*, vol. 36, no. 4, pp. 618–626, 2016, doi: 10.1002/jat.3253.

[30] K. Zhang, Y. Wu, W. Wang, B. Li, Y. Zhang, and T. Zuo, “Recycling indium from waste LCDs: A review,” *Resour. Conserv. Recycl.*, vol. 104, no. 100, pp. 276–290, 2015, doi: 10.1016/j.resconrec.2015.07.015.

[31] M.Kumagai and G. L. Messing, “Controlled Transformation and Sintering of a Boehmite Sol-Gel by α-Alumina Seeding,” *J. Am. Ceram. Soc.*, vol. 68, no. 9, pp. 500–505, 1985, doi: 10.1111/j.1151-2916.1985.tb15818.x.

[32] C. S. Nordahl and G. L. Messing, “Sintering of a-Al2O3 seeded nanocrystalline g-Al2O3 powders,” *J. Eur. Ceram. Soc.*, vol. 22, pp. 415–422, 2002.doi: 10.1016/S0955-2219(01)00285-0

[33] P. B. Vandiver, O. Soffer, B. Klima, and J. Svoboda, “The origins of ceramic technology at Dolni Věstonice, Czechoslovakia,” *Science (80-.).*, vol. 246, no. 4933, pp. 1002–1008, 1989, doi: 10.1126/science.246.4933.1002.

[34] O. B.-Y. Xiaohong Wu, Chi Zhang, Paul Goldberg, David Cohen, Yan Pan, Trina Arpin, “Early Pottery at 20,000 Years Ago in Xianrendong Cave, China,” *Science (80-.).*, vol. 336, no. June, pp. 1696–1700, 2015, doi: 10.1002/9781118683682.bref.

[35] D. D. L. Chung, “Development, design and applications of structural capacitors,” *Appl. Energy*, vol. 231, no. September 2018, pp. 89–101, 2018, doi: 10.1016/j.apenergy.2018.09.132.

[36] P. Boyer, D. Huten, P. Loriaut, V. Lestrat, C. Jeanrot, and P. Massin, “Is alumina-on-alumina ceramic bearings total hip replacement the right choice in patients younger than 50 years of age? A 7- to 15-year follow-up study,” *Orthop. Traumatol. Surg. Res.*, vol. 96, no. 6, pp. 616–622, 2010, doi: 10.1016/j.otsr.2010.02.013.

[37] A. S. Kumar, A. R. Durai, and T. Sornakumar, “Wear behaviour of alumina based ceramic cutting tools on machining steels,” *Tribol. Int.*, vol. 39, no. 3, pp. 191–197, 2006, doi: 10.1016/j.triboint.2005.01.021.

[38] F. Taylan, O. Çolak, and M. C. Kayacan, “Investigation of TiN Coated CBN and CBN cutting tool performance in hard milling application,” *Stroj. Vestnik/Journal Mech. Eng.*, vol. 57, no. 5, pp. 417–424, 2011, doi: 10.5545/sv-jme.2010.059.

[39] K. Broniszewski, J. Wozniak, M. Kostecki, K. Czechowski, L. Jaworska, and A. Olszyna, “Al2O3–V cutting tools for machining hardened stainless steel,” *Ceram. Int.*, vol. 41, no. 10, pp. 14190–14196, 2015, doi: 10.1016/j.ceramint.2015.07.044.

[40] N.Hernandez, “What is Hip Replacement? A Review of Total Hip Arthroplasty - A Review of Total Hip Arthroplasty, Hip Resurfacing and Minimally-Invasive Hip Surgery,” *U.W.Orthopaedics and Sports Medicine*, 2020. https://orthop.washington.edu/patient-care/articles/hip/what-is-hip-replacement-a-review-of-total-hip-arthroplasty.html (accessed Apr. 07, 2020).

[41] C. Y. Hu and T. R. Yoon, “Recent updates for biomaterials used in total hip arthroplasty,” *Biomater. Res.*, vol. 22, no. 1, pp. 1–12, 2018, doi: 10.1186/s40824-018-0144-8.

[42] Jacksonville Orthopaedic Institute, “What to Expect After Having a Total Hip Replacement,” *Jacksonville Orthopaedic Institute*, 2020. https://www.joionline.net/trending/content/what-expect-after-having-total-hip-replacement (accessed Jan. 15, 2021).

[43] T. Shimizu, K. Matsuura, H. Furue, and K. Matsuzak, “Thermal conductivity of high porosity alumina refractory bricks made by a slurry gelation and foaming method,” *J. Eur. Ceram. Soc.*, vol. 33, no. 15–16, pp. 3429–3435, 2013, doi: 10.1016/j.jeurceramsoc.2013.07.001.

[44] Z. Živcová, E. Gregorová, W. Pabst, D. S. Smith, A. Michot, and C. Poulier, “Thermal conductivity of porous alumina ceramics prepared using starch as a pore-forming agent,” *J. Eur. Ceram. Soc.*, vol. 29, no. 3, pp. 347–353, 2009, doi: 10.1016/j.jeurceramsoc.2008.06.018.

[45] Z. Zivcová, E. Gregorová, and W. Pabst, “Alumina ceramics prepared with new pore-forming agents,” *Process. Appl. Ceram.*, vol. 2, no. 1, pp. 1–8, 2008, doi: 10.2298/pac0801001z.

[46] L. B. Chen, “Yttria-stabilized zirconia thermal barrier coatings - A review,” *Surf. Rev. Lett.*, vol. 13, no. 5, pp. 535–544, 2006, doi: 10.1142/S0218625X06008670.

[47] D. Naumenko, V. Shemet, L. Singheiser, and W. J. Quadakkers, “Failure mechanisms of thermal barrier coatings on MCrAlY-type bondcoats associated with the formation of the thermally grown oxide,” *J. Mater. Sci.*, vol. 44, no. 7, pp. 1687–1703, 2009, doi: 10.1007/s10853-009-3284-3.

[48] K. Hong, T. H. Lee, J. M. Suh, S. H. Yoon, and H. W. Jang, “Perspectives and challenges in multilayer ceramic capacitors for next generation electronics,” *J. Mater. Chem. C*, vol. 7, no. 32, pp. 9782–9802, 2019, doi: 10.1039/c9tc02921d.

[49] “Ceramic Capacitor: C0G, X7R, Y5V, NP0, etcitle,” *Electronic Notes*. https://www.electronics-notes.com/articles/electronic_components/capacitors/ceramic-dielectric-types-c0g-x7r-z5u-y5v.php (accessed Apr. 09, 2020).

[50] M. Jayalakshmi and K. Balasubramanian, “Simple capacitors to supercapacitors - An overview,” *Int. J. Electrochem. Sci.*, vol. 3, no. 11, pp. 1196–1217, 2008.

[51] P. K. Panda and B. Sahoo, “PZT to lead free piezo ceramics: A review,” *Ferroelectrics*, vol. 474, no. 1, pp. 128–143, 2015, doi: 10.1080/00150193.2015.997146.

[52] M. G. Kang, W. S. Jung, C. Y. Kang, and S. J. Yoon, “Recent progress on PZT based piezoelectric energy harvesting technologies,” *Actuators*, vol. 5, no. 1, 2016, doi: 10.3390/act5010005.

[53] P. K. Panda, “Review: Environmental friendly lead-free piezoelectric materials,” *J. Mater. Sci.*, vol. 44, no. 19, pp. 5049–5062, 2009, doi: 10.1007/s10853-009-3643-0.

[54] S. Trolier-McKinstry, S. Zhang, A. J. Bell, and X. Tan, “High-Performance Piezoelectric Crystals, Ceramics, and Films,” *Annu. Rev. Mater. Res.*, vol. 48, no. 1, pp. 191–217, 2018, doi: 10.1146/annurev-matsci-070616-124023.

[55] G. J. Exarhos and X. D. Zhou, “Discovery-based design of transparent conducting oxide films,” *Thin Solid Films*, vol. 515, no. 18, pp. 7025–7052, 2007, doi: 10.1016/j.tsf.2007.03.014.

[56] A. R. West, *Solid State Chemistry and its Applications, 2nd Edition*. John Wiley & Sons, Inc, 2014.

[57] V. Parihar, M. Raja, and R. Paulose, “A brief review of structural, electrical and electrochemical properties of zinc oxide nanoparticles,” *Rev. Adv. Mater. Sci.*, vol. 53, no. 2, pp. 119–130, 2018, doi: 10.1515/rams-2018-0009.

[58] M. Hadis and O. Umit, *Zinc Oxide - Fundamentals, Materials and Device Technology*. WILEY-VCH, 2007.

[59] S. J. P. Chennupati Jagadish, *Zinc Oxide Bulk, Thin Films and Nanostructures*, First Edit. Elsevier, 2006.

[60] D. Schmeißer, K. Henkel, and C. Janowitz, “Ionicity of ZnO - A key system for transparent conductive oxides,” *Epl*, vol. 123, no. 2, 2018, doi: 10.1209/0295-5075/123/27003.

[61] G. C. Zhou, L. Z. Sun, X. L. Zhong, X. Chen, L. Wei, and J. B. Wang, “First-principle study on bonding mechanism of ZnO by LDA + U method,” *Phys. Lett. Sect. A Gen. At. Solid State Phys.*, vol. 368, no. 1–2, pp. 112–116, 2007, doi: 10.1016/j.physleta.2007.03.061.

[62] A. Ashrafi and C. Jagadish, “Review of zincblende ZnO: Stability of metastable ZnO phases,” *J. Appl. Phys.*, vol. 102, no. 7, 2007, doi: 10.1063/1.2787957.

[63] L. Z. Kou, W. L. Guo, and C. Li, “Piezoelectricity of ZNO and its nanostructures,” *2008 Symp. Piezoelectricity, Acoust. Waves, Device Appl. SPAWDA 2008*, pp. 354–359, 2008, doi: 10.1109/SPAWDA.2008.4775808.

[64] I. Dakua and N. Afzulpurkar, “Piezoelectric energy generation and harvesting at the nano-scale: Materials and devices,” *Nanomater. Nanotechnol.*, vol. 3, no. 1, 2013, doi: 10.5772/56941.

[65] R. S. Koster, C. M. Fang, M. Dijkstra, A. Van Blaaderen, and M. A. Van Huis, “Stabilization of rock salt ZnO nanocrystals by low-energy surfaces and Mg additions: A first-principles study,” *J. Phys. Chem. C*, vol. 119, no. 10, pp. 5648–5656, 2015, doi: 10.1021/jp511503b.

[66] Y. Wang, T. Hou, S. Tian, S. T. Lee, and Y. Li, “Influence of doping effect on zinc oxide by first-principles studies,” *J. Phys. Chem. C*, vol. 115, no. 15, pp. 7706–7716, 2011, doi: 10.1021/jp111203e.

[67] Y. Zhang, Z. Gao, and Y. Gu, “First-principles studies on the structural transition of ZnO nanowires at high pressure,” *J. Nanomater.*, vol. 2010, 2010, doi: 10.1155/2010/462032.

[68] K. A. Adegoke, M. Iqbal, H. Louis, S. U. Jan, A. Mateen, and O. S. Bello, “Photocatalytic conversion of co2 using zno semiconductor by hydrothermal method,” *Pakistan J. Anal. Environ. Chem.*, vol. 19, no. 1, pp. 1–27, 2018, doi: 10.21743/pjaec/2018.06.01.

[69] N. Aggarwal, A. Vasishth, B. Singh, and B. Singh, “Investigation of room temperature ferromagnetic behaviour in dilute magnetic oxides,” *Integr. Ferroelectr.*, vol. 186, no. 1, pp. 10–16, 2018, doi: 10.1080/10584587.2017.1369317.

[70] P. M. . Raja and A. R. Barron, “7.1: Crystal Structure,” *LibreTexts*, 2020. https://chem.libretexts.org/Bookshelves/Analytical_Chemistry/Book%3A_Physical_Methods_in_Chemistry_and_Nano_Science_(Barron)/07%3A_Molecular_and_Solid_State_Structure/7.01%3A_Crystal_Structure (accessed Jan. 19, 2021).

[71] Ü. Özgür *et al.*, “A comprehensive review of ZnO materials and devices,” *J. Appl. Phys.*, vol. 98, no. 4, pp. 1–103, 2005, doi: 10.1063/1.1992666.

[72] A. Janotti and C. G. Van De Walle, “Native point defects in ZnO,” *Phys. Rev. B - Condens. Matter Mater. Phys.*, vol. 76, no. 16, pp. 1–22, 2007, doi: 10.1103/PhysRevB.76.165202.

[73] N. S. Parmar, L. A. Boatner, K. G. Lynn, and J. W. Choi, “Zn Vacancy Formation Energy and Diffusion Coefficient of CVT ZnO Crystals in the Sub-Surface Micron Region,” *Sci. Rep.*, vol. 8, no. 1, pp. 1–8, 2018, doi: 10.1038/s41598-018-31771-1.

[74] K. Jug and V. A. Tikhomirov, “Influence of Intrinsic Defects on the Properties of Zinc Oxide,” *J. Comput. Chem.*, vol. 32, no. Febuary 2008, pp. 2251–2254, 2008, doi: 10.1002/jcc.

[75] A. Janotti and C. G. Van De Walle, “Fundamentals of zinc oxide as a semiconductor,” *Reports Prog. Phys.*, vol. 72, no. 12, 2009, doi: 10.1088/0034-4885/72/12/126501.

[76] A. Kohan, G. Ceder, D. Morgan, and C. G. Van de Walle, “First-principles study of native point defects in ZnO,” *Phys. Rev. B - Condens. Matter Mater. Phys.*, vol. 61, no. 22, pp. 15019–15027, 2000, doi: 10.1103/PhysRevB.61.15019.

[77] G. W. Tomlins, J. L. Routbort, and T. O. Mason, “Zinc self-diffusion, electrical properties, and defect structure of undoped, single crystal zinc oxide,” *J. Appl. Phys.*, vol. 87, no. 1, pp. 117–123, 2000, doi: 10.1063/1.371832.

[78] L. Schmidt-Mende and J. L. MacManus-Driscoll, “ZnO - nanostructures, defects, and devices,” *Mater. Today*, vol. 10, no. 5, pp. 40–48, 2007, doi: 10.1016/S1369-7021(07)70078-0.

[79] S. E. Harrison, “Conductivity and Hall effect of ZnO at low temperatures,” *Phys. Rev.*, vol. 93, no. 1, pp. 52–62, 1954, doi: 10.1103/PhysRev.93.52.

[80] A. R. Hutson, “Hall effect studies of doped zinc Oxide single crystals,” *Phys. Rev.*, vol. 108, no. 2, pp. 222–230, 1957, doi: 10.1103/PhysRev.108.222.

[81] A. Janotti and C. G. Van De Walle, “Oxygen vacancies in ZnO,” *Appl. Phys. Lett.*, vol. 87, no. 12, pp. 1–3, 2005, doi: 10.1063/1.2053360.

[82] C. G. Van De Walle, “Defect analysis and engineering in ZnO,” *Phys. B Condens. Matter*, vol. 308–310, pp. 899–903, 2001, doi: 10.1016/S0921-4526(01)00830-4.

[83] M. A. Borysiewicz, “ZnO as a functional material, a review,” *Crystals*, vol. 9, no. 10, 2019, doi: 10.3390/cryst9100505.

[84] C. G. Van De Walle, “Hydrogen as a cause of doping in zinc oxide,” *Phys. Rev. Lett.*, vol. 85, no. 5, pp. 1012–1015, 2000, doi: 10.1103/PhysRevLett.85.1012.

[85] A. Kolodziejczak-Radzimska and T. Jesionowski, “Zinc oxide-from synthesis to application: A review,” *Materials (Basel).*, vol. 7, no. 4, pp. 2833–2881, 2014, doi: 10.3390/ma7042833.

[86] J. Hu and R. G. Gordon, “Textured fluorine-doped ZnO films by atmospheric pressure chemical vapor deposition and their use in amorphous silicon solar cells,” *Sol. Cells*, vol. 30, no. 1–4, pp. 437–450, 1991, doi: 10.1016/0379-6787(91)90076-2.

[87] B. Liu, M. Gu, X. Liu, S. Huang, and C. Ni, “First-principles study of fluorine-doped zinc oxide,” *Appl. Phys. Lett.*, vol. 97, no. 12, pp. 1–4, 2010, doi: 10.1063/1.3492444.

[88] E. Guilmeau *et al.*, “Inversion Boundaries and Phonon Scattering in Ga:ZnO Thermoelectric Compounds,” *Inorg. Chem.*, vol. 56, no. 1, pp. 480–487, 2017, doi: 10.1021/acs.inorgchem.6b02354.

[89] M. F. Ogawa, Y. Natsume, T. Hirayama, and H. Sakata, “Preparation and electrical properties of undoped zinc oxide films by CVD,” *J. Mater. Sci. Lett.*, vol. 9, no. 11, pp. 1351–1353, 1990, doi: 10.1007/BF00726543.

[90] J. C. Fan, K. M. Sreekanth, Z. Xie, S. L. Chang, and K. V. Rao, “P-Type ZnO materials: Theory, growth, properties and devices,” *Prog. Mater. Sci.*, vol. 58, no. 6, pp. 874–985, 2013, doi: 10.1016/j.pmatsci.2013.03.002.

[91] C. Singh and E. Panda, “Variation of electrical properties in thickening Al-doped ZnO films: Role of defect chemistry,” *RSC Adv.*, vol. 6, no. 54, pp. 48910–48918, 2016, doi: 10.1039/c6ra06513a.

[92] Z. Chen, W. Li, R. Li, Y. Zhang, G. Xu, and H. Cheng, “Fabrication of highly transparent and conductive indium-tin oxide thin films with a high figure of merit via solution processing,” *Langmuir*, vol. 29, no. 45, pp. 13836–13842, 2013, doi: 10.1021/la4033282.

[93] M. Ahmadi, M. Asemi, and M. Ghanaatshoar, “Mg and N co-doped CuCrO 2 : A record breaking p-type TCO,” *Appl. Phys. Lett.*, vol. 113, no. 24, 2018, doi: 10.1063/1.5051730.

[94] M. Gabás *et al.*, “Differences in n-type doping efficiency between Al- and Ga-ZnO films,” *J. Appl. Phys.*, vol. 113, no. 16, 2013, doi: 10.1063/1.4803063.

[95] H. Kim *et al.*, “Electrical, optical, and structural properties of indium-tin-oxide thin films for organic light-emitting devices,” *J. Appl. Phys.*, vol. 86, no. 11, pp. 6451–6461, 1999, doi: 10.1063/1.371708.

[96] V. Sittinger, F. Ruske, W. Werner, C. Jacobs, B. Szyszka, and D. J. Christie, “High power pulsed magnetron sputtering of transparent conducting oxides,” *Thin Solid Films*, vol. 516, no. 17, pp. 5847–5859, 2008, doi: 10.1016/j.tsf.2007.10.031.

[97] M. Lokanc, R. Eggert, and M. Redlinger, “The Availability of Indium: The Present, Medium Term, and Long Term,” *Natl. Renew. Energy Lab.*, vol. October, no. October, pp. 1–90, 2015, [Online]. Available: www.nrel.gov/publications.%0Awww.nrel.gov/publications.%0Awww.nrel.gov/publications.%0Ahttps://www.nrel.gov/docs/fy16osti/62409.pdf.

[98] J. S. Jang *et al.*, “Comparison study of ZnO-based quaternary TCO materials for photovoltaic application,” *J. Alloys Compd.*, vol. 793, pp. 499–504, 2019, doi: 10.1016/j.jallcom.2019.04.042.

[99] L. A. Xue and I. -W Chen, “Low-Temperature Sintering of Alumina with Liquid-Forming Additives,” *J. Am. Ceram. Soc.*, vol. 74, no. 8, pp. 2011–2013, 1991, doi: 10.1111/j.1151-2916.1991.tb07825.x.

[100] D. Hardy and D. J. Green, “Mechanical properties of a partially sintered alumina,” *J. Eur. Ceram. Soc.*, vol. 15, no. 8, pp. 769–775, 1995, doi: 10.1016/0955-2219(95)00045-V.

[101] I. Levin and D. Brandon, “Metastable alumina polymorphs: Crystal structures and transition sequences,” *J. Am. Ceram. Soc.*, vol. 81, no. 8, pp. 1995–2012, 1998, doi: 10.1111/j.1151-2916.1998.tb02581.x.

[102] H.-L. Gross and W. Mader, “On the crystal structure of k-alumina,” *Chem. Commun.*, pp. 55–56, 1997, doi: 10.1246/bcsj.1.62.

[103] H. C. Stumpf, A. S. Russell, J. W. Newsome, and C. M. Tucker, “Thermal Transformations of Aluminas and Alumina Hydrates - Reaction with 44% Technical Acid.,” *Ind. Eng. Chem.*, vol. 42, no. 7, pp. 1398–1403, 1950, doi: 10.1021/ie50487a039.

[104] G. Ervin, “ Structural interpretation of the diaspore–corundum and boehmite–γ-Al 2 O 3 transitions ,” *Acta Crystallogr.*, vol. 5, no. 1, pp. 103–108, 1952, doi: 10.1107/s0365110x52000216.

[105] G. . Brindley, “The reaction series, gibbsite→chi alumina→kappa alumina→corundum,” *Am. Mineral.*, vol. 46, pp. 771–785, 1961, [Online]. Available: http://www.minsocam.org/ammin/AM46/AM46_771.pdf.

[106] B. C. Lippens and J. H. de Boer, “Study of phase transformations during calcination of aluminum hydroxides by selected area electron diffraction,” *Acta Crystallogr.*, vol. 17, no. 10, pp. 1312–1321, 1964, doi: 10.1107/s0365110x64003267.

[107] L. Kovarik, M. Bowden, A. Genc, J. Szanyi, C. H. F. Peden, and J. H. Kwak, “Structure of δ-alumina: Toward the atomic level understanding of transition alumina phases,” *J. Phys. Chem. C*, vol. 118, no. 31, pp. 18051–18058, 2014, doi: 10.1021/jp500051j.

[108] R. Den Hand, “Alumina yield in the Bayer process,” *Essent. Readings Light Met.*, vol. 1, pp. 522–527, 2017, doi: 10.1007/978-3-319-48176-0.

[109] “Alumina - Chemical Compound,” *Britannica*. https://www.britannica.com/science/alumina#ref148550 (accessed Sep. 16, 2020).

[110] B. Xu and P. Smith, “Dehydration kinetics of boehmite in the temperature range 723-873 K,” *Thermochim. Acta*, vol. 531, pp. 46–53, 2012, doi: 10.1016/j.tca.2011.12.025.

[111] B. Dash, B. C. Tripathy, I. N. Bhattacharya, S. C. Das, C. R. Mishra, and B. K. Mishra, “Precipitation of boehmite in sodium aluminate liquor,” *Hydrometallurgy*, vol. 95, no. 3–4, pp. 297–301, 2009, doi: 10.1016/j.hydromet.2008.07.002.

[112] S. J. Wilson, “The dehydration of boehmite, γ-AlOOH, to γ-Al2O3,” *J. Solid State Chem.*, vol. 30, no. 2, pp. 247–255, 1979, doi: 10.1016/0022-4596(79)90106-3.

[113] X. Krokidis, P. Raybaud, A. E. Gobichon, B. Rebours, P. Euzen, and H. Toulhoat, “Theoretical study of the dehydration process of boehmite to γ-alumina,” *J. Phys. Chem. B*, vol. 105, no. 22, pp. 5121–5130, 2001, doi: 10.1021/jp0038310.

[114] P. Alphonse and M. Courty, “Structure and thermal behavior of nanocrystalline boehmite,” *Thermochim. Acta*, vol. 425, no. 1–2, pp. 75–89, 2005, doi: 10.1016/j.tca.2004.06.009.

[115] S. J. Wilson, “The development of porous microstructures during the dehydration of boehmite,” *Mineral. Mag.*, vol. 43, no. 326, pp. 301–306, 1979, doi: 10.1180/minmag.1979.043.326.14.

[116] H. Saalfeld and M. Wedde, “Refinement of the crystal structure of gibbsite, A1(OH)3,” *Zeitschrift fur Krist. - New Cryst. Struct.*, vol. 139, no. 1–2, pp. 129–135, 1974, doi: 10.1524/zkri.1974.139.1-2.129.

[117] R. J. Hill, “Crystal structure refinement and electron density distribution in diaspore,” *Phys. Chem. Miner.*, vol. 5, no. 2, pp. 179–200, 1979, doi: 10.1007/BF00307552.

[118] F. J. Ewing, “The crystal structure of diaspore,” *J. Chem. Phys.*, vol. 3, no. 4, pp. 203–207, 1935, doi: 10.1063/1.1749634.

[119] M. Hatipoğlu, N. Türk, S. C. Chamberlain, and A. M. Akgün, “Gem-quality transparent diaspore (zultanite) in bauxite deposits of the İlbir Mountains, Menderes Massif, SW Turkey,” *Miner. Depos.*, vol. 45, no. 2, pp. 201–205, 2010, doi: 10.1007/s00126-009-0262-2.

[120] L. D. Hou, S. K. Tiku, H. A. Wang, and F. A. Kröger, “Conductivity and creep in acceptor-dominated polycrystalline Al2O3,” *J. Mater. Sci.*, vol. 14, no. 8, pp. 1877–1889, 1979, doi: 10.1007/BF00551027.

[121] K. Matsunaga, A. Nakamura, T. Yamamoto, and Y. Ikuhara, “Theoretical study of defect structures in pure and titanium-doped alumina,” *Solid State Ionics*, vol. 172, no. 1-4 SPEC. ISS., pp. 155–158, 2004, doi: 10.1016/j.ssi.2004.01.044.

[122] J. Pappis and W. . Kingery, “Electrical Properties of Single-Crystal and Polycrystalline Alumina at High Temperatures,” *J. Am. Ceram. Soc.*, vol. 44, no. 9, pp. 459–464, 1961, doi: 10.2115/fiber.31.11_P360.

[123] T. Matsumura, “The Electrical Properties of Alumina At High Temperatures,” *Can. J. Phys.*, vol. 44, no. 8, pp. 1685–1698, 1966, doi: 10.1139/p66-143.

[124] P. Harrop and R. . Creamer, “The high-temperature electrical conductivity of single-crystal alumina,” *Br. J. Appl. Phys.*, vol. 14, 1963.

[125] F. G. Will, H. G. DeLorenzi, and K. H. Janora, “Conduction Mechanism of Single-Crystal Alumina,” *J. Am. Ceram. Soc.*, vol. 75, no. 2, pp. 295–304, 1992, doi: 10.1111/j.1151-2916.1992.tb08179.x.

[126] P. Auerkari, “Mechanical and physical properties of engineering alumina ceramics,” 1996.

[127] X. Teng, H. Liu, and C. Huang, “Effect of Al2O3 particle size on the mechanical properties of alumina-based ceramics,” *Mater. Sci. Eng. A*, vol. 452–453, pp. 545–551, 2007, doi: 10.1016/j.msea.2006.10.073.

[128] Y. T. O, J. B. Koo, K. J. Hong, J. S. Park, and D. C. Shin, “Effect of grain size on transmittance and mechanical strength of sintered alumina,” *Mater. Sci. Eng. A*, vol. 374, no. 1–2, pp. 191–195, 2004, doi: 10.1016/j.msea.2004.02.015.

[129] A. M. Lazar *et al.*, “Corrosion protection of 304L stainless steel by chemical vapor deposited alumina coatings,” *Corros. Sci.*, vol. 81, pp. 125–131, 2014, doi: 10.1016/j.corsci.2013.12.012.

[130] E. M. Moroz, D. A. Zyuzin, V. Y. Tregubenko, I. E. Udras, A. S. Belyi, and V. A. Likholobov, “Effect of structural defects in alumina supports on the formation and catalytic properties of the active component of reforming catalysts,” *React. Kinet. Mech. Catal.*, vol. 110, no. 2, pp. 459–470, 2013, doi: 10.1007/s11144-013-0599-5.

[131] Y. Dong *et al.*, “Corrosion resistance characterization of porous alumina membrane supports,” *Mater. Charact.*, vol. 62, no. 4, pp. 409–418, 2011, doi: 10.1016/j.matchar.2011.01.012.

[132] W. Qin, C. Peng, M. Lv, and J. Wu, “Preparation and properties of high-purity porous alumina support at low sintering temperature,” *Ceram. Int.*, vol. 40, no. 8 PART B, pp. 13741–13746, 2014, doi: 10.1016/j.ceramint.2014.05.044.

[133] W. Qin, B. Lei, C. Peng, and J. Wu, “Corrosion resistance of ultra-high purity porous alumina ceramic support,” *Mater. Lett.*, vol. 144, pp. 74–77, 2015, doi: 10.1016/j.matlet.2014.12.082.

[134] H. Pines and W. O. Haag, “Alumina: Catalyst and Support. I. Alumina, its Intrinsic Acidity and Catalytic Activity,” *J. Am. Chem. Soc.*, vol. 82, no. 10, pp. 2471–2483, 1960, doi: 10.1021/ja01495a021.

[135] D. S. Maciver, H. H. Tobin, and R. T. Barth, “Catalytic aluminas I. Surface chemistry of eta and gamma alumina,” *J. Catal.*, vol. 2, no. 6, pp. 485–497, 1963, doi: 10.1016/0021-9517(63)90004-6.

[136] R. S. Schiffino and R. P. Merrill, “A mechanistic study of the methanol dehydration reaction on γ-alumina catalyst,” *J. Phys. Chem.*, vol. 97, no. 24, pp. 6425–6435, 1993, doi: 10.1021/j100126a017.

[137] N. P. Bansal and A. R. Boccaccini, *Ceramics and Composites Processing Methods*, 1st ed. Hoboken: John Wiley & Sons, Inc, 2012.

[138] B. Bikramjit and B. Kantesh, “Sintering of Ceramics,” in *Advanced Structual Ceramics*, First Edit., John Wiley & Sons, Inc, 2011, pp. 76–103.

[139] M. F. Ashby, “A first report on sintering diagrams,” *Acta Metall.*, vol. 22, no. 3, pp. 275–289, 1974, doi: 10.1016/0001-6160(74)90167-9.

[140] F. B. Swinkels and M. F. Ashby, “A second report on sintering diagrams,” *Acta Metall.*, vol. 29, no. 2, pp. 259–281, 1981, doi: 10.1016/0001-6160(81)90154-1.

[141] R. L. Coble, “Sintering crystalline solids. I. intermediate and final state diffusion models,” *J. Appl. Phys.*, vol. 32, no. 5, pp. 787–792, 1961, doi: 10.1063/1.1736107.

[142] R. L. Coble, “Sintering crystalline solids. II. experimental test of diffusion models in powder compacts,” *J. Appl. Phys.*, vol. 32, no. 5, pp. 793–799, 1961, doi: 10.1063/1.1736108.

[143] R. Bjork, V. Tikare, H. L. Frandsen, and N. Pryds, “The sintering behavior of close-packed spheres,” *Scr. Mater.*, vol. 67, no. 1, pp. 81–84, 2012, doi: 10.1016/j.scriptamat.2012.03.024.

[144] J. Rojek, S. Nosewicz, M. Maździarz, P. Kowalczyk, K. Wawrzyk, and D. Lumelskyj, “Modeling of a Sintering Process at Various Scales,” *Procedia Eng.*, vol. 177, pp. 263–270, 2017, doi: 10.1016/j.proeng.2017.02.210.

[145] H. E. Exner, “Solid-state sintering: Critical assessment of theoretical concepts and experimental methods,” *Powder Metall.*, vol. 23, no. 4, pp. 203–209, 1980, doi: 10.1179/pom.1980.23.4.203.

[146] W. D. Kingery and M. Berg, “Study of the initial stages of sintering solids by viscous flow, evaporation-condensation, and self-diffusion,” *J. Appl. Phys.*, vol. 26, no. 10, pp. 1205–1212, 1955, doi: 10.1063/1.1721874.

[147] K. Raju and D. H. Yoon, “Sintering additives for SiC based on the reactivity: A review,” *Ceram. Int.*, vol. 42, no. 16, pp. 17947–17962, 2016, doi: 10.1016/j.ceramint.2016.09.022.

[148] B. Basu and K. Balani, *Advanced Structural Ceramics*. John Wiley & Sons, Inc, 2011.

[149] O. Guillon *et al.*, “Field-assisted sintering technology/spark plasma sintering: Mechanisms, materials, and technology developments,” *Adv. Eng. Mater.*, vol. 16, no. 7, pp. 830–849, 2014, doi: 10.1002/adem.201300409.

[150] M. Suarez *et al.*, “Challenges and Opportunities for Spark Plasma Sintering: A Key Technology for a New Generation of Materials,” *Sinter. Appl.*, 2013, doi: 10.5772/53706.

[151] R. Muccillo, M. Kleitz, and E. N. S. Muccillo, “Flash grain welding in yttria stabilized zirconia,” *J. Eur. Ceram. Soc.*, vol. 31, no. 8, pp. 1517–1521, 2011, doi: 10.1016/j.jeurceramsoc.2011.02.030.

[152] D. M. Roy, G. R. Gouda, and A. Bobrowsky, “Very high strength cement pastes prepared by hot pressing and other high pressure techniques,” *Cem. Concr. Res.*, vol. 2, no. 3, pp. 349–366, 1972, doi: 10.1016/0008-8846(72)90075-0.

[153] D. M. Roy and G. R. Gouda, “High strength generation in cement pastes,” *Cem. Concr. Res.*, vol. 3, no. 6, pp. 807–820, 1973, doi: 10.1016/0008-8846(73)90013-6.

[154] N. Yamasaki, K. Yanagisawa, M. Nishioka, and S. Kanahara, “A hydrothermal hot-pressing method: Apparatus and application,” *J. Mater. Sci. Lett.*, vol. 5, no. 3, pp. 355–356, 1986, doi: 10.1007/BF01748104.

[155] A. Ndayishimiye *et al.*, “Hydrothermal Sintering for Densification of Silica. Evidence for the Role of Water,” *J. Eur. Ceram. Soc.*, vol. 38, no. 4, pp. 1860–1870, 2018, doi: 10.1016/j.jeurceramsoc.2017.10.011.

[156] J. Andrews, D. Button, and I. M. Reaney, “Advances in Cold Sintering,” *Johnson Matthey Technol. Rev.*, no. 2, pp. 219–232, 2020, doi: 10.1595/205651320x15814150061554.

[157] H. Guo, A. Baker, J. Guo, and C. A. Randall, “Protocol for Ultralow-Temperature Ceramic Sintering: An Integration of Nanotechnology and the Cold Sintering Process,” *ACS Nano*, vol. 10, no. 11, pp. 10606–10614, 2016, doi: 10.1021/acsnano.6b03800.

[158] R. Boston, J. Guo, S. Funahashi, A. L. Baker, I. M. Reaney, and C. A. Randall, “Reactive intermediate phase cold sintering in strontium titanate,” *RSC Adv.*, vol. 8, no. 36, pp. 20372–20378, 2018, doi: 10.1039/c8ra03072c.

[159] H. Guo, J. Guo, A. Baker, and C. A. Randall, “Hydrothermal-Assisted Cold Sintering Process: A New Guidance for Low-Temperature Ceramic Sintering,” *ACS Appl. Mater. Interfaces*, vol. 8, no. 32, pp. 20909–20915, 2016, doi: 10.1021/acsami.6b07481.

[160] G. Taveri, S. Grasso, F. Gucci, J. Toušek, and I. Dlouhy, “Bio-Inspired Hydro-Pressure Consolidation of Silica,” *Adv. Funct. Mater.*, vol. 28, no. 48, pp. 1–8, 2018, doi: 10.1002/adfm.201805794.

[161] X. Y. Hong *et al.*, “The preparation of high-density aluminum-doped zinc oxide ceramics by cold sintering process,” *J. Alloys Compd.*, vol. 832, 2020, doi: 10.1016/j.jallcom.2019.153241.

[162] I. J. Induja and M. T. Sebastian, “Microwave dielectric properties of cold sintered Al2O3-NaCl composite,” *Mater. Lett.*, vol. 211, pp. 55–57, 2018, doi: 10.1016/j.matlet.2017.09.083.

[163] B. Suleiman, Q. Yu, Y. Ding, and Y. Li, “Fabrication of form stable NaCl-Al2O3 composite for thermal energy storage by cold sintering process,” *Front. Chem. Sci. Eng.*, vol. 13, no. 4, pp. 727–735, 2019, doi: 10.1007/s11705-019-1823-2.

[164] C. J. Boxley, J. J. Watkins, and H. S. White, “Al2O3 Film Dissolution in Aqueous Chloride Solutions,” *Electrochem. Soc.*, vol. 6, no. 10, 2003, doi: 10.1149/1.1603013.

[165] T. H. De Beauvoir and C. Estournès, “Translucent γ-AlOOH and γAl2O3 glass-ceramics using the cold sintering process,” vol. 194, 2020, doi: 10.1016/j.scriptamat.2020.113650.

[166] J. Guo, S. S. Berbano, H. Guo, A. L. Baker, M. T. Lanagan, and C. A. Randall, “Cold Sintering Process of Composites: Bridging the Processing Temperature Gap of Ceramic and Polymer Materials,” *Adv. Funct. Mater.*, vol. 26, no. 39, pp. 7115–7121, 2016, doi: 10.1002/adfm.201602489.

[167] X. Zhao, J. Guo, K. Wang, T. Herisson De Beauvoir, B. Li, and C. A. Randall, “Introducing a ZnO–PTFE (Polymer) Nanocomposite Varistor via the Cold Sintering Process,” *Adv. Eng. Mater.*, vol. 20, no. 7, pp. 1–8, 2018, doi: 10.1002/adem.201700902.

[168] D. Wang *et al.*, “Cold-Sintered Temperature Stable Na0.5Bi0.5MoO4-Li2MoO4 Microwave Composite Ceramics,” *ACS Sustain. Chem. Eng.*, vol. 6, no. 2, pp. 2438–2444, 2018, doi: 10.1021/acssuschemeng.7b03889.

[169] D. Wang *et al.*, “Temperature stable cold sintered (Bi0.95Li0.05)(V0.9Mo0.1)O4-Na2Mo2O7 microwave dielectric composites,” *Materials (Basel).*, vol. 12, no. 9, pp. 1–10, 2019, doi: 10.3390/ma12091370.

[170] IOMA (International Molybdenum Association), “Overview of Molybdenum in Biology,” 2021. https://www.imoa.info/HSE/environmental_data/molybdenum_in_biology.php (accessed Jan. 11, 2021).

[171] Metalary, “Molybdenum Price,” *2021*. https://www.metalary.com/molybdenum-price/ (accessed Jan. 11, 2021).

[172] D. Wang *et al.*, “Cold sintered CaTiO3-K2MoO4 microwave dielectric ceramics for integrated microstrip patch antennas,” *Appl. Mater. Today*, vol. 18, p. 100519, 2020, doi: 10.1016/j.apmt.2019.100519.

[173] D. Sohrabi Baba Heidary, M. Lanagan, and C. A. Randall, “Contrasting energy efficiency in various ceramic sintering processes,” *J. Eur. Ceram. Soc.*, vol. 38, no. 4, pp. 1018–1029, 2018, doi: 10.1016/j.jeurceramsoc.2017.10.015.

[174] S. H. Bang *et al.*, “Toward a size scale-up cold sintering process at reduced uniaxial pressure,” *J. Am. Ceram. Soc.*, vol. 103, no. 4, pp. 2322–2327, 2020, doi: 10.1111/jace.16976.

[175] A. Roosen, “Tape Casting,” *Ceram. Sci. Technol.*, vol. 3–4, pp. 39–62, 2013, doi: 10.1002/9783527631940.ch33.

[176] G. Manoharan, M. Karuppiah, N. K. Sahu, and K. Hembram, “High performance multi-layer varistor (MLV) from doped ZnO nanopowders by water based tape casting: Rheology, sintering, microstructure and properties,” *Ceram. Int.*, vol. 44, no. 7, pp. 7837–7843, 2018, doi: 10.1016/j.ceramint.2018.01.218.

[177] M. Jabbari, R. Bulatova, A. I. Y. Tok, C. R. H. Bahl, E. Mitsoulis, and J. H. Hattel, “Ceramic tape casting: A review of current methods and trends with emphasis on rheological behaviour and flow analysis,” *Mater. Sci. Eng. B Solid-State Mater. Adv. Technol.*, vol. 212, pp. 39–61, 2016, doi: 10.1016/j.mseb.2016.07.011.

[178] E. Liniger and R. Raj, “Packing and Sintering of Two-Dimensional Structures Made fro Bimodal Particle Size Distributions,” *J. Am. Ceram. Soc.*, vol. 70, no. 11, pp. 843–849, 1987, doi: 10.1111/j.1151-2916.1987.tb05638.x.

[179] S. John Milne, M. Patel, and E. Dickinson, “Experimental studies of particle packing and sintering behaviour of monosize and bimodal spherical silica powders,” *J. Eur. Ceram. Soc.*, vol. 11, no. 1, pp. 1–7, 1993, doi: 10.1016/0955-2219(93)90052-S.

[180] R. M. German, “Prediction of packing and sintering density for bimodal powder mixtures,” *Adv. Powder Metall.*, vol. 3, no. May, pp. 1–15, 1992, doi: 10.1016/0026-0657(93)92034-3.

[181] A. Azzolini, V. M. Sglavo, and J. A. Downs, “Novel method for the identification of the maximum solid loading suitable for optimal extrusion of ceramic pastes,” *J. Adv. Ceram.*, vol. 3, no. 1, pp. 7–16, 2014, doi: 10.1007/s40145-014-0088-y.

[182] J. M. F. Ferreira and H. M. M. Diz, “Effect of solids loading on slip-casting performance of silicon carbide slurries,” *J. Am. Ceram. Soc.*, vol. 82, no. 8, pp. 1993–2000, 1999, doi: 10.1111/j.1151-2916.1999.tb02031.x.

[183] M. C. C. Giacovazzo, H.L Monaco, G. Artioli, D. Viterbo, M. Milanesio, G. Ferraris, G. Gilli, P. Gilli, G. Zanotti, *Fundamentals of Crystallography*, 3rd ed. Oxford Science Publications, 2011.

[184] University of Cambridge, “Raman Spectroscopy,” *University of Cambridge*, 2007. https://www.doitpoms.ac.uk/tlplib/raman/index.php.

[185] Moxfyre, “Energy-level diagram showing the states involved in Raman spectra,” *Wikipedia*, 2009. https://en.wikipedia.org/wiki/Raman_spectroscopy#/media/File:Raman_energy_levels.svg.

[186] W. D. Callister and D. G. Rethwisch, *Materials Science and Engineering*, 8th Editio. Wiley, 2011.

[187] A. Abdullah and A. Mohammed, “Scanning Electron Microscopy (SEM): A Review Scanning Electron Microscopy (SEM): A Review,” *Int. Conf. Hydraul. Pneum.*, no. January, pp. 1–9, 2019.

[188] G.D.Danilatos, “Review and outline of environmental SEM at present.”, ESEM Research Laboratory, 1991, Vol 162, Issue 3, Journal of Microscopy, doi: 10.1111/j.1365-2818.1991.tb03149.x

[189] X. Llovet, A. Moy, P. T. Pinard, and J. H. Fournelle, “Electron probe microanalysis: A review of recent developments and applications in materials science and engineering,” *Prog. Mater. Sci.*, vol. 116, no. May 2020, p. 100673, 2021, doi: 10.1016/j.pmatsci.2020.100673.

[190] D. Henry, “Wavelength-Dispersive X-Ray Spectroscopy (WDS),” *Louisiana State University*, 2016. https://serc.carleton.edu/research_education/geochemsheets/wds.html.

[191] Ponor, “Electron-matter interaction volume and types of signal generated,” *Wikipedia*, 2020. https://en.wikipedia.org/wiki/Scanning_electron_microscope#/media/File:Electron-matter_interaction_volume_and_various_types_of_signal_generated_-_v2.svg.

[192] J. T. S. Irvine, D. C. Sinclair, and A. R. West, “Electroceramics: Characterization by Impedance Spectroscopy,” *Adv. Mater.*, vol. 2, no. 3, pp. 132–138, 1990, doi: 10.1002/adma.19900020304.

[193] X. Wang, “Non-Destructive Characterisation Of Structural Ceramics Using Impedance Spectroscopy,” 2001.

[194] Y. Jing *et al.*, “Remarkably improved electrical conductivity of ZnO ceramics by cold sintering and post-heat-treatment,” *Ceram. Int.*, vol. 44, no. 16, pp. 20570–20574, 2018, doi: 10.1016/j.ceramint.2018.07.192.

[195] X. Jiang *et al.*, “Preparation of high density ZnO ceramics by the Cold Sintering Process,” *Ceram. Int.*, vol. 45, no. 14, pp. 17382–17386, 2019, doi: 10.1016/j.ceramint.2019.05.298.

[196] F. Leiter, H. Alves, D. Pfisterer, N. G. Romanov, D. M. Hofmann, and B. K. Meyer, “Oxygen vacancies in ZnO,” *Phys. B Condens. Matter*, vol. 340–342, pp. 201–204, 2003, doi: 10.1016/j.physb.2003.09.031.

[197] K. Vanheusden, W. L. Warren, C. H. Seager, D. R. Tallant, J. A. Voigt, and B. E. Gnade, “Mechanisms behind green photoluminescence in ZnO phosphor powders,” *J. Appl. Phys.*, vol. 79, no. 10, pp. 7983–7990, 1996, doi: 10.1063/1.362349.

[198] R. K. Sendi and S. Mahmud, “Impact of sintering temperature on the structural, electrical, and optical properties of doped ZnO nanoparticle-based discs,” *Appl. Surf. Sci.*, vol. 261, pp. 128–136, 2012, doi: 10.1016/j.apsusc.2012.07.115.

[199] A. P. Hynes, R. H. Doremus, and R. W. Siegel, “Sintering and characterization of nanophase zinc oxide,” *J. Am. Ceram. Soc.*, vol. 85, no. 8, pp. 1979–1987, 2002, doi: 10.1111/j.1151-2916.2002.tb00391.x.

[200] Y. Du, M. S. Zhang, J. Hong, Y. Shen, Q. Chen, and Z. Yin, “Structural and optical properties of nanophase zinc oxide,” *Appl. Phys. A Mater. Sci. Process.*, vol. 76, no. 2, pp. 171–176, 2003, doi: 10.1007/s003390201404.

[201] A. Serrano *et al.*, “Cold sintering process of ZnO ceramics: Effect of the nanoparticle/microparticle ratio,” *J. Eur. Ceram. Soc.*, vol. 40, no. 15, pp. 5535–5542, 2020, doi: 10.1016/j.jeurceramsoc.2020.05.059.

[202] K. Lu, “Sintering of nanoceramics,” *Int. Mater. Rev.*, vol. 53, no. 1, pp. 21–38, 2008, doi: 10.1179/174328008X254358.

[203] P. Singh, A. Kumar, Deepak, and D. Kaur, “Growth and characterization of ZnO nanocrystalline thin films and nanopowder via low-cost ultrasonic spray pyrolysis,” *J. Cryst. Growth*, vol. 306, no. 2, pp. 303–310, 2007, doi: 10.1016/j.jcrysgro.2007.05.023.

[204] M. Šćepanović, M. Grujić-Brojčin, K. Vojisavljević, S. Bernikc, and T. Srećković, “Raman study of structural disorder in ZnO nanopowders,” *J. Raman Spectrosc.*, vol. 41, no. 9, pp. 914–921, 2010, doi: 10.1002/jrs.2546.

[205] R. L. de S. e. Silva and A. Franco, “Raman spectroscopy study of structural disorder degree of ZnO ceramics,” *Mater. Sci. Semicond. Process.*, vol. 119, no. July, p. 105227, 2020, doi: 10.1016/j.mssp.2020.105227.

[206] R. Cuscó *et al.*, “Temperature dependence of Raman scattering in ZnO,” *Phys. Rev. B - Condens. Matter Mater. Phys.*, vol. 75, no. 16, 2007, doi: 10.1103/PhysRevB.75.165202.

[207] A. Ndayishimiye *et al.*, “Comparing hydrothermal sintering and cold sintering process: Mechanisms, microstructure, kinetics and chemistry,” *J. Eur. Ceram. Soc.*, vol. 40, no. 4, pp. 1312–1324, 2020, doi: 10.1016/j.jeurceramsoc.2019.11.049.

[208] A. V. Ghule *et al.*, “In situ thermo-TOF-SIMS study of thermal decomposition of zinc acetate dihydrate,” *J. Mass Spectrom.*, vol. 39, no. 10, pp. 1202–1208, 2004, doi: 10.1002/jms.721.

[209] A. V. Ghule, B. Lo, S. H. Tzing, K. Ghule, H. Chang, and Y. C. Ling, “Simultaneous thermogravimetric analysis and in situ thermo-Raman spectroscopic investigation of thermal decomposition of zinc acetate dihydrate forming zinc oxide nanoparticles,” *Chem. Phys. Lett.*, vol. 381, no. 3–4, pp. 262–270, 2003, doi: 10.1016/j.cplett.2003.09.125.

[210] B. Dargatz *et al.*, “FAST/SPS sintering of nanocrystalline zinc oxide-Part I: Enhanced densification and formation of hydrogen-related defects in presence of adsorbed water,” *J. Eur. Ceram. Soc.*, vol. 36, no. 5, pp. 1207–1220, 2016, doi: 10.1016/j.jeurceramsoc.2015.12.009.

[211] S. Kohiki, M. Nishitani, T. Wada, and T. Hirao, “Enhanced conductivity of zinc oxide thin films by ion implantation of hydrogen atoms,” *Appl. Phys. Lett.*, vol. 64, no. 21, pp. 2876–2878, 1994, doi: 10.1063/1.111401.

[212] M. W. Wu, P. H. Lai, C. H. Hong, and F. C. Chou, “The sintering behavior, microstructure, and electrical properties of gallium-doped zinc oxide ceramic targets,” *J. Eur. Ceram. Soc.*, vol. 34, no. 15, pp. 3715–3722, 2014, doi: 10.1016/j.jeurceramsoc.2014.05.022.

[213] G. Gonçalves, E. Elangovan, P. Barquinha, L. Pereira, R. Martins, and E. Fortunato, “Influence of post-annealing temperature on the properties exhibited by ITO, IZO and GZO thin films,” *Thin Solid Films*, vol. 515, no. 24 SPEC. ISS., pp. 8562–8566, 2007, doi: 10.1016/j.tsf.2007.03.126.

[214] T. Prasada Rao and M. C. Santhosh Kumar, “Physical properties of Ga-doped ZnO thin films by spray pyrolysis,” *J. Alloys Compd.*, vol. 506, no. 2, pp. 788–793, 2010, doi: 10.1016/j.jallcom.2010.07.071.

[215] A. de Souza Gonçalves, S. Antonio Marques de Lima, M. Rosaly Davolos, S. Gutierrez Antônio, and C. de Oliveira Paiva-Santos, “The effects of ZnGa2O4 formation on structural and optical properties of ZnO:Ga powders,” *J. Solid State Chem.*, vol. 179, no. 5, pp. 1330–1334, 2006, doi: 10.1016/j.jssc.2006.01.046.

[216] S. Shawuti, M. M. Can, M. A. Gülgün, and T. Firat, “Grain size dependent comparison of ZnO and ZnGa2O4 semiconductors by impedance spectrometry,” *Electrochim. Acta*, vol. 145, pp. 132–138, 2014, doi: 10.1016/j.electacta.2014.08.084.

[217] C. Bundesmann *et al.*, “Raman scattering in ZnO thin films doped with Fe, Sb, Al, Ga, and Li,” *Appl. Phys. Lett.*, vol. 83, no. 10, pp. 1974–1976, 2003, doi: 10.1063/1.1609251.

[218] S. Kumar, G. Sarau, C. Tessarek, M. Göbelt, S. Christiansen, and R. Singh, “Study of high quality spinel zinc gallate nanowires grown using CVD and ALD techniques,” *Nanotechnology*, vol. 26, no. 33, 2015, doi: 10.1088/0957-4484/26/33/335603.

[219] J. Akedo, “Aerosol deposition of ceramic thick films at room temperature: Densification mechanism of ceramic layers,” *J. Am. Ceram. Soc.*, vol. 89, no. 6, pp. 1834–1839, 2006, doi: 10.1111/j.1551-2916.2006.01030.x.

[220] J. J. Choi, B. D. Hahn, J. Ryu, W. H. Yoon, B. K. Lee, and D. S. Park, “Preparation and characterization of piezoelectric ceramic-polymer composite thick films by aerosol deposition for sensor application,” *Sensors Actuators, A Phys.*, vol. 153, no. 1, pp. 89–95, 2009, doi: 10.1016/j.sna.2009.04.025.

[221] DuPont, “Kapton® HN general-purpose polyimide film.” https://www.dupont.com/products/kapton-hn.html.

[222] “Kapton,” *Wikipedia*, 2021. https://en.wikipedia.org/wiki/Kapton (accessed Jul. 22, 2021).

[223] N. M. Jennett, “Good Practice Guide The Scratch Test : Calibration , Verification and the Use of a Certified,” no. 54.

[224] J. Kim, K. S. Kim, and Y. H. Kim, “Mechanical effects in peel adhesion test,” *J. Adhes. Sci. Technol.*, vol. 3, no. 1, pp. 175–187, 1989, doi: 10.1163/156856189X00146.

[225] N. M. M. Ramos, M. L. Simões, J. M. P. Q. Delgado, and V. P. De Freitas, “Reliability of the pull-off test for in situ evaluation of adhesion strength,” *Constr. Build. Mater.*, vol. 31, pp. 86–93, 2012, doi: 10.1016/j.conbuildmat.2011.12.097.

[226] B. Dargatz, J. Gonzalez-Julian, and O. Guillon, “Anomalous coarsening of nanocrystalline zinc oxide particles in humid air,” *J. Cryst. Growth*, vol. 419, no. June, pp. 69–78, 2015, doi: 10.1016/j.jcrysgro.2015.02.101.

[227] D. Landek, L. Ćurković, I. Gabelica, M. Kerolli Mustafa, and I. Žmak, “Optimization of Sintering Process of Alumina Ceramics Using Response Surface Methodology,” *Sustainability*, vol. 13, no. 12, p. 6739, 2021, doi: 10.3390/su13126739.

[228] S. Castet, J. L. Dandurand, J. Schott, and R. Gout, “Boehmite solubility and aqueous aluminum speciation in hydrothermal solutions (90-350°C): Experimental study and modeling,” *Geochim. Cosmochim. Acta*, vol. 57, no. 20, pp. 4869–4884, 1993, doi: 10.1016/0016-7037(93)90126-H.

[229] M. Conroy *et al.*, “Importance of interlayer H bonding structure to the stability of layered minerals,” *Sci. Rep.*, vol. 7, no. 1, pp. 1–10, 2017, doi: 10.1038/s41598-017-13452-7.

[230] S. S. Division, U. Kingdom, A. Energy, A. Energy, and I. Introduction, “The Strength of Metal / Alumina Interfaces,” vol. 3, pp. 571–576, 1968.

[231] A. Nagode *et al.*, “The effect of sol–gel boehmite coatings on the corrosion and decarburization of C45 steel,” *J. Sol-Gel Sci. Technol.*, vol. 86, no. 3, pp. 568–579, 2018, doi: 10.1007/s10971-018-4664-4.

[232] M. S. Djošić, V. B. Miskovic-Stankovic, D. T. Janaćković, Z. M. Kačarević-Popović, and R. D. Petrović, “Electrophoretic deposition and characterization of boehmite coatings on titanium substrate,” *Colloids Surfaces A Physicochem. Eng. Asp.*, vol. 274, no. 1–3, pp. 185–191, 2006, doi: 10.1016/j.colsurfa.2005.08.048.

[233] A. V. de C. Braga, D. C. B. do Lago, A. R. Pimenta, and L. F. de Senna, “The influence of heat treatment of inorganic conversion coatings produced by sol-gel dip coating on the anticorrosive properties of alumina films deposited on steel substrate – Part I: Single conversion coatings,” *Surf. Coatings Technol.*, vol. 372, no. February, pp. 190–200, 2019, doi: 10.1016/j.surfcoat.2019.05.040.

[234] R. Brajpuriya and T. Shripathi, “Investigation of Fe/Al interface as a function of annealing temperature using XPS,” *Appl. Surf. Sci.*, vol. 255, no. 12, pp. 6149–6154, 2009, doi: 10.1016/j.apsusc.2009.01.070.

[235] B. Ratzker, A. Wagner, M. Sokol, S. Kalabukhov, M. P. Dariel, and N. Frage, “Optical and mechanical properties of transparent alumina fabricated by high-pressure spark plasma sintering,” *J. Eur. Ceram. Soc.*, vol. 39, no. 8, pp. 2712–2719, 2019, doi: 10.1016/j.jeurceramsoc.2019.03.025.

[236] D. Liu *et al.*, “Stress-enhanced grain growth in a nanostructured aluminium alloy during spark plasma sintering,” *Philos. Mag. Lett.*, vol. 94, no. 11, pp. 741–748, 2014, doi: 10.1080/09500839.2014.975295.

[237] J. Besson and M. Abouaf, “Grain growth enhancement in alumina during hot isostatic pressing,” *Acta Metall. Mater.*, vol. 39, no. 10, pp. 2225–2234, 1991, doi: 10.1016/0956-7151(91)90004-K.

[238] J. X. Xue, J. X. Liu, B. H. Xie, and G. J. Zhang, “Pressure-induced preferential grain growth, texture development and anisotropic properties of hot pressed hexagonal boron nitride ceramics,” *Scr. Mater.*, vol. 65, no. 11, pp. 966–969, 2011, doi: 10.1016/j.scriptamat.2011.08.025.

[239] J. R. Seidensticker and M. J. Mayo, “Dynamic and static grain growth during the superplastic deformation of 3Y-TZP,” *Scr. Mater.*, vol. 38, no. 7, pp. 1091–1100, 1998, doi: 10.1016/S1359-6462(98)00004-9.

[240] M. F. Ashby and R. A. Verrall, “Diffusion-accommodated flow and superplasticity,” *Acta Metall.*, vol. 21, no. 2, pp. 149–163, 1973, doi: 10.1016/0001-6160(73)90057-6.

[241] D. S. Wilkinson and C. H. Cáceres, “On the mechanism of strain-enhanced grain growth during superplastic deformation,” *Acta Metall.*, vol. 32, no. 9, pp. 1335–1345, 1984, doi: 10.1016/0001-6160(84)90079-8.

[242] J. R. Seidensticker and M. J. Mayo, “A topological rationale for the dependence of grain growth on strain during superplastic deformation,” *Acta Mater.*, vol. 46, no. 14, pp. 4883–4893, 1998, doi: 10.1016/S1359-6454(98)00201-8.

[243] D. Moldovan, D. Wolf, and S. R. Phillpot, “Theory of diffusion-accommodated grain rotation in columnar polycrystalline microstructures,” *Acta Mater.*, vol. 49, no. 17, pp. 3521–3532, 2001, doi: 10.1016/S1359-6454(01)00240-3.

[244] A. J. Haslam, D. Moldovan, V. Yamakov, D. Wolf, S. R. Phillpot, and H. Gleiter, “Stress-enhanced grain growth in a nanocrystalline material by molecular-dynamics simulation,” *Acta Mater.*, vol. 51, no. 7, pp. 2097–2112, 2003, doi: 10.1016/S1359-6454(03)00011-9.

[245] M. Upmanyu, D. J. Srolovitz, A. E. Lobkovsky, J. A. Warren, and W. C. Carter, “Simultaneous grain boundary migration and grain rotation,” *Acta Mater.*, vol. 54, no. 7, pp. 1707–1719, 2006, doi: 10.1016/j.actamat.2005.11.036.

[246] B. Ratzker, A. Wagner, M. Sokol, S. Kalabukhov, and N. Frage, “Stress-enhanced dynamic grain growth during high-pressure spark plasma sintering of alumina,” *Acta Mater.*, vol. 164, pp. 390–399, 2019, doi: 10.1016/j.actamat.2018.11.001.

[247] Y. Noel, R. Demichelis, F. Pascale, P. Ugliengo, R. Orlando, and R. Dovesi, “Ab initio quantum mechanical study of γ-AlOOH boehmite: Structure and vibrational spectrum,” *Phys. Chem. Miner.*, vol. 36, no. 1, pp. 47–59, 2009, doi: 10.1007/s00269-008-0257-z.

[248] Y. Jiang, Y. Xie, and H. Guo, “A computational study of energy barriers of structural transformations and hydrogen transfer in boehmite,” *RSC Adv.*, vol. 8, no. 5, pp. 2377–2384, 2018, doi: 10.1039/c7ra12273j.

[249] H. D. Ruan, R. L. Frost, and J. T. Kloprogge, “Comparison of Raman spectra in characterizing gibbsite, bayerite, diaspore and boehmite,” *J. Raman Spectrosc.*, vol. 32, no. 9, pp. 745–750, 2001, doi: 10.1002/jrs.736.

[250] X. Zhou *et al.*, “The solvothermal synthesis of γ-AlOOH nanoflakes and their compression behaviors under high pressures,” *RSC Adv.*, vol. 7, no. 9, pp. 4904–4911, 2017, doi: 10.1039/c6ra27571k.

[251] J. Zuo, C. Xu, Y. Liu, and Y. Qian, “Crystallite size effects on the Raman spectra of Mn3O4,” *Nanostructured Mater.*, vol. 10, no. 8, pp. 1331–1335, 1998, doi: 10.1016/S0965-9773(99)00002-1.

[252] S. Cava *et al.*, “Structural characterization of phase transition of Al2O3 nanopowders obtained by polymeric precursor method,” *Mater. Chem. Phys.*, vol. 103, no. 2–3, pp. 394–399, 2007, doi: 10.1016/j.matchemphys.2007.02.046.

[253] B. Jongsomjit, J. Panpranot, and J. G. Goodwin, “Effect of zirconia-modified alumina on the properties of Co/γ -Al2O3 catalysts,” *J. Catal.*, vol. 215, no. 1, pp. 66–77, 2003, doi: 10.1016/S0021-9517(02)00102-1.

[254] E. Smith and G. Dent, *Modern Raman Spectroscopy: A Practical Approach*. Wiley, 2005.

[255] O. N. Shebanova and P. Lazor, “Raman spectroscopic study of magnetite (FeFe2O4): A new assignment for the vibrational spectrum,” *J. Solid State Chem.*, vol. 174, no. 2, pp. 424–430, 2003, doi: 10.1016/S0022-4596(03)00294-9.

[256] Y. Liu *et al.*, “Study of Raman spectra for γ-Al2O3 models by using first-principles method,” *Solid State Commun.*, vol. 178, pp. 16–22, 2014, doi: 10.1016/j.ssc.2013.09.030.

[257] A. S. Jbara, Z. Othaman, A. A. Ati, and M. A. Saeed, “Characterization of γ- Al2O3 nanopowders synthesized by Co-precipitation method,” *Mater. Chem. Phys.*, vol. 188, pp. 24–29, 2017, doi: 10.1016/j.matchemphys.2016.12.015.

[258] X. Xue *et al.*, “Raman investigation of nanosized TiO 2: Effect of crystallite size and quantum confinement,” *J. Phys. Chem. C*, vol. 116, no. 15, pp. 8792–8797, 2012, doi: 10.1021/jp2122196.

[259] J. Lankford, “Compressive strength and microplasticity in polycrystalline alumina,” *J. Mater. Sci.*, vol. 12, no. 4, pp. 791–796, 1977, doi: 10.1007/BF00548172.

[260] J. K. Kim and S. T. Yi, “Application of size effect to compressive strength of concrete members,” *Sadhana - Acad. Proc. Eng. Sci.*, vol. 27, no. PART 4, pp. 467–484, 2002, doi: 10.1007/BF02706995.

[261] A. Samimi, M. Zakeri, B. Maleki, and D. Mohebbi-Kalhori, “Experimental and statistical assessments of the mechanical strength reliability of gamma alumina catalyst supports,” *Particuology*, vol. 21, pp. 74–81, 2015, doi: 10.1016/j.partic.2014.10.002.

[262] G. H. Watson, W. B. Daniels, and C. S. Wang, “Measurements of Raman intensities and pressure dependence of phonon frequencies in sapphire,” *J. Appl. Phys.*, vol. 52, no. 2, pp. 956–958, 1981, doi: 10.1063/1.328785.

[263] B. Montanari, B. Civalleri, C. Zicovich-Wilson, and R. Dovesi, “Influence of the Exchange-Correlation Functional in All-Electron Calculations of the Vibrational Frequencies of Corundum (a-Al2O3),” *Int. J. Quantum Chem. J.*, vol. 106, no. 7, pp. 1703–1714, 2006, doi: 10.1002/qua.

[264] S. P. S. Porto and R. S. Krishnan, “Raman effect of corundum,” *J. Chem. Phys.*, vol. 47, no. 3, pp. 1009–1012, 1967, doi: 10.1063/1.1711980.

[265] J. Thapa, B. Liu, S. D. Woodruff, B. T. Chorpening, and M. P. Buric, “Raman scattering in single-crystal sapphire at elevated temperatures,” *Appl. Opt.*, vol. 56, no. 31, p. 8598, 2017, doi: 10.1364/ao.56.008598.

[266] M. Kadleíková, J. Breza, and M. Veselý, “Raman spectra of synthetic sapphire,” *Microelectronics J.*, vol. 32, no. 12, pp. 955–958, 2001, doi: 10.1016/S0026-2692(01)00087-8.

[267] J. L. Woolfrey, “Effect of Green Density on the Initial-Stage Sintering Kinetics of UO2s,” *J. Am. Ceram. Soc.*, vol. 55, no. 8, pp. 383–389, 1972, doi: 10.1111/j.1151-2916.1972.tb11318.x.

[268] M. N. Rahaman, L. C. De Jonghe, and M. -Y Chu, “Effect of Green Density on Densification and Creep During Sintering,” *J. Am. Ceram. Soc.*, vol. 74, no. 3, pp. 514–519, 1991, doi: 10.1111/j.1151-2916.1991.tb04053.x.

[269] L. Pach, R. Roy, and S. Komarneni, “Nucleation of Alpha Alumina in Boehmite Gel,” *J. Mater. Res.*, vol. 5, no. 2, pp. 278–285, 1990, doi: 10.1557/JMR.1990.0278.

[270] R. Boulesteix, A. Maître, L. Chrétien, Y. Rabinovitch, and C. Sallé, “Microstructural evolution during vacuum sintering of yttrium aluminum garnet transparent ceramics: Toward the origin of residual porosity affecting the transparency,” *J. Am. Ceram. Soc.*, vol. 96, no. 6, pp. 1724–1731, 2013, doi: 10.1111/jace.12315.

[271] H. P. Cahoon and C. J. Christensen, “Sintering and Grain Growth,” *J. Am. Ceram. Soc.*, vol. 71, 1956, doi: 10.1887/0750309024/b1147c10.

[272] R. L. Coble, “Sintering Alumina: Effect of Atmospheres,” *Am. Ceram. Soc. Ceram. Stud. Sect.*, vol. 97, pp. 123–127, 1955.

[273] J. G. J. Peelen, “Alumina : sintering and optical properties,” *Eindhoven Tech. Hogesch. Eindhoven*, no. 1977, 1977, doi: 10.6100/IR4212.

[274] A. R. Boccaccini and C. Kaya, “Alumina ceramics based on seeded boehmite and electrophoretic deposition,” *Ceram. Int.*, vol. 28, no. 8, pp. 893–897, 2002, doi: 10.1016/S0272-8842(02)00070-6.

[275] I. J. Bae and S. Baik, “Abnormal grain growth of alumina,” *J. Am. Ceram. Soc.*, vol. 80, no. 5, pp. 1149–1156, 1997, doi: 10.1111/j.1151-2916.1997.tb02957.x.

[276] A. Zwiren and T. F. Murphy, “Comparison of Binder Jetting Additive Manufacturing to Press and Sinter 316L Stainless Steel,” *Int. J. powder Metall.*, vol. 54, no. 4, 2018.

[277] R. J. Brook, “Pore-Grain Boundary Interactions and Grain Growth,” *J. Am. Ceram. Soc.*, vol. 52, no. 1, pp. 56–57, 1969, doi: 10.1111/j.1151-2916.1969.tb12664.x.

[278] L. Shi, T. Qu, D. Liu, Y. Deng, B. Yang, and Y. Dai, *Process of Thermal Decomposition of Lithium Carbonate*. 2020.

[279] B. Cockayne and B. Lent, “The Czochralski growth of single crystal lithium aluminate, LiAlO2,” *J. Cryst. Growth*, vol. 54, no. 3, pp. 546–550, 1981, doi: 10.1016/0022-0248(81)90511-X.

[280] H. Cao, B. Xia, Y. Zhang, and N. Xu, “LiAlO2-coated LiCoO2 as cathode material for lithium ion batteries,” *Solid State Ionics*, vol. 176, no. 9–10, pp. 911–914, 2005, doi: 10.1016/j.ssi.2004.12.001.

[281] H. Li, X. Xi, J. Ma, K. Hua, and A. Shui, “Low-temperature sintering of coarse alumina powder compact with sufficient mechanical strength,” *Ceram. Int.*, vol. 43, no. 6, pp. 5108–5114, 2017, doi: 10.1016/j.ceramint.2017.01.024.

[282] I. B. Cutler, C. Bradshaw, C. J. Christensen, and E. P. Hyatt, “Sintering of Alumina at Temperatures of 1400°C. and Below,” vol. 40, no. 1949, 1954.

[283] H. Alumina, L. A. Xue, and I. Chen, “Deformation and Grain Growth of Low-Temperature-Sintered High-Purity Alumina,” pp. 3518–3521, 1990.

[284] D. I. Matkin, W. Munro, and T. M. Valentine, “The fabrication of α-alumina by reactive hot-pressing,” *J. Mater. Sci.*, vol. 6, no. 7, pp. 974–980, 1971, doi: 10.1007/BF00549948.

[285] J. L. McArdle and G. L. Messing, “Transformation, Microstructure Development, and Densification in alpha-Fe2O3,-Seeded Boehmite-Derived Alumina,” *J. Am. Ceram. Soc.*, vol. 76, no. 1, pp. 214–222, 1993.

[286] B. Dargatz, J. Gonzalez-Julian, and O. Guillon, “Improved compaction of ZnO nano-powder triggered by the presence of acetate and its effect on sintering,” *Sci. Technol. Adv. Mater.*, vol. 16, no. 2, 2015, doi: 10.1088/1468-6996/16/2/025008.

[287] R. Boston, J. Guo, S. Funahashi, A. L. Baker, I. M. Reaney, and C. A. Randall, “Reactive intermediate phase cold sintering in strontium titanate,” *RSC Adv.*, vol. 8, no. 36, pp. 20372–20378, 2018, doi: 10.1039/c8ra03072c.

[288] A. Sawalha, M. Abu-Abdeen, and A. Sedky, “Electrical conductivity study in pure and doped ZnO ceramic system,” *Phys. B Condens. Matter*, vol. 404, no. 8–11, pp. 1316–1320, 2009, doi: 10.1016/j.physb.2008.12.017.

APPENDIX 1 – ZnO/GZO Grain Sizes

Table A.1: Raw calculated average and median grain sizes, and grain size distributions for all samples based upon SEM data

Powder	Pressure (MPa)	Temp (°C)	Average Grain Size (nm)	Median Grain Size (nm)	Standard Deviation Grain Size Distribution (nm)
nZnO	Raw	Raw	59	55	21
nZnO	190	125	105	96	42
nZnO	190	200	127	119	46
nZnO	190	300	408	366	155
nZnO	250	125	97	96	23
nZnO	250	200	326	302	107
nZnO	250	300	786	722	874
nZnO	375	125	68	62	26
nZnO	375	200	196	172	98
nZnO	375	300	1119	874	733
cZnO	Raw	Raw	171	156	81
cZnO	190	125	176	153	105
cZnO	190	200	301	272	173
cZnO	190	300	285	235	154
cZnO	250	125	200	179	105
cZnO	250	200	286	237	173
cZnO	250	300	505	401	330
cZnO	375	125	313	260	177
cZnO	375	200	226	206	132
cZnO	375	300	538	364	458
GZO	Raw	Raw	31	30	7
GZO	190	300	244	208	215
GZO	250	300	224	137	197
GZO	375	200	31	29	10
GZO	375	300	218	191	158